School of Physics and Astronomy

Probing the electronic and geometric structure of adsorbed porphyrins and fullerenes

Simon Taylor MSci (Hons)

Supervisor: Prof. Philip Moriarty

Thesis submitted to the University of Nottingham

for the degree of Doctor of Philosophy

May 2016

Abstract

In this thesis, the geometric and electronic structure of tetra(4-bromophenyl) porphyrin (Br_4TPP) and $H_2O@C_{60}/C_{60}$ molecules are studied on Cu, Au and Ag surfaces. Developing an understanding of the physics at the single molecule level is not only important to the nanoscience field, but also in future progression towards nanoscale devices.

Adsorption of Br_4TPP molecules on Au(111) and Cu(111) substrates reveal two conformers. It was previously understood that chemisorption drove conformational changes of the molecules with respect to the substrate, but work resulting from studies in this thesis using STM for single molecule manipulation, combined with DFT and MD simulations concludes that large conformational changes are dominated by van der Waals interactions. The mechanochemical response of Br_4TPP was also investigated, and by using NC-AFM it was found that there was a large difference in requirements for lateral force manipulation between the two conformers. Dispersion corrected DFT calculations emphasise significant differences in diffusion barrier for each conformer. STM was also used to reproducibly de-brominate Br_4TPP in a controlled sequence, and the electronic mapping of molecular orbitals is also presented.

In the second half of this thesis, $H_2O@C_{60}/C_{60}$ has been investigated on Cu(111) and $H_2O@C_{60}$ on Ag(111) surfaces using STM/NC-AFM and XPS/NIXSW respectively. Both STM and NC-AFM are unable to distinguish between filled and empty C_{60} cages. Remarkably, $H_2O@C_{60}$ behaves similarly to C_{60} during molecule-induced surface reconstruction on

Cu(111). A careful NC-AFM study shows apparent intermolecular bonding between neighbouring $H_2O@C_{60}/C_{60}$ molecules. This highlights the fact that intermolecular artifacts are common across all SPM studies. Due to the shortfall of STM and NC-AFM in this particular case, XPS was used to further probe the C_{60} cages to see if they were encapsulated with H_2O, and was confirmed by the O1s peak at 532eV. Unsurprisingly, valence band spectra reiterated the similarity between filled and empty C_{60} molecules. NIXSW was used to attempt to triangulate the O1s signal within the C_{60} cage. Initial calculations suggest the encapsulated water molecule is located 5.6Å relative to the Ag(111) substrate, which is approximately central in inside the C_{60} cage.

Peer reviewed publications

Samuel P. Jarvis, **Simon Taylor**, Jakub D. Baran, Damien Thompson, Alexander Saywell, Barry Mangham, Neil R. Champness, J. Andreas Larsson and Philip Moriarty. *"Physisorption Controls the Conformation and Density of States of an Adsorbed Porphyrin"*. Journal of Physical Chemistry C, 119 (50), pp 27982-27994 (2015)

Samuel P. Jarvis, **Simon Taylor**, Jakub D. Baran, Neil. R. Champness, J. Andreas Larsson and Philip Moriarty. *"Measuring the mechanical properties of molecular conformers"*. Nature Communcations 6, 8338 (2015)

Samuel P. Jarvis, Mohammed A. Rashid, Adam Sweetman, Jeremy Leaf, **Simon Taylor**, Philip Moriarty and Jeanette Dunn. *"Intermolecular artifacts in probe microscope images of C_{60} assemblies"*. Physical Review B 92, 241405(r) (2015)

Publications in preparation

Simon Taylor, Samuel P. Jarvis, Salvatore Mamone, Jeremy Leaf, Philipp Rahe, Adam Sweetman, Alex Saywell, Richard A. J. Woolley, Robert Jones, Richard Whitby, Antony Horsewill, Malcolm Levitt and Philip Moriarty. *"Molecules within molecules: X-ray standing wave spectroscopy of incarcerated H_2O"*. (In preparation), (2016)

Acknowledgements

If someone told me ten years ago that I could do a PhD, I would have laughed at them, hysterically. This journey has not only drastically expanded my knowledge, determination and will to learn new things, but it has also transferred into other areas in my life. If you have a dream, or an idea, no matter how crazy it is- try it.

To my supervisor, Philip Moriarty, I could thank you a $1x10^6$ times over and it still wouldn't be enough. Your passion, dedication and astonishing work ethic towards science motivated me every day. I feel incredibly fortunate to have had you as my supervisor, so thank you for giving me this opportunity. I hope one day I can return the favour, even if it's in the form of massive quantities of roasted and salted peanuts.

I would like to thank Sam Jarvis for the years of effort to teaching me how to use the Createc system, and in general for being my experimental and slow-cooker recipe mentor through the entirety of my PhD. Rich Woolley, thanks for letting me loose on the Createc before my PhD even started, for everything you taught me and for putting up with my silly questions throughout.

To my current and former colleagues; Adam Sweetman, Peter Sharp, Julian Stirling, Ioannis Lekkas, Philipp Rahe, Morten Moller, Alex Saywell, Rob Jones, Peter Beton, Alex Summerfield, Dave Farmer, Robert Temperton, Karsten Handrup, Alex Allen, Maria Wieland, Simon Svatek and Izabela Cebula, thank you for your help along the way, you all made PhD life that little bit easier, including the fruitful conversations from low pass filtering vuvuzelas, to correct deadlift form. A big thank you to the Diamond Light Source staff on beamline I09; Tien-Lin Lee, Pardeep Kumar Thakur and David Duncan. I'd also like to thank Dave Stefanyszyn and Tom Barrett, whilst most people envied your performance during undergraduate years, I was inspired. I wouldn't be here now if your work ethic didn't motivate me to pull my socks up. Thank you to my friends back home (you know who you are) for your encouragement and 'banter'. I still need to take you into the lab to prove the Createc is not just an elaborate looking coffee roaster.

Finally I'd like to thank two very special people in my life, my Nan and Grandad. Raising me alone must have been quite a challenge, let alone all of the encouragement and support you've given me along the way. None of this would have happened if it wasn't for you both. Thank you- for everything.

Contents

1 Overview

In the past three decades, the imaging and manipulation of atoms and molecules on surfaces has been studied extensively. Although, relatively speaking, still in its early days, the experimentation of such small scale systems acts as a foundation for the building blocks of future nanoscale devices. The vast majority of the surface experiments have been performed using scanning probe microscopy (SPM) at low temperatures. In 1990, IBM were amongst the first to demonstrate the capabilities of the scanning tunnelling microscope (STM), where they manipulated 35 Xe atoms on a Ni(110) surface to display the smallest IBM logo created [1].

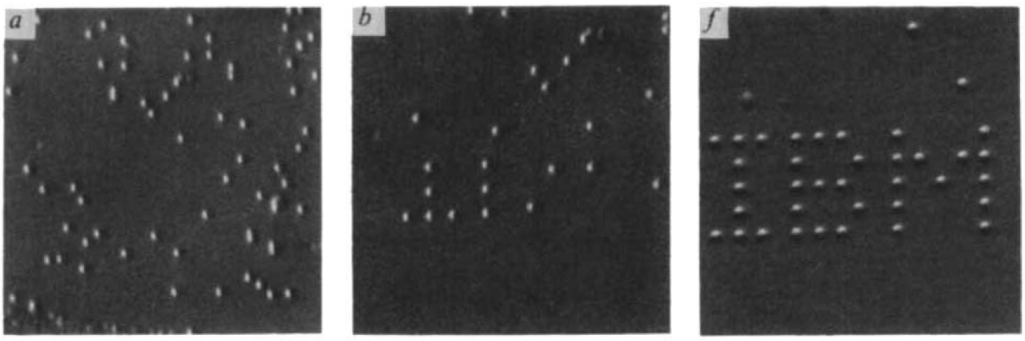

Figure 1: *Sequence of images showing the formation of the IBM logo using Xe atoms on a Ni(110) surface, each letter is 50Å in height. Images from [1].*

Since then, there has been substantial progress towards nanoscale devices; quantum confinement in both two- and three-dimensions [2–5], the formation of an atomic wire [6], single atomic dopants at surfaces [7], vertical manipulation of atoms on semiconductor surfaces [8] and conformational changes of molecules at surfaces [9–13] to name but a few.

Another essential tool for the nanoscientist is the atomic force microscope

(AFM), which substantially extends the achievements of the STM. The first successful non-contact AFM (NC-AFM) image was taken by Giessibl in 1995 [14].

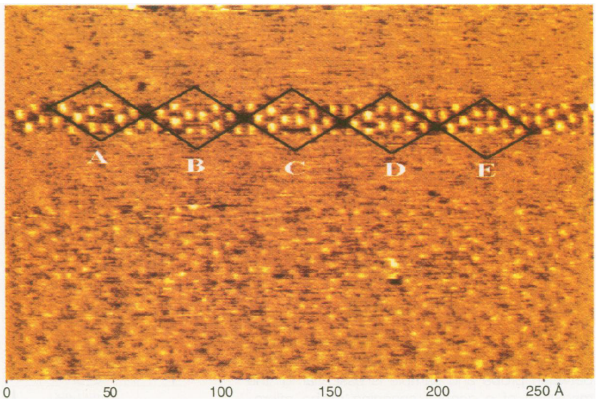

Figure 2: *NC-AFM image of Si(111)-(7 x 7) showing atomic resolution (with defects) across a small band in the image. Image from [14].*

In terms of atomic and molecular manipulation, NC-AFM can exploit pure (chemo)mechanical force- in the absence of a bias voltage and tunnelling current- to extract, move and/or deposit atoms [15]. Figure 3 shows the first atomic pattern created using NC-AFM, where individual atoms were laterally manipulated on a surface by Sugimoto and coworkers [16].

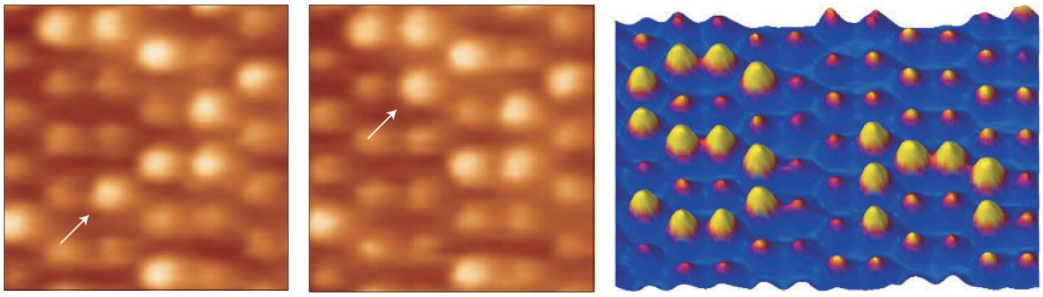

Figure 3: *NC-AFM images showing the lateral manipulation of Sn adatoms on the Ge(111)-c(2 x 8) surface. Images left and centre 4x4nm, image on right 7.7x7.7nm (in plane view). Images from [16].*

A key goal of surface microscopy for many decades was to resolve individual atoms. Although field ion microscopy (FIM) had already achieved atomic resolution as long ago as 1955, it wasn't until the invention of the STM in the early eighties when single atom imaging and manipulation was made possible on a wide variety of flat surfaces, in a range of environments, and with spectroscopy (and spectromicroscopy) capabilities that are simply not possible with FIM. Since 2009, however, NC-AFM has achieved even higher resolution in real-space, enabling the identification of intramolecular chemical structure. Gross and co-workers achieved sub-molecular resolution of pentacene, noting that the key to performing such experiments is using functionalized tips [17].

The functional properties of other molecules such as porphyrins and other tetrapyrrole macrocycles have also been studied extensively by the SPM community (planar and close-to-planar molecules such as linear acenes, phthalocyanines, and porphyrins are particularly amenable to scanning probe analysis). The structure of the porphyrin macrocycle, consisting of four pyrrole rings connected by methine units was proposed a little over a century ago [18]. The first synthesis of tetraphenylporphyrin (TPP) followed just over two decades later in 1936 [19]. It is well known that the porphyrin macrocycle is flexible, which allows for non-planar conformations; such distortions frequently determine the physicochemical properties of the molecule. The most commonly studied class of porphyrin molecules in the SPM community is the metalloporphyrin: a porphyrin with a metal core within the tetradendate ligand framework. Metalloporphyrins occur naturally and play a key role in fundamental life processes such as catalytic

based functions, photosynthesis and the transport of respiratory gases [20]; examples of which are chlorophyll [21] and haem [22]. In the past two decades, a plethora of uses for porphyrin-base molecules has been envisaged, such as chemosensors [23], organic light emitting diodes (LEDs) [24] and even anti-cancer [25] and anti-human immunodeficiency virus (HIV) drugs [26]. It is evident that they are functional units for nanoscale applications. However, porphyrins must be isolated at the single molecule level for deeper investigations to control their nanoscale properties, and to elucidate and control the relationship between their electronic intricacies and molecular conformation.

Another molecule of especial interest in the SPM community is C_{60}, which has been exceptionally well documented on metal surfaces since its fabrication in 1985. Apart from its remarkable ability to self assemble on surfaces, the continuous interest also stems from its chemical properties, geometric/electronic structure [27–29] and also as a potential use in molecular electronics [30–34] and biological applications [35].

Almost immediately after the discovery of C_{60}, the first encapsulation process was carried out, and resulted in La@C_{60} [36]. Since then numerous endohedral fullerenes have been synthesized, with the 'encapsulates' ranging from H_2 and H_2O and even metals and multiatomic clusters. The molecule-within-a-molecule form of an endohedral fullerene presents an intriguing challenge for the scanning probe microscopist: is it possible to detect the incarcerated molecule within the fullerene cage (via STM, AFM, and/or any of the associated electronic and force spectroscopies, which to date has

no literature backing)? H_2O is a particularly interesting molecule to be able to study during encapsulation, because it is very difficult in itself to isolate a water molecule; it also exhibits a nuclear spin isomerism, [37, 38] and in theory, when encapsulated, should behave as a polar molecule- even when encapsulated by C_{60}. As one will see, distinguishing between encapsulated and empty C_{60} can prove very difficult. SPM is of course only one surface technique (albeit, an exceptionally powerful one). Other photon based and electron-based probes can provide a great deal more complementary information and have chemical specificity that is currently far beyond the reach of SPM techniques. Sychrotron-based surface science tools are particularly powerful in this regard, namely x-ray photoelectron spectroscopy (XPS) and x-ray standing wavefields (XSW). We used XPS to confirm the presence of encapsulated water using the O1s signal, and also attempted to triangulate the position of the water molecule within the C_{60} cage using XSW.

The scope of this thesis is as follows: Chapter 2 begins with background information on the history of the techniques and molecules studied in SPM, low energy electron diffraction (LEED), XPS and XSW.

The third chapter delves into the theoretical concepts behind the experimental techniques used, including important mathematical derivations which prove crucial to the development of the equipment.

The experimental equipment/methods used to prepare sample surfaces and deposit molecules, and to perform measurements are detailed in Chapter 4.

In Chapter 5, the deposition of bromine terminated porphyrin molecules (Br_4TPP) on both Au and Cu surfaces is investigated. Using STM allows the molecular orbitals of the molecule to be probed, and further experimentation using both STM and AFM, combined with density functional theory (DFT), show that large conformational changes are dominated by van der Waals interactions between the molecule and substrate. We also show that there is a large difference between the lateral forces required for manipulation of the two conformers of Br_4TPP molecules.

Both C_{60} and $H_2O@C_{60}$ are deposited onto a Cu surface and studied in Chapter 6. Remarkably, both STM and AFM cannot distinguish between filled and empty fullerenes. It is also shown that a $H_2O@C_{60}/C_{60}$ mixture induces surface reconstruction when deposited onto a room temperature surface, in the same fashion as C_{60}. Intermolecular contrast on $H_2O@C_{60}/C_{60}$ islands is also presented, in the absence of hydrogen or halogen bonding, which highlights that intermolecular artifacts are ubiquitous in dynamic force microscopy.

Chapter 7 details the results from a series of XPS and XSW experiments performed as a team (Myself, Samuel Jarvis, Salvatore Mamone, Jeremy Leaf, Philipp Rahe, Adam Sweetman, Alex Saywell, Robert Jones and Philip Moriarty) at Diamond Light Source, Oxford. $H_2O@C_{60}$ was deposited on an Ag surface for experimentation. Having been very fortunate to participate in beam-time, we show that water is in fact encapsulated in C_{60} cages by the detection the O1s signal using XPS. XSW was used in

an attempt to triangulate the water molecule respective to the Ag surface. Finally, chapter 8 discusses the conclusions arising from this thesis.

2 Background

2.1 Scanning tunnelling- and atomic force- microscopy

The fundamental principle behind the operation of a STM is the quantum mechanical tunnelling of electrons between two electrodes (the tip and the sample). For quantum mechanical tunnelling to occur, the conducting electrodes must be separated by no more than a few nanometres. This effect was first observed by Giaever in 1960, who realised that when a voltage was applied to an $Al/Al_2O_3/Pb$ sandwich, electrons would penetrate through the Al_2O_3 layer (which acts as a potential barrier) in either current flow direction between the Al and Pb layers [39]. Binnig and Rohrer used this phenomenon, in combination with raster scanning a probe to create the STM in 1983 [40]. They won the Nobel Prize in physics in 1986 for their invention.

A schematic showing the basic setup of a STM is shown in Figure 4. A sharp tip is required in order to reduce the effect of tip convolution. STM tips are commonly made from W or Pt-Ir, and can be made sharp by either mechanical pulling, or chemical etching. Chemical etching will be discussed in more detail later. Figure 4a shows a sharp tip scanned over the surface of a sample, where the distance between the tip and surface is typically around 1nm. The x, y and z movements of the tip are all controlled by a piezoelectric material. Figure 4b describes Figure 4a 'zoomed in' on the atomic scale. Assuming a negatively charged sample, electrons tunnel from the sample atoms into the atom at the tip apex, the tip subsequently responds to the peak in tunnelling current by moving away from the sample

surface by a few Å causing the tip to follow the curvature of the 'atom'. (Figure 4 from http://www.ieap.uni-kiel.de)

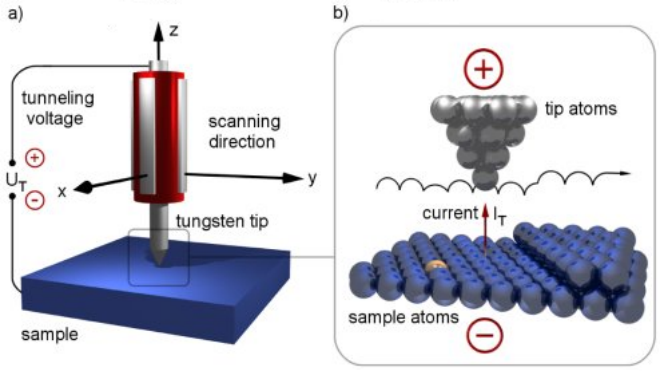

Figure 4: *Schematic describing the principle of STM operation.*

Shortly after the invention of the STM, the AFM followed in 1986 [41]. In the first prototype STM was used as a height detection mechanism. The operation of the AFM cantilever is an oscillating probe that senses tip-sample interactions. When brought close to the sample, the cantilever can be described as a weakly perturbed harmonic oscillator. The tip-sample interaction causes a change to its resonant frequency, the eigenfreqency f_0, to $f = f_0 + \Delta f$.

2.1.1 Porphyrin molecules

STM and AFM provide the toolset to collect expansive information about isolated molecules, including electronic characteristics, tip-induced conformational changes and adsorption geometry. Molecular switching mechanisms have been studied extensively [42–46], and also supramolecular assembly [47–49], which could provide the foundations for single molecule devices. Previous simulations suggest that chemical or steric effects are the cause of the macrocycle distortion as a result of molecule-substrate

interactions [50], however it is now thought that, in some cases at least, dispersion forces alone from the pyrrole and phenyl constituents are responsible as shown by one of the relevant publications by Jarvis *et al.* later in this thesis [51].

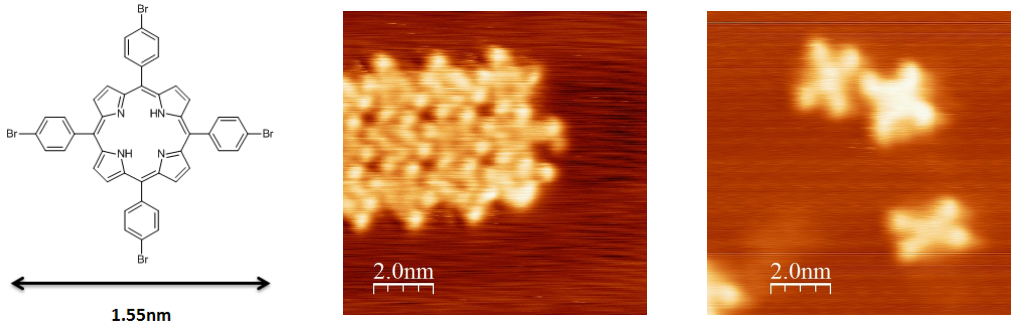

(a) (b) (c)

Figure 5: *a) Molecular structure of Br_4TPP. A porphyrin based centre and four Br terminated benzene rings. b) STM image showing deposition of Br_4TPP on Au(111) at a sample temperature of 150K. Close-packed networks have formed. c) STM image showing deposition of Br_4TPP on Cu(111) at a sample temperature of 77K. Dispersed single Br_4TPP molecules are formed on the surface.*

It is known that the electronic structure of molecules can be altered through a molecule-surface charge transfer process [52,53], and STM can be used to resolve sub-molecular detail of intramolecular distortions in adsorbed porphyrins on metal substrates [54–56], however studies into the effect that electronic manipulation plays in the modification of the molecular orbitals (MOs) of free-base porphyrins remain elusive.

The controlled engineering of molecular nanostructures from single molecular units represents a central goal in the field of nanotechnology. It has been previously shown that molecular networks 'locked' by covalent interactions can be constructed on Au surfaces from functionalized porphyrin

molecules using thermal activation [57] [49]. Although well controlled, a complete understanding of the exact step-by-step mechanism has remained elusive. A number of distinct Br_4TPP conformers are observed on Au and Cu substrates as a result of the preserved gas-phase flexibility and any associated ligands of the porphyrin macrocycle, but again, exact mechanisms underpinning the process of conformation has not been well documented.

When two molecules of the same chemical composition differ in structure via rotations around intramolecular bonds- that is, the breaking and reforming of bonds is not required to superimpose the two structures- we describe the molecules as conformers [58]. This has very important consequences as the conformation of a molecule can affect key physicochemical properties such as conductance, reactivity, and optical absorption/emission and can be especially important in biological systems [59, 60]. Scanning probe microscopy enables conformation to be switched and examined on an individual molecule basis, providing fascinating insights into mechanochemical changes. With STM one can identify static molecular conformers [54] and examine their physiochemical properties [61–63]. In addition, a wide range of STM experiments demonstrating molecular manipulation have now been reported including rolling [64–66], translating [67] and switching of molecules [42–44]. Scanning probe studies of molecules capable of adopting multiple conformations, however, have been much fewer in number [46, 68–70], and there has not been an attempt to date to elucidate the differences in the response of different conformers to tip-induced forces.

The conformation of a molecule can determine its physicochemical proper-

ties along with its ability to respond to changes in its local environment. Structural flexibility is a key prerequisite for variations in conformation, which in turn can lead a close dependence between the form and function of the molecule. Porphyrin molecules, and related molecules which possess four pyrrole rings held together by direct covalent bonds (tetrapyrrole), can couple conformational and functional change in a number of ways, including via distortion of the core macrocycle [71–73]. Tetrapyrrole molecular frameworks are the basis of hemes [74] (including a hemoglobin) and the distortion of the macrocycle is widely exploited in such biological systems.

The potential of metallo(porphyrins) as elements of prototypical molecular electronics systems has led to significant increase in the number of studies of their interactions with metal surfaces such as Au, Ag and Cu. The gas phase flexibility of the porphyrin macrocycle and any associated ligands seems to be preserved at metal surfaces, and a number of distinct conformers can be observed.

There is a vast amount of literature surrounding porphyrin adsorption on noble metal surfaces [75]. The variety of combinations of different systems, from metalated and non-metalated cores, to molecules possessing ligands and the various noble metal surfaces they're adsorbed on (Au, Cu, Ag) makes it difficult to deduce a direct comparison between each individual system.

Until now there were two primary explanations governing porphyrin adsorption. One explanation is noted by Brede *et al.*, who investigated the ad-

sorption and conformation of a range of teraphenyl porphyrins on Cu(111), Cu(100) and Au(111) substrates [76]. It was concluded that the geometry, molecular conformation and adsorption site were determined by the attractive van der Waals (vdW) interaction of the phenyl legs and the (steric) repulsion of the pyrrole units at the core of the molecule with the respective substrate. The authors note that the identity of the metallic centre of a metalloporphyrin does not affect the adsorption geometry. A later report [77] also suggested that molecule-substrate interactions induced bending in the porphyrin core, leading to a subtle interplay between the 'leg' geometry and the core distortion, and this coupling is reported as a commonly observed feature of functionalized porphyrin adsorption [45, 76–79].

The lack of interactions arising from the metalated core with respect to the adsorption geometry is important to note, as this suggests chemical interactions between the core N atoms and the surface are insignificant, and this may be expected in the case where the N atoms are already coordinated to a metal centre. Furthermore, to enhance the validity of the metalated core having negligible effects upon adsorption geometry, Iancu *et al.* also observe two molecular conformers, which are extremely similar in appearance to what is described later in this report for the non-metalated Br_4TPP.

The other explanation is that adsorption is dominated by chemical interactions between the iminic nitrogens of the core and the metal substrate. Supporting evidence from recent papers [78, 80–82] shows a bonding interaction between the iminic nitrogen atoms in the porphyrin core and the Cu(111) substrate. Doyle *et al.* carried out photoemission and x-ray ab-

sorption spectroscopy on Br_4TPP, which were interpreted as a formation of an intermediate Br_4TPP-Cu complex involving Cu-iminic nitrogen bonding [82].

Shortly after Doyle *et al.'s* publicated data, photoelectron spectroscopy data for a sub monoloayer coverage of 2HTPP on Cu(111) supported the claim of the formation of strong localized bonds between the iminic N atoms and the Cu surface [80]. Diller *et al.* also found that the iminic nitrogen atoms of the 2H-TPP molecule interacted strongly with the Cu(111) substrate, with the N lone pairs pointing downwards towards the Cu(111) surface [78]. Their photoemission data strongly suggested that photoelectron diffraction was responsible for variations in the intensity of the iminic and pyrrolic components of the N1s core-level peak. This points to a well-defined adsorption site driven by the N-Cu interaction, as a coherent binding site is a prerequisite for photoelectron diffraction. Diller *et al.* importantly suggest that binding energy shifts observed in XPS spectra may not necessarily arise from a strong chemical interaction, and can in fact be due to the screening of a photoinduced core hole. There was also a recent study by Mielke *et al.* where trapped metal adatoms on Au(111) can affect the appearance of TPP molecules in STM [83].

There are relatively few initial investigations aimed at modelling TPP adsorption that consider dispersion corrections [79]. It has been shown by the Tkatchenko group, that benzene adsorption on metals has a critical dependence on vdW interactions by using a variety of dispersion corrected DFT calculations [84, 85]. Much larger molecules such as diindoperylene have

also been examined where the attractive components of adsorption were found to depend almost entirely on vdW interactions [86], so great in fact, that the adsorption energy was modified by more than 5eV on Cu(111). In relation to the substrate, it was noted that vdW interactions on Cu(111) were significantly more reactive than other noble metal surfaces, and almost double that on Au(111).

To date, the exact assignment of adsorption sites of porphyrin conformers relative to the atomic structure of the Cu(111) surface, along with detailed simulations of the structures observed by STM, has not been made. In this thesis, Br_4TPP is examined using a combination of atomic and submolecular resolution STM with both DFT with dispersion and classical molecular dynamics (MD) calculations to determine the relationship between the precise adsorption geometry of Br_4TPP on Cu(111). All theoretical calculations were carried out by Baran and Thompson.

Experimental measurements are carried out at low temperatures providing greater stability and reducing the possibility of potential temperature-driven effects at higher temperatures. By making a direct comparison between the experimentally determined adsorption position and the complete geometry calculated with DFT with dispersion we unambiguously determine the adsorption structure of each conformer. Furthermore, our results are supported by simulated STM images which are compared with the experimental appearance of the Br_4TPP molecules in each conformation. We show that controlled, and purely mechanical, translation of a Br_4TPP molecule from one adsorption site to another at low temperatures (5K) re-

sults in switching between conformers via an intermediate conformational 'hybrid'. Moreover, MD and DFT with dispersion calculations reveal a critical dependence on vdW forces and an absence of significant chemical interaction, which is, surprisingly and perhaps counterintuitively, found to significantly modify the molecular energy levels.

To investigate the chemomechanical properties of a conformer during manipulation, it is essential that the interaction between the scanning probe and the molecule is purely mechanical. NC-AFM, with its sensitivity to force rather than current, is ideally suited to this task. Although atomic manipulation with NC-AFM is now well established [87], manipulation of molecules is still very much an emerging field of study. Whilst a small number of groups have reported molecular manipulation with NC-AFM (for example [88,89]), very few have recorded the forces involved, and generally only relatively simple molecules have been investigated. The lateral force responsible for moving metal adatoms and CO molecules was first quantified by Ternes *et al.* [90]. Since then, larger molecules, such as perylene-tetracarboxylic-dianhydride (PTCDA) [91,92] and H_2P_c [93] have been investigated. These studies, however, examine either small or flat molecules which are structurally rigid and so have significantly limited internal degrees of freedom compared with other commonly investigated large molecules. Consequently, it remains an open question as to whether the force for manipulation can be measured for complex molecular structures, and, in particular, whether conformational dependencies can be identified.

2.1.2 Fullerenes and endohedral fullerenes

Osawa suggested that a C_{60} molecule may be chemically stable in 1970 [94]. In 1973, Bochvar and Gal'perin, using Huckel calculations, studied the electronic structure of C_{60}, and suggested that the gap between the highest occupied molecular orbital (HOMO) and the lowest unoccupied molecular orbital (LUMO) was large [95]. Sir Harry Kroto *et al.* discovered buckminsterfullerene in 1985 by laser evaporation of graphite, establishing the stability of C_{60} molecules in the gas phase [96]. Three of the authors were subsequently awarded the Nobel Prize in chemistry for their discovery in 1996.

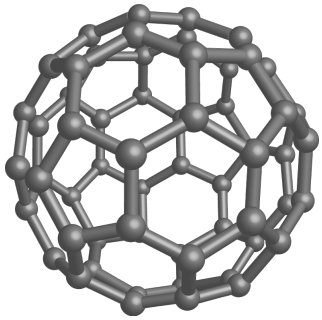

Figure 6: *Graphic representing the C_{60} molecule, consisting of sixty carbon atoms. The shape of the cage-like structure is known as a trunctuated icosahedron.*

C_{60} consists of a cage-like structure of sixty carbon atoms (a trunctuated icosahedron). This polyhedron has 60 vertices (carbon atoms) and 90 edges (C-C bonds); consisting of 12 pentagonal and 20 hexagonal faces. C_{60} is roughly 7Å in diameter, and each carbon atom forms three σ bonds with its neighbours. The π states allow for some degree of electron delocalization, but in general, it is poor for C_{60}. The structure was named *buckminsterfullerene* after the American architect Buckminster Fuller, who designed

the geodesic dome in the shape of such a polyhedron.

The term fullerene is used as a classification for the discovery of similar molecules since 1985. A selection of C_n (where $n > 20$) molecules were discovered by Kroto *et al.* in 1985, including C_{70}. Other discoveries of fullerenes include substitutional fullerenes, where a single carbon atom is replaced by a nitrogen or boron atom, yielding $C_{59}N$ or $C_{59}B$ respectively.

It is also possible to synthesize endohedral fullerenes, which are fullerenes with additional atoms, ions or clusters enclosed within their inner spheres. The process has been described appropriately as 'molecular surgery' and presents the SPM enthusiast with the unique opportunity to be, in theory, able to probe a molecule within a molecule. Whilst it is possible to insert a small molecule (such as molecular hydrogen) by bombardment, larger molecules require an open orifice on the fullerene cage, encapsulate bombardment, and a 'chemical-reversal' to close the fullerene cage.

The Cu(111) surface is ideal for the growth of C_{60} films similar to the bulk [97]. The lattice mismatch is small at 2% of the bulk C_{60} crystal lattice constant, compared to four times the Cu-Cu nearest neighbour (NN) distance of 10.2Å [98]. Charge is donated from the Cu substrate to the LUMO (in a similar fashion as K does in K_xC_{60} films), and successive C_{60} layer-by-layer growth can be achieved on the Cu(111) surface. XPS confirms that the Cu substrate donates charge to the LUMO of C_{60} molecules [99].

Until recently, there were conflicting views on the geometry of C_{60} adsorbed on the Ag(111) surface. One study concluded that C_{60} adsorbs in top sites in a 'pentagon facing down' fashion through HOMO and LUMO imaging [100, 101]. Another study concluded that C_{60} adsorbs in hollow sites in a 'hexagon facing down' orientation [102,103]. A more recent study by Li *et al.* concludes that C_{60} does indeed bond to the Ag(111) surface in a hexagon down orientation [104]. The authors also note that the stable monolayer ejects Ag surface atoms, or in other words, adsorbed C_{60} causes Ag surface reconstruction, which will be discussed in detail later.

A common method to deposit C_{60} onto a substrate in the literature is by vacuum sublimation of micro crystalline C_{60} powder heated at 600K [100, 105–111]. Deposition on Cu(111) appears to result in C_{60} adsorption near Cu step edges, and as coverage increases, C_{60} islands grow from steps towards terraces [98, 112, 113]. Cuberes *et al.* show that C_{60} can be manipulated from Cu step edge locations toward terraces at room temperature [114]. Sometimes, the C_{60} image varies, this could be the orientation of the molecule on the surface, as shown in Fig. 7.

Heiney suggests that rotated C_{60} at step edges is likely due to broken symmetry and a weaker interaction with the substrate. Molecules can also align by intermolecular interactions, or immediately through substrate Cu back bondings [115]. The bonding of C_{60} to the Cu(111) substrate can be described by three parameters; polar angle (which part of the C_{60} cage bonds to the surface), bonding site (which part of the surface the cage bonds to) and the azimuthal angle (the rotational orientation of the cage).

It is straight forward to determine the polar angle by symmetry of STM images, however it is much more difficult to determine the bonding site.

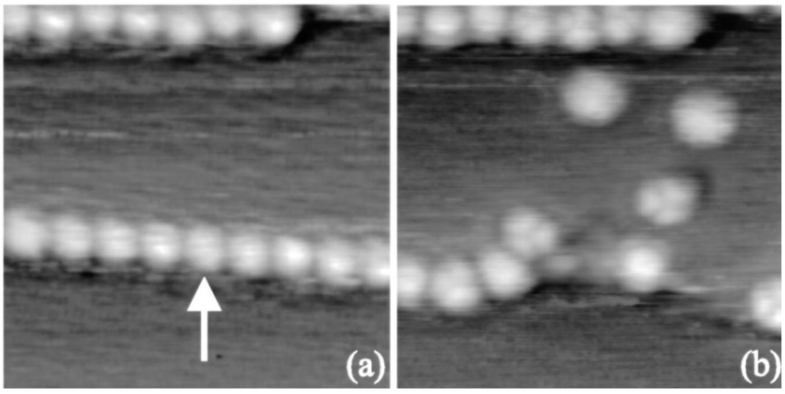

Figure 7: *STM images by Cuberes et al. during repositioning of C_{60} from step terrace sites. Image from [114].*

Early publications show the annealing of C_{60} monolayers leading to well ordered (4 x 4) structures on Cu(111), where the C_{60} molecules were oriented in the same way, and it was concluded that fullerenes were oriented with a 6-membered ring toward the surface as shown in Figure 8 [98,102,112,113]. Fasel *et al.* found C_{60} on Cu(111) bonds in the same way but with molecules in two different equivalent azimuthal orientations using x-ray photoelectron diffraction [116].

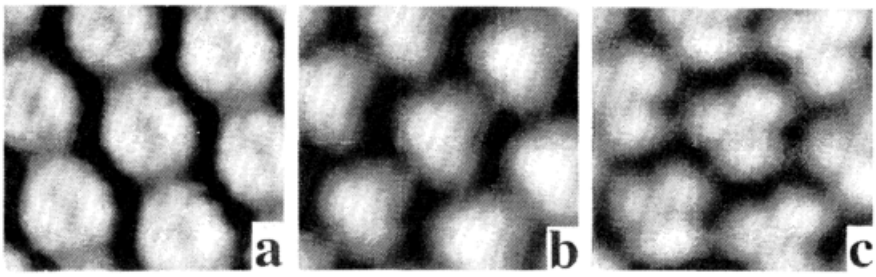

Figure 8: *STM images by Hashizume et al. representing C_{60} uniformly adsorbed on the Cu(111) surface. Image from [98].*

Within the next decade, it was quickly realised that deposition and/or annealing temperatures of C_{60} above 300K resulted in substantial reconstructions of the underlying substrate, causing rough C_{60}/Cu(111) interface geometries. Surface reconstruction was first observed on more open metal surfaces [113,117–119], but later on (111)-oriented metal surfaces [120,121] including Cu(111) [122], as shown in Fig. 9.

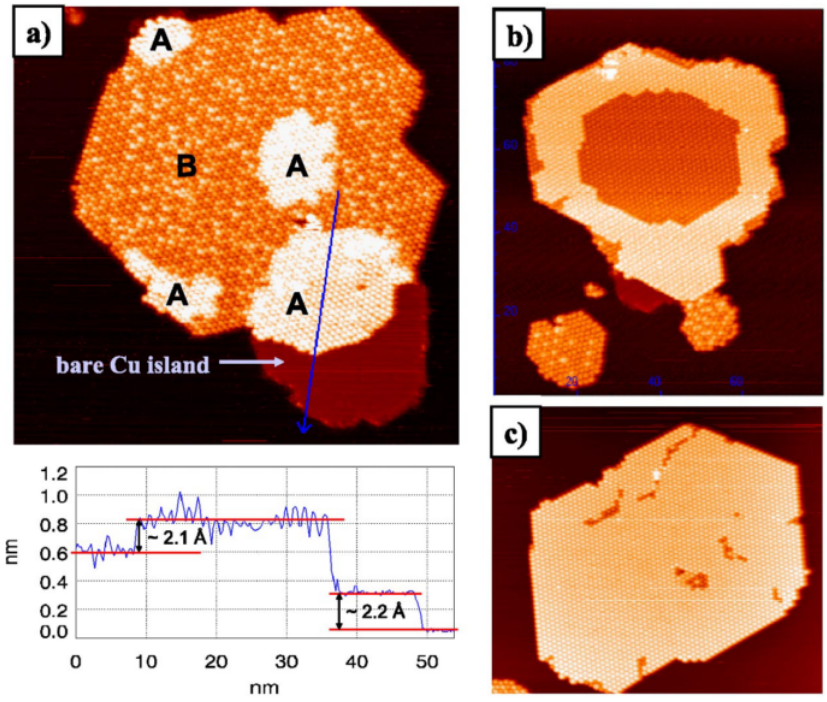

Figure 9: *STM images by Pai et al. representing C_{60} adsorbate-induced Cu(111) surface reconstruction. Image from [122].*

Strozecka *et al.* successfully grew small islands of C_{60} on Cu(111) well below room temperature, so this ruled out surface reconstruction. The authors note that C_{60} bonds at the six-membered ring or six-six bond towards the surface [123], as shown in Fig. 10.

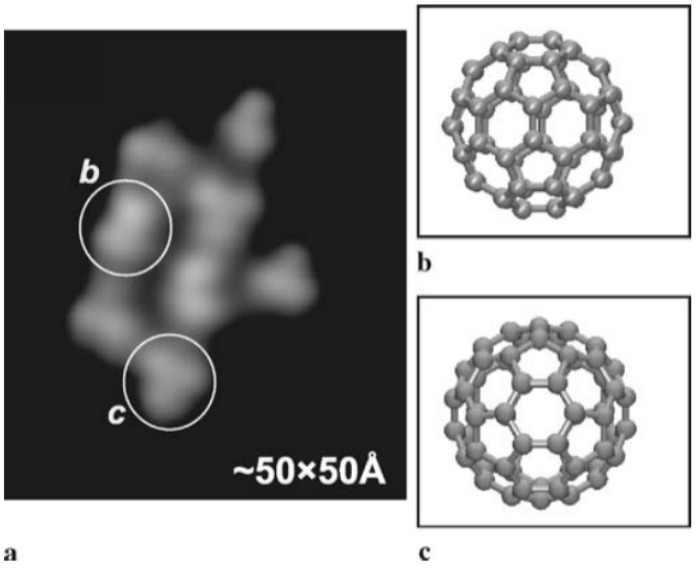

Figure 10: *STM images by Strozecka et al. showing C_{60} on a non-reconstructed Cu(111) surface. Image from [123].*

Saunders *et al.* showed the formation of endohedral complexes, namely $He@C_{60}$ and $Ne@C_{60}$ in 1993 [124]. This was quickly followed by $Ar@C_{60}$, $Kr@C_{60}$ and $Xe@C_{60}$ in 1994 [125]. The encapsulation process by Saunders *et al.* was carried out by bombarding C_{60} with each respective noble gas in a high pressure (3kbar+) environment. It was reported that around 1 in 880,000 fullerenes were encapsulated. During the next decade, numerous attempts to incorporate larger molecules were made [126–128], and one method is shown in Figure 11.

Komatsu *et al.* and co-workers were able to completely encapsulate molecular hydrogen by complex chemical reactions, firstly by opening the C_{60} cage, then by molecular hydrogen bombardment, then reversing the complex chemical process to close the cage [129] shown in Figure 12.

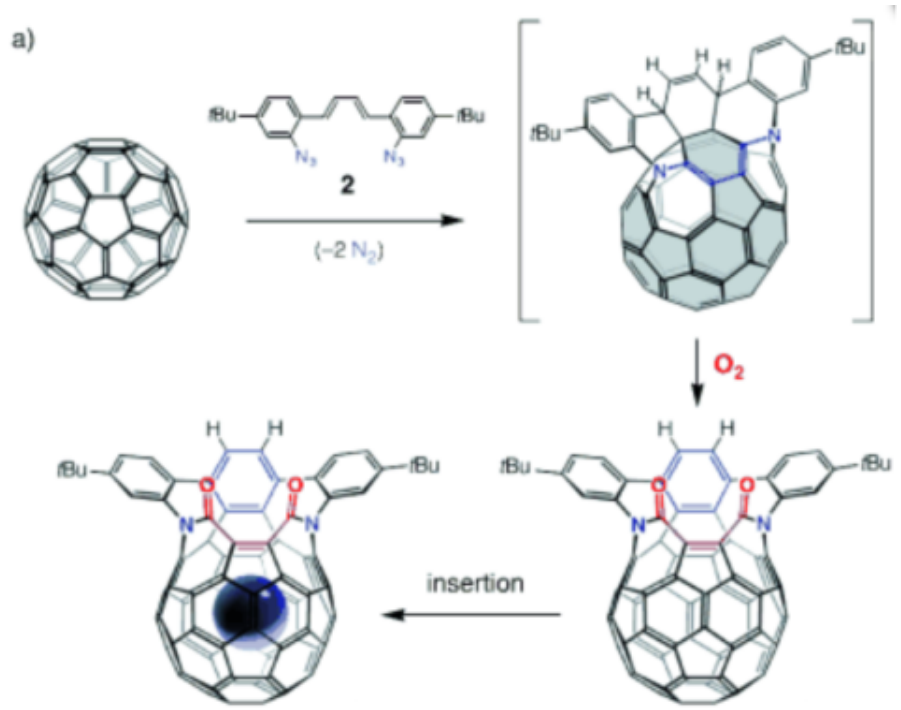

Figure 11: *Schematic describing the process that was attempted by Rubin et al. for insertion of He into a C_{60} cage. Image from [126].*

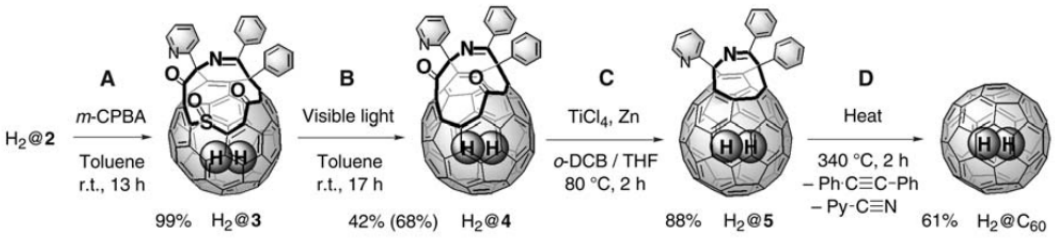

Figure 12: *Illustration by Komatsu et al. describing the encapsulation of molecular hydrogen into a C_{60} cage. Image from [129].*

It wasn't until 2011 however, that H_2O was encapsulated by Kurotobi and Murata [130]. Perhaps the most critical aspect of encapsulation of small atoms/molecules in C_{60} is determining whether the volume inside the cage is large enough for accommodation. Fortunately, the inner void of C_{60} has a diameter in excess of 3.5 Å . It is therefore possible for small atoms and

molecules (i.e. He or H_2) to be incorporated under high pressure environments, as mentioned previously, but with very very small yields. To yield much greater quantities of endohedral fullerenes, complex reaction mechanisms are required to create an orifice in the C_{60} cage, where the user can define to great accuracy the ratio of encapsulated:non-encapsulated C_{60} that is required.

Figure 13 shows an illustration of the encapsulation process. To encapsulate a water molecule inside a C_{60} cage, Kurotobi and Murata first synthesized an open cage derivative. The cage was then heated to 120°C to enlarge the orifice and high pressure H_2O admitted at 9kbar. Finally the orifice was closed via chemical reactions. The authors note that there is no escape of the water molecule at 420°C for 30 minutes and the energy levels of $H_2O@C_{60}$ closely resemble H_2O in free space at low temperatures.

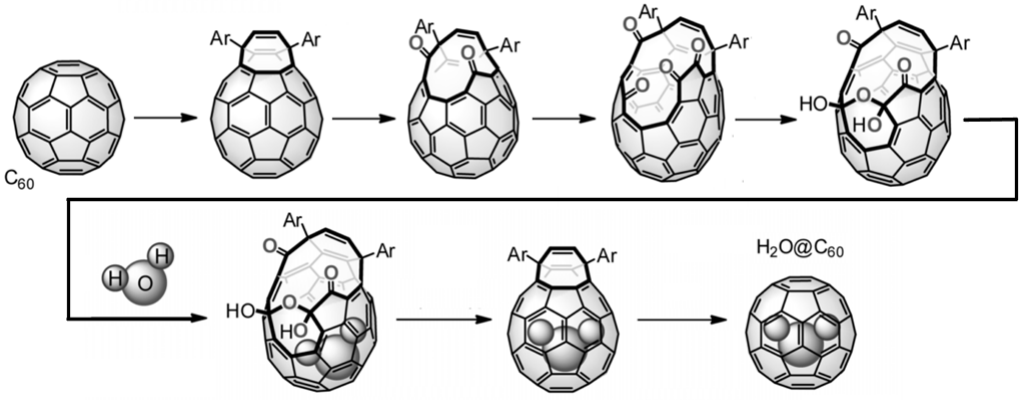

Figure 13: *Graphical representation of the steps to encapsulate a water molecule inside a C_{60} cage, taken from [130].*

2.1.3 Intra- and inter-molecular interactions

Intermolecular interactions are fundamental in nature, governing the chemistry 'beyond the molecule' [131, 132] responsible for stabilizing self-assembled arrays of molecules and supramolecular systems. The potential to investigate intermolecular interactions at the single bond limit is therefore particularly attractive. As such, scanning probe microscopy has especially promising potential for the investigation of molecular and supramolecular self-assembly at surfaces [49,133,134]. In a few short years, dynamic force microscopy (also called NC-AFM) has provided unprecedented submolecular detail at the single bond level for a variety of systems [17, 135–141]. This has been achieved by terminating the scanning probe with a single molecule [142, 143] or via spontaneous termination of the tip apex [144–147], which is subsequently moved so close to the underlying molecule that repulsive tip-sample interactions from the molecular skeleton yield exceptionally high resolution.

Pavliček *et al.* also demonstrated submolecular resolution investigating dibenzo[a,h]thianthrene (DBTH) molecules on 2ML thick NaCl/Cu(111). The authors used CO-functionalized tips for high resolution NC-AFM images, and discovered two stable configurations, as shown in Fig. 14 [148].

Zhang *et al.* claimed a real-space visualization of the formation of hydrogen bonding on 8-hydroxyquinoline (8-hq) molecular assemblies on a Cu(111) substrate using NC-AFM in 2013 [149]. Claims that dynamic force microscopy has the capability to resolve intermolecular bonds in real space continue to be vigorously debated. Later in this thesis, the observation

of intermolecular artifacts over much larger distances in 2D assemblies of $H_2O@C_{60}/C_{60}$ molecules, with compelling evidence that in our case the tip apex is terminated by a $H_2O@C_{60}/C_{60}$ molecule (rather than the CO termination typically exploited in ultrahigh resolution force microscopy). The complete absence of directional interactions such as hydrogen or halogen bonding, the nonplanar structure of $H_2O@C_{60}/C_{60}$, and the (endohedral) fullerene termination of the tip apex in our case highlight that intermolecular artifacts are ubiquitous in dynamic force microscopy (DFM).

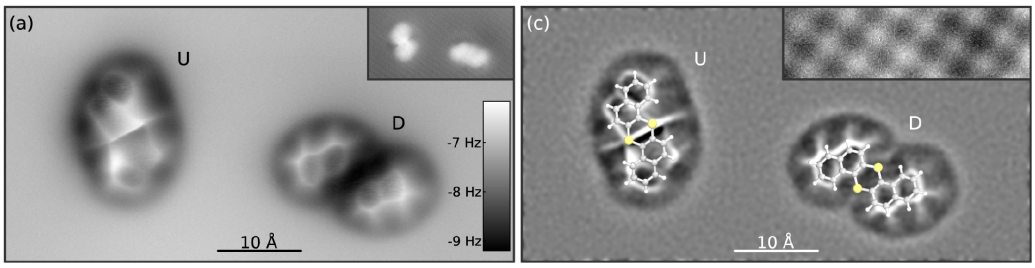

Figure 14: *Constant height NC-AFM images showing the intramolecular structure of DBTH on NaCl(2ML)/Cu(111). Image from [148].*

In addition to resolving the internal structure of a molecule, NC-AFM and the scanning tunnelling hydrogen microscopy method pioneered by Termirov and co-workers [150], as shown in Fig. 15. This was made possible by releasing molecular hydrogen into the scan chamber whilst scanning at 10K. At such surface temperatures, molecular hydrogen condensed on the substrate between the tunnelling junction. This allowed the STM contrast to be switched between the conventional electronic DOS mapping to a new geometric imaging through molecular hydrogen, known as scanning tunnelling hydrogen microscopy (STHM) [150]. The position of the condensed H_2 is determined by Pauli repulsion within the junction between the tip and the sample. This can be interpreted by modelling the trapped molec-

ular hydrogen as a type of tranducer, which (depending upon the degree of change in the Pauli repulsion) modulates the STM signal.

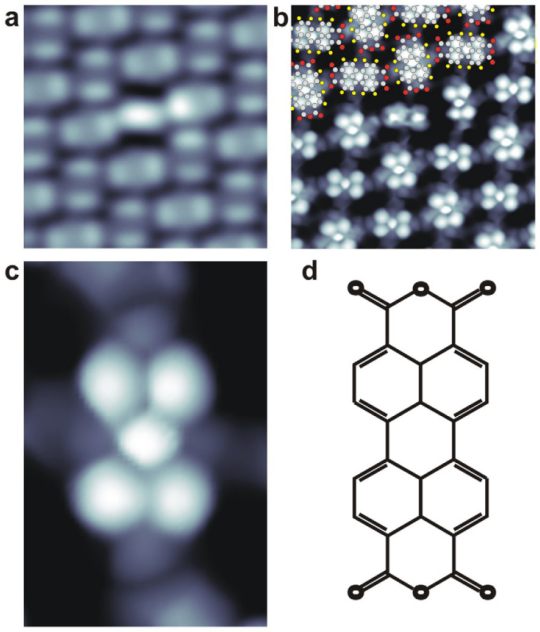

Figure 15: *Spectroscopic imaging of PTCDA on the Ag(111) substrate in the geometric mode, in this example, the tip is sensitized using deuterium. a) Constant current STM image. b) Constant height dI/dV image of area shown in a). c) 'Zoomed' image of b). d) Structure of PTCDA. Images from [150].*

Both NC-AFM and STHM have shown that apparent intermolecular features can be resolved in molecular assemblies, stabilized either through hydrogen bonds [146, 149, 151, 152] or, very recently, halogen-bonding interactions [153].

Although initial DFT modelling of the tip-sample interaction in hydrogen bonded assemblies showed good agreement with experimental line profile measurements above inter- and intra-molecular features, it failed to reproduce the striking features observed in experiment [146], where the bonds

appeared much sharper. Several studies have now shown that tip flexibility [154–156], especially at very close tip-sample separations, is responsible for the striking intra- and inter-molecular resolution observed with various SPM techniques [151, 156, 157], and that apparent intermolecular features can be observed with NC-AFM even when no bonding interaction is present, as seen in bis(para-pyridyl)acetylene (BPPA) molecules [152]. This suggests that the features are, in fact, an artifact (shown in Fig. 16) and cannot be interpreted as a real-space image of an intermolecular bond. Aspects of this interpretation have, however, in turn been challenged very recently [158].

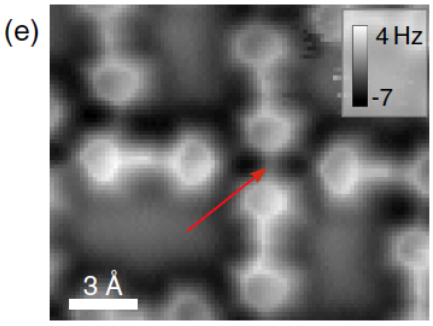

Figure 16: *AFM image of the tetramer indicating (red arrow) apparent intermolecular bonds between BPPA molecules. Image from [152].*

Figure 17 shows the high spatial resolution results of intermolecular hydrogen bonds published in the literature. It was noted by Sweetman *et al.* that intermolecular contrast is only visible within the short range force interaction between tip and sample [146]. Zhang *et al.* note that the contrast only becomes visible under short range Pauli repulsion with respect to the substrate [149]. The authors also explain that recently observed covalent bonds in NC-AFM are comparable to the contrast of hydrogen bonding Δf data.

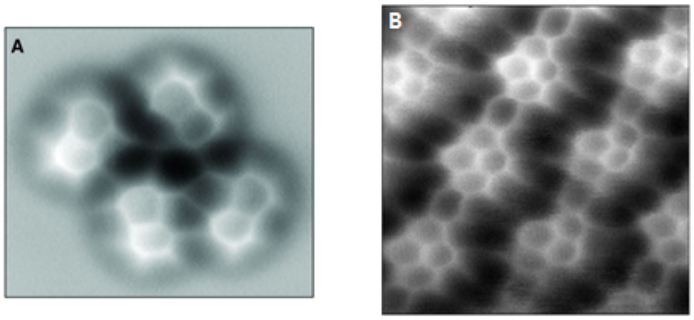

Figure 17: *A) Real-space visualization of the formation of hydrogen bonding in 8-hq molecular assemblies on Cu(111) by Zhang et al. [149] B) Constant height DFM image of a hydrogen-bonded NTCDI island on the Ag:Si(111)-($\sqrt{3}$ x $\sqrt{3}$)R30° surface by Sweetman et al. [146].*

In each of the reported cases where intermolecular resolution has thus far been observed, the molecules under study have all been planar in structure and generally stabilized through hydrogen bonding interactions with interatomic separations below the sum of the vdW radii. Here we show that apparent intermolecular features can also be observed over much larger distances in two-dimensional assemblies of C_{60} molecules that are neither planar in structure nor stabilized through any other intermolecular bonding mechanism beyond vdW forces. By modelling the tip-sample interaction using a variant of the simple Lennard-Jones models introduced in earlier work [151,152,156], we show that a C_{60}-terminated tip which is free to move on the end of the force microscope probe can account for the intermolecular features observed experimentally. As the intermolecular interactions in C_{60} islands arise solely from dispersion forces, it is clear that entirely artifactual contrast between molecules can arise even for systems which are nonplanar and where the apex of the tip of the force microscope is not terminated with a CO molecule. This has significant implications for the interpretation of high resolution force microscope images.

2.2 Low energy electron diffraction

The low energy electron diffraction (LEED) technique was pioneered by Davisson and Germer in 1927 [159]. They discovered that, when electrons with energies in the 5-500eV range were incident on a nickel crystal, they behaved like waves and produced diffraction patterns. In 1931, Davisson and Thomson shared the Nobel Prize for the discovery of matter waves. It wasn't until the 1960s, however, that UHV technology enabled clean surfaces to be studied with LEED. Low energy electrons interact strongly with matter, as the electron mean free path λ_e is small. This means only electrons scattered from near the surface can 'reflect', making LEED a surface-sensitive technique. LEED can be used qualitatively, where the diffraction pattern is recorded, and by analysing the spot positions, the size, symmetry and rotational alignment of the adsorbate unit cell with respect to the substrate unit cell. The technique can also be used quantitatively, where the intensities of diffracted beams are recorded as a function of the incident electron beam energy in order to produce I-V curves. The I-V curves may be used to provide information on atomic positions. In this thesis, the qualitative application is only considered.

2.3 X-ray -photoelectron spectroscopy and -standing wavefields

XPS (also known as electron spectroscopy for chemical analysis (ESCA)) is derived from the photoelectric effect. In 1887, Hertz showed that electrodes bathed in ultraviolet light created electric sparks more easily [160]. In 1905, Einstein explained the quantum nature of photons incident on a

conductive surface; they excited electrons and caused them to eject [161]. Millikan demonstrated the photoelectric effect, and determined an experimental value for Planck's constant, h, in 1916 [162]. Einstein was awarded the Nobel Prize in physics in 1921 for his discovery [163], and Millikan in 1923 for his work on the photoelectric effect [164]. XPS was further developed in the 1950s and 1960s by Siegbahn and colleagues to cater for solid surfaces. They were awarded the Nobel Prize in physics in 1981 for their contributions [165].

XPS irradiates a sample surface with low energy x-rays (lab-based x-ray sources typically use photons of 1253.6 or 1484.6eV, known as soft x-rays). The soft x-rays excite the electrons of the sample atoms, and assuming that the binding energy is less than that of the x-rays, electrons will be ejected from the parent atoms as photoelectrons. Typically, photoelectrons at a depth of 10-100Å below the surface can escape, making XPS a very surface sensitive analysis technique.

The XSW technique can reveal element specific structural information at surfaces and interfaces, using a combination of diffraction and spectroscopy measurements. The availability of third generation synchrotron light (high intensity and tunability) caused an increase in the frequency (no pun intended) of this technique being used in surface science.

It is understood that the first reports of XSW experiments surfaced in the 1960s. A similar concept was recognised by von Laue in 1941, described as 'x-ray beats' [166]. Another similar notion is known as the Kossel effect,

when fluorescence radiation is emitted from atoms within the crystal lattice, constructive or destructive interference is observed depending on the elastic scattering of the radiation by atomic planes. Emitted radiation is therefore either enhanced or diminished along certain angular directions, resulting in a spatial pattern of Kossel lines (or cones) [167].

Another similar idea to the XSW technique is the Borrmann effect, which is described as 'the anomalous transmission of x-rays through thick absorbing crystal in the so-called Laue case' [168]. In this case, Bragg diffraction of an incident wave gives rise to two wave fields in the crystal, where one wave field has nodes commensurate with the atomic planes, and is anomalously strongly transmitted, whereas the other wave field with antinodes on the atomic planes is anomalously absorbed [169].

Batterman, who reported that a superposition of incident and Bragg reflected x-ray waves were formed inside a crystal (known then as an x-ray interference field (XIF), but now as XSW), published the first paper of its kind in 1964 [170]. The elegance of Batterman's idea is that x-ray fluorescence radiation could track the movement and location of the x-ray wave field during Bragg reflection. In 1974 Golovchenko, Batterman and Brown located impurity arsenic atoms diffused into a shallow surface region on a silicon substrate [171]. In 1980, it was demonstrated that x-ray wave fields extend into regions beyond the surface by Cowan, Golovchenko and Robbins. Cowan *et al.* reported that bromine atoms on the Si(110) surface were located using the XSW technique [172].

At the extreme limit, the structure of molecular membranes has also been investigated. This is somewhat difficult due to the fact that the interlayer spacings are of the order of hundreds of Å which is much greater than the standing wave periodicity generated by Bragg reflection. One way to bypass this problem is to use XSW at high grazing incidence to exploit the total reflection, which renders the substrate irrelevant due to the membrane causing the scattering [173].

The most widespread application of XSW is the study of epitaxial films. XSW is normally used in two ways in such studies, firstly to determine the structure at the interface, and secondly to check the quality of the crystalline films. A majority of these studies has been on semiconductor-on-semiconductor growth, due to the importance in recent times of the semiconductor electronics age. As Si and Ge can be grown to exceptionally high precision, XSW can be performed at an arbitrary incidence and not confined to normal incidence x-ray standing wavefields (NIXSW). Most semiconductor studies have focussed on Si(100) ([174–176] for Ge, Ge/Si and Ge/Si respectively); some metal-on-semiconductor studies are apparent in the literature ([177] [178–180] [181–183] for, Ag/Au, Co, and Ni respectively); and fewer insulators-on-semiconductors ([184–187] for CaF_2, CaF_2, SrF_2 and RbBr respectively).

On metallic surfaces, there has been far less characterisation of overlayer growth, but NIXSW is a powerful tool for investigating the structural properties of molecules adsorbed on metal surfaces [188–191]. A particularly interesting area of research due to the interest in surface chemistry and

heterogenous catalysis (where the phase of the catalyst differs from that of the reactants), is molecular adsorption. In particular, the O1s binding energy is approximately 530eV, and even though typical NIXSW experiments are conducted at a few kiloelectronvolts (and as a results the photoabsorption cross section is very low), NIXSW experiments have proven possible in such cases. One example is the study of CH_3O on Al(111) [192].

Another area of growing interest is that of much larger molecules adsorbed on metal surfaces, namely exohedral [193], endohedral fullerenes and phthalocyanines [194–196], in order to understand the structure of films with potentially perplexing electronic properties. NIXSW can be used to gain a handle on the position of the encapsulated atoms relative to the atomic planes of the metal. Since the diameter of the C_{82} cage is large in comparison to atomic plane spacing, however, there is some potential ambiguity in results interpretation for these experiments. Respectively, it was concluded that there was no preference for a specific site location and a preference to occupy the upper half of the C_{82} cage for $Ce@C_{82}$ and $La@C_{82}$.

The XSW method is an x-ray interference technique in its most basic form. The convolution of incident and Bragg diffracted x-ray waves (standing waves) can be tuned, such that atomic positions within the crystal lattice structure can be determined. Due to the extension of the standing wave field above the sample surface, adsorbates and their positions can be calculated relative to the substrate surface, assuming that the signal that one is measuring is strong enough and the crystal lattice structure beneath the surface is perfectly constructed. A poorly constructed crystal will have

a sigma broadening which is too great for any meaningful experimentation (explained further in results chapter), however the development of the NIXSW means that somewhat imperfect crystals can also be used. This is because the sine function in the Bragg equation is at a turning point at normal incidence (i.e. 90°), hence an insensitivity to small variations in angle and the ability for NIXSW to be insensitive to surface imperfections.

3 Theory

3.1 Basics of scanning probe microscopy

3.1.1 Requirements for STM operation

The coarse positioning system of the STM should be able to cope with μm x, y and z movement to position the tip where desired over a sample, and it should also be capable of extremely fine movement to scan very small areas (down to the order of pm), shown in Figure 18.

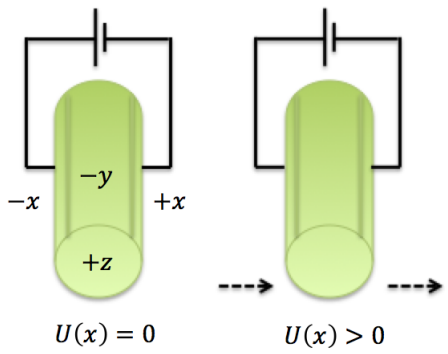

Figure 18: *The x, y and z movements of the tip are all controlled by a piezoelectric material, which responds by contracting or expanding when a potential difference is applied.*

A high sensitivity current-voltage (I-V) converter and pre-amplifier (sensitivity of order $10^9 \mathrm{VA}^{-1}$) are also required to increase the magnitude of the tunnelling current signal, as typical tunnelling currents measured in STM are in the pA or nA range. A negative feedback loop is essential to regulate the tip, which refers to a user defined current (known as the set point), and compares that to the actual tunnelling current between the tip and sample. In constant current mode, the tip is raster scanned across the surface, whilst the tip z position relative to the surface is varied. The z

heights are recorded with the corresponding x and y positions of the tip and a 3D height map of the surface can be generated. An alternative mode of operation is constant height mode, where the tip is fixed in the z position, but again allowed to raster scan in x and y directions, whilst the magnitude of the current between the tip and sample is measured. The main risk with constant height mode is that the feedback loop is disabled, so a 'rough' surface could cause undesirable tip-sample collisions, and reduced sharpness of the tip. Constant height mode in STM is useful to reduce feedback induced noise when scanning a surface. A digital signal processor for the tip positioning along with useful data logging and signal/image processing are all usually readily available with computer based software.

Vibration isolation is essential in STM, as without, the tip-sample distance (of around 1nm) required for electron tunnelling could not be maintained (without tip crashing into the sample surface, or tip moving further away from sample surface). Internal damping is provided by an Eddy current damping system where the STM stage 'floats' on vertical springs. External damping is carried out by pneumatic air legs to decouple the system from vibrations from the immediate environment.

3.1.2 STM theory

Figure 19 presents the basic physics which defines the operation of an STM. In quantum mechanics, a particle has a non zero probability of penetrating a potential barrier. It is important to note that in Figure 19 the energy of the wavefunction is unchanged either side of the barrier, it is the amplitude, and thus the probability that changes when the wavefunction has 'passed

through' the potential barrier of width W, shown in region C.

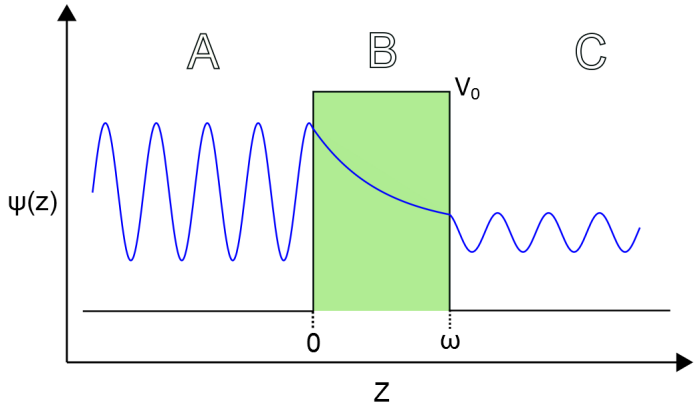

Figure 19: *Schematic showing an electron wavefunction incident on a 1D barrier. Region A shows the travelling electron, region B describes the wavefunction exponentially decaying through the potential barrier of width s and region C shows the electron wavefunction with a diminished amplitude.*

3.1.3 The finite potential barrier

The time-independent Schrödinger equation is

$$\hat{H}\Psi_z = E\Psi_z \tag{1}$$

where $\hat{H}$ is the Hamiltonian operator, Ψ_z is the wavefunction in one dimension and E is the kinetic energy of the particle. By expanding the Hamiltonian, a particle confined to 1D can be explicitly written as

$$-\frac{\hbar^2}{2m}\frac{d^2\Psi}{dz^2} + V(z)\Psi(z) = E\Psi(z) \tag{2}$$

The wavefunction in region A can be described as

$$\Psi_A(z) = Ae^{ikz} + Be^{-ikz} \tag{3}$$

in region B as

$$\Psi_B(z) = Ce^{\alpha z} + De^{-\alpha z} \tag{4}$$

and in region C as

$$\Psi_C(z) = Fe^{ikz} \tag{5}$$

where $k = \frac{\sqrt{2mE}}{\hbar}$, and the decay constant $\alpha = \frac{\sqrt{2m(V_0-E)}}{\hbar}$. Assuming that the voltage applied is smaller than the work function of the sample (i.e. $V << \phi$) so that tunnelling occurs from states that are close to the Fermi level, then $\alpha = \frac{\sqrt{2m\phi}}{\hbar}$. A more detailed explanation can be found in the appendix.

The ratio between the probability flux of the transmitted wave in region C and the wave incident in region A is known as the transmission coefficient, T, where $T = |\frac{F}{A}|^2$. To get an expression for T we impose smooth and continuous conditions at $z = 0$ and $z = w$ (at the tip-vacuum and vacuum-sample boundaries) for equations 3-5 and their corresponding derivatives. By combining the equations, T can be related to the tunnelling current, I

$$T \propto I \propto e^{-2\alpha w} \tag{6}$$

By using typical values of ϕ (4-5eV), I changes by an order of magnitude when the barrier width w is changed by ~ 1Å [197]. A thorough derivation

of the transmission coefficient can be found in the appendix.

This description only accommodates for a single electron. There is a strong distance dependence on the tunnelling current, so assuming that there is a single atom at the end of the tip, and there is sufficient vibration isolation in the system, then it is possible to resolve the electronic structure of a conducting surface at an atomic scale with an STM.

Figure 20 shows three different scenarios for the tunnelling of electrons between the tip and sample. Figure 20a shows an 'open circuit' between the tip and sample. The Fermi levels are aligned because there is electrical contact and a zero bias voltage. Figure 20b depicts the effect when a negative bias voltage is applied to the sample, E_{Fs} is offset by an energy eV (with respect to E_{Ft}) so that electrons tunnel from filled states in the sample to empty states in the tip. Figure 20c is the reverse of Fig. 20b, so a positively charged bias, causes E_{Ft} offset by an energy of eV (with respect to E_{Fs}), but now electrons tunnel from filled states in the tip to empty states in the sample.

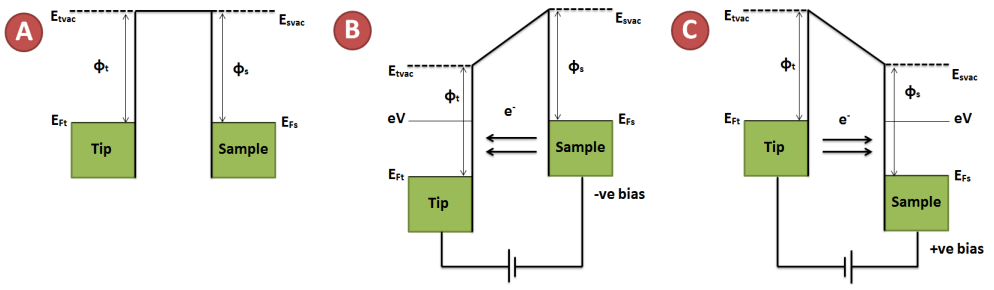

Figure 20: *Schematic of electrons tunnelling between a metal tip and sample. E_{Ft} and E_{Fs} are the quasi Fermi levels of the tip and sample, ϕ_t and ϕ_s are the work functions of the tip and sample and E_{tvac} and E_{svac} are the vacuum levels of the tip and sample.*

3.1.4 Tersoff-Hamann approach

Tersoff and Hamann suggested a simplified spherical STM tip model to understand the physics of the electronic tip-sample interaction [198]. They considered an *s*-wave for the tip wavefunction in the form

$$\psi(\mathbf{r}) \sim \frac{1}{|\mathbf{r}-\mathbf{r}_0|} e^{(-k|\mathbf{r}-\mathbf{r}_0|)} \tag{7}$$

where $\mathbf{r}_0$ is the centre of the spherical tip.

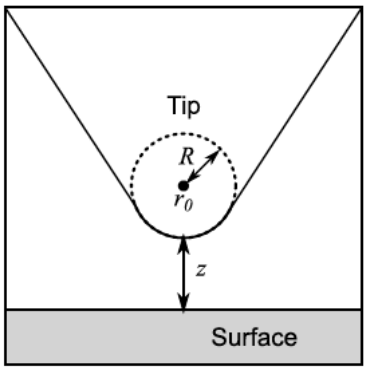

Figure 21: *Schematic of the Tersoff-Hamann s-wave tip model [198].*

Bardeen [199] described the tunnelling current for small bias voltages as

$$I \propto V\rho(\mathbf{r}_0, E_F) \tag{8}$$

and

$$\rho(\mathbf{r}, E) = \sum_i |\Psi_i(\mathbf{r})|^2 \delta(E - E_i) \tag{9}$$

where $\rho(\mathbf{r}, E)$ is the local density of states (LDOS) of the surface, $\Psi_i(\mathbf{r})$ is the surface wavefunction with energy E_i, and E_F is the Fermi energy. By scanning the tip over the surface, an STM image using Tersoff-Hamann's

theory can be obtained through a map of the surface LDOS.

An extension of the Tersoff-Hamann approach for a finite bias voltage can be expressed, assuming the electronic structure of the tip can be ignored

$$\frac{dI(V)}{dV} \propto \rho(\mathbf{r}_0, E_F + eV) \tag{10}$$

and therefore

$$I(V) \propto \int_{E_F}^{E_F+eV} \rho(\mathbf{r}_0, E)dE \tag{11}$$

simply put, equation 10 means that by fixing the tip above a point on the surface, the bias voltage can be varied to produce a local spectrum, known as scanning tunnelling spectroscopy (STS). Importantly, the formulae derived by Tersoff and Hamann suggests that the electronic density of states of a surface is probed, and not atomic position directly.

Tip termination is crucial, since the apex of the tip directly effects Tersoff and Hamann's theory, and the s-wave approximation is much too simple in general. A tip, in reality, can consist of several atoms rather than a single atom, which can influence both STM and STS. Bardeen [199] states that as long as the distance between the sample and the tip is large enough, such that the tip-sample interaction can be modelled as a small perturbation, then the tunnel current can be represented by

$$I = \frac{2\pi e}{\hbar} \sum_{\mu,\nu} [f(E_\mu) - f(E_\nu)]|M_{\mu\nu}|^2 \delta(E_\mu - E_\nu + eV) \tag{12}$$

and

$$M_{\mu\nu} = \frac{\hbar^2}{2m} \int_S (\psi_\mu^* \nabla \psi_\nu - \psi_\nu \nabla \psi_\mu^*) d\mathbf{S} \tag{13}$$

where $f(E)$ is the Fermi distribution function, and ψ_μ and ψ_ν are the wavefunctions of the sample surface and tip respectively, and are also eigenfunctions of the isolated system which can be solved independently. $\int_S d\mathbf{S}$ represents an integral over an arbitrary plane S which separates the tunnelling gap into respective tip and sample regions.

Not all atomic species will appear as bright spots, or protrusions. Some elements can appear as dark spots on an STM image, or in other words, the atomic corrugation shows negative displacement. Chen considered a W tip as terminating in a d orbital, and thus, extended the Tersoff-Hamann theory to accommodate for non s-wave tips, and found a derivative rule [200]. According to the derivative rule, the tunnelling matrix elements for d- and p-tip states are proportional to the z derivative of the surface atom wavefunction at the centre of the tip apex atom, so it was predicted that the best candidates for STM tips are d-band metals and semiconductors with p dangling bonds. A strong example of the use of this technique is by Gross *et al.*, where various molecules were imaged at high resolution (submolecular) using the p-wave orbitals of the CO molecule [201]. As a result, probing the LDOS doesn't necessarily correspond to the spatial arrangement of surface atoms or adsorbed molecules, so careful interpretation is required.

3.1.5 AFM theory

If the tip is a large distance away from the surface, in UHV, then a cantilever can be described as a damped simple harmonic oscillator.

By starting with Hooke's Law

$$F(z) = -kz \tag{14}$$

and introducing Newton's Second Law, this is equated as

$$m\frac{d^2z}{dt^2} = -kz \tag{15}$$

by taking the simplest approach, such that there are two additional forces besides the tension in the spring, namely the damping force

$$F_{damp} = -b\frac{dz}{dt} \tag{16}$$

and the driving force

$$F_{driv} = A_0 cos(\omega t) \tag{17}$$

where the driving force has a maximum amplitude of A_0 and a frequency ω. By summing the forces we get

$$F_{sum} = F_{spring} + F_{damp} + F_{driv} = -kz \tag{18}$$

when written explicitly is

$$m\frac{d^2z}{dt^2} = -kz - b\frac{dz}{dt} + A_0 cos(\omega t) \tag{19}$$

Q is the quality factor of the spring, which is defined as

$$Q = \frac{\omega_0}{2\beta} \tag{20}$$

where ω_0 is the resonant frequency of the damped driven oscillator, which can be written as

$$\omega_0 = \frac{\sqrt{\omega_0^2 - 2b^2}}{2\beta} \tag{21}$$

and $\beta = b/2m$. By substitution and rearrangement

$$b = \frac{m\omega_0}{\sqrt{Q^2 + 1/2}}. \tag{22}$$

and by assuming that $Q >> 1$, then

$$b = \frac{m\omega_0}{Q} \tag{23}$$

and finally, by substituting into the full equation of motion for $b = m\omega_0/Q$

$$m\frac{d^2z}{dt^2} = -kz - \frac{m\omega_0}{Q}\frac{dz}{dt} + A_0 cos(\omega t) \tag{24}$$

or alternatively, by using $\omega^2 = k/m$

$$\frac{d^2z}{dt^2} = -\omega_0^2 z - \frac{\omega_0}{Q}\frac{dz}{dt} + \frac{A_0}{m} cos(\omega t) \tag{25}$$

3.1.6 Different forces on the AFM tip

The total force, F_{tot}, between tip and sample in UHV AFM can be written as

$$F_{tot} = F_{vdW} + F_{el} + F_{chem} \tag{26}$$

where F_{vdW} represents long range vdW forces [202], F_{el} accounts for long range electrostatic forces and F_{chem} is the short range chemical forces contribution [203].

Van der Waals forces

VdW forces are caused by fluctuations of the local dipole moment of atoms, and subsequently, the interaction of their dipoles with dipoles induced in nearby atoms. More specifically, vdW force can be of a number of different types: interactions between two permanent dipoles (Keesom), a permanent dipole and an induced dipole (Debye) and induced dipole-induced dipole interactions (London Dispersion) [202, 204, 205].

The attractive vdW force for two atoms separated by a distance r scales as r^{-6}. When considering two bodies, such as a tip and sample, one may sum (or integrate) the energies of all the atoms in one body, with all the atoms in the other and thus obtain the 'two-body' potential for an atom near a surface. In this context, a Hamaker approach is required, which determines the vdW interaction of two macroscopic bodies by carrying out the so-called Hamaker-type integration of all the intermolecular interactions. For a spherical tip of radius R at a distance z from a flat surface

$$F_{vdW} = -\frac{HR}{6z^2} \tag{27}$$

where H is the Hamaker constant, which varies depending upon the tip and sample materials, but for most solids and interactions across a vacuum, H is $\sim$ 1eV [206]. Taking typical values of R=50nm and $z = 5$Å we find that $F_{vdW} = 10$nN.

Electrostatic forces

An electrostatic force arises when there's a difference in the work function between the tip and sample, and a potential difference can be applied between the tip and sample to null the electrostatic force. The force between a conductive tip and a charge distribution on an insulating film is given by

$$F_{charge} = q_t E_z \tag{28}$$

where q_t is the induced charge on the tip and E_z is the electric field. The induced charge has two contributions

$$q_t = -(q_s + CV) \tag{29}$$

where q_s is induced on the tip by the surface charge distribution, and the term CV originates from the bias voltage V between the tip and back electrode with capacitance C.

The tip and the sample can be modelled as a circuit (similar to the STM theory section) with a z distance dependence on the capacitance $C(z)$.

$$F_{capacitance} = \frac{1}{2}\frac{dC}{dz}V^2 \tag{30}$$

Where $\frac{dC}{dz}$ is the gradient of the capacitance between the tip and sample surface [207]. $\frac{dC}{dz}$ is dependant upon the tip geometry but is always negative.

The total electrostatic force F_{el} is then described by the sum of F_{charge} and $F_{capacitance}$

$$F_{el} = q_t E_z + \frac{1}{2}\frac{dC}{dz}V^2 = -(q_s + CV)E_z + \frac{1}{2}\frac{dC}{dz}V^2 \tag{31}$$

in the first approximation, E_z is proportional to the charge on the sample, so the first two terms are a measure of the charge distribution.

Chemical forces

If the overlap between the electron wavefunction in the tip and the sample become significant, i.e. at tip-sample distances of the order of interatomic spacings, then short range forces become significant. Moreover there is always a background vdW contribution, and the short range chemical force is 'buried' in within this background. Chemical forces can be attractive or repulsive, depending on the distance between the tip and the sample. Short range repulsive forces between two atoms are due to the Pauli exclusion principle, which stops matter from collapsing. A good approximation for describing chemical forces is the Lennard-Jones force potential

$$V_{LJ} = E_b\left[\left(\frac{z_0}{z}\right)^{12} - 2\left(\frac{z_0}{z}\right)^{6}\right] \tag{32}$$

where E_b is the binding energy, or potential minimum and z_0 is the equilibrium distance between two atoms [202, 206, 208]. When modelling an atom-atom vdW interaction, the attractive part of the Lennard-Jones force potential gradient is the $\sim z^{-6}$ and the repulsive $\sim z^{-12}$.

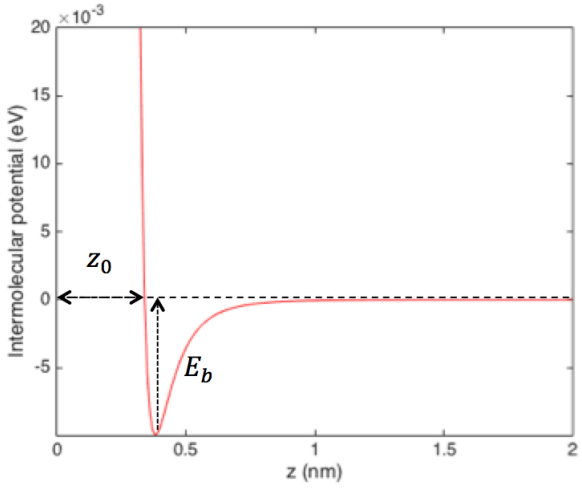

Figure 22: *A plot of intermolecular potential energy against atomic distance, representing the potential energy interaction between two single atoms.*

The force is the negative derivative of the potential

$$F = -\frac{\partial V}{\partial z} \tag{33}$$

AFM (and for this thesis, a qPlus sensor) probes the strength and geometry of chemical bonds between single atoms and molecules, and in particular, the force gradient, so the chemical force interaction between the tip and the sample is of utmost importance for spectroscopy and high resolution images.

3.1.7 Detecting atomic corrugation

In order to detect atomic corrugation is the force between the tip and the sample (F_{ts}) is required. F_{ts} (shown later) is calculated as

$$\Delta f = -\frac{f_0}{\pi k A_0} \int_{-1}^{1} F_{ts} \left[d_0 + A_0(1+u) \right] \frac{u}{\sqrt{1-u^2}} du \tag{34}$$

and is a function of the frequency shift (Δf) caused by the tip-sample interaction, where F_{ts} is the force interaction between the tip and the sample, A_0 is the amplitude, d_0 is the distance of closest approach, k is the cantilever stiffness, f_0 is the unperturbed resonant frequency and $u = cos(\omega t)$. Unlike STM, AFM instruments are not confined to conducting (or semiconducting) tip and sample materials, as described in the previous sections. There are several force interactions detected by the cantilever, including Pauli repulsion, short range chemical, long range vdW and long range electrostatic or magnetic forces, and consequently, feedback design and image interpretation in AFM are greater in complexity compared to STM.

The deflection of a cantilever can be modelled as a spring, and the most common method for measuring this is via displacement of a laser beam, which is reflected from the back side of the cantilever [209] (In this thesis however, a mechanically excited qPlus sensor was used, which is explained in detail in the experimental methods section).

Consider a weakly perturbed harmonic oscillator. The Hamiltonian of the cantilever is

$$\hat{H} = \frac{p^2}{2m^*} + \frac{kq'^2}{2} + V_{ts}(q) \tag{35}$$

where $p = m^* \frac{dq'}{dt}$, $q'(t)$ is the deflection of the cantilever, $q = d$ is the distance of closest approach (between tip and sample), A_0 is the amplitude of oscillation and $q(t) = q'(t) + d + A_0$.

The unperturbed motion of the cantilever can be described as

$$q'(t) = A_0 cos(\omega t) \tag{36}$$

and

$$\omega_0 = \sqrt{\frac{k}{m^*}} \tag{37}$$

where m^* is the effective mass of the cantilever and k is its stiffness. A force F_{ts} between the tip and the sample will cause a change in k. Assuming that the cantilever amplitude A_0 is smaller than the distance between the tip and sample, i.e. $A_0 << d$, then $k' = k + k_{ts}$, where k_{ts} is the force gradient $-\frac{\partial F}{\partial z}$ at $z = d + A_0$ [206], then

$$\omega = \sqrt{\frac{k + k_{ts}}{m^*}} \tag{38}$$

if we then assume $k >> k_{ts}$ or in other words, the force gradient to be small in comparison to k, and constant in the z direction during a complete cantilever oscillation cycle then

$$\omega = \omega_0 \left(1 + \frac{k_{ts}}{2k}\right) \tag{39}$$

and the frequency shift can be approximated to

$$\frac{\Delta\omega}{\omega_0} = \frac{\Delta f}{f_0} = \frac{k_{ts}}{2k} = \frac{1}{2k}\frac{\partial F}{\partial z} \tag{40}$$

so for small amplitudes, $\Delta f \propto \frac{\partial F}{\partial z}$ however large amplitudes (where $A > d$) are commonly used in AFM. Dürig [210, 211] and Livshits *et al.* [212] described a more arbitrary expression for Δf starting with a Fourier series in an action integral, and can be written as

$$\bar{S} = \int_0^{T_0} \left[\frac{1}{2}\dot{s}^2 - \frac{1}{2}\omega_0^2 s^2 - \frac{\omega_0^2}{k}U_{ts}(s + s_0)\right] \tag{41}$$

where s is the oscillatory motion, s_0 is an offset parameter that fixes the position of the sample relative to the spring, ω_0 is the resonant frequency of the cantilever, k is the cantilever stiffness and U_{ts} is the potential energy of the tip-sample interaction. By minimising the action, $\bar{S}$, then

$$\Delta f = -\frac{f_0}{\pi k A_0}\int_{-1}^{1} F_{ts}\left[d_0 + A_0(1+u)\right]\frac{u}{\sqrt{1-u^2}}du \tag{42}$$

(full derivation in appendix) where F_{ts} is the force interaction between the tip and the sample, A_0 is the amplitude, d_0 is the distance of closest approach, k is the cantilever stiffness, f_0 is the unperturbed resonant frequency and $u = cos(\omega t)$.

3.1.8 Force deconvolution

The issue here is Δf is a function of F_{ts}, so the the relationship needs to be inverted to get F_{ts} as a function of Δf. Furthermore, in practise, F_{ts} is inclusive of all tip-sample forces (vdW, chemical, magnetic and electrostatic) so a subtraction of the 'background' is required to extract the short

range interactions [213]. Sader and Jarvis [214] approximated an inversion procedure of equation 42

$$F(z) = 2k \int_z^\infty \left(1 + \frac{a^{\frac{1}{2}}}{8\sqrt{\pi(t-z)}}\right) \Omega(t) - \frac{a^{\frac{3}{2}}}{\sqrt{2(t-z)}} \frac{d\Omega(t)}{dt} dt \qquad (43)$$

where $\Omega(t) = \frac{\Delta\omega}{\omega_0}$ and a is the amplitude of oscillation. This equation has been used later in this report in a Matlab script for the deconvolution of $\Delta f(z)$ spectra taken with the AFM in the experimental section.

Giessibl also managed to invert equation 42, and expressed it as a matrix equation for discrete values

$$\Delta f_i = \sum_{j=1}^{N} W_{ij} F_{ts,j} \qquad (44)$$

and the inverse matrix $M = W^{-1}$ can be used to calculate F_{ts} from Δf for a given $\Delta f(z)$ curve

$$F_{ts,j} = \sum_{i=1}^{N} M_{ji} \Delta f_i \qquad (45)$$

The matrix method requires data points $\Delta f_i = \Delta f(z_i)$ with equidistant spacing along the z axis [215].

The Sader-Jarvis or Giessibl deconvolution methods are required to convert from Δf to F_{ts}. Welker *et al.* investigated the deconvolution quality on oscillation amplitude [215]. A coefficient of determination (CoD) describes how well data fits a statistical model, where the CoD, R^2 is 1, it means there is a perfect match, but typically $0 < R^2 \leq 1$.

Figures 23a and 23b show the amplitude dependence of the CoD for a Morse and Lennard-Jones (L-J) force law respectively by Welker *et al.* [215]. Both models have a CoD of roughly 1 at 300pm but the Sader-Jarvis has the lowest CoD of 0.990 at an amplitude of 137pm, this translates to a deviation of 109pN to 13pN in residuals.

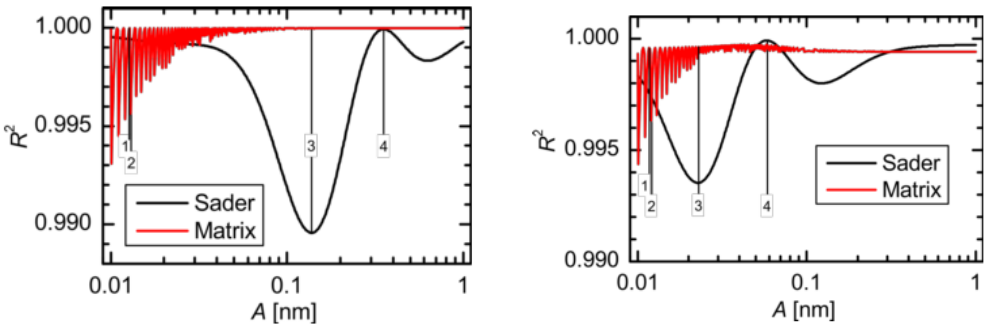

(a) (b)

Figure 23: *a) Amplitude dependence of the CoD for a Morse force law. 1,2 3 and 4 are amplitudes of 12.8pm, 12.9pm, 137pm and 352pm respectively. b) Amplitude dependence of the CoD for a L-J force law. 1,2 3 and 4 are amplitudes of 11.7pm, 12.0pm, 23pm and 58.3pm respectively.*

3.2 Low energy electron diffraction

3.2.1 LEED theory

By using the principle of wave-particle duality to describe the underlying physical process of LEED, a beam of electrons can be regarded as a succession of electron waves incident on a crystal. The incident electron waves will be scattered by the crystal's surface atoms (i.e. in regions of high localised electron density), which are considered as 'point scatterers'.

The electron wavelength is described by the de Broglie relation

$$\lambda = h/p \tag{46}$$

where h is Planck's constant, and p is the electron momentum. By using the relationship $p = mv = \sqrt{2mE_k}$ the de Broglie equation can be written as

$$\lambda = \frac{h}{\sqrt{2mE_k}} \tag{47}$$

where m is the mass of one electron and E_k is the electron's kinetic energy. As a example, an electron with an energy of 20eV has a corresponding wavelength of 2.7Å , which is comparable with atomic spacing distance. This is a necessary condition for electron diffraction in order for atomic structure to be observable.

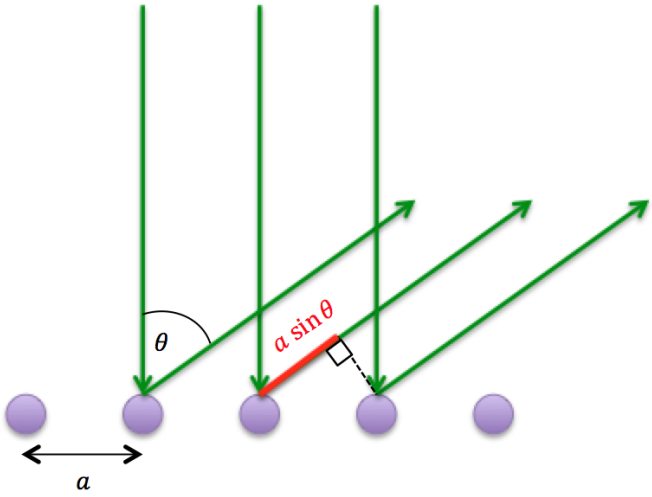

Figure 24: *Schematic showing incident electrons with energy E on a surface layer of atoms. Electrons are scattered at an angle θ relative to the normal, with a constant path difference d = asinθ.*

By considering a 1D lattice of atoms, with atomic separation a and the electron beam at normal incidence to the surface, a simple model for the

scattering of electrons by the topmost layer of atoms in a crystal can be drawn in Figure 24. By considering the backscattering of electrons in Figure 24 from two adjacent atoms at an angle θ to the surface normal, then it's clear a path difference d exists between the distance the radiation has to travel from the scattering centre to a detector. The path difference is illustrated by two green 'ray paths' after diffraction has occurred.

The path difference is defined as

$$d = asin\theta \tag{48}$$

the magnitude of the path difference d must be equal to an integral number of wavelengths for constructive interference to occur when the scattered electron beams meet at the detector

$$d = asin\theta = n\lambda \tag{49}$$

where λ is the electron wavelength and n is an integer. The diffraction intensity will be at its largest magnitude when the Bragg condition is satisfied exactly, i.e.

$$asin\theta = n\lambda \tag{50}$$

all surface diffraction patterns show a symmetry which is commensurate with that of the actual atomic surface structure. LEED patterns are centrally symmetric, and scale inversely according to both $\sqrt{E}$ and the size of the surface unit cell. An Ewald sphere can be used as a geometric construct with a LEED pattern, which can determine the maximum resolution

available for a given electron wavelength and the unit cell dimensions.

As an example, an $fcc(110)$ surface is sketched in Figure 25. The atomic structure in real space is shown on the left, which can be imagined as if one is viewing from the position of the electron gun, whilst the diffraction pattern on the right shows a schematic of the scattered electrons interacting with the fluorescent screen of the LEED optics, which create bright spots. The diffraction pattern on the right shows a similar rectangular symmetry to the real space atomic lattice, but is stretched due to the nature of the reciprocal dependence upon the lattice parameter (discussed later). The diffraction pattern is also symmetric around the centre spot; this is representative of the diffracted beam from electrons incident exactly normal to the surface (the $n = 0$ case in the 1D model). The diffraction pattern in Figure 25 illustrates the first order ($n = 1$) electron beams, such that θ is small enough for the diffracted beam to be incident on the fluorescent screen.

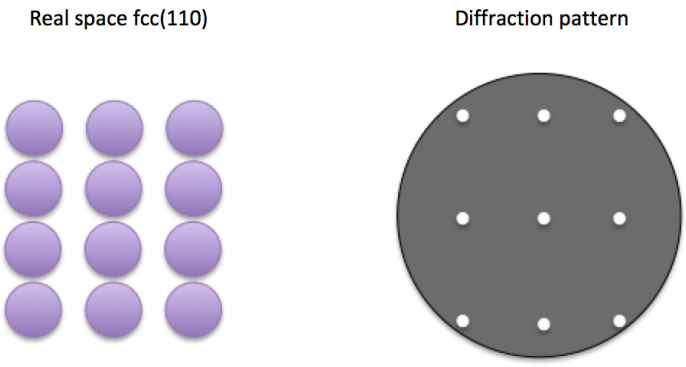

Figure 25: *Illustration showing the real space lattice of an fcc(110) atomic structure and the expected diffraction pattern.*

Figure 26 shows a similar illustration to Figure 25 but with the electron energy doubled in magnitude. Some of the second order diffraction spots are

now visible ($n = 2$) and the pattern has contracted toward the central-most diffraction spot. In the case of a simple LEED pattern like the $fcc(110)$ crystal orientation, it's possible to explain the diffraction patterns in terms of scattering of electrons by rows and columns of atoms of the crystal surface. As an example, rows of atoms in real space would give rise to a set of diffracted beams in reciprocal space, as rows, and leading to the diffraction spots running through the central-most diffraction spot. In general, the further the rows of atoms in real space, the closer the equivalent the rows will be in the diffraction pattern.

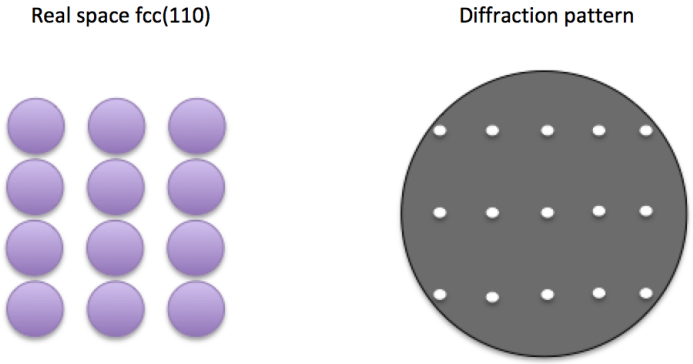

Figure 26: *Illustration showing the real space lattice of an fcc(110) atomic structure and the expected diffraction pattern if the electron energy was doubled in comparison to Fig. 25.*

A much better approach is to consider the LEED diffraction pattern in the context of reciprocal space. The reciprocal *net* is determined by the reciprocal lattice vectors, specifically $\mathbf{a}_1^*$ and $\mathbf{a}_2^*$ for the substrate and $\mathbf{b}_1^*$ and $\mathbf{b}_2^*$ for the adsorbate. The reciprocal lattice vectors are related to the real space unit cell vectors by the scalar product relations

$$\mathbf{a}_1.\mathbf{a}_2^* = \mathbf{a}_1^*.\mathbf{a}_2 = 0 \tag{51}$$

and

$$\mathbf{a}_1.\mathbf{a}_1^* = \mathbf{a}_2^*.\mathbf{a}_2 = 1 \tag{52}$$

this means mathematically that $\mathbf{a}_1$ is perpendicular to $\mathbf{a}_2^*$, and $\mathbf{a}_2$ is perpendicular to $\mathbf{a}_1^*$.

An inverse relationship exists between the lengths of $\mathbf{a}_1$ and $\mathbf{a}_1^*$ (and $\mathbf{a}_2$ and $\mathbf{a}_2^*$) of the form

$$|\mathbf{a}_1| = \frac{cosA}{|\mathbf{a}_1^*|} \tag{53}$$

where A is the angle between vectors $\mathbf{a}_1$ and $\mathbf{a}_1^*$. When $A = 0°$ then $|\mathbf{a}_1| = 1/|\mathbf{a}_1^*|$. The same mathematical principles hold for the adsorbate real space and reciprocal vectors $\mathbf{b}_1$, $\mathbf{b}_2$, $\mathbf{b}_1^*$ and $\mathbf{b}_2^*$.

The mathematical vector relationships are given for the $fcc(100)$ atomic structure and adsorbate over-layer in Table 1, and Figure 27 shows the real and reciprocal space patterns for a primitive (2 x 2) adsorbate lattice over an $fcc(100)$ substrate.

$\mathbf{b}_1^*$ is perpendicular to $\mathbf{b}_2$	$\mathbf{b}_2^*$ is perpendicular to $\mathbf{b}_1$
$\mathbf{b}_1^*$ is parallel to $\mathbf{b}_1$	$\mathbf{b}_2^*$ is parallel to $\mathbf{b}_2$
Angle B, between $\mathbf{b}_1^*$ and $\mathbf{b}_1$ is 0	Angle B, between $\mathbf{b}_2^*$ and $\mathbf{b}_2$ is 0
$\|\mathbf{b}_1^*\| = 1/\|\mathbf{b}_1$	$\|\mathbf{b}_2^*\| = 1/\|\mathbf{b}_2$
$\|\mathbf{b}_1\| = 2\|\mathbf{a}_1\|$; $\|\mathbf{b}_1^*\| = \|\mathbf{a}_1^*\|/2$	$\|\mathbf{b}_2\| = 2\|\mathbf{a}_2\|$; $\|\mathbf{b}_2^*\| = \|\mathbf{a}_2^*\|/2$

Table 1: *Real and reciprocal space vector properties relating to Fig. 27.*

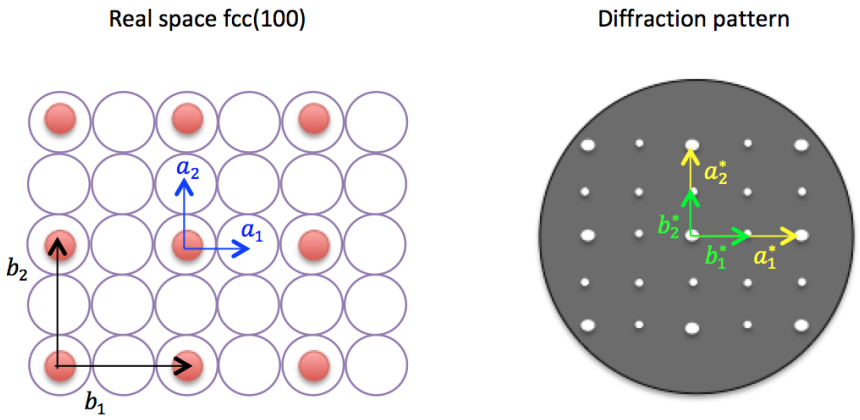

Figure 27: *Illustration showing the real space lattice of an fcc(100) atomic structure and the expected diffraction pattern if a* (2 x 2) *adsorbate overlayer was apparent (red).*

3.3 X-ray photoelectron spectroscopy

3.3.1 XPS description

In a photoemission experiment, the sample is irradiated by a monochromatic light source of a certain energy $\hbar\omega$, and the kinetic energy distribution of the ejected photoelectrons is recorded by an electron analyser. XPS is a semi-quantitative technique used to determine the composition of atomic species using the photoelectric effect.

Figure 28 shows the physical process for photoelectron emission. An incident photon of energy $\hbar\omega > E_b + \Phi$ is required for photoelectron ejection. If the binding energy of the atomic species decreases, then the kinetic energy of the photoelectron will increase, assuming that the incident photon energy (monochromatic) remains constant. The intensity of photoemission is also proportional to the intensity of the irradiating photons. The method

in which detection of specific atomic species is viable is through analysis of the kinetic energies of photoelectrons. A range of kinetic energies can be detected if there is a broad valence band, and since each element has a unique set of core electron levels, then the kinetic energies of ejected photoelectrons can be used as a fingerprint. The valence is strictly defined as the highest range of electron energies in which electrons are present at 0K, or put more simply, they occupy the outer most electron shells. Oppositely, core electrons are not valence electrons, do not participate in bonding and are located at lower energies at the inner most shells. Inter-atomic bonding can cause a significant broadening of valence electron bands.

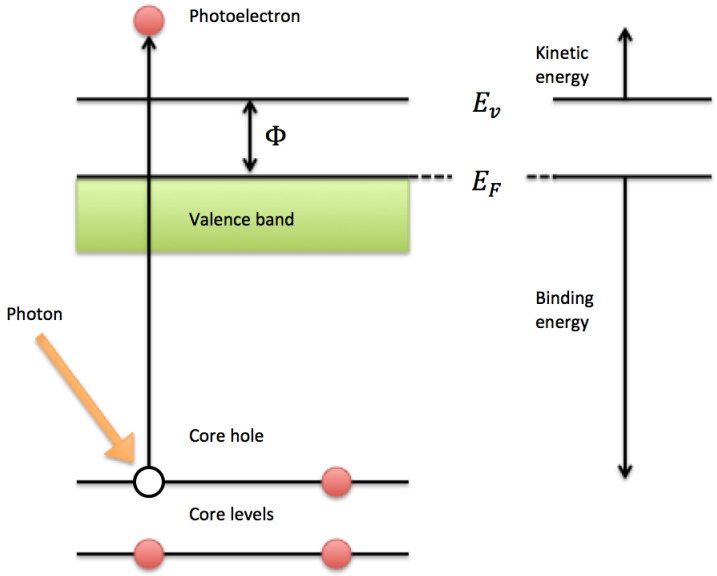

Figure 28: *An illustration showing the photoemission process. An incident photon with energy $\hbar\omega > E_b + \Phi$ causes a core electron to be ejected as a photoelectron.*

Figure 29 shows the mechanism of Auger electron emission and x-ray fluorescence.

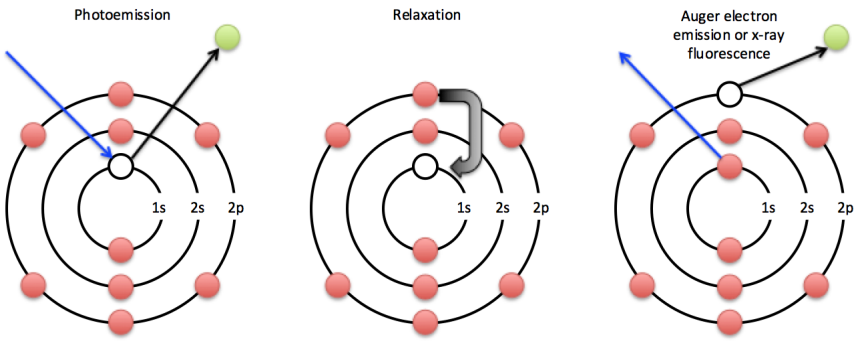

Figure 29: *An illustration showing the possible secondary mechanisms of the photoemission process. Incident photon with energy* $\hbar\omega > E_b + \Phi$ *causes core electron to be ejected as a photoelectron. Further photoemission can then occur due to relaxation of another electron filling a 'photo hole', namely Auger electron emission or x-ray fluorescence.*

The photoemission process can be envisaged as three steps: firstly, absorption and ionisation; secondly, the response of the atom, and creation of photoelectron; and finally the transport of the electron to the surface and escape.

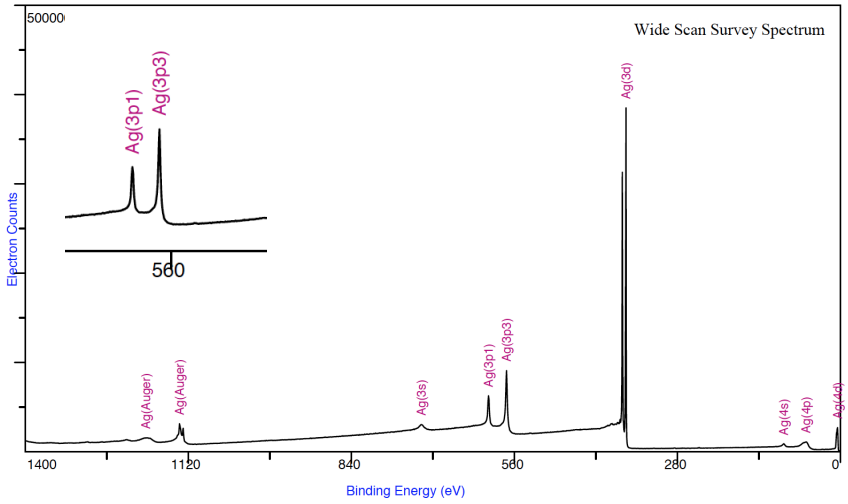

Figure 30: *A wide XPS survey of clean Ag, taken from XPS International. Inset: zoom of the 3p spin orbit split states.*

XPS spectra shows a characteristic 'stepped' background (as shown in Figure 30), which is due to inelastic processes, or in other words, extrinsic losses from the bulk electrons. Electrons deeper in the surface lose some of their 'ejection potential' and emerge with reduced kinetic energy, with an apparent increase in binding energy. Electrons that are very deep in the surface lose all of their energy before escaping the solid and cannot be detected.

Electrons in orbitals with orbital angular momentum experience a coupling between the magnetic fields of spin, and angular momentum, denoted s and l respectively, as shown by Figure 31.

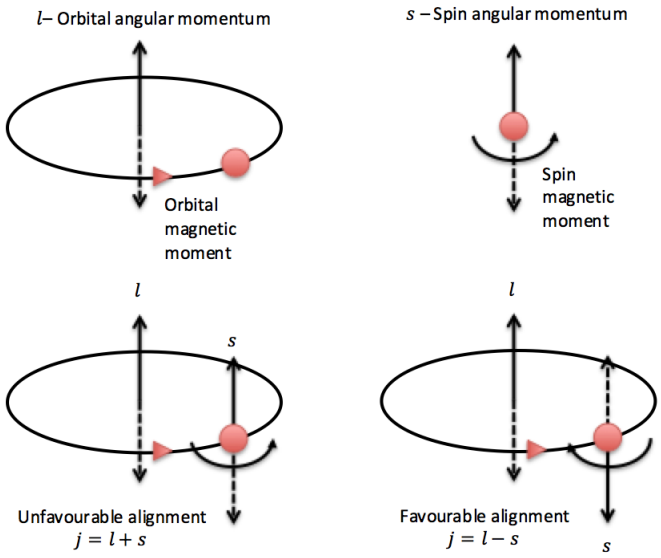

Figure 31: *An illustration showing the coupling between spin and orbital angular momentum.*

This is known as spin orbit coupling, and can be seen in XPS spectra, where the total angular momentum $j = l + s$. It is important to note that s orbitals are not spin-orbit split (known as 'singlets' in XPS), whereas p,

d and f orbitals are spin-orbit split (known as 'doublets' in XPS). This can be seen in Figure 30. The binding energy of the lower j value of a doublet is greater in magnitude than the higher j value (i.e. E_b of $2p_{1/2} > E_b$ of $2p_{3/2}$). The magnitude of spin-orbit splitting also increases with atomic number Z, and decreases with distance from the nucleus.

Auger peaks (also seen in Fig. 30) result from a surplus of energy from an atom after core-hole creation, or relaxation. Auger peaks always accompany XPS, but are broader and more complex in structure than photoemission peaks, and interestingly, the kinetic energy of Auger electrons is independent of the incident photon energy that caused them. Peak asymmetry is the result of small energy electron-hole excitations near E_f (for core electrons, and not Auger electrons) of the metal, also known as a Doniach-Šunjić line shape; the degree of asymmetry is proportional to the DOS at E_f.

3.3.2 XPS theory

The physics behind a photoemission experiment is an incident photon of energy $\hbar\omega$ hitting an electron of initial state i with wavefunction ψ_i, and transforming it into a final electron state f with a wavefunction ψ_f. The final electron wavefunction ψ_f is also used to described the emitted photoelectron. It is assumed that the remaining electrons within the system $(N-1)$ respond to the 'photohole' and that the ejected photoelectron does not.

3.3.3 Fermi's Golden Rule

The transition probability w between the N-electron states ψ_i and ψ_f is governed by Fermi's Golden Rule

$$w \propto \frac{2\pi}{\hbar}|\langle\psi_f|\mathcal{V}|\psi_i\rangle|^2\delta(E_f - E_i - \hbar\omega) \tag{54}$$

where the δ-function enforces the energy conservation of the photoexcitation in the system, and

$$\mathcal{V} = \frac{e}{2mc}(\mathbf{A}\hat{\mathbf{p}} + \hat{\mathbf{p}}\mathbf{A}) + \frac{e^2}{2mc^2}\mathbf{A}\mathbf{A} = \frac{e}{mc}\mathbf{A}\hat{\mathbf{p}} \tag{55}$$

is an operator which describes the incident photon to the N-electron system coupling. $\mathbf{A}$ is the vector potential which describes the photon, which is operated on by the momentum operator $\hat{\mathbf{p}} = i\hbar\overrightarrow{\nabla}$. The Coulomb gauge, or fixing condition $\overrightarrow{\nabla}\mathbf{A} = 0$ can further be simplified by ignoring two photon transitions. The spatial modulation of the vector field $\mathbf{A}$ can also be ignored under the assumption that the wavelength of incident photons is much larger than the size of the excited molecular orbital, which means $\mathbf{A}$ is taken as a constant vector potential, $\mathbf{A_0}$, commonly known as a dipole approximation.

The initial state wavefunction ψ_i can also be written as a multiplication of the excited electron wavefunction Φ_k and the initial wavefunction of the remaining electron system $\psi^k_{i,R}(N-1)$ and the ejected photoelectron wavefunction $\Phi_{f,KE}$. This leads to a modification of Fermi's Golden rule

$$w \propto |\langle \Phi_{f,KE} | \mathbf{A}\hat{\mathbf{p}} | \Phi_k \rangle|^2 \left| \langle \psi^k_{f,R}(N-1) | \psi^k_{i,R}(N-1) \rangle \right|^2 \ldots \qquad (56)$$
$$\ldots \delta(E_{KE} + E_f(N-1) - E_i(N) - \hbar\omega)$$

where the photocurrent is dependent upon the product of the first term (which is one electron matrix element) and the overlapping integral for the initial and final states of the $(N-1)$ remaining electrons.

If the overlap integral equals unity, known as the 'frozen approximation', a more simple relationship between the binding energy E_b of the emitting orbital and the kinetic energy of the emitted photoelectron is possible. Furthermore, assuming that the initial and final states of the residual electrons $(N-1)$ are equal, such that $E_f(N-1) = E_i(N-1)$, then

$$E_{KE} = \hbar\omega(E_f(N-1) - E_i(N)) = \hbar\omega - E_b - \Phi \qquad (57)$$

This relationship is adapted for photoemission from single metal crystals, with work function Φ.

3.4 The x-ray standing wave method

3.4.1 NIXSW description

XSW analysis uses Bragg reflection, that is, the coherent scattering of incident x-rays from a crystal lattice, to establish a standing wave at the surface of a substrate to determine the position of surface atoms. The (NIXSW) technique restricts incident x-rays along the normal to the (*hkl*)

set of planes. A distinct advantage of the NIXSW technique is that it can be applied to almost all single crystal samples, as most metal crystals contain too many surface (and bulk) imperfections to be used at any other angle other than normal incidence. The accuracy of XSW as a structural technique can be as good as 20pm, and as mentioned, requires long range order across single crystal surfaces to successfully establish a coherent standing wave, but the adlayer does not. Each element on the surface of the substrate can be determined independently, and by using primary and/or secondary emission peak data such as x-ray photoelectrons and Auger electrons, chemical analysis can be extracted.

The XSW technique provides two structural parameters; the coherent position and the coherent fraction per element per (hkl) set of planes used. The coherent position and fraction are related to the distribution of positions with respect to the (hkl) scatterer planes. In order to triangulate adatom positions in three dimensions, at least two sets of planes; one parallel to the sample surface and one (or more) at an angle to it are required. Triangulation is the strength of XSW, but it is also a weakness; in reality there will only be a limited number of available (hkl) planes. This can lead to a limited number of coherent position and fraction pairs, and assuming the element of interest is in multiple adsorption sites, then there could be a shortfall of data to determine all of the atomic positions.

3.4.2 XSW theory

3.4.3 Bragg's law

Two coherent waves (of fixed wavelength and phase relationship) that overlap will form standing waves. Bragg's law states that

$$n\lambda = 2d_H sin\theta \tag{58}$$

where n is the order of diffraction (for a fixed phase relationship and thus for constructive interference, n must be of integer value), d_H is the layer spacing of x-ray scatterer planes, and θ is the angle btween the x-ray scatterer planes and the x-ray beam. In NIXSW, $\theta = 90°$ so that $d\text{sin}\theta/d\theta$ is at a minimum. From a kinematical perspective, Bragg x-ray diffraction can be realised by fixing λ and varying θ or vice-versa. Under NIXSW conditions, $\theta = 90°$ and therefore $\lambda = 2d_H$, so the phase, ϕ of the standing wave cannot be altered, implying no absorption by the crystal. This problem was noted by Darwin in 1914, and he postulated that as an incident x-ray passes each scattering plane, an amount is reflected back out, and the amplitude of the penetrating x-rays drops off [216]. This was known as Darwin's theory of extinction. Expanding on this idea, each scattering event acts to modify the phase relationship between incident and reflected waves, which defines a finite width of reflection that was not predicted by the Bragg equation. These effects combine to form a Darwin reflection curve.

Figure 32 shows an example of a Darwin reflectivity curve, where its asymmetry is characteristic of the phase modification due to each scattering event.

3.4.4 Darwin's reflectivity curve

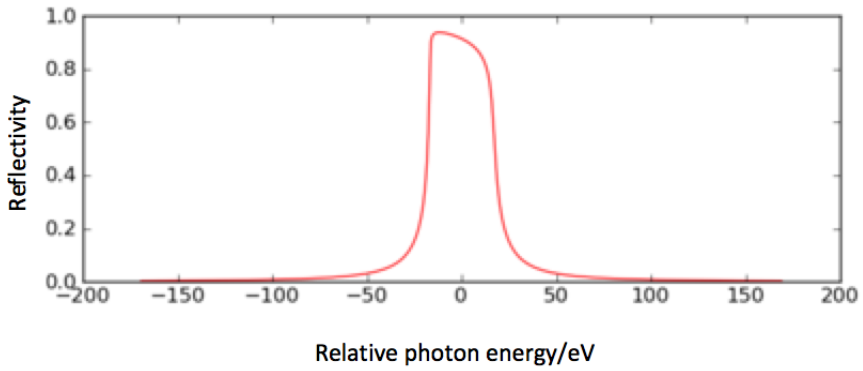

Figure 32: *A graphical representation of Darwin's reflectivity curve, showing an asymmetric peak.*

The reflectivity, R, in the Darwin curve is defined as

$$R = \left| \frac{E_0}{E_H} \right|^2 \tag{59}$$

where E_0 is the incident complex electric field amplitude, and E_H is the Bragg reflected complex electric field amplitude. It is the phase relationship (below) between E_0 and E_H that is paramount to the XSW technique

$$E_H = E_0 \sqrt{R} e^{i\phi} \tag{60}$$

where ϕ is the phase angle between E_H and E_0. Batterman [170] also noted that

$$I(\mathbf{r}) = \frac{|E_0 + E_H|^2}{|E_0|^2} = \left| 1 + \frac{E_H}{E_0} e^{-2\pi i \mathbf{H}.\mathbf{r}} \right|^2 \tag{61}$$

where $|\mathbf{H}| = 1/d_H$ is the reciprocal lattice vector relating to the Bragg reflection, or the difference between the incident and reflected x-ray prop-

agation vectors with $|\mathbf{K}_H| = |\mathbf{K}_0| + |\mathbf{H}|$.

Figure 33 shows a schematic of a standing x-ray wavefield. For an atom within the range of the interference field, high standing wave intensity will lead to photo-absorption, and the atom will radiate electrons or x-rays (fluorescence). Oppositely, an atom located in a low intensity region of the standing wavefield will radiate minimally. The wavefield position can be manipulated by changing the phase of one of the incident x-rays, for example, a relative shift of π radians will exchange the position of maxima and minima. Equation 61 is normalised by the division of $|E_0|^2$, assuming that the electric field vectors E_0 and E_H are parallel.

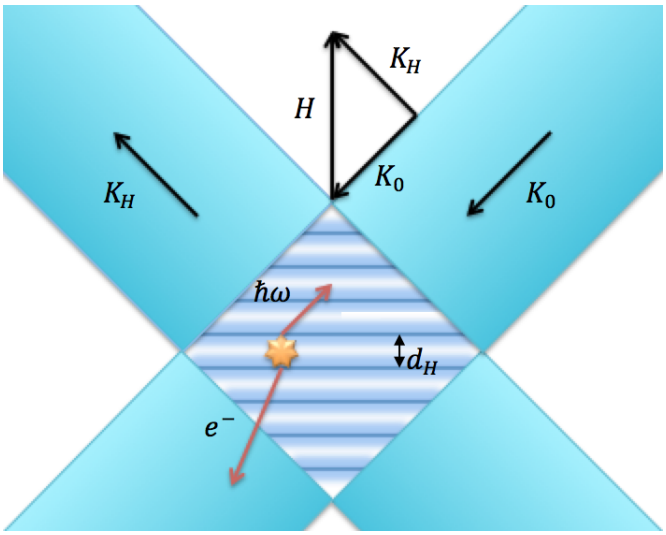

Figure 33: *Illustration showing the two coherent plane x-ray waves of energy E_0 and E_H, uniform along K_0 and K_H respectively. In the overlapping region, a standing wave is formed where the intensity is spatially modulated in the direction* **H** *with spacing d_H.*

By substitution

$$I(\mathbf{r}) = \left|1 + \sqrt{R}e^{(i\phi - 2\pi i\mathbf{H}.\mathbf{r})}\right|^2 \tag{62}$$

by expanding and incorporating Euler's interpretation of trigonometric functions represented by exponentials

$$I(\mathbf{r}) = 1 + R + 2\sqrt{R}cos(\phi - 2\pi\mathbf{H}.\mathbf{r}) \tag{63}$$

the scalar product $\mathbf{H}.\mathbf{r}$ describes the spatial modulation of the wavefield intensity, and can be represented by $\mathbf{H}.\mathbf{r} = z/d_H$, where z is the direction along $\mathbf{H}$ and the wavefield intensity is periodically modulated with spacing $d_H = H^{-1}$, and $H = |\mathbf{H}|$. The wavefield intensity is constant when normal to $\mathbf{H}$. The reflectivity, R, and the phase, ϕ, are both functions of the electric field vectors, E_0 and E_H. If either the incident angle or the energy (λ) is altered, then the phase will vary, which will disrupt the standing wave. The vertical adsorption position of the atom can be analysed using equation 63. The photon absorption yield Y (discussed later) can also be quantified by the use of secondary emission processes, namely fluorescence or Auger electrons.

During early XSW experiments, the angle was altered in order to triangulate atomic positions, but with recent developments in synchrotron radiation light, it is easier to vary the photon energy whilst fixing the crystal position. Suppose that the photon energy was such that the antinodal planes of the XSW lay directly on the scattering (hkl) planes. This means absorption would be at a maximum, and denoted by the high energy region of the Darwin reflectivity curve. If one was then to decrease the photon energy such that the nodal planes now lay on the scattering (hkl) plane, i.e. antinodal planes shifted away from crystal lattice by $d_H/2$, so the phase is shifted by π, then absorption would be at a minimum and is denoted by the

low energy side of the Darwin curve. This description holds for analysing a bulk crystal lattice site, for analysis of adsorbates on the crystal surface, the theory takes a steeper turn.

3.4.5 Detecting adsorbates

An adsorbate irradiated in x-rays will eject electrons, known as photoelectrons. The yield of photoelectrons emitted, Y, is directly proportional the the x-ray intensity, $I(\mathbf{r})$. A normalised distribution function, $f(\mathbf{r})$, can be used to describe the possibility of a site on the surface being occupied by an adsorbate. When integrated over the entire volume $\int_v f(\mathbf{r})d\mathbf{r} = 1$. By substituting the normalised distribution function into equation 63

$$Y = 1 + R + 2\sqrt{R}\int_v f(\mathbf{r})cos(\phi - 2\pi\mathbf{H}.\mathbf{r})d\mathbf{r} \tag{64}$$

and substituting in $\mathbf{H}.\mathbf{r} = z/d_H$

$$Y = 1 + R + 2\sqrt{R}\int_{d_H} f(z)cos(\phi - \frac{2\pi z}{d_H})dz \tag{65}$$

where z is the component of the adsorbate position at $\mathbf{r}$, which is parallel to $\mathbf{H}$. If one assumes that summation of the cosine function in question retains identical frequencies, but varying phases and amplitudes, then that in itself is a cosine function of particular amplitude and phase. In other words, a cosine function can be represented by a phase shifted sine function under integration, and vice versa. By using this

$$Y = 1 + R + 2\sqrt{R}F_{co}cos\left(\phi - 2\pi P_{co}\right) \tag{66}$$

where P_{co} is the coherent position, and F_{co} is the coherent fraction. These

are known as the structural parameters, and can both take a value between 0 and 1. P_{co} describes the averaged vertical position in fraction of the Bragg plane distance, where $P_{co} = D/d_H$, above the closest Bragg plane. The position D (formerly z) is now ambiguous and can only be determined relative to the periodicity of the XSW. F_{co} describes the fraction of objects which are found at the position P_{co}, commonly interpreted as a parameter to describe vertical ordering between 0 and 1.

Equation 66 can also be written in the form

$$Y = F_{co}(1 + R + 2\sqrt{R}cos(\phi - 2\pi P_{co})) + (1 - F_{co})(1 + R) \qquad (67)$$

where the first term represents the ideal case of a single absorber position, and the second term is the 'incoherent sum' of the incident and reflected waves. The 'incoherent' fraction $(1 - F_{co})$ takes the value of 0 if $F_{co} = 1$; suggesting that all adsorbed atoms/molecules are located exactly at the same height D corresponding to the coherent position P_{co}. On the other hand, if adsorbates are completely disordered (homogenous distribution) relative to the x-ray diffraction plane, then $F_{co} = 0$. This would mean the absorption profile will reduce to the reflectivity (or rocking) curve for the substrate, and a calculating a value for the coherent position, P_{co}, is not possible. Realistically, F_{co} is usually close to but not quite unity, which is down to the influence of statistical effects like vertical disorder and the vibrations of the substrate atoms, causing the standing wave to be slightly less than perfectly coherent.

Equations 65 and 66 can be equated

$$F_{co}cos(\phi - 2\pi P_{co}) = \int_0^{d_H} f(z)cos(\phi - 2\pi P_{co})dz \tag{68}$$

and by using the substitution $cos(\theta) = \frac{1}{2}(e^{i\theta} + e^{-i\theta})$

$$F_{co}e^{2\pi i P_{co}} = \int_0^{d_H} f(z)e^{2\pi i P_{co}}dz \tag{69}$$

which means the structural parameters P_{co} and F_{co} are proportional to the absorber site distribution, or alternatively, P_{co} and F_{co} represent the phase and amplitude respectively of a Fourier component of $f(z)$. This form can be especially convenient when dealing with multiple site adsorption, as Fourier analysis can be carried out. By rewriting equation 69

$$F_{co}e^{2\pi i P_{co}} = \sum_{k=1}^{N} n_k F_k^{co} e^{2\pi i P_k^{co}} \tag{70}$$

and the sum of relative contributions n_k of all adsorption sites has to be normalised to 1

$$\sum_{k=1}^{N} n_k = 1 \tag{71}$$

the structural parameters F_{co} and P_{co} can be plotted in a polar coordinate system (Argand diagram) as a vector $\mathbf{z}$, where P_{co} determines the length of vector $\mathbf{z}$, or the absolute value, and its polar angle is given by $2\pi P_{co}$.

Figure 34 assumes two distinguishable absorption sites A and B which have equal probability of occupation, such that $n_A = n_B = 0.5$. The vectors $\mathbf{z}_A$ and $\mathbf{z}_B$ have been scaled by 0.5 and summed to $\mathbf{z}_{A+B}$ with corresponding coherent positions and fractions P_{A+B}^{co} and F_{A+B}^{co}.

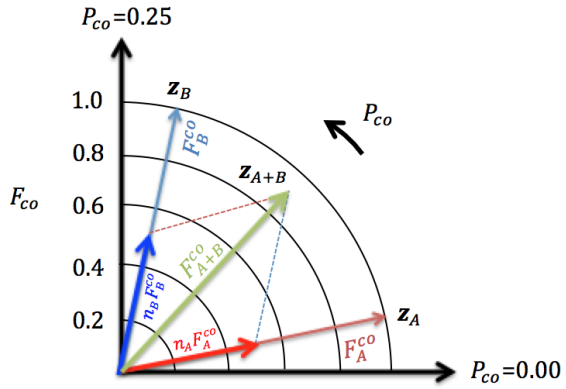

Figure 34: *An Argand illustration using hypothetical data for two different adsorption sites A and B, which have equal probability of occupation.*

4 STM/AFM Experimental setup

4.1 AFM Instrumentation and measurement protocols

As mentioned, imaging using an AFM arises from the force interaction between the tip and the sample. Most AFMs today are built by microfabricating cantilevers with integrated tips. Cantilevers are characterised by their spring constant k, eigenfrequency f_0 and quality factor Q, where $Q = \frac{f_0}{\delta f}$ and δf is the bandwidth of the resonance. A frequently used detection scheme is a laser beam reflected from the back side of a cantilever as shown below in Figure 35, and there are two commonly used types of imaging technique used in AFM, which are contact or non-contact AFM.

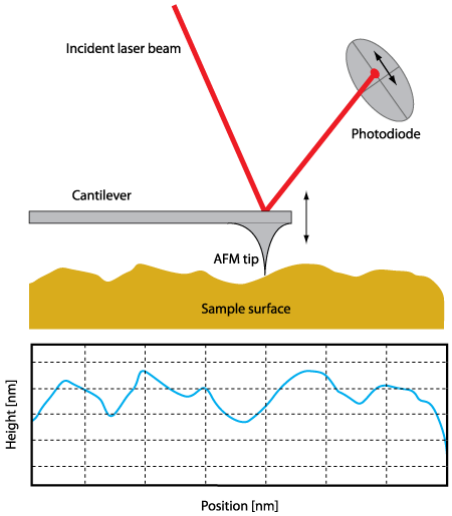

Figure 35: *Diagram showing the basic principle behind a generic AFM cantilever system. Incident laser is reflected onto a photodiode split into four quadrants. As the cantilever is deflected due to interatomic forces 'bending' cantilever, the displacement can be traced with the movement of the laser (or shift in photocurrent) and a 'height slice' can be mapped in 3D.*

4.1.1 Contact AFM

In contact AFM, the force between the tip and the sample is measured directly by the deflection of the cantilever:

$$F_{ts} = -k\Delta d \tag{72}$$

Where F_{ts} is the force between the tip and the sample, k is the cantilever stiffness and Δd is the deflection of the cantilever, so the more the cantilever bends, the stronger the force interaction. This equation can only be used when the deflection of the cantilever is greater than the deflections of the tip and the sample.

When contact mode was first introduced, no atomic defects were seen due to the large contact area, and coincidentally, the similar atomic periodicity with the sample. When contact mode is used, the cantilever deflection is kept constant (at a user defined setpoint) by a feedback loop and $z(x, y, F = const.)$ are recorded.

4.1.2 Non-contact AFM

It wasn't until 1995 when the first 'true' non-contact atomic resolution AFM image of Si(111)-(7 x 7) surface was taken [217]. 'True' atomic resolution was realised when defects became apparent on the Si(111)-(7 x 7) surface. In NC-AFM, the cantilever undergoes a mechanically induced oscillation, at a resonant frequency f_0. This means the tip can be operated stably at small tip-sample distances. The NC-AFM technique typically operates in the attractive region of the Lennard-Jones potential. It

is commonly subject to low frequency noise $\left(\frac{1}{f}\right)$ but this can be filtered relatively easily by using a bandpass filter centred around f_0. Within NC-AFM, there are two means of modulating the tip, which are amplitude modulation (AM) and frequency modulation (FM).

4.1.3 Amplitude modulation

In amplitude modulated AFM (AM-AFM), the cantilever is driven at a fixed frequency. Once the tip is close to the sample the amplitude of the oscillation changes due to tip-sample interactions, so the amplitude of the cantilever is used as a means of feedback signal for imaging the surface of a sample. To resolve atomic corrugations, a high Q factor is desirable, however in AM-AFM, a high Q (especially when in ultra high vacuum $Q \sim 10^4 - 10^5$) dramatically increases the integration time that is required for the change in amplitude to decay $\left(\tau \sim \frac{2Q}{f_0}\right)$. Ultimately, this means AM-AFM is slow.

4.1.4 Frequency modulation

In frequency modulated AFM (FM-AFM) Q decays on a timescale of $\tau \sim \frac{1}{f_0}$ which is much faster than AM-AFM. The feedback loop in FM-AFM ensures a constant amplitude as opposed to a constant frequency in AM-AFM. The deflection signal (which is a shift in the resonant frequency, represented by Δf) is routed through a bandpass filter, phase shifted and fed back to the cantilever. A phase-locked-loop (PLL) determines the oscillation frequency $f = f_0 + \Delta f$. For the purpose of this report, AM-AFM will be omitted because all results presented on atomic scale imaging in AFM are with the FM-AFM technique.

4.1.5 FM-AFM setup

Figure 36 shows the PLL controlled FM-AFM setup. If the z feedback loop is open then constant height imaging will take place. If the z feedback loop is closed, then it will image in constant frequency mode (or Δf mode).

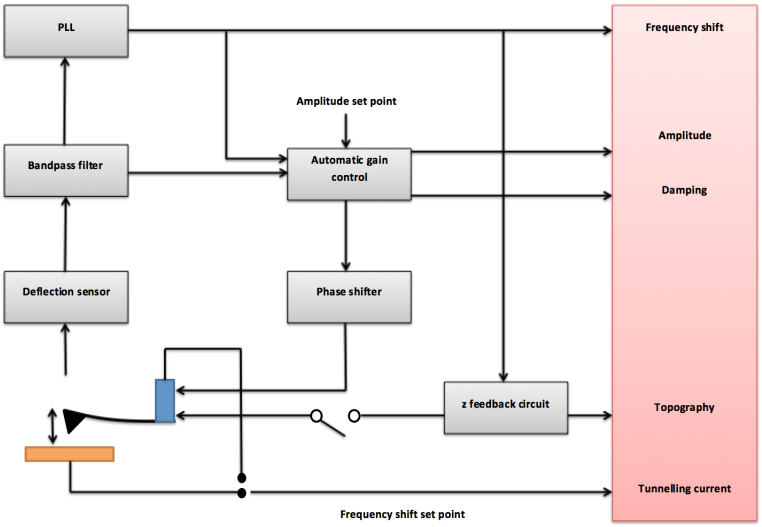

Figure 36: *Schematic showing the PLL controlled FM-AFM setup.*

4.1.6 PLL

The FM-AFM setup uses a closed loop frequency control system. A PLL detects the phase difference between the input and output signals of a controlled oscillator.

Figure 37 shows how the PLL works in FM-AFM. The force interactions between the tip and the sample change the amplitude and frequency of the cantilever over the oscillation cycle. Attractive tip-sample interactions cause a reduction in f_0 (negative frequency shift). Repulsive tip-sample interactions increase f_0 (positive frequency shift). The changes are then

measured a used as feedback signals to control the system. The phase detector (PD) detects the input signal V_i, which is then low pass filtered and output as an FM signal. V_c carries the FM output to the voltage control oscillator (VCO) which adjusts the frequency according to V_c. V_0 (output of V_c) is then output to the PD at 0° phase shift and the amplitude modulator (AM) output at a $\frac{\pi}{2}$ phase shift.

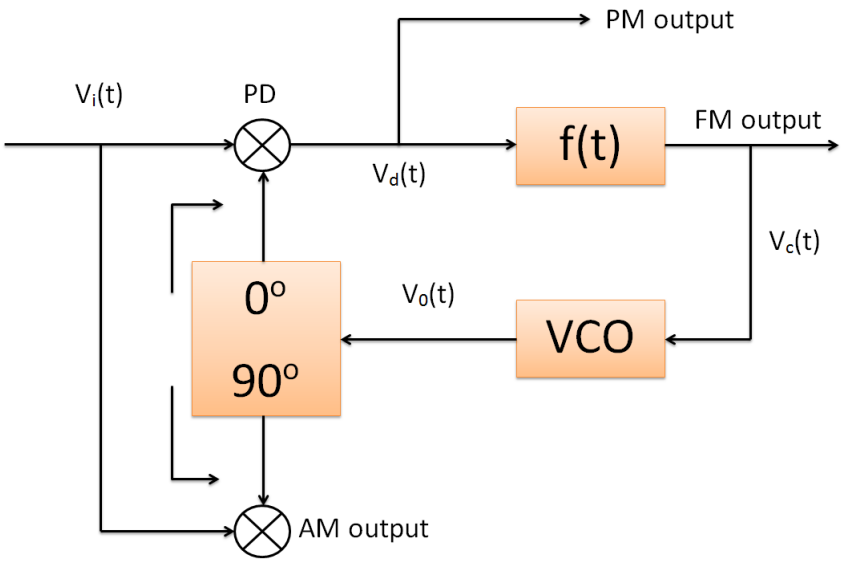

Figure 37: *Schematic showing the PLL control within the FM-AFM setup. V_i is the incoming signal, PD is the phase detector, $f(t)$ is the low pass filter, VCO is the voltage control oscillator, V_c is the frequency that the VCO adjusts to, V_d is the phase detector output and V_0 is the outgoing signal.*

4.2 Equipment

A Createc low temperature STM/AFM, commercially available from Createc Fischer & Co GmbH was used (design by Gerhard Meyer).

The system 'floats' on four pneumatic legs for thorough vibration isola-

tion from low frequency mechanical vibrations. The UHV chamber is split into two chambers; preparation and qPlus, which are separated via a gate valve to ensure that the measurement side remains uncontaminated from sample preparations. The qPlus chamber also houses the $l\mathrm{N}_2/l\mathrm{He}$ cryostat. The base pressure of the prep chamber is $\sim$ 2x10^{-10}mbar and the qPlus is slightly lower. There is a mass spectrometer accessible in the prep chamber and low energy electron diffraction optics for rapid surface characterisation.

For sample preparation, an ion gun attachment is used with a Ne gas source to enable accelerated ion sputtering. To deposit molecules a home-made crucible was used, where different materials can be evaporated from by resistive heating. A single crystal Cu(111) and a Au(111) on mica sample was mounted on resistive heaters on their respective sample holders and annealing temperatures are usually measured using a pyrometer.

4.3 Au(111) sample preparation

The Au(111) sample used is a thin layer of Au(111) on mica. The sample once in the prep chamber, is sputtered with Ne whilst maintaining a $P_{prep} \sim$ 6x10^{-6}mbar. Whilst sputtering, the ion pump valve is closed and the load lock valve is opened with the turbo molecular pump on. Sputtering cycles usually take between 15-30 mins. Once sputtered, the Au(111) sample is annealed by resistive heating on the sample holder at 2A/3.5V at a temperature of 600K for 30 mins (measured by a pyrometer). If the lights are switched off in the laboratory, a very faint red glow over the sample can be seen. The Au(111) sample is then cryogenically cooled using the manipulator arm with $l\mathrm{N}_2$ so it cools down faster in the scan head.

4.4 Cu(111) sample preparation

The Cu(111) sample used is a single crystal. It is sputtered also with Ne at $P_{prep} \sim 6\text{x}10^{-6}$mbar. The Cu(111) sample is usually sputtered for 30 mins and then annealed at 2A/3.5V at a temperature of 650K for up to 60 mins, again a dull red glow once the laboratory lights are switched off can be seen. The sample is then cooled cryogenically using $l\text{N}_2$ with the manipulator arm, in a similar fashion to the Au(111) sample.

The manipulator arm is attached to the side of the prep chamber and has movement in x, y and z directions to high accuracy, and can also be rotated along its longitudinal axis. The manipulator arm can also be cryogenically pumped with $l\text{N}_2$ to enable cool sample preparation. The sample storage in the prep chamber can house up to six sample holders or tip transfer tools, or a combination of both.

The STM/AFM stage is based on the Besocke beetle design [218]. The tuning fork sensor (and STM tip) is attached to a Cu disc resting on three sapphire balls glued to PZT piezo tubes. The Besocke bettle design is similar to slip stick motion, which can be rotated by applying sawtooth shaped voltage pulses to the piezos. The Cu disc has three slopes in its bottom side, so it can also be used to control vertical (z) motion, including coarse movement. The whole STM/AFM stage is suspended by three springs combined with an Eddy current damping system to reduce lateral movements. The inner radiation shield is connected to the inner cryostat (which houses $l\text{N}_2$ or lHe) whilst the outer radiation shield is thermally connected to the outer cryostat (which can only house $l\text{N}_2$).

The qPlus sensor uses a quartz tuning fork with $f_0 \sim 20$kHz and theoretical spring constant $k \sim 1800\text{Nm}^{-1}$. One prong of the tuning fork is thermally glued to an insulating ceramic cylinder with a $\sim 1400\mu$m W wire directly attached to the apex of the free prong to serve as the AFM/STM tip.

To avoid cross talk between AFM/STM signals, a 10μm Au wire is connected to the W tip to measure tunnelling current independently, whilst the tuning fork electronics are used for deflection detection. As mentioned, the tuning fork is mounted onto a ceramic cylinder which can be transferred in vacuum with the manipulator arm to and from the qPlus chamber (as long as the sample is removed from the STM/AFM head first).

STM/AFM operation is controlled by a Createc high voltage amplifier, this is used to control the piezos in the scan head. The high voltage controller is connected to a Nanonis Createc interface controller, for signal conditioning, oscillation control and real time control.

The internal op-amps are fixed close to the microscope stage in UHV on the outer radiation shield (which is at 77K). Deflection of the tuning fork is further enhanced by an external amplifier. The bias voltage when using STM mode is always applied to the sample, with the tip at a virtual ground. The PLL is Nanonis software based. The tip has to be scanned very slowly (by using a higher integration time) in AFM to keep noise levels to a minimum. Our typical qPlus operation is ~ 20pA (but is capable

of operation at 5pA) in STM and an amplitude of $a_0 \sim 300$pm in AFM. A lower operational amplitude would cause the PLL to struggle with the noise-signal separation, whilst a higher amplitude would cause the tip to 'fall outside' of the non-contact regime.

4.5 Br_4TPP on Au/Cu(111) sample preparation

The Au(111) and Cu(111) samples were prepared as described in the sample preparation section. The Br_4TPP molecules were deposited using a home-made resistively heated crucible using a modified sample holder. This allows easy removal of the crucible from the system without venting. The crucible was resistively heated to approximately 240±50°C (1.3A/2.4V) for 60 mins to outgas. The Au(111) and Cu(111) samples were cryogenically cooled to 77K with the manipulator arm then quickly placed over a circular aperture approximately 3cm above the crucible for 10-15s. A lower rate of deposition ensured local networks were not formed (combined with a cool sample to reduce thermal diffusion).

Once the Br_4TPP molecules had been deposited, the sample was transferred to the STM/AFM head for scanning. Typical STM parameters were 30pA/2V for initial approach (to reduce the probability of the tip damaging the scan area), and then altered to 50pA/1V for scanning post approach. AFM parameters were typically a_0=300-400pm and a small (variable) bias voltage was required to be input as a software bias offset for true 0V bias voltage (this procedure was carried out during NC-AFM, when the tip was close to the molecule/surface, a small tunnelling current would be apparent of the order of pA, this was minimised manually by adjusting the bias

voltage usually in mV from scan to scan ($Q \sim 8000/30000$ and $f_0 \sim 20$kHz at T=77/5K).

4.6 $H_2O@C_{60}/C_{60}$ on Cu(111) sample preparation

The $H_2O@C_{60}/C_{60}$ molecules were deposited using a home-made resistively heated crucible, modified from a sample holder. The crucible was cleaned by ultra-sonication in toluene, acetone, methanol and isopropanol for 10 minutes respectively to ensure it was UHV clean and clear of the previous C_{60} molecules used for experimentation. The $H_2O@C_{60}/C_{60}$ molecules were then placed in the crucible, and it was returned to the prep chamber and resistively heated (1.3A/1.4V) for approximately six hours until base pressure was achieved. The molecules were then allowed to cool whilst the Cu(111) substrate was prepared as described previously. The molecules were then resistively heated at 1.2A/1.3V for 45 minutes then deposited for a range of deposition times (1-25 minutes) whilst the Cu(111) sample was held at a range of temperatures between 77K and 300K for the duration of deposition. In some instances the sample was warmed from 77K to 200K and 260K respectively then returned to 77K rapidly before the sample was placed in the scan head. Specific experimental procedures will be mentioned respective to their results ahead.

4.7 UHV and low temperature operation

The Createc's outer cryostat has a maximum capacity of $15l$ and the inner cryostat can hold $4l$ of liquid cryogenic fluid. If both cryostats hold $l N_2$ the system can maintain 77K for 6 days. If the system is required to be at 5K for experiments, then the inner cryostat (filled with lHe) needs to be

topped up every 72 hours and the outer cryostat (which holds $l\mathrm{N}_2$) needs to be topped up every 48 hours.

A turbo molecular pump is attached to the load lock on the prep chamber side of the system, and is typically only used during bakeout (reaching pressures between $\sim$ 10^{-7}-10^{-9}mbar) or if a sample or tip needs to be completely removed from the system. After a bakeout, the turbo pump is switched off to reduce mechanical vibrations and the titanium sublimation pumps (TSPs) are used in conjunction with ion pumps to maintain pressure $\sim$ 10^{-10}-10^{-11}mbar. The TSPs are ramped to $\sim$ 40A and reduce the pressure in the system by coating the inner walls of the prep and qPlus chambers (3 TSP elements in each chamber) with Ti.

Once the system has cooled to room temperature ($\sim$ 300K), which takes a few days after bakeout is complete, the cryostats can be filled. The $l\mathrm{N}_2$ boil off usually occurs at a much faster rate than the usual 6 days of capacity, so a more frequent top up is required initially after bakeout.

In terms of measurements on the Createc AFM/STM, $l\mathrm{N}_2$ is usually used when acquiring STM data and constant Δf AFM data. In order to acquire constant height AFM data, lHe is desired to minimise thermal drift between the tip and the sample. When transitioning between room temperature, $l\mathrm{N}_2$ and lHe the piezo calibrations need to be altered to compensate for the reduction of piezo movement as the temperature of the system drops.

4.8 Tip preparation

The tip attached to the qPlus sensor is a W wire of 50μm diameter and final etch length of around 1400μm. The tip has to be at this length because the z-range of the piezos on the Createc STM/AFM are relatively short in comparison to other commercial systems. A sharp tip apex is constructed through an electrochemical etching process.

The tip is submerged into a 2M concentration of NaOH in a relatively shallow petri dish. A 10mA current is then passed through the W wire where it acts as a cathode, and a steel shaped ring also submerged near the edge of the dish acts as an anode.

The reactions at the anode are

$$W(s) + 6OH^- \rightarrow WO_3(s) + 6e^- + 3H_2O \tag{73}$$

$$WO_3(s) + 2OH^- \rightarrow WO_4^{2-}(aq) + H_2O \tag{74}$$

and the cathode

$$6H_2O + 6e^- \rightarrow 3H_2(g) + 6OH^- \tag{75}$$

and overall

$$W(s) + 2OH^- + 2H_2O \rightarrow 3H_2(g) + WO_4^{2-}(aq) \tag{76}$$

Where (s), (aq) and (g) mean solid, aqueous and gas counterparts respectively [219]. Once the tip has been etched, confirmed by a sudden drop in current (and can be seen visually by a section of W wire sinking from the NaOH/air interface with a sharp eye) the whole qPlus sensor is soaked in IPA to clean the NaOH solution from the device. The tip is then placed into the load lock where it is ready to be placed back into the system. A focussed ion beam (FIB) to 'sharpen' or condition the tip before placement in the head is not used on the system. There have been frequent instances where the tip can acquire instant atomic resolution upon first approach, but if tip prep is required, then it will be bias pulsed away from an area of interest at 4-7V or prepared by a tip crash, where the tip penetrates the surface by 500pm-10nm (depending on how severe the tip condition is) with a -5V lifting bias when it is being retracted from inside the surface.

5 XPS/XSW Experimental setup

5.1 Equipment

The spectroscopy experiments were performed at beamline I09 of Diamond Light Source (DLS) in Didcot, Oxfordshire. I09 is designed for high energy resolution studies of surface and interfaces. A $1cm^2$ single crystal Ag(111) substrate acquired from MaTeck[1] was used for the experiments. Prior to insertion into the ultra high vacuum (UHV) chamber, the Ag(111) crystal was attached to a modified Omicron sample plate.

[1]MaTecK GmbH, Im Langenbroich 20, Juelich, 52428, Germany

5.2 Ag(111) sample preparation

The Ag(111) sample was cleaned in UHV using repeated argon ion sputter (500eV, drain current 6mA, for 30 minutes at a base pressure 5x10^{-5}mbar) and anneal cycles (resistively heated at a temperature of 600°C for 30 minutes, with a slow cool down of approximately 50°C/10s).

A low energy electron diffraction (1 x 1) pattern was observed for the clean Ag(111) sample, with a low diffuse background and sharp, bright diffraction spots. X-ray photoelectron spectroscopy scans were performed at 700eV on the clean Ag(111) surface, which showed no evidence of contamination. The position of the Bragg peak and broadening due to instrumentation was calculated after taking a reflectivity curve (also known as a rocking curve) using normal incidence x-ray standing wave spectroscopy measurements of the Ag(111) substrate.

5.3 Molecule deposition

100mg of $H_2O@C_{60}$ molecules in the form of powder was transferred to a ceramic crucible and placed in a Knudsen cell (K-cell), which was thoroughly degassed at 100°C under UHV, and raised to 300°C over a period of 2 hours, followed by further degassing at 110°C overnight. The K-cell aperture was approximately 20mm in diameter and 250mm away from the Ag(111) surface, with a gate valve in between. Multilayer $H_2O@C_{60}$ was deposited onto the clean Ag(111) substrate at room temperature, using the K-cell at 410°C for approximately 1 hour, and a base pressure of 8x10^{-10}mbar. A monolayer coverage of $H_2O@C_{60}$ on Ag(111) was acquired by annealing the multilayer deposition on Ag(111) at approximately 350°C for 2.5 hours.

5.4 Detection methods

Low energy electron diffraction was used to complement XPS and NIXSW experiments (it is imperative for the crystal to have a highly ordered 3D lattice for NIXSW experiments). It offers a rapid method to determine the long range surface structure of both Ag(111), and once deposited, the $H_2O@C_{60}$ molecules, without the presence of a scanning probe. As the name suggests, a collimated beam (approximately 0.1mm wide) of low energy electrons from a hot filament are accelerated towards the grounded sample, once diffracted by the surface Ag(111) atoms, electrons can constructively interfere under the condition that the path difference, d, between diffracted electrons is commensurate with an integral number of the electron wavelengths, $n\lambda$. The constructive interference pattern appears as bright spots on a fluorescent screen, which is a to scale version of the reciprocal lattice of the unit cell. The hemispherical nature of the fluorescent screen means the reciprocal lattice can be observed without distortion. It is important to note that the inverse lattice and real inter-planar distance are inversely proportional.

Photoemission spectra were recorded using a hemispherical VG Scienta EW4000 HAXPES electron analyser, positioned perpendicular to the incoming x-rays (This removes issues associated with asymmetry in photoemission based XSW, usually addressed via the use of the so-called Q factor [220, 221]). All experiments were carried out under ultra high vacuum (UHV) conditions at a base pressure of $4\text{x}10^{-10}$mbar and a Ag(111) sample temperature of either 300K or 90K. To minimise H_2O contamination on the Ag(111) surface, after the sample was cooled to 90K (low enough to con-

dense H_2O on Ag(111) in UHV) using lN_2 , the sample temperature was then increased to 200K to desorb any water-surface contamination from the $H_2O@C_{60}$ source, before being cooled back down to 90K again. This assumes the background from H_2O is low enough so that H_2O does not adsorb from the vacuum.

5.5 XPS Details

Experiments were carried out at beam line I09 at Diamond Light Source (DLS), in Didcot, Oxfordshire. DLS houses a 0.5km circumference synchrotron, which is capable of producing beams of electrons at 3GeV. Electrons are injected from an electron gun into a booster synchrotron. Once the electrons are accelerated close to c, they are then injected into the storage ring, which contains 48 straight sections mated with 48 bending magnets.

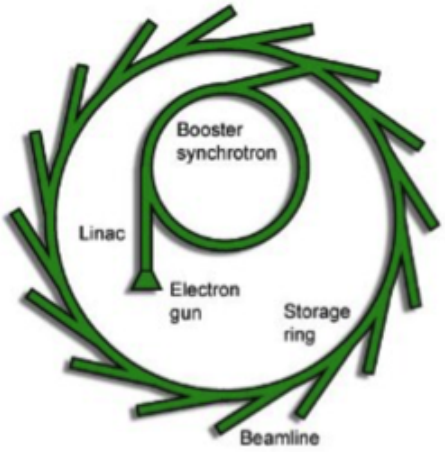

Figure 38: *Schematic of the DLS synchrotron [222].*

The magnets are used to 'steer' bunched electrons around the storage ring. Once the magnets bend the electron beam, it loses energy across a broad

spectrum of high energy radiation, including high-energy photons (x-rays), which are channelled down beam lines tangential to the storage ring. Inside the beam line is the optics hutch, where the light is filtered and focussed, the experimental hutch, where the sample is located and experiments carried out, and finally the control cabin where the experiments are conducted.

The energy of the soft x-rays (photons) is selected through a plane grating monochromator where they reach the optics hutch; monochromatic light is then directed at the Ag(111) sample at an angle of incidence (usually depicted by the orientation of the crystal planes). For the work described in this thesis, the energy of the soft x-rays used was generally 700eV for XPS (unless stated otherwise). X-rays excite electrons on the Ag(111) surface, and as a result, electrons are ejected towards a VG Scienta EW4000 HAXPES hemispherical analyser (perpendicular to the incoming x-rays). The kinetic energy of an ejected electron from the sample surface is

$$E_{KE,e^-} = \hbar\omega - E_b - \Phi \tag{77}$$

where $\hbar\omega$ is the energy of the x-ray, E_b is the binding energy of the electron orbital from which the photoelectron orignates, and Φ is the work function (of the analyser). If the kinetic energy of the electrons can be measured, then the binding energy can be calculated, and the element of the parent atom from which the electron was ejected can be determined. By placing a negative charge on the outer plate of the hemisphere of the analyser, and a positive charge on the inner plate, the electrons are forced into a small orbit at an approximate radius of 200mm. The potential difference between the outer and inner hemispherical plates acts as an electron 'gate', such that

if the electron energy is too low, it will crash into the inner plate, and if too high it will crash into the outer plate. For constant resolution, the bias between the hemispheres is kept constant. The electrons are retarded by the electron optics in front of the entrance slit of the hemispheres, and the retardation voltage is ramped in order to obtain an electron energy spectrum.

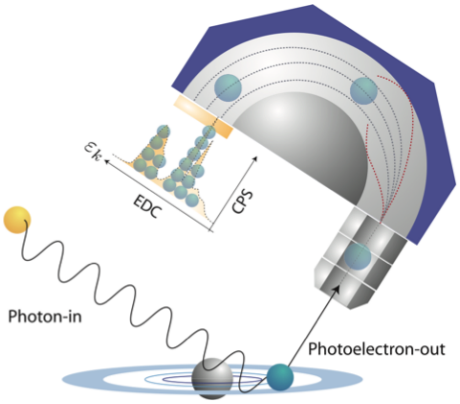

Figure 39: *Schematic representing an incoming x-ray exciting an electron, and ejecting a photoelectron from a substrate. Its trajectory through the hemispherical analyser to the electron detector is shown. Taken from [223].*

XPS analysis can provide chemical bonding information as well. Depending on the binding characteristics of the parent atom to another element, the binding energy of the emitted photoelectrons may be shifted. The exact binding energy of an electron depends on the oxidation state of the atom, the local chemical and physical environment along with the level from which photoemission occurs. These changes can give rise to small shifts in the peak position of the spectrum, known as chemical shifts. Such shifts are easier to interpret in XPS in comparison to Auger electron emission, because the core levels are discrete with a well-defined energy, but more importantly, photoemission is a one electron process. Atoms which have a higher positive oxidation state retain a greater binding energy due

to the extra Coulombic interaction between the photoelectron and the ion core, as shown in Figure 40. One of the major strengths of the XPS technique is this ability to differentiate between different oxidation states and chemical environments.

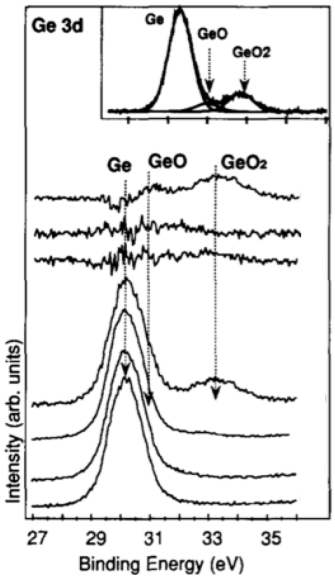

Figure 40: *Experimental results illustrating intensity versus binding energy (eV) for Ge, GeO and GeO_2 and showing corresponding chemical shifts to higher binding energy respectively, from [224].*

The analyser can perform a high-resolution scan to reveal more accurate characteristics, the only down side to this is the energy window needs to be constrained. In general, XPS results are plotted as an intensity (counts per second) versus binding energy graph, referenced to a Fermi edge at the same potential as the sample or core level peaks that arise in the spectrum with exactly known values. The Ag(111) sample was prepared as described in the experimental method in this report. LEED was then performed on the clean sample prior to a broad XPS survey between -5.5eV and 600eV using soft x-rays (at a photon energy of 700eV). $H_2O@C_{60}$ was then deposited as a thick film, and further XPS surveys were taken. Monolayer $H_2O@C_{60}$ was

achieved by annealing the sample as described in the experimental method section, whilst XPS was carried out simultaneously.

5.5.1 Clean Ag(111)

Figure 41 shows an XPS survey between 0eV and 600eV using a photon energy of 700eV, on a clean Ag(111) substrate. Ag valence band structure was observed around 10eV, a pair of Ag Auger peaks at 350eV, Ag $3d_{5/2}$ and Ag $3d_{3/2}$ at 367eV and 373eV respectively and finally the Ag $3p_{3/2}$ at 580eV. More importantly there are no peaks observed for the $C1s_{1/2}$ and $O1s_{1/2}$ states at 284eV and 532eV respectively, indicating negligible Ag(111) surface contamination. The Ag $3d_{5/2}$ peak is around one-and-a-half times greater in intensity than the Ag $3d_{3/2}$ peak.

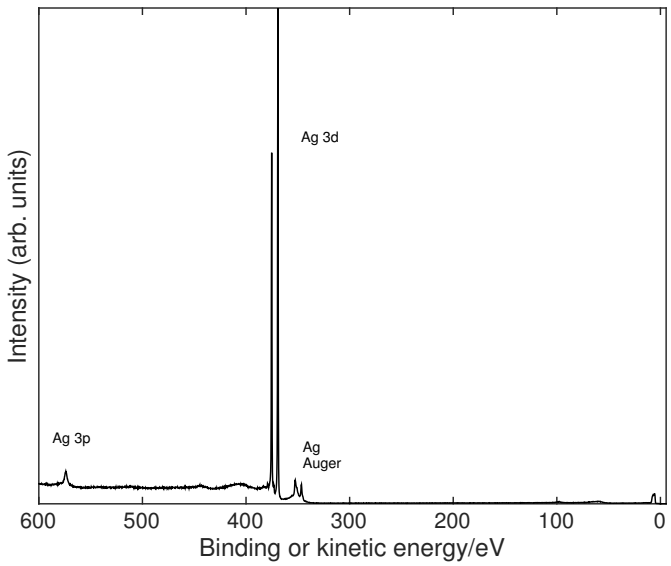

Figure 41: *XPS survey of clean Ag(111) showing intensity (counts per second) versus binding energy (0-600eV). Various peaks are observed across the spectrum.*

5.6 NIXSW Details

Experiments were carried out on beam line I09, and the Ag(111) sample was prepared and analysed (using LEED and XPS), as described in the XPS experimental section, before XSW analysis commenced. The hard x-rays used in XSW are filtered through a Si(111) double-crystal monochromator where they reach the optics hutch, and in this report, the energy of the hard x-rays used was 2636eV for XSW (unless stated otherwise, to match the Ag(111) Bragg energy). Due to the nature of hard x-rays, the hutch needs to be evacuated to perform experiments. Once this has been completed, a gate in the system is allowed to be opened, this allows the high-energy monochromatic light to be directed at the Ag(111) sample. The sample was cooled using $l\mathrm{N}_2$ to approximately 90K.

For completeness, a reflectivity curve was taken whenever the sample was moved with the manipulator arm, which allowed the Bragg energy to be clearly defined prior to every XSW experiment. This was taken as half of the difference between the energy axes intercepts of the full width half maximum (FWHM) of the reflectivity curve to determine an accurate value; this is due to its asymmetry arising from Darwin's extinction theory. The broadening of the reflectivity curve at the FWHM gives a measure to the quality of the crystal structure beneath the surface of the sample. A large broadening, e.g. greater than 2eV, would indicate a poor crystal construction beneath the surface, and examples of this will be shown. A good crystal would be one with a broadening of 1eV or less, which was achieved, shown in Fig. 92b and Fig. 42. The penetration depth of hard x-rays (microns to millimetres) is much greater in comparison to soft x-rays. In a similar fash-

ion, XSW excites electrons beneath the Ag(111) surface, and electrons are ejected towards a VG Scienta EW4000 HAXPES hemispherical analyser, perpendicular to the incoming x-rays, as described in the XPS experimental details section. If the exact pattern and position of the XSW is known, and one has the ability to manipulate it, information about the real space distribution of inelastically scattered objects can be obtained [168].

Decay channels such as Auger electron emission, x-ray fluorescence and photoelectrons are important in NIXSW experiments, and can be used as signature signals when the XSW is shifted in real space. It is important to note that these signals are surface sensitive channels, and are a key tool in the analysis of a monolayer of adsorbed molecules. A strong signal would be indicative of the XSW maxima coinciding with atomic positions, and oppositely, a weak signal would suggest minima of the XSW are in line with the atomic positions. Since the standing wave field spacing is proportional to the atomic plane separation, atomic positions can be analysed. The Ag(111) crystal was then rotated along azimuthal, polar, and linear directions to set up experiments in different crystal orientations (in this thesis the (111), ($\bar{1}$11) and (200) directions are used). The combination of different Ag lattice orientations allows the triangulation of atomic positions, and since the standing wave field extends above the Ag surface, the position of the incarcerated O1s state within the $H_2O@C_{60}$ cage can also be triangulated relative to the Ag(111) surface.

XSW experiments were carried out at 80K to reduce beam damage, typically, a set of XSW experiments would be taken over 15-20 minutes, then

the sample would be moved so beam exposure would occur at a different point on the sample. The procedure for correctly aligning the beam reflection was firstly to adjust the CCD (used to see the reflection of the standing wave from the crystal) to a fairly high exposure. The photon energy was then set to approximately the Bragg energy (determined by both the lattice orientation and the energy the reflectivity curve maxima), and then rotated gently through the polar angle (i.e. if the (111) plane was used for experimentation, x-rays would have been incident along the surface normal, when using the $(\bar{1}11)$ orientation, the polar angle would have been approximately 70.5° from the (111) direction). Once a spot had appeared, it was positioned using azimuthal and linear axes such that the spot was in between the beam entrance and exit cavities in the system, making sure that the polar angle was not adjusted. The intensity monitor could then be checked to make sure a band of (blue/white/yellow) counts was visible.

5.6.1 Reflectivity curve for clean Ag(111)

Figure 42 shows the reflectivity curve for the (111) lattice orientation for ML $H_2O@C_{60}$ on Ag(111).The experimental value of E_{Bragg} is very close to its theoretical value of 2625eV. The broadening value for the (111) plane is approximately 1eV, suggesting a high quality crystal lattice structure beneath the surface. The asymmetry of the reflectivity curve (a physical effect of a reduction in scattering events as the standing wave propagates deeper into the single crystal, as defined by Darwin's extinction theory) is pronounced. See appendix for similar reflectivity curves for the $(\bar{1}11)$ and (200) planes.

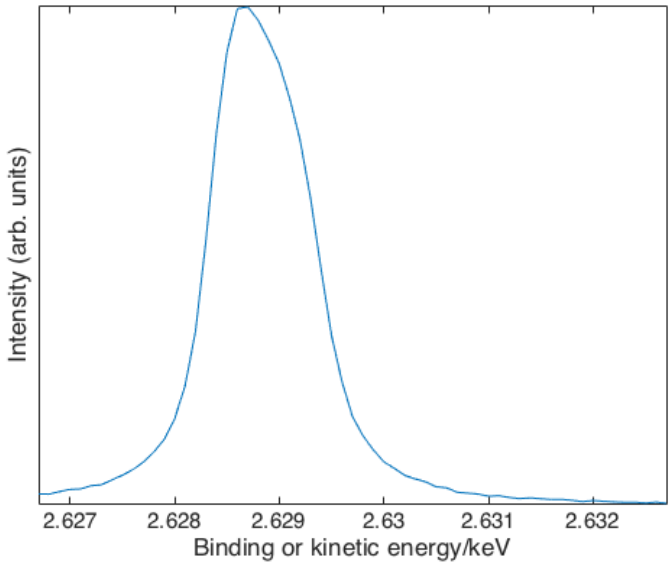

Figure 42: *Reflectivity curve for the (111) Ag lattice orientation. Bragg energy 2628.8eV.*

5.6.2 Ag Auger curves for clean Ag(111)

Figure 43 shows the x-ray standing wave data for the Ag Auger measurements. The results show a coherent position of 1.00 for the (111) orientation, i.e. the bulk spacing for an Ag lattice, and a very high coherent fraction of 0.994, which is what would be expected for a high quality crystal. The broadening is 0.19eV, so that was used for all (111) data herein. For the $(\bar{1}11)$ lattice, both coherent position and coherent fraction are also high at 0.963 and 1.00 respectively, with a broadening of 0.3eV. This should be the same broadening as the (111) planes, but an increase could be due to a mosaic spread of angles in the crystal lattice. A broadening of 0.3eV will be used for subsequent $(\bar{1}11)$ data. The (200) orientation has also a high coherent position of 1.00, but a lower coherent fraction of 0.827 is indicative of the XSW picking up disorder parallel to the surface in this lattice direction, as shown in Table 2. A broadening of 0.24eV will be used

for (200) data.

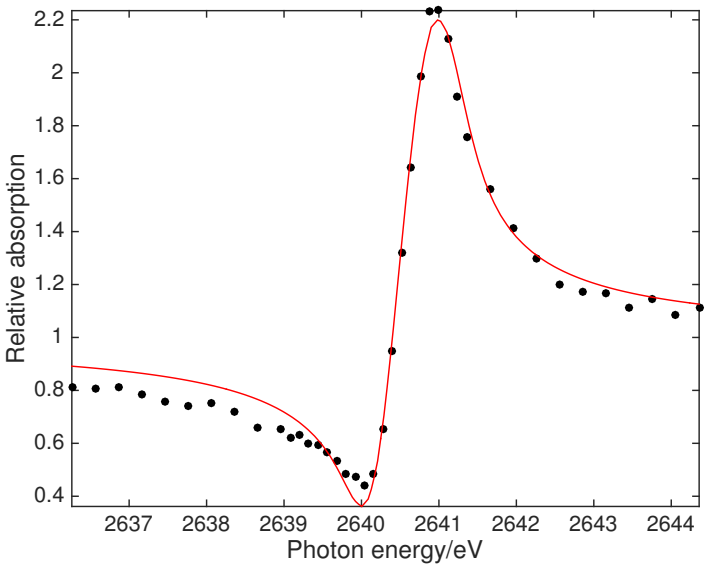

Figure 43: *Ag Auger XSW data for the (111) Ag lattice orientation. Bragg energy 2640eV.*

	(111)
SB	0.189
$\mathbf{P}_c$	1.00
$\mathbf{F}_c$	0.994
$\mathbf{E}_{Bragg}$	2640.00

Table 2: *Broadening (SB in eV), coherent position (P_c), coherent fraction (F_c), Q and Bragg energy (E_{Bragg} in eV) values for the Ag Auger data in Fig. 43.*

6 The role of vdW forces in the adsorption and manipulation of porphyrins

6.1 Tip interactions

It is impossible to determine the *exact* termination of a scanning probe. It is however, possible to make a broad guess at what the tip termination may be by performing force spectroscopy. In this section, a W tip is crashed (in a controlled manner) into Au and Cu surfaces (which could provide Au- and Cu-terminated tips respectively), and also over Br_4TPP molecules (which could produce a molecule-terminated tip) in an attempt to induce different tip terminations. It is important to note that the tip can become spontaneously terminated with a molecule just by scanning in STM mode. Au and Cu tip interactions with Br_4TPP, and Br_4TPP-Br_4TPP interactions were examined to determine how tip termination affects the interaction strength with the surface bound molecule. As detailed later in this thesis, a controlled method to try and terminate the tip (in this case, with another molecule) becomes essential in order to acquire 'enhanced' contrast in NC-AFM. All experiments in this section were carried out at 77K, unless stated.

6.1.1 Results and discussion

Br_4TPP on Au(111)

Figure 44 shows a schematic and a single Br_4TPP molecule on Au(111). The molecule is constructed as a free base porphyrin core terminated with four flexible brominated phenyl groups. It is always difficult to determine

the tip termination, however in AFM mode we can broadly classify tips on the basis of the strength of their interaction. The centre and right images in Figure 44 show constant current STM and constant height AFM data in the Δf channel respectively. It is clear that the molecular structure in the right image is distorted and irregular, so this could indicate the possibility of a Br_4TPP-terminated tip.

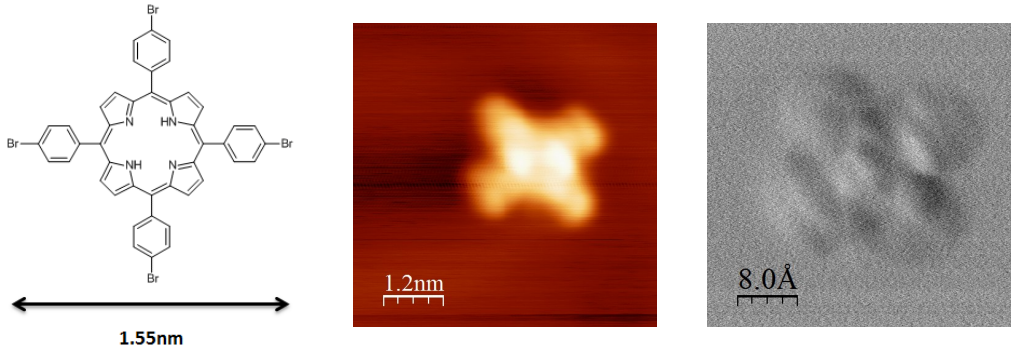

(a) (b) (c)

Figure 44: *a) Schematic of the Br_4TPP molecule. b) STM image, $V = +1.6V$, $I = 10pA$. c) Constant height AFM frequency shift channel, $a_0 = 400pm$, $V = 100mV$, $z = -150pm$ relative to b).*

Force-distance data are presented, also known as 'force spectroscopy'. For this experiment, the tip is oscillated above a molecule in AFM mode. The tip is then moved closer to the molecule (decrease in tip-sample distance) whilst the frequency shift is measured. A deconvolution in Matlab is carried out in order to convert from a frequency shift to a force. To correct the force-distance curves, an 'Off' spectrum was taken away from the molecule over the Au surface so long range force interactions can be subtracted. This should leave the short-range chemical forces for analysis. 1D force spectroscopy was performed over Br atoms and the centre of a molecule, with both a suspected Br_4TPP- and Au-terminated tip.

The experimental data of Figure 45 show a greater interaction over the core of the molecule with both molecular- and Au-terminated tips, with a force turnaround of -0.39 ± 0.05nN and -2.07 ± 0.05nN respectively; a higher value for metal probes is expected as metal-terminated tips are more reactive.

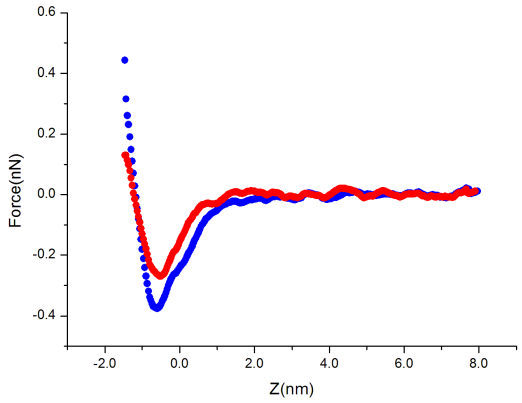

(a)

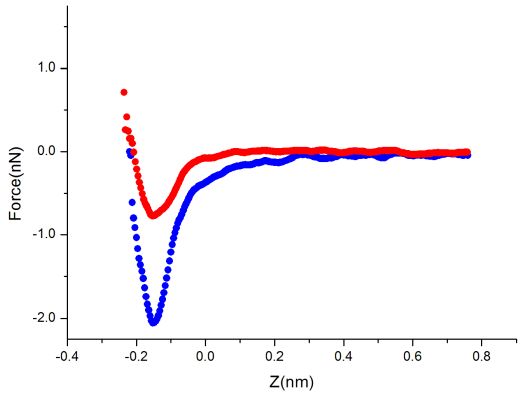

(b)

Figure 45: *a) 1D force spectroscopy with a suspected molecule-terminated tip. b) A suspected Au-terminated tip. Red curve indicates data taken over Br leg, blue indicates data taken over the Br_4TPP core.*

Br_4TPP on Cu(111)

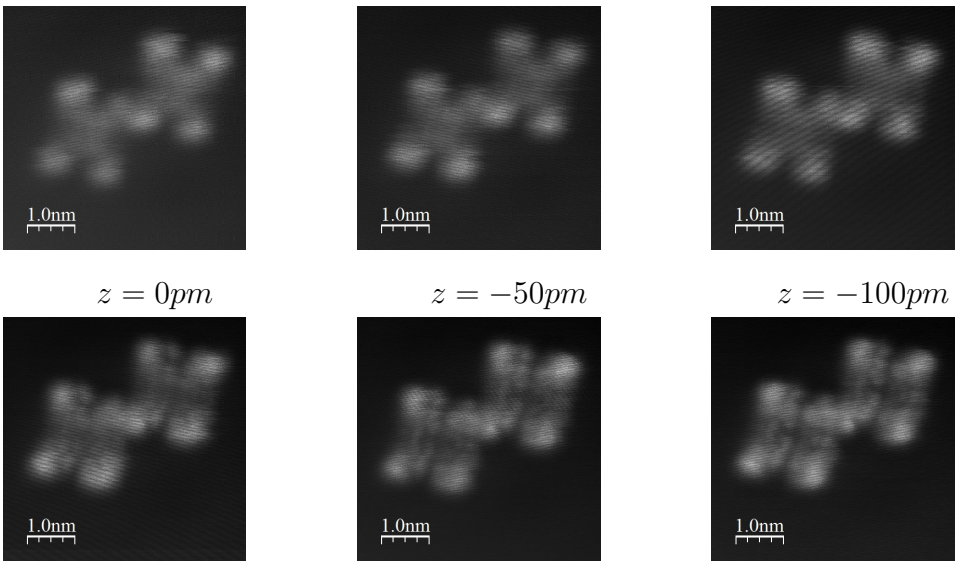

$z = 0pm$ $z = -50pm$ $z = -100pm$

$z = -150pm$ $z = -200pm$ $z = -250pm$

Figure 46: *Sequence of images showing two Br_4TPP molecules in constant height AFM current channel, with decreasing tip-molecule distance. (Relative z heights listed).* $a_0 = 400pm$, $V = 100mV$, $T = 5K$.

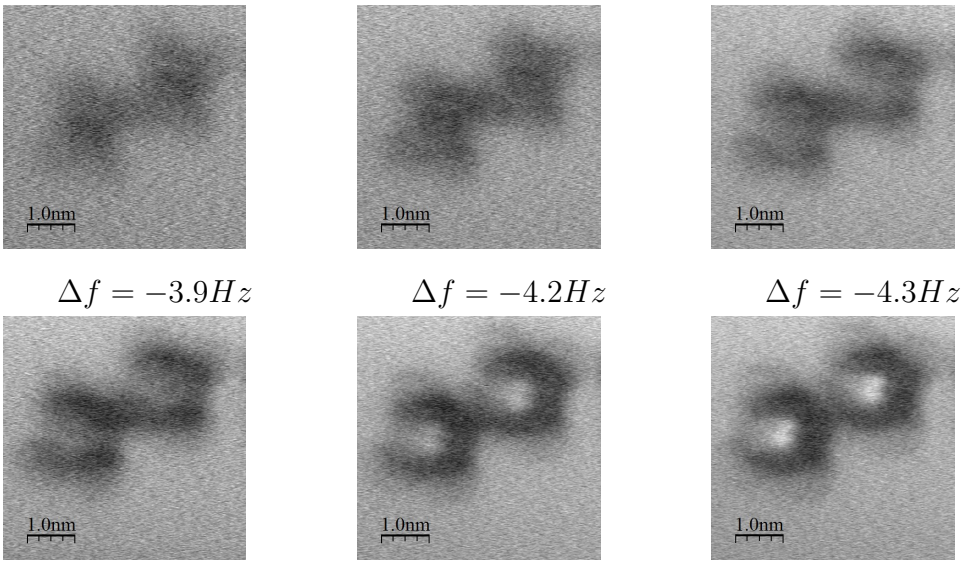

$\Delta f = -3.9Hz$ $\Delta f = -4.2Hz$ $\Delta f = -4.3Hz$

$\Delta f = -4.7Hz$ $\Delta f = -5.0Hz$ $\Delta f = -5.9Hz$

Figure 47: *Constant height AFM frequency shift channel corresponding to the above sequence in Figure 46.* $a_0 = 400pm$, $V = 100mV$, $T = 5K$.

Figures 46 and 47 show a sequence of images taken in constant height AFM mode, from the current and Δf channels. A very small bias voltage of 100mV was set to acquire the current data simultaneously. It is possible that the tip was Cu-terminated, as there is some clarity and even internal molecular structure in the Δf channel (as well as electron tunnelling at such small bias voltages), indicated by the repulsive chemical interaction in the core. However, the images are still somewhat distorted. This could point towards an asymmetric tip or even a possible molecule-terminated tip.

Figure 48 shows the $F(z)$ curve over a Br leg compared to the molecular core with a molecule-terminated tip. The force "turnarounds" are -0.87 ± 0.05nN and -0.70 ± 0.05nN respectively. In comparison to the Au(111) data, the Cu-terminated tip frequently experienced a stronger interaction over the Br legs with the above figure measuring -1.95 ± 0.05nN force turnaround, but this was dependent upon the conformation of the Br_4TPP molecule.

Figure 49 shows a histogram of force-distance data extracted from $F(z)$-spectroscopy measurements and counts versus force turnaround plotted in 0.1nN ranges. The data shows two broad classes of force interaction, and suggests that around 80% of experiments were conducted with a molecule tip termination (due to low force turnarounds of < 1nN). Most of the Au tip termination experiments were with a molecule-terminated tip, and metal-terminated tips were largely accounted for by experiments on Cu(111).

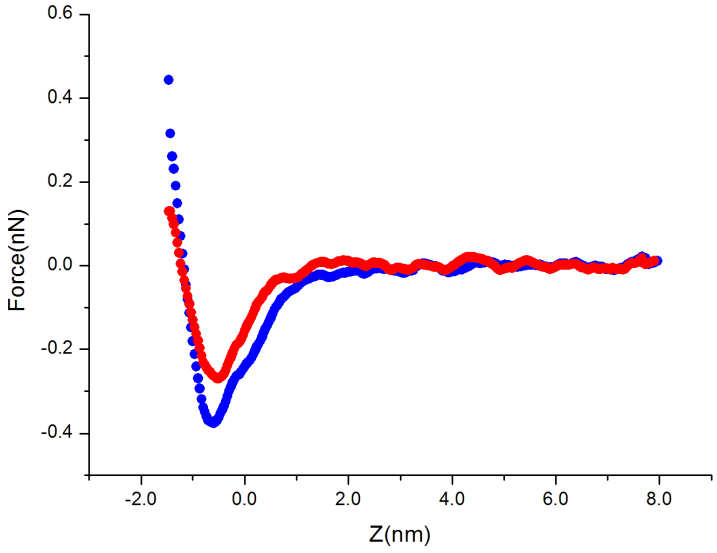

(a)

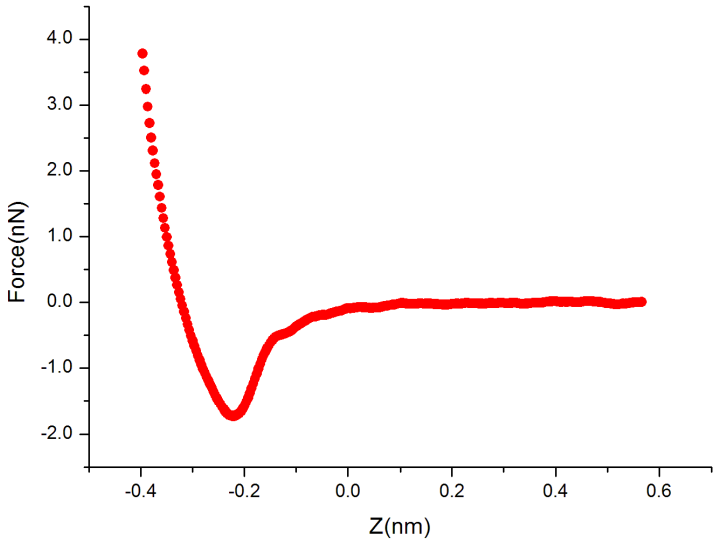

(b)

Figure 48: *a) 1D force spectroscopy with a suspected molecule-terminated tip. b) A suspected Cu-terminated tip. Red curve indicates data taken over Br leg, blue indicates data taken over the Br_4TPP core.*

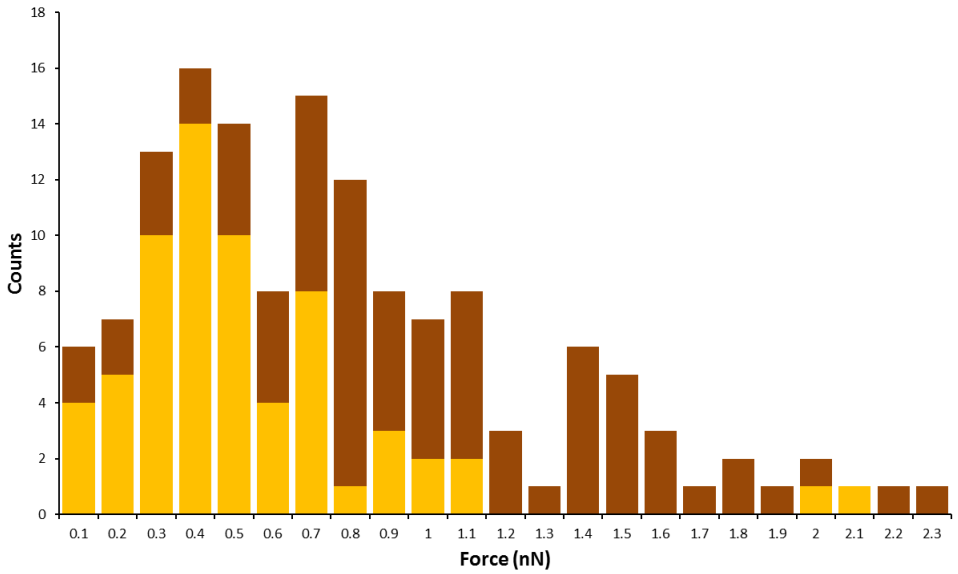

Figure 49: *A histogram showing counts versus turnaround force for Au (yellow), Cu (brown) and Br_4TPP tip terminations (< 1nN) over all experiments carried out. The histogram shows 81% of the total number of force turnarounds indicate a molecule-terminated tip whilst 19% were metallic based on the assumption that a molecule terminated tip is one with F(z)< 1nN.*

6.2 3D force mapping

3D grid spectroscopy measurements were carried out at 5K on two conformations of molecules. All Br_4TPP molecules adopted a saddle configuration respective to the Cu surface, however Type 1 had a more square geometry from plane view and Type 2 had a more rectangular shape. The grid spectroscopy was software based interface, and was constructed by taking $\Delta f(z)$ measurements across a 2D x-y grid. There was minimal drift over the 8hr data collection period due to the stability of the Createc STM/AFM at 5K.

Figure 50 shows a schematic of the principle behind applying 3D grid spec-

troscopy measurements.

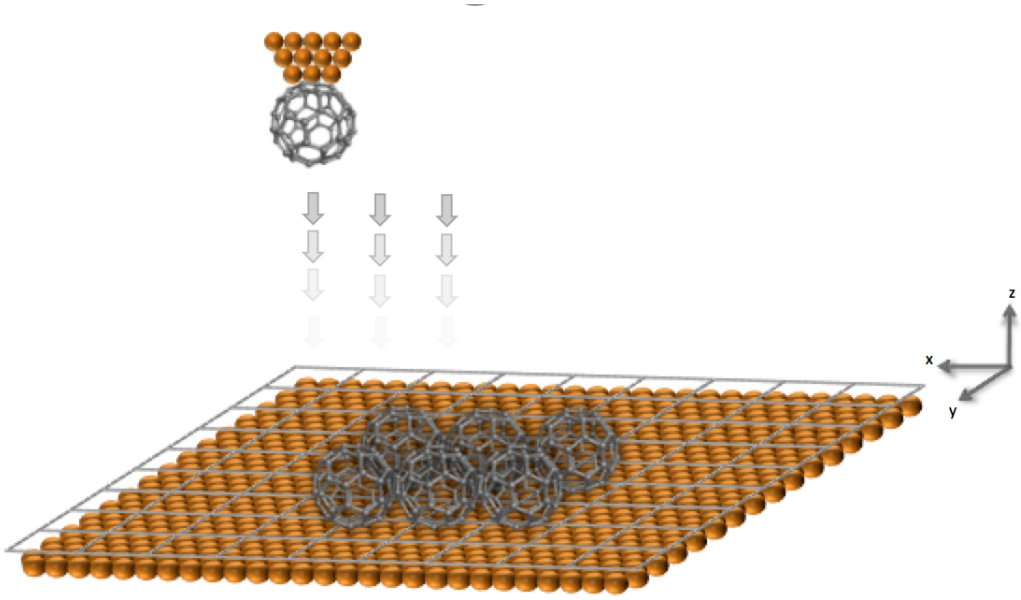

Figure 50: *A schematic describing the operation of 3D grid spectroscopy. The tip is held above one x-y point over a 'virtual grid' on sample surface whilst $\Delta f(z)$ spectroscopy is taken. The tip then moves to the next x-y point and repeats $\Delta f(z)$ spectra. An array of 2D x-y plane slices can then be extracted from different z positions over the grid surface to create a 3D grid.*

Figure 51 shows three slices in the *x-y* plane of a 3D grid spectroscopy experiment with two Br_4TPP molecules. The left image shows no force interaction at a relative z height of 0pm. The central image shows a similar attractive interaction over the centre of the Type 1 Br_4TPP molecule compared to the Type 2 Br_4TPP molecule beneath, confirming that the core of Type 2 molecules has a higher attractive interaction than its Br legs so it cannot be a planar molecule. The image on the far right shows repulsive interactions on both Br_4TPP molecules at a relative z height of -170pm.

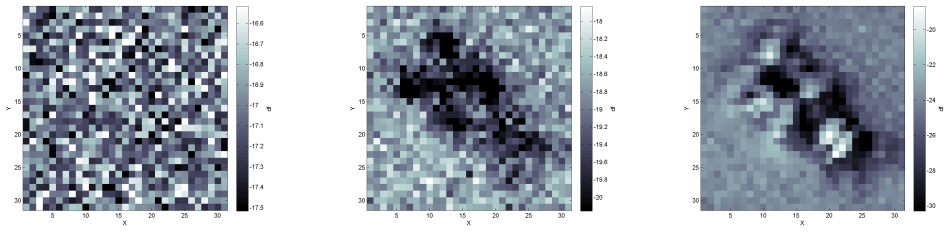

$z = 0$ $z = -70pm$ $z = -170pm$

Figure 51: *3D grid spectroscopy slices taken at three different relative z heights, decreasing from left to right above a Br_4TPP pair.*

6.3 Exploring the electronic structure of Br_4TPP on Cu(111)

The controlled dehalogenation of Br_4TPP on Cu(111) was attempted to determine whether the 'legs' of the porphyrin molecule played a role in its conformation. If the Br atoms played an important role, then the conformation of the molecule may change as a direct result of the manipulation procedure.

6.3.1 Results and discussion

Figure 52a (left) introduces the idea of a saddled conformation. From a side on view, one can see the buckled nature of the conformer. Although Figure 52a (right) is described as a planar conformation, it is in fact saddle, the only difference is it's less buckled. From herein, we describe 'planar' as Type 1 and 'saddle' as Type 2 conformers for clarity. Figure 52b and 52c shows STM and constant height AFM images of Br_4TPP molecules displaying Type 1 and Type 2 conformations. The constant height AFM image shows a similar attractive force over the entirety of the Type 1 compared to the core of the Type 2 Br_4TPP molecule.

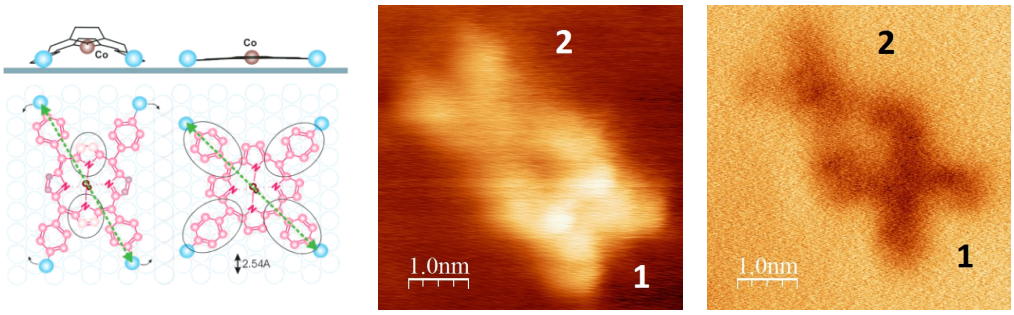

(a) (b) (c)

Figure 52: *a) left: The saddle (Type 2) and right: planar (Type 1) conformations of TBrPP-Co. Image from [45]. b) STM image of two Br_4TPP molecules on Cu(111) showing Type 1 and Type 2 conformations. c) Constant height AFM image of the same two molecules from b).*

Atom by atom dehalogentation of Br_4TPP on Cu(111) is shown in Fig. 53. The first STM image (Fig 53a) shows a Type 1 and Type 2 conformer with the whole of the Br_4TPP molecule intact. Upon the first electron injection, (a range of bias voltages was used, in this case between 2.3-3.3V, or 2.3-2.6V for Fig. 53 specifically) the Type 1 molecule switches conformation to Type 2, and in the process becomes dehalogenated. The detached Br consituents can be located in close proximity due to suppressed diffusion at 5K. Each successive debromination was carried out between 2.3-2.6V which is lower than the reported cleavage for Br_4TPP-Co on Ag(111) [225, 226] and TBrPP on Au(111) [49], but much higher than other studies on Cu(111). The injection sites were directly over the Br atom in STM but in some cases, with varied (higher) bias voltages and site injection, more than single atom dehalogenation occured, until bias pulses of 4V caused the entire molecule to dissociate. Fig. 53e shows an NC-AFM of the final STM image which reveals a similar macrocyclic and methine group structure in the dehalogenated species compared to the intact Br_4TPP. This could

suggest the Br-terminated phenyl legs do not contribute to conformation or adsorption factors, but this can't be deduced by having similar topographic appearances alone.

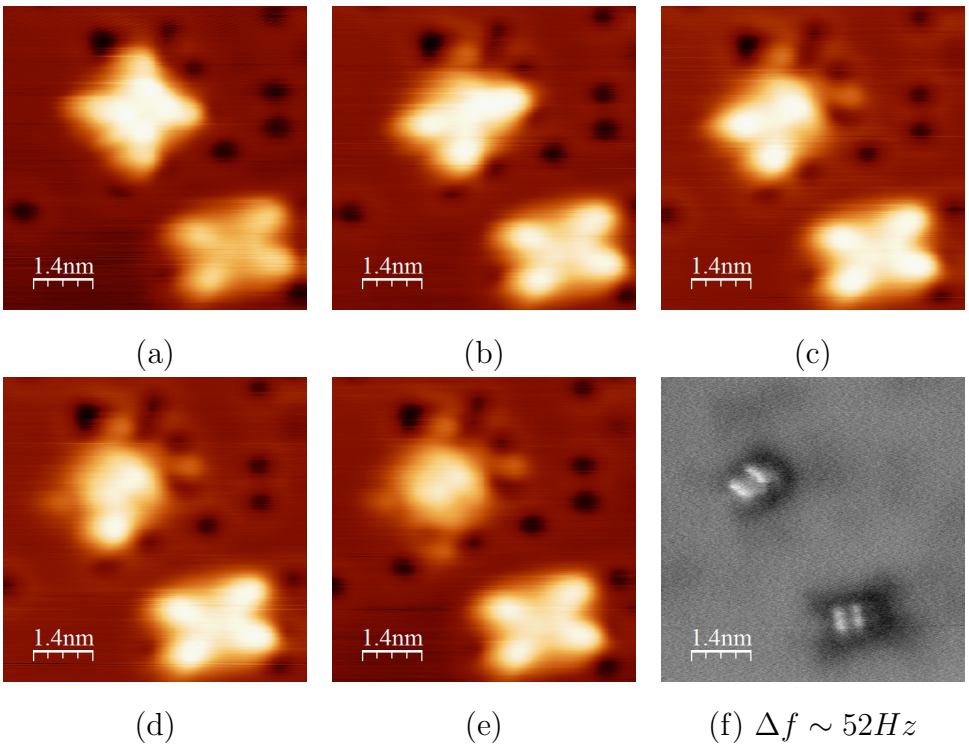

Figure 53: *(a)-(e) Constant current STM images showing the removal of a single Br atom using a bias voltage pulse ranging between 2.3V and 2.6V. Each successive image shows the further removal of another Br unit until (e) where the Br_4TPP molecule is completely dehalgoenated ($I = 10pA$, $V = +1V$) (f) shows constant height NC-AFM image revealing a similar macrocyclic and methine group structure after electronic cleavage. a_0=300pm, V=0V, T=5K.*

NC-AFM was used to confirm the atomic structure of Br_4TPP in direct comparison to the STM studies. Two distinct conformations of Br_4TPP on Cu(111) were apparent as previously mentioned; Type 1 and a Type 2. Respectively, there appeared to be a similar force attraction over the entirety of the Type 1 Br_4TPP molecule in comparison to the core of the Type 2. This could infer that the core of the Br_4TPP in Type 2 molecules

is a greater distance away from the Cu surface than its Br legs (i.e. the molecule is not planar or flat against the Cu surface). This has previously been suggested by Iancu *et al.* in STM, albeit with a slightly different porphyrin core base (Co instead of the Br_4TPP N-H base) [45]. As mentioned, between Fig. 53a and Fig. 53b, there is a conformational change of the de-brominated Br_4TPP molecule from Type 1 to Type 2. Iancu *et al.* report they were successful in carrying out this procedure but with a slightly lower bias pulse voltage of +2.2V [45].

Figure 54 shows further examples of dehalogenation and conformational switching, bias voltages used for localised electron transfer ranged from 2-4V. The cleaved Br atom in Fig. 54b is not visible due to enhanced diffusion at 77K. It is important to note that was much rarer to switch from Type 2 to Type 1, although this was possible in the literature with a Br_4TPP-Co molecule in close proximity to a cluster of Cu adatoms [45].

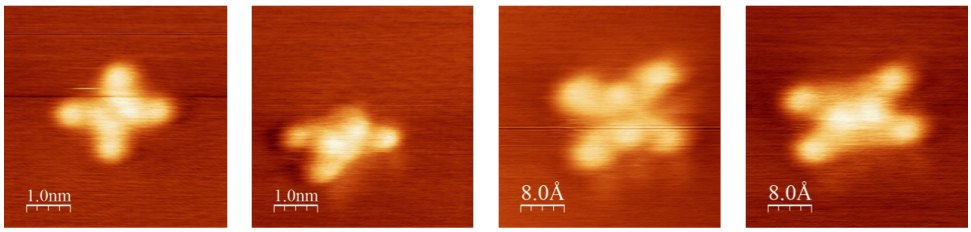

(a) (b) (c) (d)

Figure 54: *Constant current STM images showing a conformational switch upon localised electron injection, resulting in the dehalogenation of one Br atom from a) to b). c) to d) A conformational change from Type 1 to Type 2 with no Br atoms removed. V=-0.7V, I=5pA T=77K.*

Figure 55 shows a sequence of constant current STM images with increasing bias voltages.

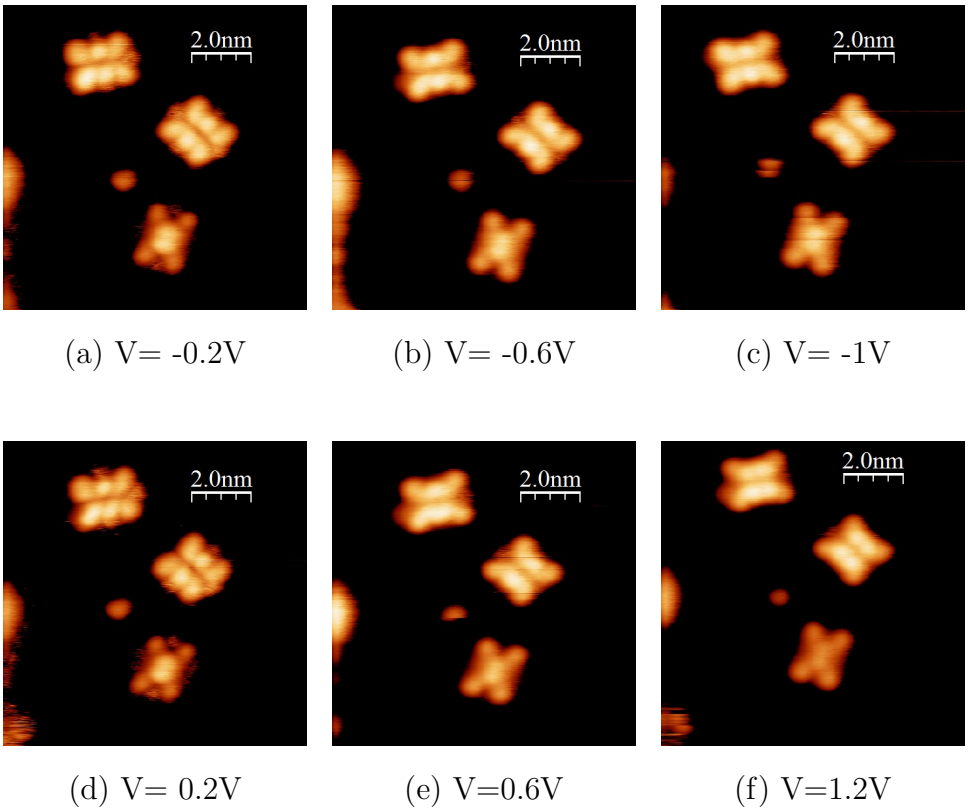

(a) V= -0.2V (b) V= -0.6V (c) V= -1V

(d) V= 0.2V (e) V=0.6V (f) V=1.2V

Figure 55: *Constant current STM images showing the electronic structure of molecular orbitals for two Type 1 and one Type 2 Br_4TPP molecules a-c) at negative bias polarity (i.e. tunnelling out of HOMO) and d-f) at positive (i.e. tunnelling into LUMO). I=2pA, T=5K.*

Distinct variations in the MO structure under the probing of electrons into the LUMO or out of the HOMO can be distinguished. In Fig. 55a at −0.2V, for Type 1 molecules, electrons are tunnelling out of the HOMO into empty states in the tip. The macrocycle and methine units appear as a bisected elliptical lobe. The Br terminated phenyl legs have a similar appearance, but protrude with an angle of inclination relative to the lobes of the macrocycle of around 45°. Fig. 55c shows a similar pattern to Fig. 55a but with slightly greater intramolecular detail, particularly for the Type 2 molecule at a lower bias voltage where the Br atoms are well-defined. The same can be described for Fig. 55d. Figure 55 is comparable to its directly

opposite (polarity) scan, but in Fig. 55f the Type 1 porphyrin macrocycle takes on a very different characteristic relative to the scan with opposing bias voltage; the methine units protrude as four independent quadrants. The Type 1 molecules also appear to be as bright across the entirety of their structure as the core of the Type 2 molecule. This is due to the more buckled adsorption of the latter conformer, where, relative to the Cu(111) surface, the Br-terminated phenyl legs are closer whilst the macrocycle and methine units are more distant.

Figure 56 shows the sequential dehalogenation of two Br atoms from a Type 1 molecule. Figure 56a shows the intact molecule whilst scanning at -1V. The molecular orbital structure is as expected; the porphyrin macrocycle and methine units appear as a bisected ellipse, with four Br-terminated phenyl components protruding at 45° relative to the core (comparable to Fig. 55a). The first Br atom is removed using a bias pulse in the range of 3.1-3.3V in Fig. 56b, but the porphyrin core appears to have transitioned from a HOMO to a LUMO structure; where the macrocycle and methine units look similar in detail to Fig. 55f (imaging at a positive bias voltage of 1.2V), but the polarity of the bias voltage in Fig. 56a-c is unchanged at -1V. Figure 56c shows the electronic structure of the Type 1 molecule after two Br atoms cleaved, where the circular quadrant core remains. The switch from HOMO-like to LUMO-like structure is a direct result of debromination. Although a rare occurrence, this is an interesting result, as the conformation of the electronically manipulated molecule remains unchanged; most Type 1 molecules instantly switched from Type 1 to Type 2 upon debromination as in Fig. 54.

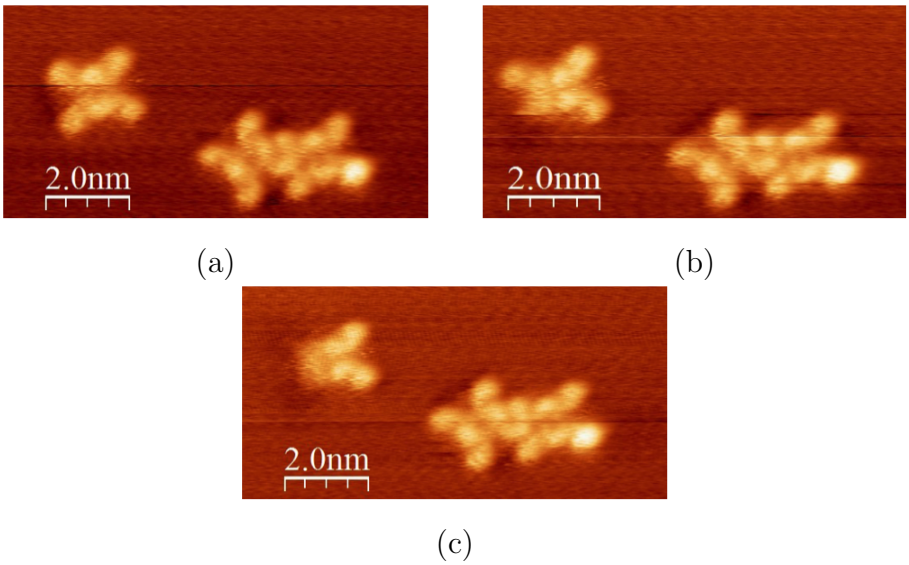

Figure 56: *Sequence of constant current STM images showing dehalogenation of a Type 1 molecule using a bias voltage pulse. a) Intact Type 1 molecule (left) and reference pair of Type 1 molecules (right). b) Br leg removed from bottom left of Type 1 molecule (left). c) Br leg removed from upper left of Type 1 molecule (left). Dissociated Br atoms not visible after cleavage due to enhanced diffusion. V=-1V, I=10pA, T=77K.*

6.4 Physisorption controls the conformation and density of states of an adsorbed porphyrin

6.4.1 Results and discussion

Another schematic of the Br_4TPP molecule is shown in Figure 57. Figure 57b shows a large STM scan (100nm) surface following a submonolayer deposition (10-20% coverage) of the Br_4TPP molecule at a substrate temperature of 77K, which prevents metalation of the porphyrin core.

Additionally, the Type 2 molecule appears darker (under the same imaging conditions) compared to Type 1, measuring topographic heights of 1.8 and 2.5Å respectively. This effect is particularly pronounced for the positive

sample biases used throughout this study. A deposition of similar molecules on Cu(111) carried out with elevated substrate temperatures results in coverages consisting of only a Type 2 conformer [227].

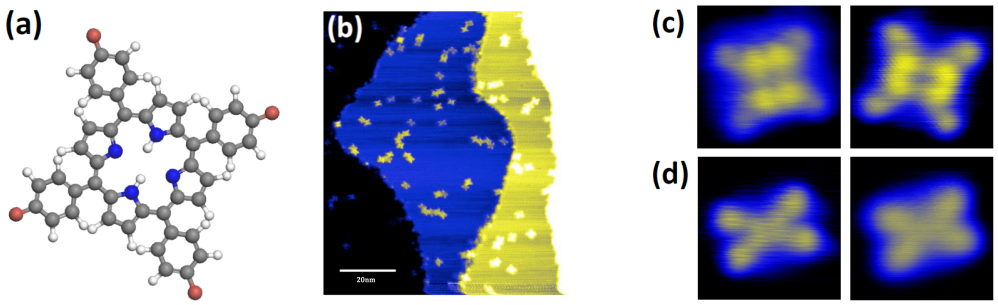

Figure 57: *Typical constant current images of Br_4TPP conformers on Cu(111). a) Schematic of gas-phase Br_4TPP molecule. b) 100x100nm overview STM scan showing representative molecular coverage across four terraces of the Cu(111) surface. Z-contrast scale has been selected to highlight the difference in contrast levels between Br_4TPP conformers. Typical high resolution images of c) Type 1 conformers 2x2nm and d) Type 2 conformers 2x2nm. STM parameters +1V/50pA. T=77K.*

Deposition was carried out onto a cold substrate in order to obtain isolated single molecules where a statistical analysis across multiple experiments revealed equal proportions of each molecular conformer (see Figure 58).

Experimental results detailing the distribution of Type 1 and 2 molecules and their relative orientations, following 77K deposition, on the Cu(111) crystal are shown in Fig. 58. As shown in Figure 58a Br_4TPP molecules adsorb in one of three unique orientations relative to the crystal directions of the Cu(111) surface. For ease of interpretation the directions have been explicitly labelled as -15°, -75° and +45° with respect to the horizontal axis of the STM image shown in Fig. 58a. Analysis across a greater number of images for a total of N=262 Br_4TPP molecules results in the distribution shown in Figure 58b, where we not only find an equal number of Type 1

and 2 conformers, but also an equal number of molecules adopting each orientation with respect to the surface. The equal distribution of conformers is consistent with the similar values of adsorption energy calculated in Table 3.

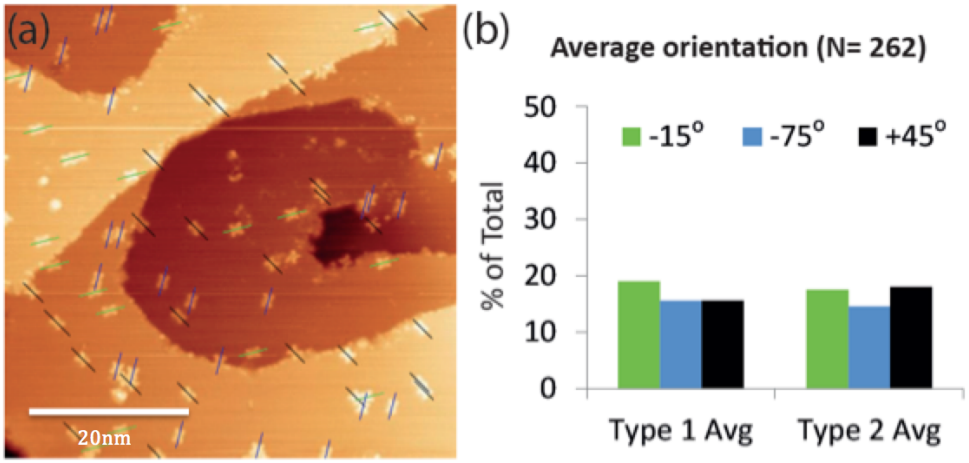

Figure 58: *Distribution of conformers and adsorption orientation. (a) Representative STM image showing the three unique orientations adopted by each Br_4TPP molecule. (b) Analysis across N=262 molecules shows an equal distribution between the number of molecules in each conformation, and the orientations they adopt with respect to the surface.*

Functional	E_{ads} (eV)	E_{ads} (eV)
	Type 1	Type 2
optB86b-vdWDF	-4.33	-4.15
PBE-D3	-5.32	-5.22
PBE-TS	-6.09	-5.86

Table 3: *Calcualted adsorption energies for each Br_4TPP conformer on Cu(111) with three different functionals [51].*

To ascertain the precise adsorption site of Br_4TPP on the Cu(111) surface and to gain further insights into the different appearances of the Type 1 and Type 2 molecules, we acquired STM images in constant height mode (also at 5K) using two different z-heights. This allows us to image the molecule

and the surrounding surface within the same scan (and, importantly, with precisely the same tip state) [228, 229]. We then overlay the atomic positions of the underlying Cu substrate onto the molecule as shown in Figure 59. By doing so we have found that both Type 1 and 2 conformers are orientated along the surface close-packed direction resulting in an even distribution of molecules rotated 60° with respect to one another (see Figure 58). As discussed in detail below, we find very good agreement between the adsorption site determined experimentally via this method and that predicted by not only density functional theory but also MD simulations.

Lateral manipulation was carried out by reducing the tip height by 500pm and laterally moving the tip across the molecule between scans. The molecules were then observed to either laterally translate, rotate, or switch conformation. Switching was most commonly observed from the Type 1 to the Type 2 conformation, suggesting that the Type 2 arrangement is more stable (later in this thesis [138] we show that this is due to a significant increase in the energy barriers for movement of the Type 2 conformer across the surface, which is reflected by an increase in the lateral force required to move the molecule relative to the Type 1 arrangement). Attempts to reverse the switching (i.e., to switch from Type 2 to Type 1), although possible, were generally unsuccessful and often resulted in damage to the molecule or a change in the tip state. Consequently, the conformational 'switch' we observe is not routinely reversible.

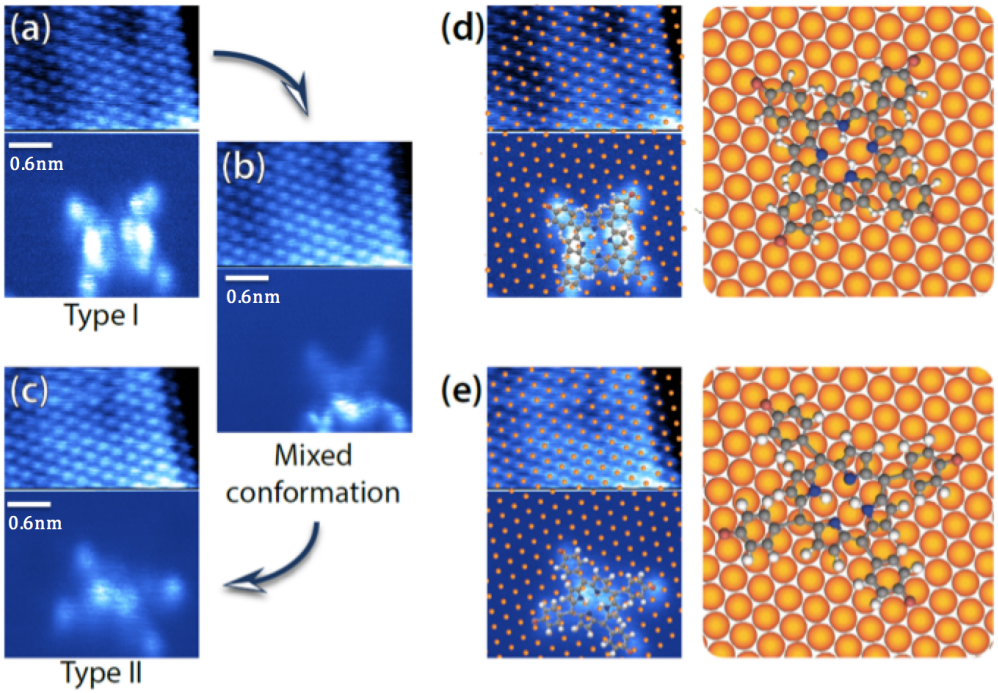

Figure 59: *Sequence of constant height STM images of a single Br_4TPP molecule and the surrounding Cu(111) suface. a) The Br_4TPP molecule when imaged in the Type 1 configuration. b) A mixed confomation oberved following manipulation of the same molecule in a) with the STM tip. c) Same molecule, now imaged in a Type 2 conformation after a spontaneous change during the scan. Superimposed structures for the Cu(111) surface and Br_4TPP molecules are shown in d) and e) where the assignment of N and N-H groups is not known from experimental data alone. STM parameters: V= 50mV, a_0=300pm; Cu(111) image height -520pm relative to z-height over Br_4TPP molecule. T=5K.*

To compare the Type 1 and 2 contrast we imaged a single molecule that was controllably switched between conformations at 5K temperatures (see Figure 60 for full sequence) using tip-induced molecular manipulation carried out at zero applied sample bias [87] (i.e. with no detectable tunnelling current that might otherwise locally heat the molecule). The scanning and the molecular manipulation in Figure 59 were carried out with an oscillation of 300pm applied to the qPlus sensor allowing simultaneous STM and

AFM imaging [230], although no AFM data are presented in this work. The lower half of the image in Figure 59a shows a molecule in the Type 1 conformation, with the atoms of the Cu(111) surface taken at a reduced tip-sample separation of $\Delta z \sim 520$pm observed in the upper half of the image. By overlaying the Cu(111) lattice onto the molecule, as in Figure 59e, we can determine its exact adsorption site. We then laterally manipulated the molecule (Figure 60) and switched it from the Type 1 to the Type 2 conformation.

The full sequence of Br_4TPP manipulation on Cu(111) is shown in Figure 60. The native Type 1 conformer is laterally translated and rotated across the surface (Figure 60a-c). Subsequent imaging of the local Cu(111) surface shows that the Type 1 conformer adopts the same adsorption site in each orientation. In Figure 60d an intermediate structure is shown adopting a mixed Type 1 and 2 arrangement obtained from the same lateral manipulation protocol. After successful translation of the mixed conformer (Figure 60e) the molecule spontaneously switched to the complete Type 2 conformation during continued scanning (Figure 60f). Subsequent manipulations show translation and rotation of the Type 2 conformer (Figure 60g-i). In this case many more attempts were required for successful manipulation, suggesting a stronger binding (or larger diffusion barrier) for the Type 2 conformer. We also note the reduction in tip quality over the Cu(111) region in Figures 60h and 60i and apparent shift of the step edge, suggesting subtle changes to the tip structure during manipulation.

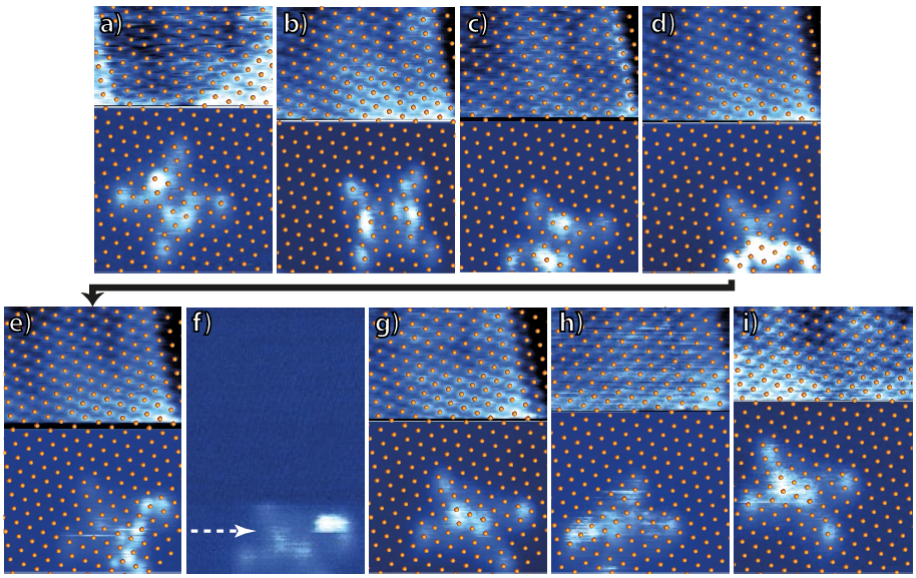

Figure 60: *Full manipulation sequence of Br_4TPP imaged with constant height STM. (a-c) Type 1 conformer in different orientations. (b,c) following lateral manipulation with the STM/NC-AFM tip with zero tunnelling current. (d-e) After half the molecule has changed to the Type 2 conformer. (f) Br_4TPP spontaneously switching to the fully Type 2 conformation during a downwards scan at the position marked by the arrow. (g-i) Images taken following lateral manipulation of the Type 2 conformer. Scan parameters: 50mV, a_0=300pm; Cu(111) image height -520pm relative to that over Br_4TPP. Image sizes 2.7x3.9nm. T=5K.*

As shown in Figure 59b and 59c, the switching process occurs via a metastable intermediate state where half of the molecule first switches to the Type 2 conformation before finally reaching an all-Type-2 state (see Figure 59d), observed during a subsequent scan (Figure 60f). The series of images in Figure 60 exhibits a high degree of consistency in the observed adsorption position for each conformer. As such we are able to determine the exact adsorption site as shown in Figure 59e and 59f for the Type 1 and 2 conformers, respectively. On the basis of these observations, and the simulations discussed below, we suggest that it is the adsorption site of the molecule that determines its conformation and that the conformation can

be modified by manipulating the molecule to an alternative adsorption site.

The ability to switch the conformation of the molecule between Type 1 and Type 2 by lateral manipulation across the surface is a clear indication that the position of the Br_4TPP molecule with respect to the underlying Cu(111) lattice plays a key role in determining which of the conformers is adopted. Additionally, the observation that the molecules can not only be reversibly mechanically switched at 5K temperatures but also that one-half of the molecule is observed to switch before the other appear to suggest that metal complexes are not necessarily involved in determining the conformation on Cu(111) [82]. The switching behavior especially excludes any possibility of complete metalation. The DFT and molecular dynamics results described in the following section strongly support this interpretation and highlight the essential role that vdW forces play in the conformational changes we observe.

Structure determination via Density Functional Theory and Molecular Dynamics

In order to calculate the full adsorption geometry of each conformer, Baran and Thompson simulated the complete molecule-surface system using classical MD in addition to extensive DFT calculations incorporating several methods to account for dispersion. Due to the high flexibility of the molecule and the relatively flat potential energy surface (PES, where the PES of a molecular system is defined as the electronic potential energy including nuclear repulsion, at a given nuclear configuration) [138], a large

number of adsorption geometries were identified as stable through DFT and MD simulations, the latter identifying as many as 12 arrangements (see Figure 61), demonstrating conformations with either planar or saddle-shaped cores. The experimentally super-imposed structures in Figure 59 were therefore essential in reducing the large parameter space in the calculations and were used to help guide the simulated structures (although some exploration was also conducted in order to confirm these were indeed the lowest energy structures).

From this comparison, and with guidance from the MD simulations, two stable adsorption configurations were identified with DFT matching the experimental data for Br_4TPP on Cu(111), resulting from different orientations of the molecule with respect to the underlying Cu(111) lattice.

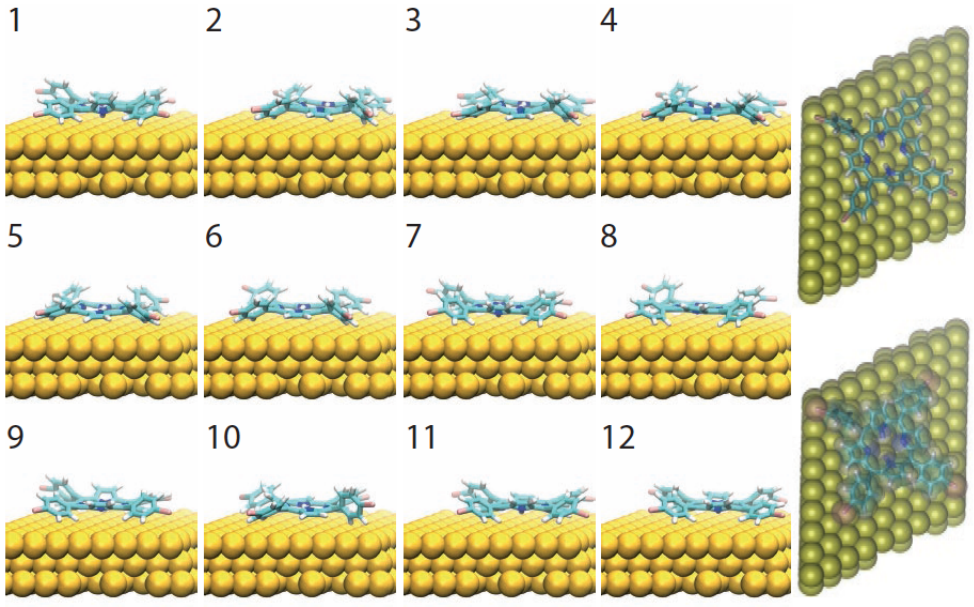

Figure 61: *Ball-and-stick diagrams of the twelve final structures obtained from MD simulations [51].*

Figure 62 shows the DFT results. In order to make a comparison with the experimental structure three primary features were compared: the alignment of the nitrogen atoms with the underlying Cu(111), the aspect ratio of the molecule and the overall orientation of the molecule as compared to the surface close-packed crystal direction. On the basis of these criteria we found that the geometries shown in Fig. 62a and c, and Fig. 62b and d match best with the Type 1 and 2 overlays shown in Figure 59, respectively.

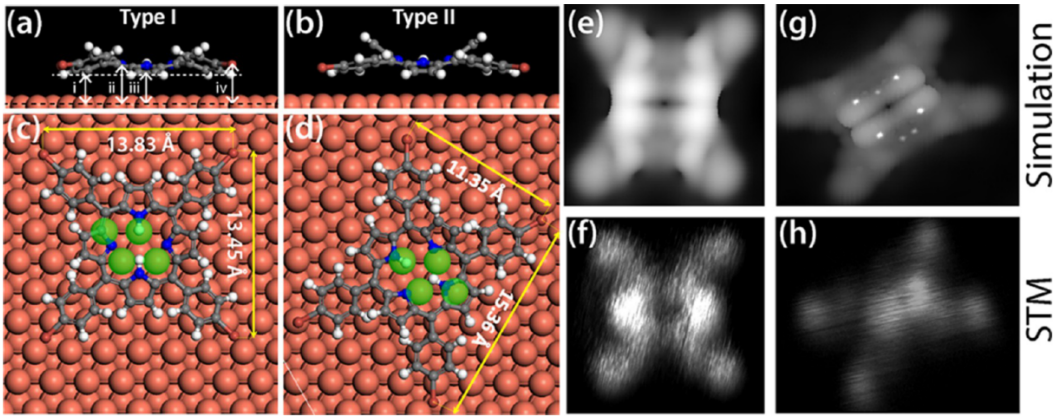

Figure 62: *Stable adsorption configurations and simulated STM of Br_4TPP on Cu(111) resulting from DFT with dispersion calculations. Side-on views of the structures matching the Type 1 and 2 conformations are shown in a) and b), respectively, both of which adopt saddle conformations. Ball-and-stick models showing the aspect ratio and exact alignment of the Type 1 and 2 conformers with the surface are shown in c) and d), respectively. Cu atoms are highlighted green to show the exact match with the experimental structures from Fig. 59. Simulated STM images are shown with their experimental counterparts for e,f) the Type 1 and g,h) the Type 2 conformers [51]. Experimental image sizes 2*x*2nm and 3*x*2nm respectively.*

The adsorption energies of the two conformers were calculated as -4.33 and -4.15eV for the Type 1 and 2 conformers, respectively, and were of the order of hundreds of meV more stable than the alternative structures which demonstrated poorer agreement based on the criteria outlined above. That is, the structures best matching the experimental data in Figure 59 corre-

spond to the lowest energy structures found. It is important to note that due to the shallow PES of the system many of the alternatively calculated metastable structures show only small deviations in the exact adsorption location on Cu(111), thus making precise determination of the correct adsorption geometry exceptionally challenging without the experimental data in Figure 59.

When dispersion interactions were omitted from the simulations, the molecular structures for both conformers (using the starting geometries shown in Figure 62) converged to a single planar structure with a reduced adsorption energy of only ∼95meV, deviating from the geometries best matching our experimental results, highlighting the important role of vdW interactions in modelling both conformers. The DFT-calculated geometries reveal important details regarding the mechanisms behind molecular adsorption. Hitherto, the conformational differences of isolated molecules on Cu(111) have been explained as due to planar and saddle orientations with respect to the surface [45].

While planar structures were observed to be stable in some of the simulations, saddle structures predominate and ultimately provided the best match with the experimental data and the lowest calculated total energies. Consequently, both of the lowest energy geometries identified are found to significantly distort the molecule from the gas-phase structure, each adopting a saddle conformation on the surface as shown in Figure 62a and 62b. The strongest alignment of the molecules with the underlying Cu(111) substrate is observed for the phenyl and pyrrole groups, which appear to

dominate the molecular adsorption. In the Type 1 geometry (Figure 62c) each of the phenyl leg groups is found to occupy positions located directly above the bridge sites of the Cu(111) in addition to three out of the four pyrrole groups.

Conversely, in the Type 2 geometry (Figure 62d) the phenyl legs and three of the pyrrole groups occupy positions located above the hollow sites of the surface. This alignment stems from a strong preference for the phenyl groups to align themselves with the surface in such a way as to maximize the vdW interaction with the Cu substrate. Therefore, although vdW interactions are often considered small (of the order of a few meV per atom pair), the cumulative interaction of the 48 atoms making up the pyrrole and phenyl groups of the Br_4TPP with the Cu surface atoms is easily capable of leading to several eV in total adsorption energy.

For the Type 2 geometry in particular, the increased amount of core distortion of the molecule incurs an energy penalty. However, due to the increased tilt of the pyrrole groups the phenyl legs are able to 'swing' into a more favourable position, reducing steric repulsion and increasing their interaction with the underlying Cu substrate, leading to similar adsorption energies for the Type 1 and Type 2 binding arrangements and a much greater diffusion barrier [138].

Table 4 shows a list of the closest molecule-surface distances of each element as depicted in Figure 62a alongside the corresponding covalent and vdW radii. In most cases the atomic distances are either in line with the

		Type 1	Type 2	covalent radii (Å)	vdW radii (Å)
i	Cu-H	2.57	2.53	$r^{H}_{cov}+r^{Cu}_{cov} = 0.37$ $+ 1.28 = 1.65$	$r^{H}_{vdW}+r^{Cu}_{vdW} = 1.20$ $+ 1.40 = 2.60$
ii	Cu-N	3.34	3.51	$r^{N}_{cov}+r^{Cu}_{cov} = 0.75$ $+ 1.28 = 2.03$	$r^{N}_{vdW}+r^{Cu}_{vdW} = 1.55$ $+ 1.40 = 2.95$
iii	Cu-C	2.70	2.74	$r^{C}_{cov}+r^{Cu}_{cov} = 0.76$ $+ 1.28 = 2.04$	$r^{C}_{vdW}+r^{Cu}_{vdW} = 1.80$ $+ 1.40 = 3.20$
iv	Cu-Br	3.28	2.85	$r^{Br}_{cov}+r^{Cu}_{cov} = 1.14$ $+ 1.28 = 2.42$	$r^{Br}_{vdW}+r^{Cu}_{vdW} = 1.85$ $+ 1.40 = 3.25$

Table 4: *Bond distances as depicted in Figure 62a shown with corresponding covalent (r_{cov}) and vdW (r_{vdW}) radii in Å taken from reference [231].*

combined vdW radii or greater. The only instance where the atomic separation falls below the vdW radii by a significant margin (yet remaining well above the covalent radii) is for the C-Cu separations and the Br-Cu distance in the Type 2 conformation. Such reductions in binding distance are reminiscent of hydrogen bonding; however, as described below, no permanent dipoles are present in our system. Although the calculations show that the Br-Cu interaction plays a much greater role for the Type 2 conformation, its effect is insufficient to compensate the high energy penalty from the increased distortion of the core macrocycle. This is supported by the calculations with vdW corrections removed where the molecule is always observed to relax back to a configuration close to the gas-phase structure. To test the possibility that displaced copper atoms from the top surface layer affect the molecule-surface bonds (as proposed by Doyle *et al.* [82]), an adsorption configuration was modelled where the surface Cu atoms located below iminic nitrogens, in addition to those closest to the surface carbon atoms and Br groups, were displaced upward by 1Å toward the molecule to a distance well within the covalent radii. The geometry opti-

mization was then performed where the final optimized structure simply relaxed back to the Type 2 configuration described above, where no copper displacements are found. This indicates that molecular 'anchorage' on the surface via coordination with displaced Cu atoms is somewhat unlikely at the low temperatures considered in this study, as supported by the experimental observation of the intermediate conformer and the manipulation at 5K described above.

Simulated STM

As described above, the Type 1 and 2 conformers of Br_4TPP appear with very distinct contrasts in STM images. As such, the constant current STM images for each of the conformers at a sample bias voltage of +1V was calculated by Baran and Thompson. A comparison between the simulated and experimental STM images is shown in Figure 62e and 62f and Figure 62g and 62h for the Type 1 and 2 conformers, respectively.

In addition to reproducing the correct appearance of the four brominated leg groups at each corner of the molecule, there is extremely good agreement for the core structure of each conformer, closely matching the two bright lobes typically observed in experiment. The experimental images shown in Figure 62 were taken in the constant height mode, which shows better detail of the molecular structure than the constant current images in Figure 59. In addition, there is also very good agreement for the aspect ratio for each conformer, which is measured as 1 and 1.35 from the ball-and-stick structure and $\sim$1.1 and $\sim$1.45 from the simulated STM, compared to

experimental values of ∼1.0 and ∼1.4, for the Type 1 and 2 conformers, respectively.

As described in detail next, the excellent agreement observed is due not only to determining the correct adsorption position of each conformer but also to significant changes to the electronic structure caused by the large vdW interaction the molecules have with the underlying Cu(111) surface. Therefore, based on the strong agreement we observe for both the STM images and the adsorption site, we can accurately assign the adsorption geometry of Br_4TPP on Cu(111) in each conformation.

vdW forces dominate adsorption

Similar to previous studies of large planar molecules [86], the calculations reveal that vdW forces dominate molecular adsorption. In good agreement with the DFT results, the MD calculations appear to reveal a subtle interplay between surface adsorption (of the molecular core and phenyl legs) and the induced strain from the saddle geometry. Isolated contributions from the core and legs shown in Figure 64d (corresponding to the MD structures in Figure 61) illustrate how the core and leg adsorption energies compensate for one another; i.e., as the core adsorption energy improves the legs are penalized and vice versa. The calculated structures and energies show that overall improvements in adsorption of the molecule as a whole compensate for geometrical strain in the core, as leg groups rotate into the space underneath bent pyrrole groups to maximize the vdW interaction with the surface. The ball-and-stick structures in Figure 61 show

the predominant saddle structure observed in the simulations, in which the pendant bromo-phenyl groups tilt to obtain a close vdW contact between the phenyl rings and the Cu(111) surface as described above. Control simulations of legless porphyrin molecules with just the core macrocycle showed always 100% planar structures.

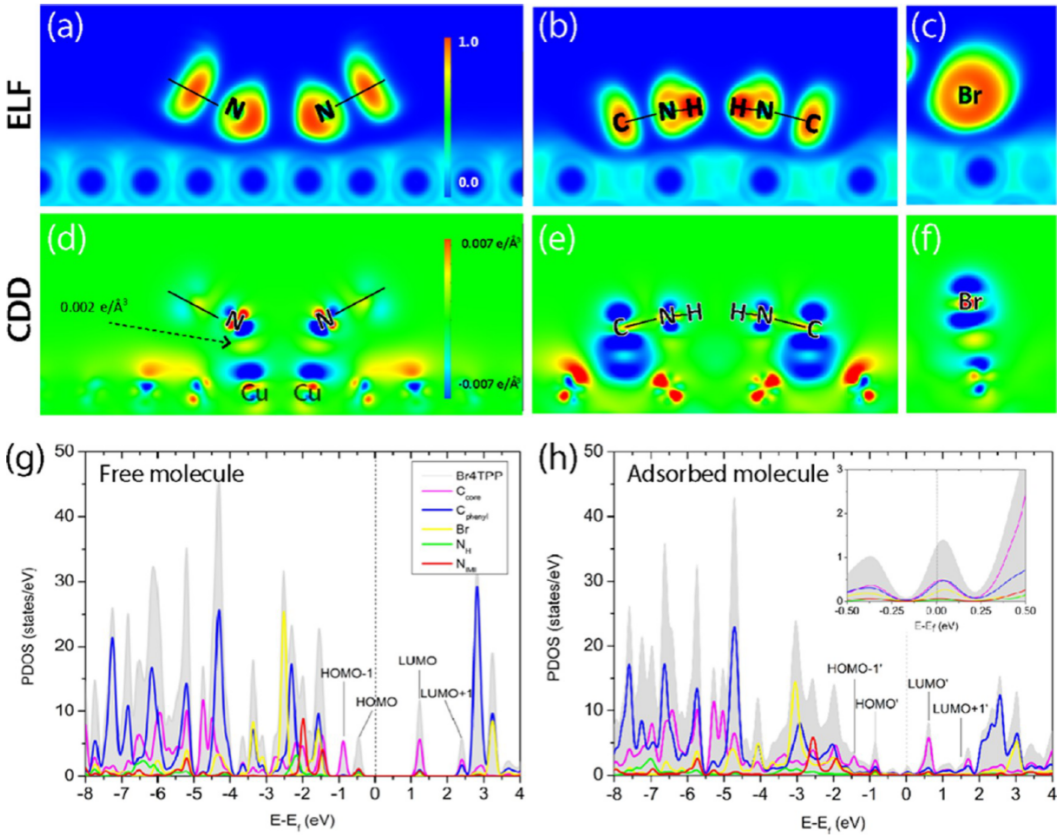

Figure 63: *Determining the interaction of Br_4TPP on Cu(111). Electron localization function (ELF) and charge density difference (CDD) plotted as a 2D slice through a),d) the iminic nitrogen atoms, b), e) pyrrolic nitrogen atoms, and c), f) bromine terminations. ELF plots show the complete absence of chemical bonding, supported by an extremely small accumulation of charge between the N_{imi}, NH, and Br atoms and copper surface shown in the CDD. Projected density of states (PDOS) of the free g) and adsorbed h) molecule where interface states (inset) are found to primarily originate from C_{core} and C_{phenyl} contributions, rather than the N_{imi} atoms [51].*

To check for the presence of chemical bonding the electronic structure of

each conformer was examined in detail by computing the electron localization function (ELF), charge density difference (CDD), and projected density of states (PDOS) at various sites across the molecule.

Neither the iminic nitrogen atoms in Fig. 63a and d, the pyrrolic nitrogen atoms in Fig. 63b and e, nor bromine terminations in Fig. 63c and f show any significant chemical interaction with the copper in either the ELF or CDD plots. The 2D CDD plots in particular show that the majority of the charge redistribution is a direct result of the 'pillow effect' discussed below and visualised in Figure 64c.

In Figure 63d there is primarily charge depletion between the iminic nitrogen/bromine atoms and the copper substrate, with only a very small region of excess charge, which is nonetheless over an order of magnitude smaller than what is expected for chemical bond formation in both covalent systems [228, 232], and N-Cu bond formation [233], suggesting only a very weak presence of chemical bonding between the molecule and the surface. In addition to the charge visualizations, the density of states projected onto the C_{core}, C_{phenyl}, Br, NH, and N_{imi} atoms was calculated for both the free (Figure 63g) and adsorbed (Figure 63h) molecule. In Figure 63h in particular it is clearly observable that the interface states formed within the HOMO-LUMO gap originate from the carbons of the core macrocycle and the legs as well as the bromine atoms, with no contribution from the nitrogen units, an effect assigned to hybrid interface states of the weakly interacting molecule [234, 235]. Critically, however, the PDOS analysis demonstrates that there is no mixing, and therefore no strong interaction,

between the nitrogen atoms of the molecule and the Cu surface. A Bader charge analysis also reveals that only a small amount of charge transfer occurs from the Cu(111) to the molecule of 0.1e and 0.07e for the Type 1 and 2 conformers, respectively, suggesting a relatively small contribution of ionic binding compared to the dominant vdW interaction.

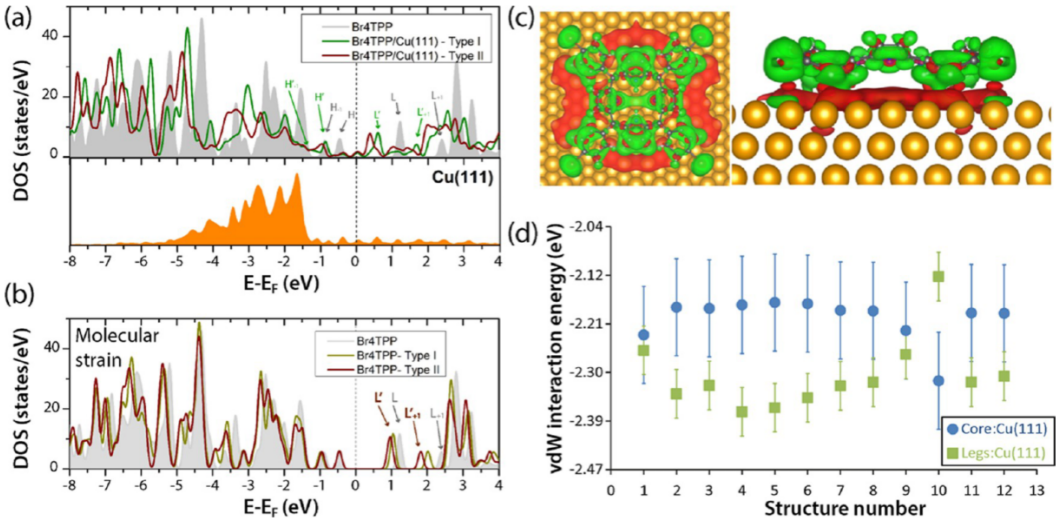

Figure 64: *Physisorption-induced changes in DOS. a) Calculated DOS for the gas-phase structure (grey), the Type 1 (green) and Type 2 (red) structures shown in Figure 62, and the Cu(111) surface (all shown relative to the Cu Fermi level). The major HOMO-LUMO peaks for the gas-phase and Type 1 molecule are marked with arrows. b) Calculated DOS for the Br_4TPP molecule in the gas phase (grey) as in a) but now shown with the DOS calculated for the isolated Br_4TPP molecule with its geometry fixed in each conformation but with the Cu(111) surface removed, i.e., the change in DOS due to the modified geometry of each conformer. Significant shifts are observed for the LUMO peaks despite the complete absence of the surface. c) Charge density difference (CDD) plotted for the Type 1 conformer showing the distinctive 'pillow effect' caused by physisorbed behaviour. Red and green corresponds to charge accumulation and depletion respectively. d) Core and leg adsorption energies extracted from molecular dynamics simulations of Br_4TPP adsorbed on Cu(111) (structure numbers relate to geometries shown in Figure 61) [51].*

As described above, the adopted saddle structure of the molecule significantly increases the vdW binding energy with the surface. This rearrangement results in significant charge redistribution around the phenyl leg groups and core pyrrole units, which are able to move closer to the Cu(111) surface. Additional, but more localized, vdW contributions are also observed, associated with the bromine terminations and the iminic nitrogen atoms (which are tilted toward the Cu substrate). If the dispersion is not included and the stable geometries shown in Figure 62 are allowed to relax using standard DFT, the adsorption energy drops to ∼95meV resulting in a planar structure. Furthermore, if the molecular geometry is instead fixed in place, and the dispersion 'switched off', the non-vdW adsorption energy takes on a positive value, suggesting that steric repulsion between the molecule and the surface makes up the primary contribution. This final point is important, as it has been previously observed that the reduced molecule-surface separation induced by vdW forces can aid the onset of chemical interactions [236], evidenced by strong localized hybridization visible in plots of the CDD. The CDD plots show no such interaction, in addition to the drastically weakened binding observed when dispersion corrections are 'switched off' (both with fixed and relaxed geometries), however, this is not the case in the above simulations.

The investigation into the question of the physisorbed versus chemisorbed state of Br_4TPP on Cu(111) can therefore be summarised as follows. Examination of the DOS spectra for each conformer shows that the LUMO remains above the Fermi level with minimal charge transfer of 0.1e at most to the molecule. This is supported by plots of the PDOS which show neg-

ligible mixing between the nitrogen units of the molecule and the copper. In addition, a direct visualisation of the charge distribution through ELF and CDD analysis reveals a lack of electronic density sufficient for chemical bonding and instead points to the dominating repulsive interaction from exchange effects (as substantiated by the positive adsorption energies calculated when dispersion corrections are removed).

To summarise, the adsorption of Br_4TPP, and likely many other TPP derivatives, depends on the cumulative vdW contributions originating from both the phenyl leg groups and the core macrocycle of the molecule. It is only due to this strong interdependence between saddle conformations and improved alignment with the Cu substrate that we are able to obtain the experimentally observed structures. One reason why chemical interactions may be suppressed in this system is the electron-withdrawing nature of the Br atoms, which may cause a reduction in the ionization potential of the molecule by 'draining' charge from the central macrocycle, similar to other systems [237]. Additionally, it may be the case that in some experiments de-protonation of the N-H occurs leading to strongly binding N radicals. This could potentially result from irradiation during photoemission measurements or the breaking of a chemical bond during annealing.

Physisorption-induced changes in DOS

In Figure 64a the calculated DOS for the gas-phase structure of Br_4TPP is compared to the two conformations it adopts on the Cu(111) surface. As shown in the Figure 65, in the calculations without dispersion there is

very little change to the DOS, observing only a small shift toward positive energies. The resultant non-vdW structures were found to deviate from the two saddle arrangements best matching our experimental results to an almost single planar structure matching neither conformer.

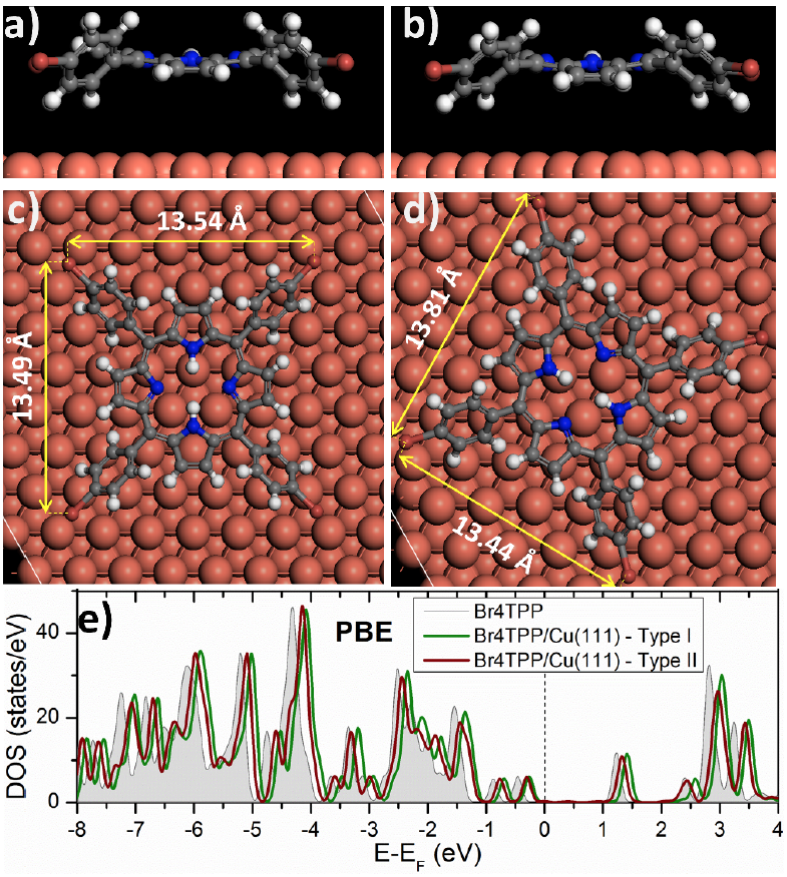

Figure 65: *Calculated structures and DOS for non-vdW corrected calculations. a) and c) show side and top views of the structure obtained using the Type 1 coordinates as the starting geometry for calculation and b) and d) using the Type 2 coordinates. Both calculations result in very similar molecular structures, with a planar macrocycle and a core position centred over a surface hollow site in both cases. e) Calculated density of states for the free gas-phase molecule (grey), and the structures shown in a) and c) (green) and b) and d) (red).*

This is despite the fact that the vdW optimized structures shown in Figure 62 were used as the starting geometries in the non-vdW calculation. Re-

markably, however, when dispersion forces are taken into account there is a much larger deviation in the DOS from that calculated in the gas phase as shown in Figure 64a. In addition to a clear broadening of the peaks, a significant shift toward more negative energy values was calculated. The maximum of the peaks that correspond to the LUMO+1/LUMO and HOMO/HOMO−1 of the free molecule are located around +1.6/0.5 and −0.9/−1.5 relative to the Cu(111) surface Fermi level. The HOMO/LUMO peaks are also easily identified by visualising the integrated local density of states of the individual peaks before and after adsorption, as shown in Figure 66.

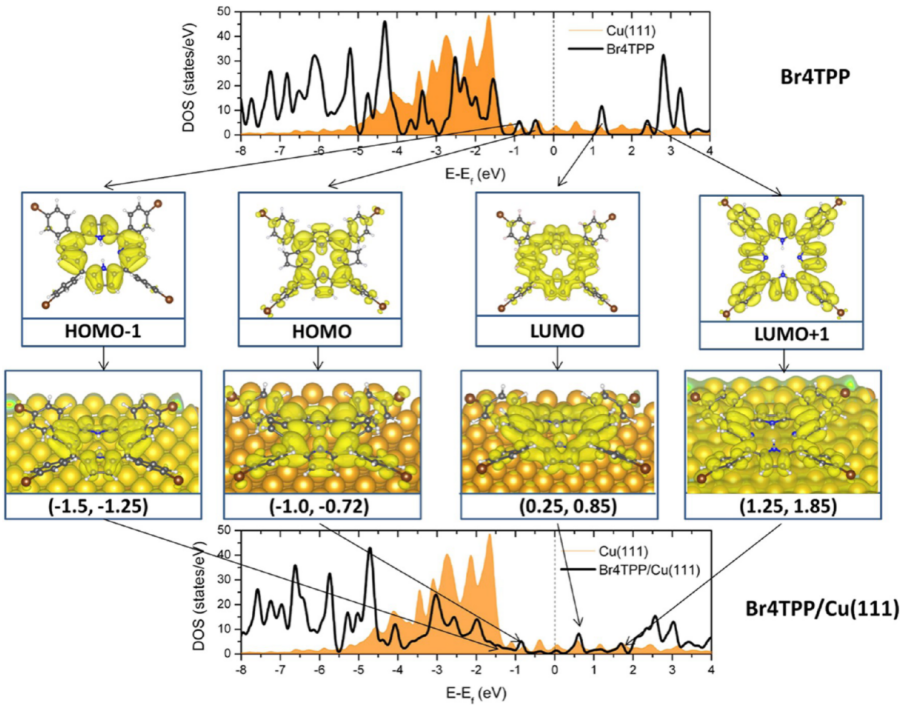

Figure 66: *Integrated local density of state (ILDOS) analysis of Br_4TPP on Cu(111). a) Calculated density of states (DOS) for the isolated gas-phase molecule and the Cu(111) surface. b) Square modulus plots of the HOMO−1, HOMO, LUMO, and LUMO+1 orbitals for the gas-phase molecule as marked with arrows. c) ILDOS plots showing the corresponding orbitals of the surface-adsorbed molecule. d) Calculated DOS for the surface-adsorbed molecule and the isolated Cu(111) surface. The location of the ILDOS plots from c) are shown with arrows.*

It is important to note, however, that despite the large shifts in DOS the LUMO peak does not cross the Fermi level. Integrated local density of states (ILDOS) plots following adsorption also appear very similar to the square modulus of the isolated orbitals of the free molecule showing that the occupied (unoccupied) states in the free molecule are consistently under (above) the Fermi level. This indicates that molecular charge donation, back-donation that could be responsible for formation of the chemical bond, is marginal. The DOS plots have little or no dependence on the choice of method to describe dispersion (see Figure 67).

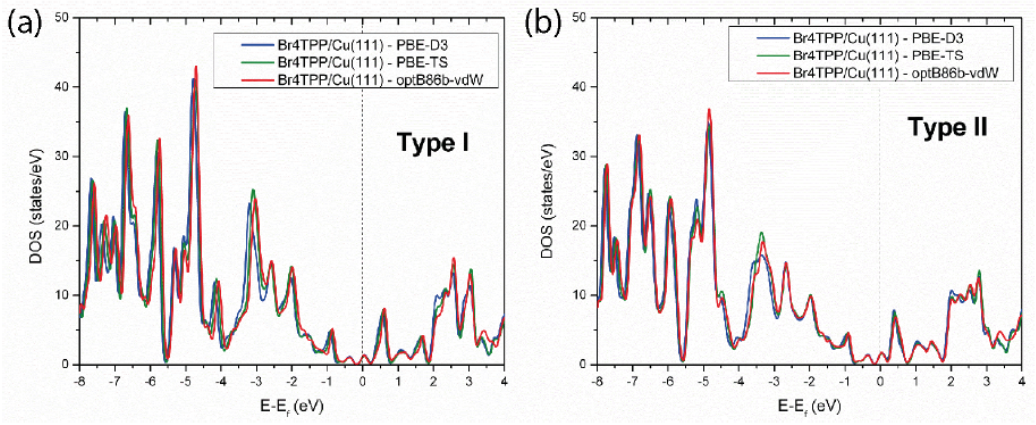

Figure 67: *Calculated DOS of the a) Type 1 and b) Type 2 adsorbed conformers using three different calculation methods showing negligible difference [51].*

The DOS for the isolated Br_4TPP and Cu(111) systems with and without dispersion was also calculated, as shown in Figure 68. In this case, however, the dispersion has very little effect. Consequently, the variations in DOS must arise from the coupled surface-molecule system.

In the gas-phase structure of Br_4TPP the HOMO-LUMO gap is found to span a large energy window of ∼1.1eV around the Cu(111) Fermi level

(where STM imaging is typically performed). Following adsorption on the surface the LUMO peak is shifted by ∼0.8eV. This has particularly significant implications for STM imaging, as the number of available states at positive energies near E_F is significantly increased. It therefore seems likely that the vdW-induced changes in DOS observed are essential for obtaining the simulated STM images shown in Figure 59. Interestingly, the observed shifts differ for each of the two molecular arrangements, highlighting the important effect of conformation on the DOS. As explained below, this is likely due to a combination of the increased strain in the Type 2 arrangement and the difference in wave function overlap with the surface.

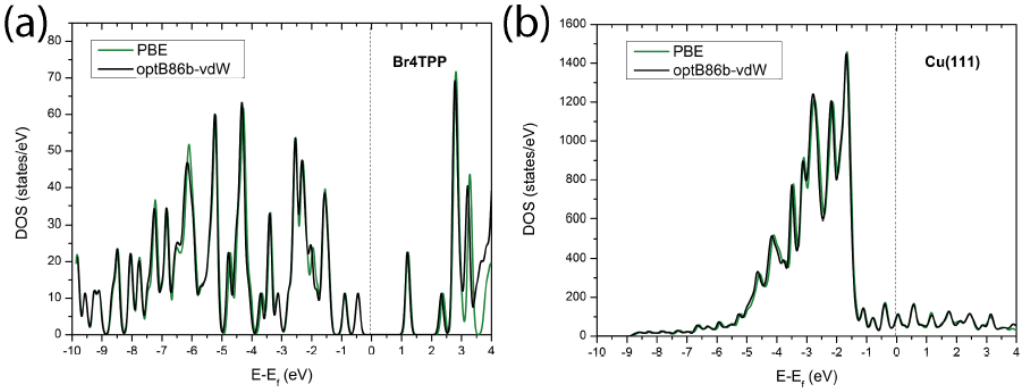

Figure 68: *Molecular DOS calculated for an isolated Br_4TPP molecule obtained using two different functionals. b) DOS calculated for the isolated Cu(111) slab obtained using the same functionals [51].*

The origin for the observed shifts in DOS can be understood within the context of both distortion of the molecular structure- thus modifying the chemical environment of its constituent parts- and induced dipole interactions caused by a significant reorganization of charge within the molecule, originating from orthogonalization of the metal and molecular wave functions.

The effect of molecular strain is shown in Figure 64, where the calculated DOS of the gas-phase (grey) molecule is compared to the DOS calculated for the isolated Br_4TPP conformers in each adsorbed geometry, i.e., the same fixed geometric structure as shown in Figure 59a-d, but with the copper surface atoms completely removed. This eliminates any possibility of a surface interaction. As can be seen in Figure 64b, this distortion of the molecule is enough by itself to drive surprisingly large changes to the chemical environment of the molecule, causing shifts in the DOS, particularly for the LUMO/LUMO+1 peaks as highlighted in the figure. This is similar to previous observations where changes in molecular geometry were observed to affect the electronic structure [46, 238].

This simple calculation demonstrates that although chemisorption almost always leads to shifts in the DOS of a molecule the opposite cannot be assumed; shifts in the DOS spectrum need not arise solely from chemical bonding. This may be particularly important in the interpretation of XPS measurements, where changes in the chemical environment of atomic elements (and the associated chemical shifts in photoemission spectra) are almost always interpreted in terms of chemisorption.

The second effect causing changes in the DOS potentially originates from the so-called 'pillow effect' [239], an exchange interaction driven by Pauli repulsion that causes a large reorganization of charge within the molecule. Similar to previous calculations [79, 240] there is a depletion of charge from the molecule as charge density is pushed away into the surface, shown in

the charge density difference (CDD) plot in Figure 65c. This results in a significant surface interface dipole, a common observation for physisorbed atoms and molecules [239]. Such exchange interactions have been shown to cause significant shifts in the energy levels of graphene when it is either physisorbed or chemisorbed [241] and to underpin work function changes due to Xe and cyclohexane adsorption [239]. The calculations reveal only a small amount of charge transfer to the molecule of $\sim$0.1e, indicating a small contribution from ionic binding and supporting that the observed interface dipole likely arises from the 'pillow effect'.

Although vdW interactions have previously been shown to affect the HOMO/LUMO structure of a molecule [236, 240], these systems are unlikely purely physisorbed. Indeed, one case reports a synergistic effect of vdW interactions in combination with chemisorption [236]. The results described in this study show that large changes to the molecular DOS can arise from an essentially physisorbed molecule. Physisorption, particularly in the case of large, flexible molecules, could potentially play a significant role in inducing large changes in DOS, a behaviour typically attributed to chemisorption.

6.5 Measuring the mechanical properties of molecular conformers

6.5.1 Results and discussion

Conformer structure imaged with non-contact atomic force microscopy

In Fig. 69 there are further high resolution constant current STM and constant height NC-AFM imaging of conformers deposited on the Cu(111) surface at 77K, and imaged at 5K.

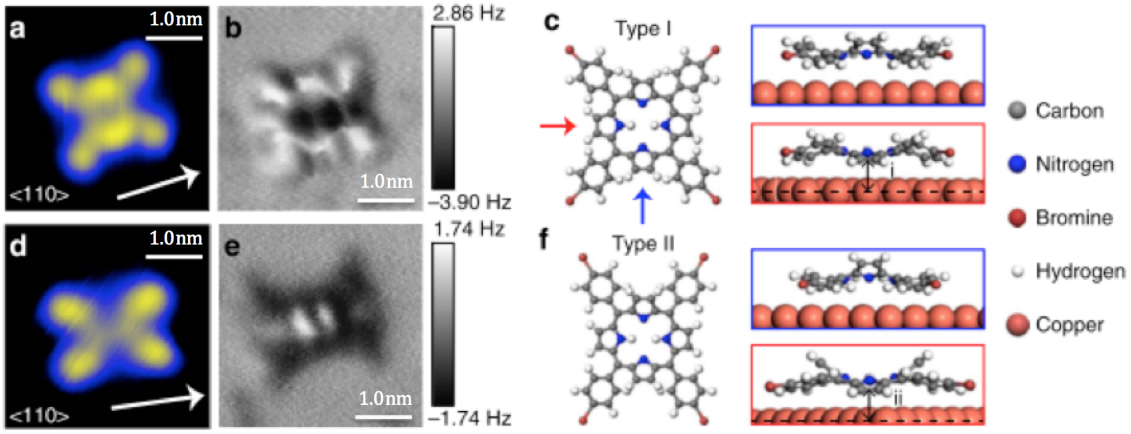

Figure 69: *Further STM and NC-AFM images of Br_4TPP conformers on Cu(111). a) constant current STM and b) constant height NC-AFM modes. Equivalent scans for the Type 2 conformer are shown in d) and e). DFT calculated structures, shown in c) and f) reveal significant differences in distortion for the Type 1 and 2 conformers, respectively. Ball-and-stick illustrations are shown from a top-down view (surface removed for clarity) and two side-on views marked with red and blue arrows and boxes. The C-Cu adsorption distance, marked as i and ii is 2.70 and 2.74Å for the Type 1 and 2 conformers, respectively. STM data were collected in separate experiments. Parameters: STM: a) $-1V/4pA$, d) $+1V/50pA$. AFM: $a_0 = 200pm$, V=50mV. Image sizes 3.5 x 3.5nm. STM images are shown with a saturated colour scale.*

We expect that in this case our tip is molecularly terminated, either by another Br_4TPP molecule or with CO, due to residual gas contaminants in the system (Figs. 70 and 71 show increased distortion of molecules and and inversion of contrast over CO adsorbates respectively, hence our suspicions).

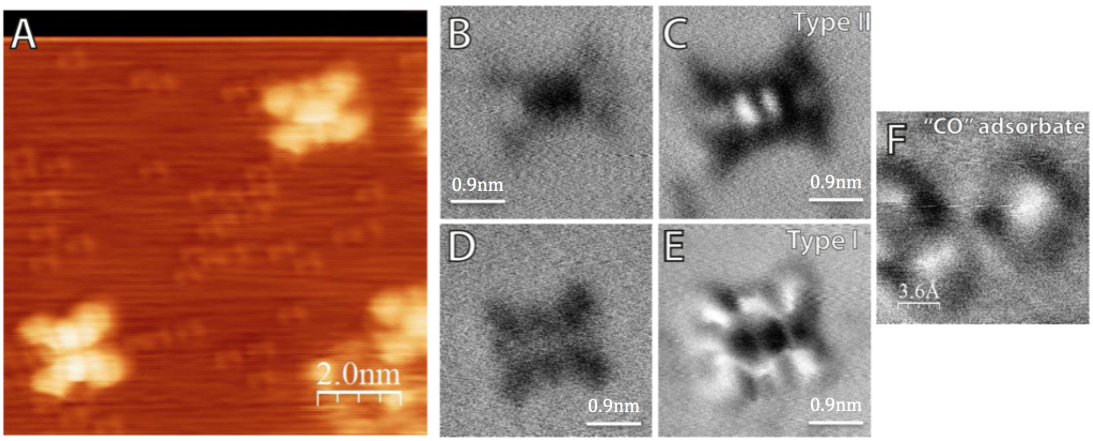

Figure 70: *STM and NC-AFM data for Fig. 69. A) Constant current STM image with a large number of potentially adsorbed CO molecules present. B) Constant height Δf image for Type 2 conformer at onset of attractive interaction. C) Lower tip-sample separations during onset of repulsive contributions (z=-80pm relative to B). D) Constant height Δf image for Type 1 conformer at same tip-sample separation as B). E) Image taken at smaller tip-sample separation (z=-150pm relative to B and D). F) Constant height images of local 'CO' adsorbates show relatively symmetric tip structure supporting the assignment of a sharp passivated tip (z=-420pm relative to B). Parameters: STM: A) -1V/20pA. AFM: a_0=200pm, V=50mV. B-E) Image sizes 3.5* x *3.5nm.*

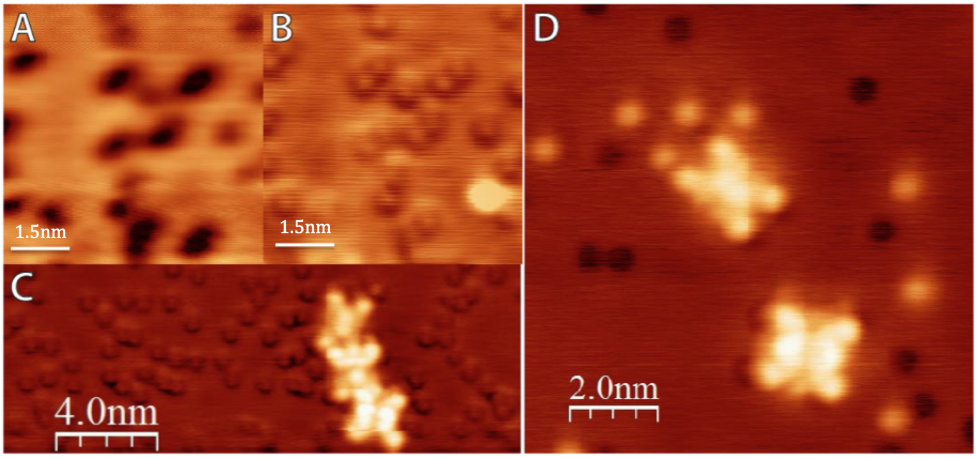

Figure 71: *Inversion of molecular adsorbate contrast in STM. A) Before and B) after images of surface adsorbates taken during successive STM images. C) Larger STM image taken directly after B). D) STM showing Br_4TPP conformers, Cu adatoms and the distinctive adsorbate features.*

The primary feature observed for the Type 1 molecule in Fig. 69b is the strong repulsion located over the phenyl leg groups and what is assumed to be two of the pyrrole units at the top and bottom of the molecule. Despite the evidence for molecular tip termination, intramolecular resolution within the aromatic rings is not observed. We note that other non-planar molecules, such as sexi-phenyl [242], appear with similar resolution. The consistent magnitude of the Δf signal observed across the molecule corresponds well to the calculated structure in Fig. 69c, which shows similar heights of the distorted core and leg groups. In contrast, the Type 2 conformer shown in Fig. 69e exhibits a significantly more repulsive core than the periphery of the molecule. This is typically observed as two bright features corresponding to the expected location of the tilted pyrrole groups within the macrocycle (Fig. 72) and is likely a direct consequence of the buckled conformational structure (Fig. 69f).

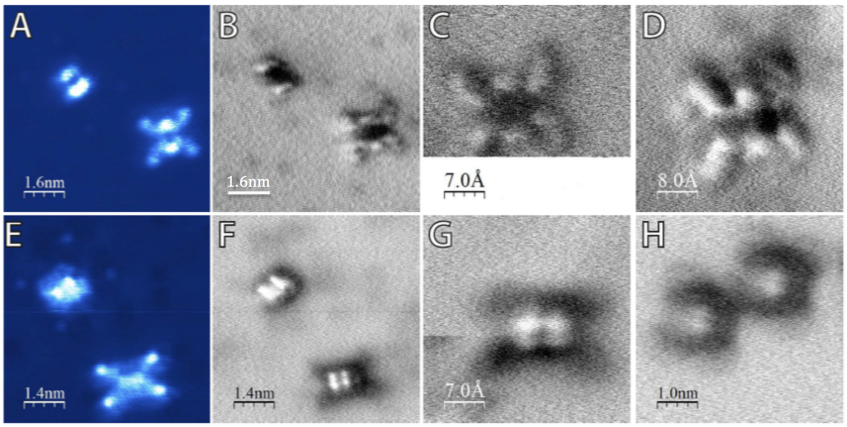

Figure 72: *Additional NC-AFM images of Br_4TPP conformers. A) Constant height current image of an intact and fully de-brominated Type 1 conformer. B) Corresponding frequency shift image. (C,D) Additional frequency shift images across different experiments showing similar structure. E) Constant height current image for intact and fully de-brominated Type 2 conformer. F) Corresponding frequency shift image. G,H) Additional frequency shift images showing similar core structure.*

Lateral force measurements

The lateral force required to move a molecule is directly related to its adsorption on the surface and the associated potential energy landscape. We therefore measured the lateral force required to displace each conformer during multiple manipulation events. By ensuring that the tip remained unchanged throughout the experiment, the forces for each conformer can be directly compared. We followed a similar protocol to Ternes *et al.* [90] where a two-dimensional map of Δf was measured as the tip was incrementally approached and scanned across the molecule in a fixed direction. After each trace, the tip was returned to its original location at an increased height to ensure that manipulation could only occur when the tip is moving in the desired direction (Fig. 73). Following collection of the two-dimensional map of $\Delta f(x, z)$ the long-range background was subtracted using an 'Off' spectrum and a conversion made to $U(x, z)$ [214] allowing the lateral, F_x, and vertical, F_z, forces to be calculated.

In Fig. 73b a typical manipulation experiment is shown where a Type 1 conformer is laterally translated with the NC-AFM tip by two lattice spacings. As described below, successful manipulation was generally only observed for metallic tips providing poorer STM resolution. To rapidly image large areas between manipulation events the molecules were scanned in constant current STM mode with the oscillating tip. During the manipulation, however, the bias voltage was reduced to 0V, minimizing the tunnelling current. We found that the Type 1 conformer could be translated along the $< 110 >$ and $< 211 >$ directions or in the directions 15°

off between the two (see Fig. 75). In all but two manipulation attempts the molecule is translated in the same direction as the NC-AFM tip trajectory. We note that tip trajectories matching the direction of the molecular diagonal (as shown in Fig. 73b) were significantly more efficient at translating the molecule than other directions, which would often cause undesired rotations.

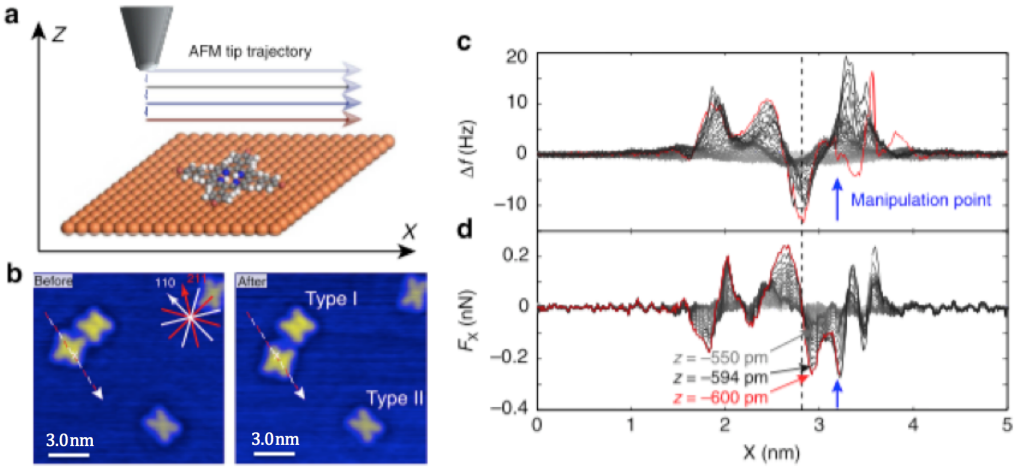

Figure 73: *a) Schematic demonstrating the manipulation protocol used to build a two-dimensional (2D) force-map. (b) STM images taken before and after manipulation of a single Type 1 molecule along a direction 15° off from the $< 211 >$ crystal direction. c) Overlaid line profile plot of the short range 2D Δf during manipulation. Darker line profile traces correspond to smaller tip-sample separations. Molecular manipulation occurs during the final trace at $z = 600pm$ (red line), marked by the blue arrow. The tip-sample separation (z) is defined relative to the initial Δf trace at $0pm$ (STM setpoint positioned on the molecule was at $z = 400pm$) d) Plot of the lateral forces obtained from the data shown in c).*

The recorded Δf map is shown in Fig. 73c as an overlaid line profile plot. At the point of manipulation we observe a jump in the Δf trace corresponding to translation of the molecule, marked by the blue arrow (white cross in Fig. 73b). To quantify the forces responsible for the manipulation we plot the corresponding F_x profile, as shown in Fig. 73d. By measuring

the value of F_x at the position marked by the blue arrow we observe that the manipulation occurred at the point of maximum attractive lateral force measured as -0.26(5) nN. The uncertainty in F_x is estimated from the uncertainty in the oscillation amplitude, which is assumed to dominate other potential sources of error such as the spring constant, and errors arising from the PLL control (see Fig. 74).

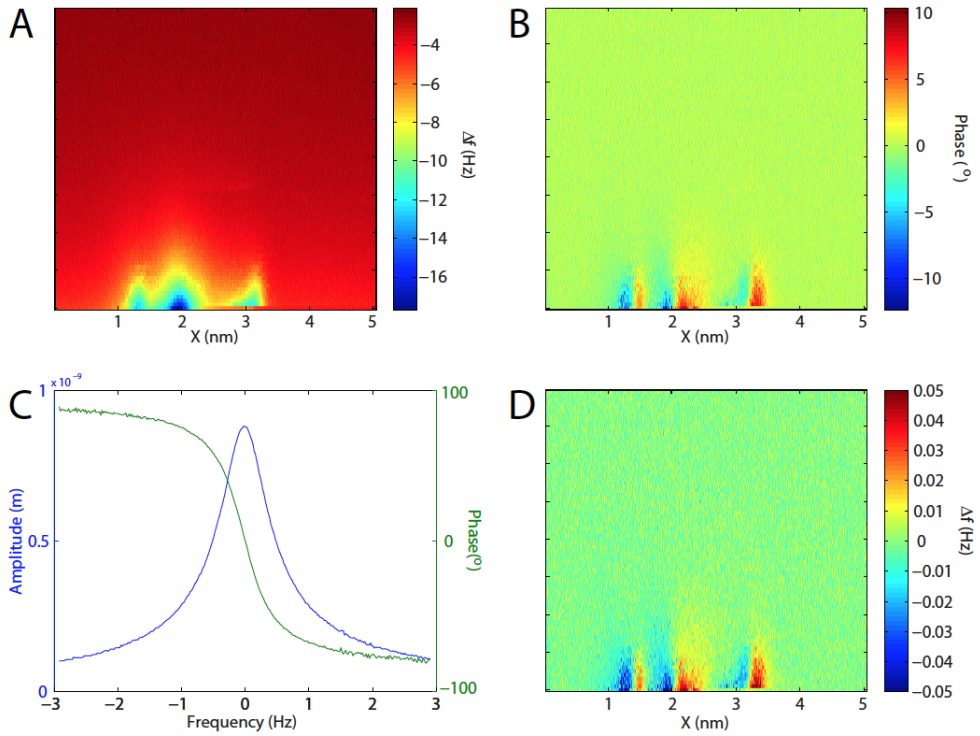

Figure 74: *Phase error analysis during lateral manipulation. A) Example Δf data during manipulation. B) Associated phase error. C) Frequency sweep taken for the tuning fork at free resonance. D) Approximated frequency error due to phase error calculated from C) [138].*

Several attempts at manipulation of the free molecule (Fig. 75F-L) resulted in translational motion and we obtained a range of F_x varying from -0.2 to -0.34nN, independent of the surface crystal direction, whereas the measured values of F_z varied from -0.25 to +0.7nN. Consequently, it seems highly

likely that lateral forces dominate the manipulation we report.

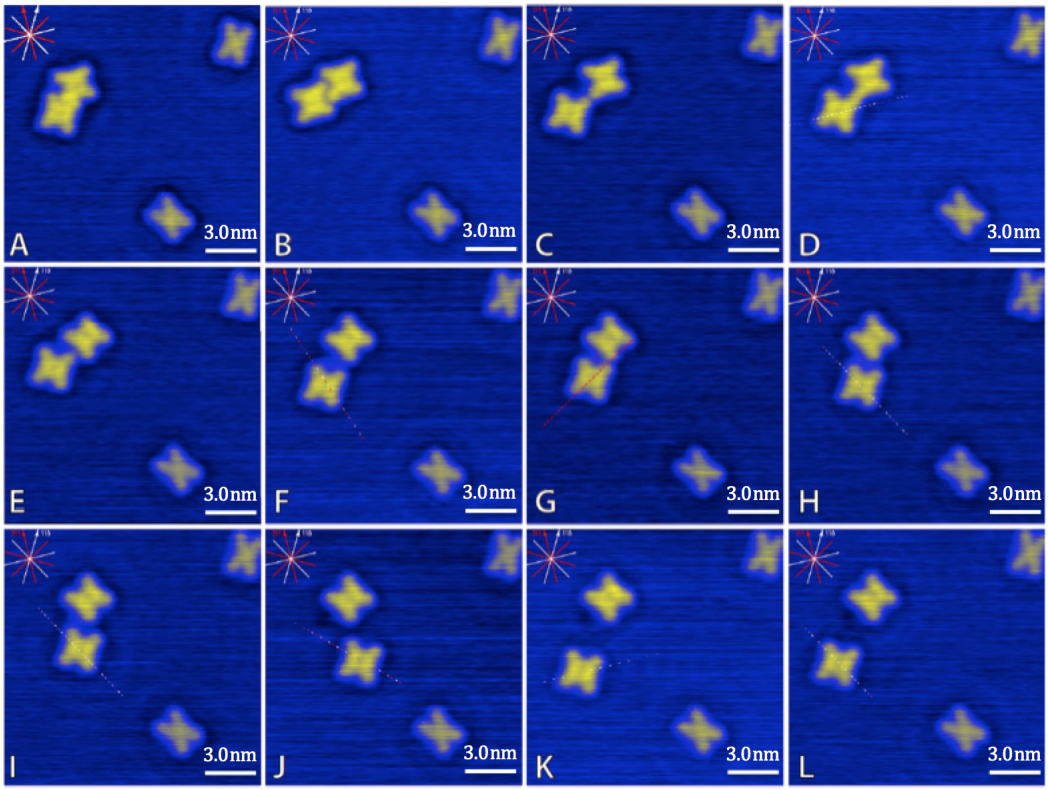

Figure 75: *Complete sequence of Type 1 conformer manipulations. After freeing the molecule in panels (A-E) the molecule was laterally translated seen times (F-L). White and red dashed lines indicate translation in* $< 110 >$ *and* $< 211 >$ *directions respectively, mixed red and white lines indicate translations 15° between the two crystal directions.*

Identification of manipulation mechanism

Further insight into the manipulation mechanism can be gained by examining extended manipulation events across several lattice sites. Figure 76a and 76b shows one such manipulation event, taken from the same experimental session, where the Type 1 conformer is translated seven lattice spacings along the $< 110 >$ surface direction. In Fig. 76c characteristic jumps are observed during the final Δf trace. These are separated by

$\sim$2.6Å corresponding to the Cu(111) atomic spacing that determines the adsorption geometry of both Br_4TPP conformers. Moreover, the manipulation trace exhibits the distinctive 'sawtooth' pattern often observed in STM experiments of adsorbate manipulation [243]. It is important to note that the frequency shift decreases in magnitude when the tip is positioned over an adsorbate (in contrast to the tunnel current). As such our data are interpreted as a distinctive 'pull' manipulation, in agreement with our extracted attractive lateral forces.

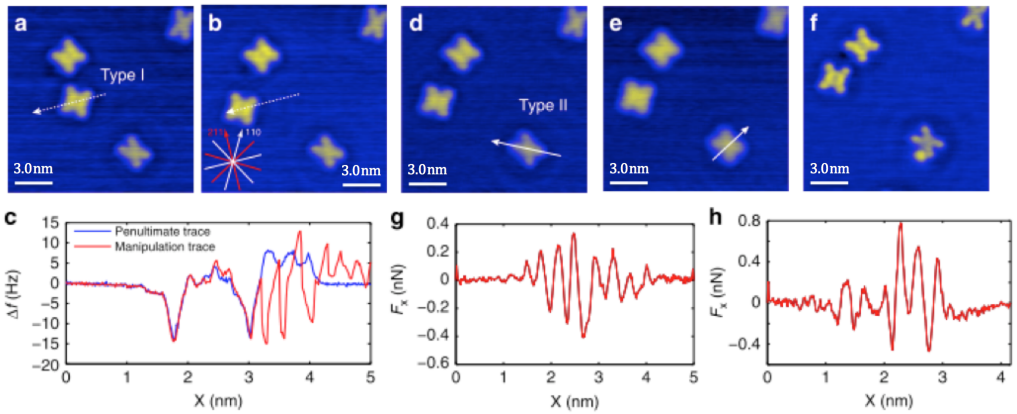

Figure 76: *Evidence for 'pull' manipulation and manipulation attempts. STM images recorded a) before and b) after long-range manipulation spanning several lattice sites. c) Δf line traces recorded immediately before and during manipulation. d-f) Manipulation attempts for a Type 2 conformer, taken during the same experimental session. The extracted lateral forces for d) and e) are shown in g) and for e) and f) shown in h). In each case the AFM tip is modified before the Type 2 Br_4TPP conformer could be manipulated. This is visible as a subtle degradation in image quality from d-e), and by the deposition of tip material from e-f).*

We observe, however, that not all manipulation traces show this behaviour, similar to reports on other molecules [92]. The assignment of a pulling mechanism is in agreement with previous work by Ternes *et al.*, who measured much smaller forces of 17 and 160pN for Co and CO, respectively,

also on Cu(111) [90]. Interestingly Langewisch *et al.* [91] report a pushing mechanism for PTCDA on Ag(111). However, their method differed in that the tip was only laterally approached up to the centre point of the molecule, potentially preventing the tip being able to pull the molecule at larger tip-sample separations.

Conformational dependence of lateral force

To measure the difference in lateral force required to manipulate the alternative Type 2 conformer we continued experiments using the same tip termination, once again across various crystal directions as shown in Fig. 76d-f. In this case, surprisingly, we were unable to instigate lateral manipulation without also incurring changes in the tip structure (Fig. 76d-f.). As a result, the lateral forces could only be extracted up until the point where a tip change was observed, thus providing a minimum value for F_x. Repeated measurements in a single experimental session produced values for F_x ranging from -0.3 to -0.7nN. In each experiment the tip was modified before the Type 2 conformer could be moved, even to the extent that tip material was deposited on the surface as in Fig. 76f. Example lateral force plots for Fig. 76d-e and 76e-f are shown in Fig. 76g and Fig. 76h, respectively. Based on the range of measured F_x we estimate that the threshold force for manipulation is 1.5-3 times greater for the Type 2 conformer as compared with the Type 1. It was shown previously in this chapter, that molecules are sometimes observed exhibiting a mixed conformation, with half of the molecule in the Type 1 arrangement and the other appearing as Type 2. Although attempts were made to manipulate such mixed con-

formers, they were found to be extremely unstable and always switched to an entirely Type 2 arrangement before manipulation could be achieved.

It should be noted that variations in tip structure between experiments can have a significant effect on measurements of F_x, in some cases resulting in values as low as 0.1nN for the Type 1 conformer. It has previously been shown that tip-induced barrier collapse is a key mechanism in atomic manipulation with NC-AFM [244, 245]. As a result we expect that the NC-AFM tip also strongly affects the barriers involved in molecular manipulation. Therefore it is only by taking multiple measurements for both molecular conformers with the same tip structure that we are able to directly compare the threshold forces for manipulation.

Repeated measurements for a range of unknown tip structures led to significant variation in tip stability. Successful manipulation was most commonly achieved for sharp tips, characterized by $|\Delta f|$ values $\leq$ 10Hz during dynamic STM measurements, Δf resulting in a success rate of $\sim$80% and $\sim$12% for the Type 1 and 2 conformers, respectively. This produced the range of forces described above. In addition, the most stable tip states- that is, those capable of repeated manipulations- generally produced lower resolution STM images (for example, the increased spatial resolution in Fig. 76f). Finally, many of the tip structures were unable to laterally manipulate the molecule. Instead, and despite following an identical manipulation protocol, molecules were often rotated, and in some rare cases switched between conformations. We propose that this behaviour can be explained by either metallic or molecularly terminated tips. Whereas it is known

that metallic tips can attractively 'pull' an adsorbed molecule, molecularly passivated tips are expected to have a significantly suppressed interaction, restricting them to 'push' type manipulations. Due to the large size of the molecule and the relatively high flexibility of the phenyl leg groups, we expect 'push' type manipulations are most likely to destabilize and rotate the molecule.

Calculated barriers for diffusion

In the DFT calculations a subtle interplay between the preference of the phenyl legs to sit closer to the copper and the increased strain of the molecular core ultimately leads to very similar values for the binding energy of each molecule, calculated as -4.1 and -3.9 eV for the Type 1 and 2 conformers, respectively. To understand the manipulation the energy barriers for molecular diffusion (using vdW-DFT and the nudged elastic band (NEB) method) were calculated. To facilitate comparison with experiment translations of each conformer in both the $< 110 >$ and $< 211 >$ directions between equivalent adsorption positions on the underlying Cu(111) surface were modelled. Ball-and-stick schematics, shown with the corresponding energy barriers for translation along the $< 211 >$ direction, are presented in Fig. 77a and 77b for the Type 1 and 2 conformer, respectively. From the calculations we determine barriers of $\sim$0.105eV and $\sim$0.170eV for the Type 1 and 2 conformers, respectively, corresponding to an approximate increase by a factor of $\sim$1.6. The energy barriers were found to be functional independent, with multiple dispersion-corrected functionals, showing similar increases in the calculated energy barrier. This is a clear indication that

the Type 2 conformer has a higher threshold for movement relative to the Type 1 arrangement, following the trend observed in our experiments.

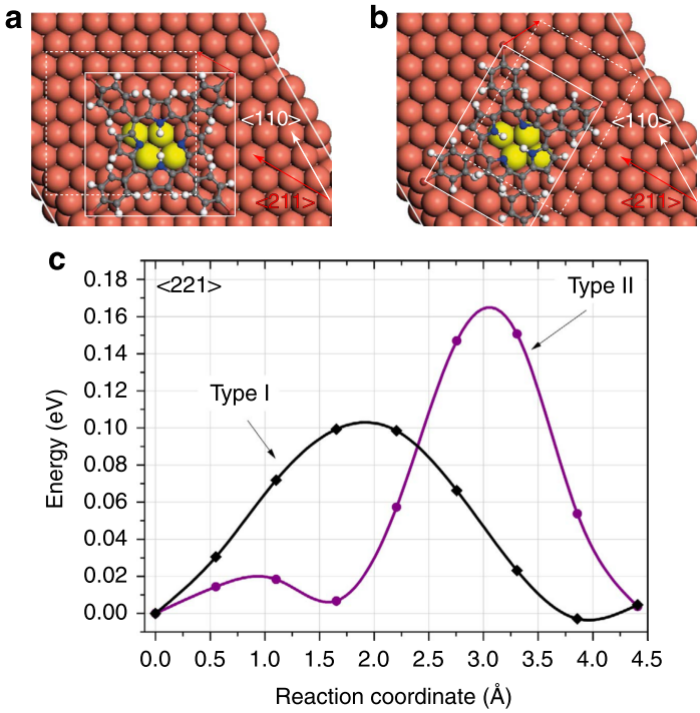

Figure 77: *NEB calculated energy barriers for translation. Calculated barriers for a) the Type 1 and b) Type 2 conformers along the* $< 211 >$ *surface direction. Ball-and-stick schematics a) and b) highlight the manipulation direction with the solid (dashed) box illustrating the initial (final) position of the molecule. Calculated energy barriers c) reveal a significantly higher energetic cost for translation of the Type 2 conformer. The reaction coordinate corresponds to the total distance that the molecule travels between the staring and final NEB point.*

The primary contribution to the vdW adsorption energy originates from the cumulative interaction between the atoms of the molecule with the surface copper. This is shown in Fig. 77 for the starting stable structures, where the phenyl and pyrrole rings predominantly occupy positions above copper bridge sites, maximizing the alignment of carbon atoms with the surface copper atoms, thus maximizing the vdW interaction. The variation

between conformers in the calculated barrier is therefore likely due to the increased distortion of the Type 2 conformer, which serves to reduce the degree of overlap between stable adsorption sites. In the calculations, the molecules show very little flexibility during translation. The importance of dispersion interactions has been highlighted in a number of recent reports [85, 246], where in some cases the adsorption was found to depend almost entirely on vdW interactions [247].

Due to the unknown nature of the NC-AFM tip a tip cluster was not included in the calculations, which instead models the diffusion of the free molecule on the Cu(111) surface. We are therefore unable to account for any potential difference in the interaction the tip might have from one conformer to another, which could play an additional role in modifying the energy barriers for manipulation. We also note that the small size of the calculated barriers imply that the molecules should diffuse at relatively low temperatures, despite experimental evidence confirming that the molecules are stable at 77K [51,76]. In addition to the known difficulties [84,248,249] in determining adsorption energies using vdW-DFT methods, this is potentially due to the absence of zero point energy corrections in the calculations, which has been observed to significantly increase the size of calculated diffusion barriers [250] for single pyrrole molecules (a major constituent of Br_4TPP). Unfortunately, however, due to the large size of the Br_4TPP molecule, zero point energy calculations are extremely costly and couldn't be performed. Consequently, making quantitative comparisons between experiment and simulation is challenging, and we instead compare the overall trends, which provide important insight into the manipulation process.

Our measurements for the Type 1 conformer show no clear variation in the lateral forces required for translation along the $< 110 >$ and $< 211 >$ directions. This observation is supported by additional NEB calculations along the $< 110 >$ direction which show almost identical barriers for diffusion along the $< 211 >$ direction shown in Fig. 78.

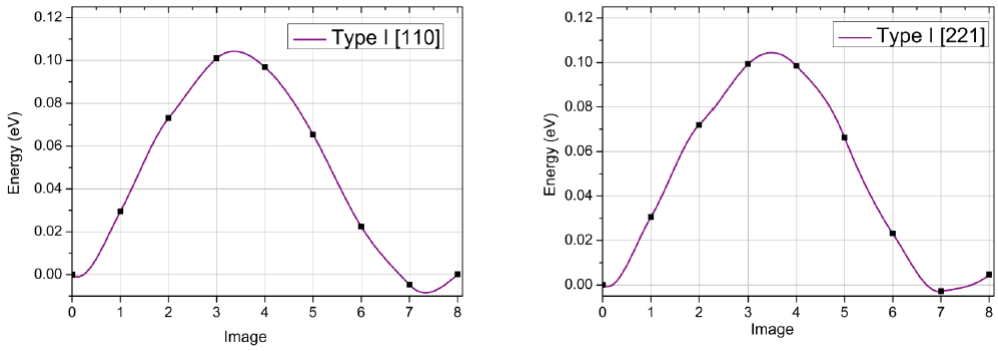

Figure 78: *Nudged elastic band energy barrier calculations for translation of the Type 1 conformer in the* $< 110 >$ *and* $< 211 >$ *surface directions [138].*

The similarity in the potential energy surface (PES) along each crystal direction is potentially due to the large vdW interaction between the Br_4TPP molecule and the Cu(111) surface which dominates the adsorption energy. In contrast, in single atom adsorbate motion, site specific chemical interactions are expected to have more directional dependence along the so-called 'hard' and 'easy' surface directions. In the case of the Br_4TPP molecule, the highest point of the barrier simply corresponds to the point of minimum alignment between the C and Cu atoms, that is, where the vdW interaction is weakest.

7 Using STM and AFM to probe empty C_{60} and $H_2O@C_{60}$

7.1 Results and analysis

7.1.1 Fullerene-induced Cu(111) surface reconstruction

A 30:70 ratio of $H_2O@C_{60}$:C_{60} was deposited onto a Cu(111) surface held at room temperature (prepared as described in the sample preparation section) for 45 minutes. The aim was to distinguish which molecules were encapsulated with H_2O and which were not, but this was complicated by the offset in apparent current (STM) and height (AFM) due to a fullerene-induced Cu(111) surface reconstruction.

Figure 79 shows a selection of STM images after the initial preparation of the $H_2O@C_{60}/C_{60}$ mixture on Cu(111) taken at 77K. There is both a suitable coverage across the surface for experimentation (as seen in Fig. 79a) and there is also enough Cu available for tip preparation.

It was possible to see particularly 'brighter' molecules in Figure 79b-f compared to some of the neighbours nearby, but this was caused by a reconstruction of the Cu(111) surface and not specifically the encapsulated water molecules.

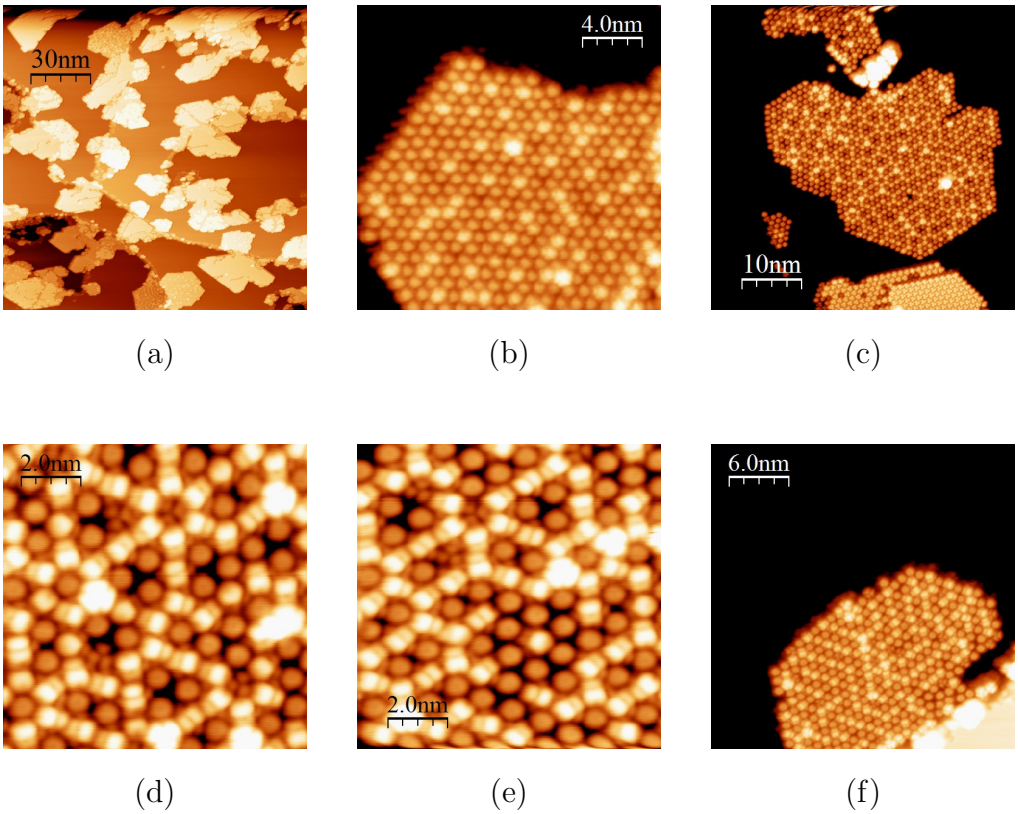

Figure 79: *(a)-(f) Array of STM images of a 30:70 ratio of $H_2O@C_{60}$:C_{60} on Cu(111). I=10pA, V=1.6V, T=77K.*

Figure 80 shows a direct comparison of STM line profiles with those of Pai and co-workers and both results indicate a reconstructed Cu(111) surface. Under initial inspection, it would appear as though a double layer of C_{60} is apparent in Fig. 80a. The difference of 2.1Å in 'double layer' heights however, is much smaller than the diameter of a C_{60} molecule. Pai *et al.* propose that this is due to a nucleated Cu island beneath the apparent 'double layer' C_{60}. The Cu step edge of 2.08Å in height, in comparison to the 7Å height of a monolayer C_{60} island, is strong supporting evidence for this proposal. The same explanation holds for the STM image in Fig. 80b where an apparent height of 2.1Å is shown for the $H_2O@C_{60}/C_{60}$ mixture, and the lower right line profile indicating the Cu island nucleation beneath

the molecule island, as opposed to another single layer of $H_2O@C_{60}/C_{60}$ mixture.

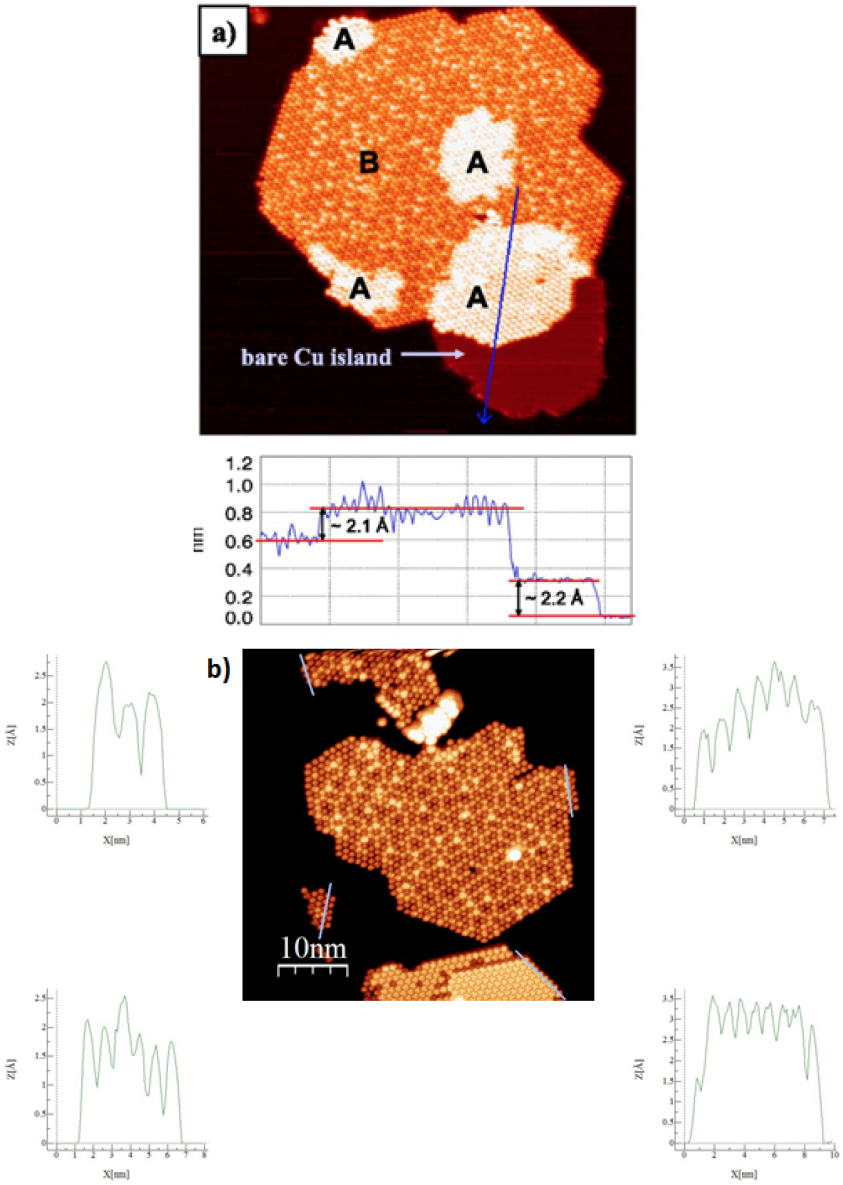

Figure 80: *a) STM image and line profile taken by Pai et al. showing the apparent height of the C_{60} molecules to be approximately 2.1Å b) STM image of the $H_2O@C_{60}/C_{60}$ mixture on Cu(111) with 4 line profiles taken showing a similar apparent height of the molecules to be 2.1Å . I=10pA, V=1.6V, T=77K.*

Figure 81 shows four metastable structures of a $H_2O@C_{60}/C_{60}$ mixture on Cu(111), each with their respective molecular contrast patterns. Fig. 81a is described as a linear-wall maze and b-d are disordered maze, p(2 x 2) and p($\sqrt{7}$ x $\sqrt{7}$) respectively.

Pai *et al.* explain that the linear wall and disordered maze phases are observed under annealing at 300-310K whereas the p(2 x 2) and p($\sqrt{7}$ x $\sqrt{7}$) appear at a slightly higher temperature of 310-330K. The equivalent metastable phases are observed for the $H_2O@C_{60}/C_{60}$ mixture on Cu(111) (with each respective ordering on the right hand side of the example from the literature). Pai and co-workers describe the four phases as a direct result of the C_{60}-induced reconstruction, due to the alteration of the competing C_{60}-C_{60} and C_{60}-Cu interactions.

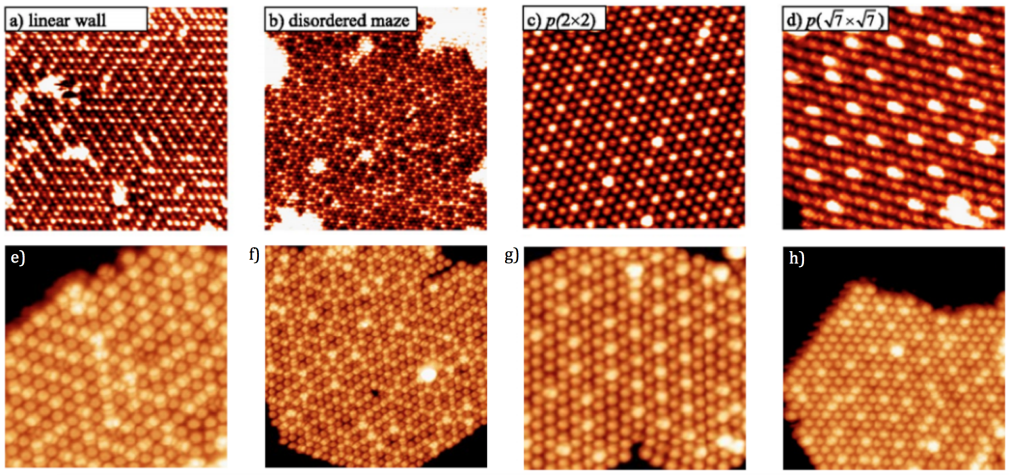

Figure 81: *a-d) Different adlayer networks of C_{60} on Cu(111) STM images taken by Pai et al. Each corresponding STM image taken by the authors has the equivalent networking pattern of the $H_2O@C_{60}/C_{60}$ mixture on Cu(111) below in e-h). I=10pA, V=1.6V, T=77K*

7.2 Blocking reconstruction

To eliminate the possibility of surface reconstruction, the deposition of the $H_2O@C_{60}/C_{60}$ mixture was therefore conducted with the Cu(111) sample held at 77K. It transpired that the coverage was sparse enough for tip preparation, however, the molecule islands were required to be larger in order to carry out reliable AFM measurements. In order to increase the island size, the sample was heated to 200K after deposition and then promptly returned to 77K; where trial and error showed that Cu(111) surface reconstruction was absent below 260K. With contrast differences apparent in the STM of the reconstructed Cu(111) data, an unreconstructed substrate is essential to note small differences in tip-molecule interactions and ultimately to determine whether we can distinguish $H_2O@C_{60}$ from empty C_{60} molecules.

7.2.1 Tip termination

In order to perform $F(z)$- and 3D grid- spectroscopy, it was quickly discovered that only a molecule-terminated tip was sufficiently stable to enable high resolution imaging. A reactive Cu-terminated tip led to an instability in $F(z)$ experiments on all occasions when the tip was pushed into the regime of positive frequency shift values.

After an extensive number of attempts, and trial and error, the tip was terminated with a $H_2O@C_{60}/C_{60}$ molecule by adhering to several crucial methods and parameters. Firstly, the tip was scanned in STM mode, and prepared via gentle "crashing" and bias voltage pulsing. The cantilever was then oscillated in D-STM mode so that the frequency shift could be

measured. $\Delta f \sim 0.5$Hz was seen on several occasions, however, *F(z)* spectroscopy was unstable using a molecule-terminated tip in such conditions. $\Delta f \sim 3-4$Hz prior to $H_2O@C_{60}/C_{60}$ tip termination was extremely stable (to as far as observing a $U(z)$ turn-around). The tip (in D-STM mode) would then be positioned above a single molecule in an island, the bias voltage reduced to 0V, and the tip moved toward the surface (in a $F(z)$ style experiment). A sharp decline in frequency shift (down to -25Hz) indicated the manipulation of the $H_2O@C_{60}/C_{60}$ molecule onto the tip. Once a molecule-terminated tip had been prepared, it was exceptionally difficult to render the tip unstable, and in some cases, a tip change was not experienced for days.

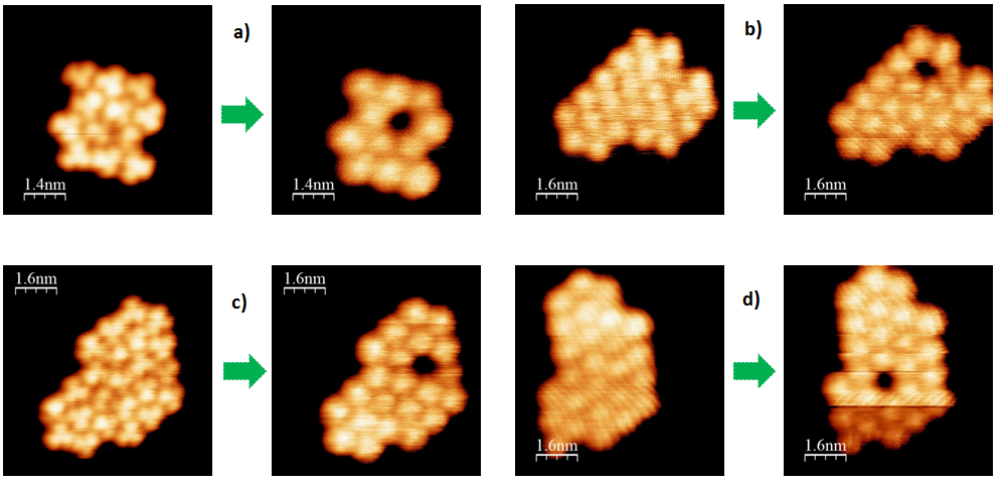

Figure 82: *a)-d) D-STM images showing scans before and after molecule-terminated tips.*

Figure 82 shows the D-STM results adhering to the methodology for acquiring a $H_2O@C_{60}/C_{60}$-terminated tip as described. The 'before' images in Fig. 82a and Fig. 82c clearly show a tri-lobe C_{60} STM characteristic, whereas the 'after' images show a far less resolved image with a molecule missing from the island. An induced mechanical noise is apparent in Fig.

82b and 82d, however, there is still clearly a molecule vacant from the island in both instances.

Figure 83 outlines two possible scenarios which could be occurring at the tip apex during molecule-termination. Fig. 83a shows a very sharp tip apex, where the frequency shift interaction between tip and surface would be very low (perhaps around the -0.5Hz that was seen in experiment), but upon molecule-termination, the tip becomes unstable when further interactions are experienced and the molecule moves further up the shank of the tip. In Fig. 83b the tip apex is slightly blunt, but a slightly higher frequency shift interaction is observed between tip and sample during tip preparation (around -3 to -4Hz).

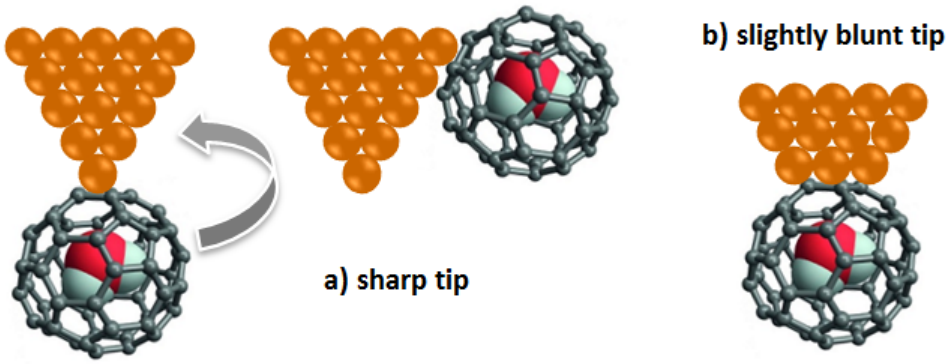

Figure 83: *A diagram showing two possible tip states during attempted molecule-termination. a) The tip has a very sharp apex, inferred as a very low frequency shift interaction between tip and sample during tip preparation. b) shows a schematic for one possible slightly blunt tip, (i.e. where the frequency shift is larger).*

This provides an ideal interface for stronger bonding of the $H_2O@C_{60}/C_{60}$ molecule once the tip is terminated. Of course, one cannot precisely tell the tip state prior or post tip-termination. Another possible scenario is

that the tip is very sharp, but the shank directly behind the outer most protruding atom is wide- this could also provide a region suitable for a stronger tip-surface interaction and ultimately provide a more stable tip once the molecule was at the apex.

It was only possible to observe a repulsive tip-molecule interaction (i.e. a positive frequency shift) once a molecule had been 'picked up' from the surface, and successfully terminating the tip with a $H_2O@C_{60}/C_{60}$ molecule sometimes took several days. A constant z image of an island of molecules was then scanned in order to minimize the tunnel current (or to get as close as possible to the true zero bias voltage). If the tunnel current was not minimized, then this could cause very strong tip-molecule interactions once pushing in close to the sample, it was also acceptable from this point, assuming the tip was stable and the tunnel current was minimized, to carry out $F(z)$ spectroscopy.

7.2.2 $F(z)$ spectroscopy

$F(z)$ spectroscopy was taken over a single $H_2O@C_{60}/C_{60}$ molecule following a molecule-terminated tip. The tip was oscillated at $a_0 = 300$pm (with an integration time of 50ms unless stated otherwise). 'Off' spectra were taken away from the molecules, over the Cu surface in order to subtract the long range force interactions from the total force spectra. This, in theory, should leave only the short range $F(z)$ interaction between the molecule at the end of the tip and the molecule on the surface. All $F(z)$ spectroscopy was carried out at 5K to minimize thermal drift. This technique was also used as a firm test for a stable tip prior to setting up a 3D grid spectroscopy.

Hundreds of spectra were taken to compare the differences in force turnaround between molecules. Of course, there were some situations where the tip became unstable and that data would be useless, especially if there were tip changes leading up to the final instability.

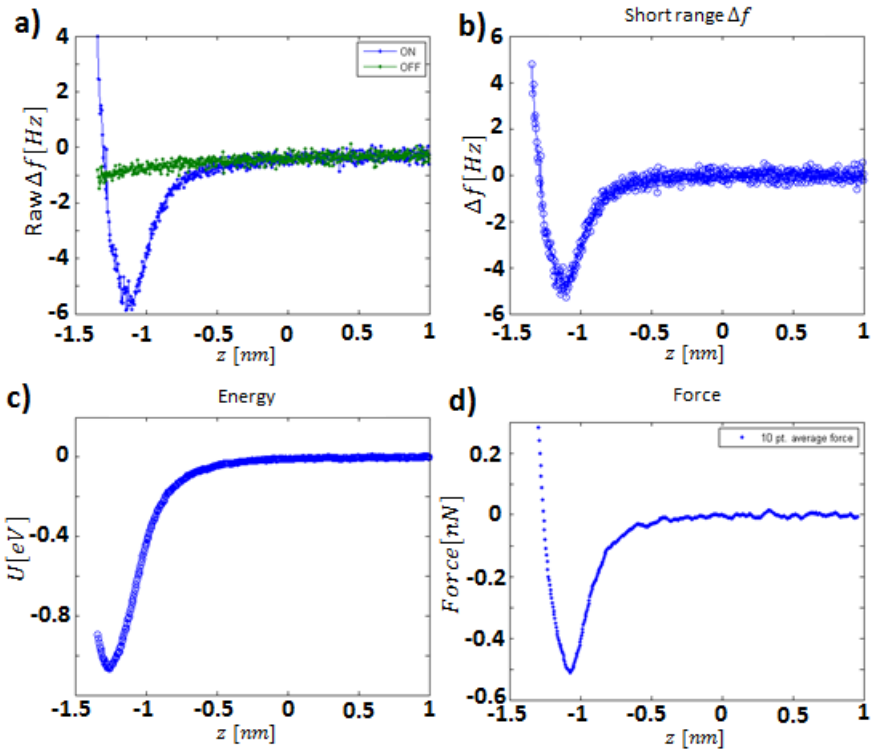

Figure 84: *a) Total frequency shift (On) and long-range frequency shift (Off). b) Short range frequency shift component (On-Off= short range Δf). c) Energy of interaction as function of z. d) Sader-Jarvis algorithm processed force interaction.*

Figure 84 shows typical force spectroscopy data with a molecule terminated tip interacting with a molecule on the surface. A maximum attractive force of ~ -0.5-0.6nN was seen in around 90% of the data (the other 10% being unreliable due to unstable tips). Data were only considered when an adequate turnaround was seen in the energy-distance graph (shown in Fig. 84c). It was hoped that the experimental $F(z)$ data would show precisely

30% of force-distance turnarounds at a stronger magnitude, however this was, disappointingly, not the case.

Figure 85 shows signature occurrence in the force spectroscopy data when a molecule from the surface jumps onto the tip. In Fig. 85a and 85b there is a sharp jump in Δf from -10Hz to -35Hz.

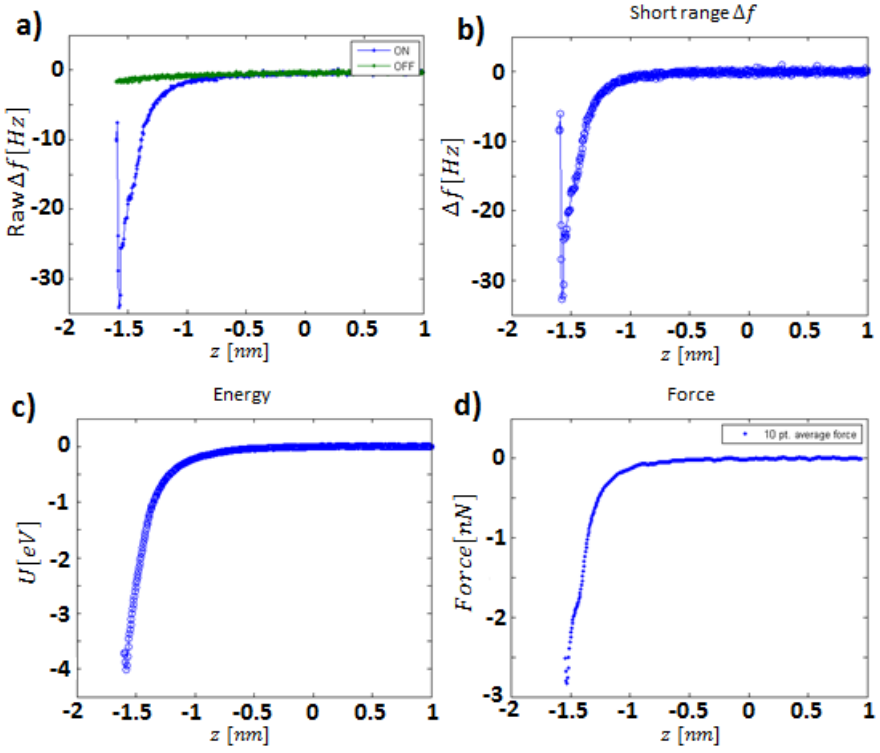

Figure 85: *a) Total frequency shift (On) and long-range frequency shift (Off). b) Short range frequency shift component. c) Energy of interaction as a function of z. d) Sader-Jarvis algorithm processed force interaction.*

This could be due to a possible Cu coated tip interacting with the encapsulated molecule, where post termination, there is a sharp decrease in attractive interaction because there is now a gap where the molecule was on the surface.

7.2.3 3D force mapping

It was then decided to carry out a 3D force map of an entire island in a bid to observe subtle differences in force interaction between $H_2O@C_{60}/C_{60}$ molecules. 3D grid spectroscopy measurements were carried out at 5K on small islands of $H_2O@C_{60}/C_{60}$ molecules, as shown in Figure 50. The scan area was sectioned into a 35 x 35 point grid, i.e. 1225 $F(z)$ spectra points. The z distance was split into 512 equidistant points, so force interaction 'slices' could be extracted.

All of the previous methods described in the previous sections (i.e. terminating the tip with a molecule, offsetting the bias voltage in constant z AFM, checking for tip stability) were necessary to set up the grid spectroscopy measurements. The experiments took a total of 19 hours each.

Figure 86 shows three slices in the x-y plane of a 3D grid spectroscopy experiment over a $H_2O@C_{60}/C_{60}$ island. The left image shows no force interaction at a relative z height of 0pm. The central image show some interaction but there are no special cases where an individual molecule is more or less interactive than the others. The image on the right shows the maximum attractive and repulsive interactions during the experiment. despite repeating this type of force spectroscopy measurement multiple times, we did not see a reliable (and statistically robust) difference between molecules. This strongly suggests that NC-AFM, like STM, is not capable of detecting the encapsulated H_2O molecule, and further evidence is apparent in the XPS chapter (i.e. similar valence band structure for both empty and filled C_{60}).

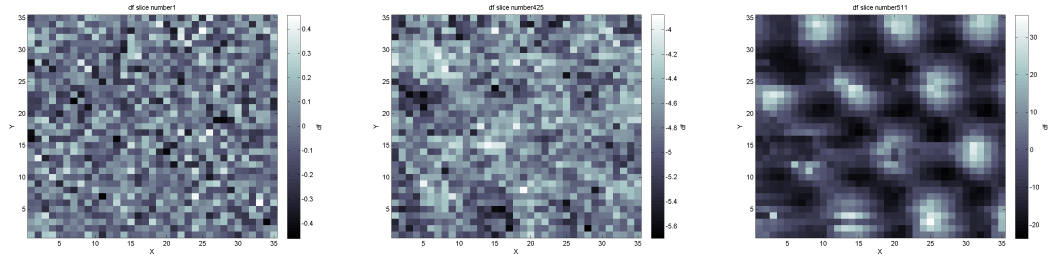

$z = 0$ $z = -1100pm$ $z = -1570pm$

Figure 86: *3D grid spectroscopy slices taken at three different relative z heights, decreasing from left to right above a $H_2O@C_{60}/C_{60}$ island.*

7.3 Intermolecular artifacts in probe microscope images of C_{60} assemblies

7.3.1 Simulation details

To simulate NC-AFM images, Rashid adapted the flexible tip method as previously reported [151, 156] to model the interaction between a sample and either a CO or C_{60}-functionalized probe. The functionalized tip is assumed to consist of a tip base (outermost atom of the metal tip) and a probe particle. The probe particle is the flexible end of the model tip and is allowed to move around the tip base. The probe particle experiences three forces: (i) due to the tip base, (ii) a sum of all pairwise forces due to interactions with atoms in the sample, and (iii) a lateral harmonic force from the tip base. In the case of a C_{60}-functionalized tip, the C_{60} molecule is taken to act in the same way as a single effective probe particle, similar to the CO tip. The parameters for the 'inter-atomic' (Lennard-Jones) potentials were chosen to take into account that the probe and tip base are not actually single atoms.

7.3.2 Results and discussion

Figure 87b shows a possible situation where intermolecular 'hydrogen bonds' are apparently seen in real-space. In this case, however, the molecules and the intermolecular strands are somewhat less defined than seen in the literature. This could be a situation where the $H_2O@C_{60}/C_{60}$ molecule on the tip apex is interacting so strongly with the $H_2O@C_{60}/C_{60}$ island, that there is a considerable amount of physical compression of either the tip-bound molecule or the molecules on the surface.

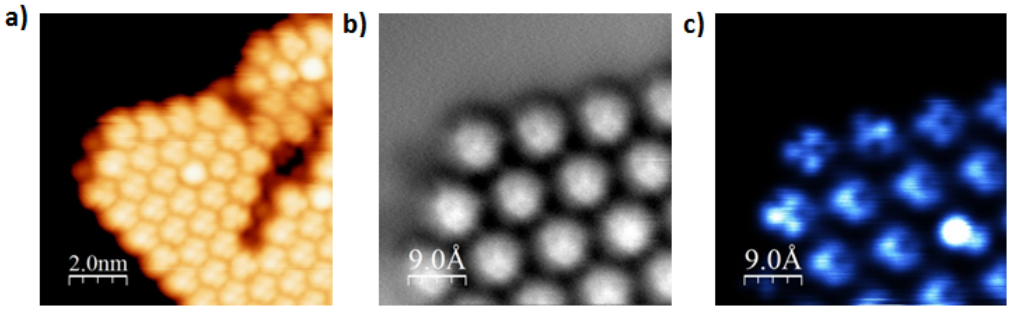

Figure 87: *a) STM image of a large island of $H_2O@C_{60}/C_{60}$ with sub-molecular contrast. b) Constant z image of the island in (a) (far left corner) with maximum frequency shift of +8Hz and -4Hz. c) Equivalent current channel data from the constant z data in b) but with no bias voltage offset.*

Such an interaction could cause 'hydrogen bonding' imitations between $H_2O@C_{60}/C_{60}$ molecules in the island. This result is interesting because there are no hydrogen bonds within the system that could cause such an apparent feature. This leads us to believe there is evidence to support a tip artifact causing the apparent "connection" between neighbouring molecules.

In Figs. 88a and 88b we show NC-AFM frequency shift images of islands of $H_2O@C_{60}/C_{60}$ on the Cu(111) surface and C_{60} on a C_{60}-terminated Si(111) surface (i.e., the substrate is a monolayer of C_{60} chemisorbed on Si(111), on

which there are physisorbed C_{60} islands, taken by Sweetman), respectively, recorded in the constant height mode at small tip-sample separation.

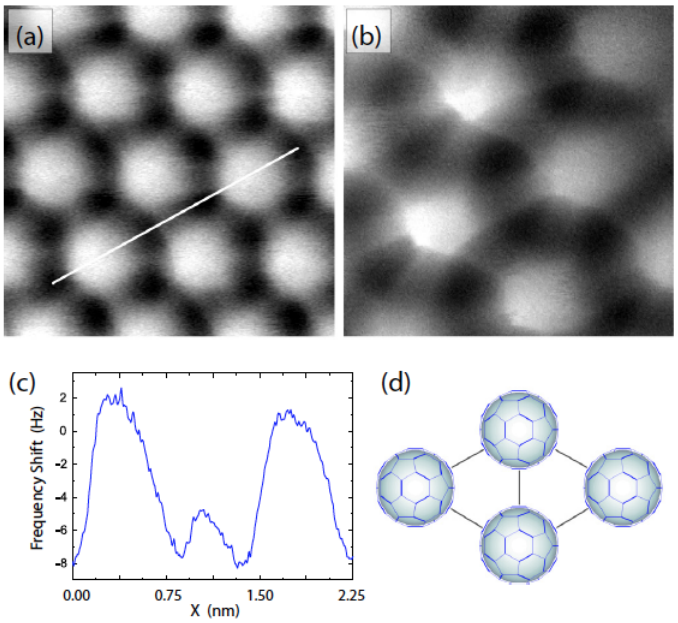

Figure 88: *Apparent intermolecular features. NC-AFM frequency shift images of a 2D assembly of a) a thick (six-layer) film of $H_2O@C_{60}/C_{60}$ and b) C_{60} molecules recorded in the constant height mode, revealing interconnecting features between nearest neighbour molecules. c) Line profile measurement along the white line shown in a). d) Schematic of the C_{60} packing arrangement and locations of apparent intermolecular features. Parameters: a) image size: 3.2x3.2nm, oscillation amplitude: a_0= 300pm; b) image size: 2.3x2.3nm, oscillation amplitude: a_0 = 110pm.*

At these distances, repulsive contributions to the tip-sample force dominate the observed contrast resulting in the fullerene molecules appearing brighter (less negative Δf) relative to the vdW background. This results in the clear appearance of the hexagonally packed arrangement of the fullerene molecules with a nearest neighbour separation of ∼1nm. Despite this large separation, in addition to the intramolecular structure observed within the individual fullerenes [228, 251, 252], clear interconnecting features are observed between each nearest neighbour molecule taking on a similar ap-

pearance to previous reports examining hydrogen bonded molecules. This is highlighted in the schematic shown in Fig. 88d and the line in Fig. 88c, where, on average, the corrugation due to the molecule itself appears ∼3-8 times brighter than the interconnecting features [253]. Both empty and filled C_{60} cages produce such similar contrast in our images, which suggests that observations of interconnecting features are general across fullerene molecules.

In order to better characterize the tip-sample interactions responsible for the artifactual intermolecular contrast, the measurements were repeated at various tip-sample separations. Figures 89b-e show a sequence of constant height frequency shift images acquired for a single layer island of C_{60} molecules deposited onto a thin film of NaCl grown on Cu(111), where the tip-sample separation was slowly reduced over the course of several hours.

The preceding constant height current image shown in Fig. 89a reveals that the island is made up from C_{60} molecules of mixed orientation forming a (2 x 2) superstructure [254]. As the tip-sample distance is reduced, attractive vdW interactions cause the C_{60} molecules to initially appear as dark depressions as shown in Fig. 89b, corresponding to a more negative frequency shift relative to the background signal. At smaller tip-sample distances, as shown in Fig. 89c, the emergence of intramolecular structure is observed within each C_{60} molecule due to the onset of repulsive interactions beyond the force interaction turnaround. Finally, at very small tip-sample separations shown in Fig. 89d and 89e, apparent intermolecular features are observed.

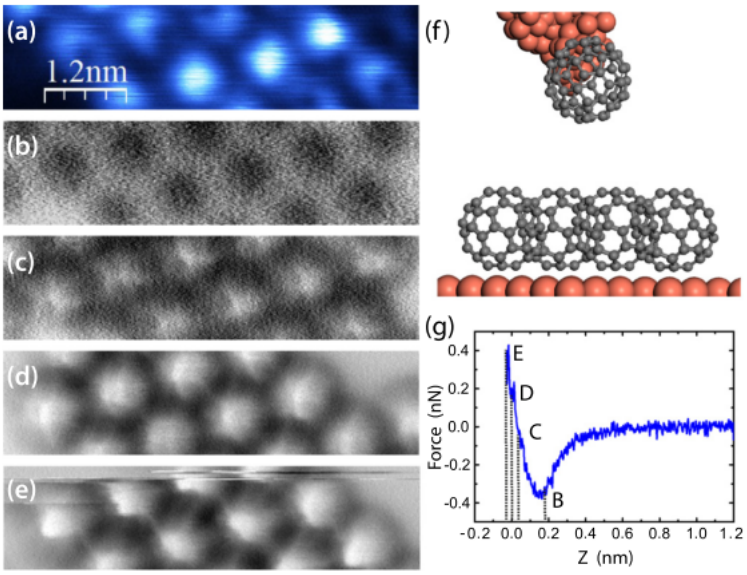

Figure 89: *a) Constant height current image of a C_{60} island prior to NC-AFM measurements (recorded at +500mV sample bias). b-e) Progression of constant height frequency shift images with decreasing tip-sample separation (recorded at 0V sample bias and oscillation amplitude: a_0 = 300pm). In b) the C_{60} molecules appear dark due to attractive vdW interactions; in c-e) the molecules appear bright due to the onset of tip-sample repulsion. Clear apparent intermolecular features are again observed in e). f) Illustrative and schematic diagram of experimental setup. Note that we show a single C_{60} molecule bound to the tip apex. It is more likely that the tip apex is covered with a number of C_{60} molecules. g) Measurement of F(z) recorded above the rightmost surface C_{60} molecule. The peak attractive force of -0.34(6) nN suggests that the NC-AFM tip is C_{60} terminated.*

Compared to the image shown in Fig. 88a, the interconnecting features observed in Fig. 89e show an asymmetry in their appearance, either appearing as single or two parallel lines, strongly suggestive of an asymmetric tip-sample interaction potential. We note that the appearance and symmetry of the intermolecular features showed no dependence on the underlying sample substrate used to support the C_{60} molecules, which is instead determined by changes in the tip structure. In addition, compared to Fig. 88c and 88d the intramolecular contrast is reduced, to the extent that it

is almost no longer observable. This is similar to observations made by Hämäläinen *et al.* [152], who note that at small tip-sample distances tip flexibility can start to 'level out' the Δf signal limiting the spatial resolution. The small tip-sample distances necessary to observe the apparent intermolecular features can also result in significant restructuring of C_{60} islands, as observed in the top part of the scan in Fig. 89e. At larger tip-sample separations, Fig. 89a-c, the locations of the C_{60} molecules remain unchanged, whereas in Fig. 89d and 89e the C_{60} molecules at the left and right edges of the island begin to move. This culminates in the complete destruction of the island in the image immediately following Fig. 89e, as the tip-sample interaction becomes so great that the entire island was swept away (often accompanied by molecules being transferred to the tip). This is consistent with the weak intermolecular interactions within the C_{60} layer.

Although intramolecular features are observed within each C_{60} molecule, the features are not as clear compared to experiments where a well defined CO tip termination revealed the atomic structure of the cage [135], suggesting a more complicated tip-sample convolution. In the experiments described here, no deliberate tip functionalization, either with CO or any other small molecule, takes place. We instead expect that the scanning probe is terminated by a C_{60} molecule picked up from the sample surface, either directly onto the metal tip or, more likely, onto a cluster of accumulated C_{60} molecules. From an experimental perspective, this is partly motivated by the relative ease with which the molecular islands can be disturbed during scanning in both STM and NC-AFM modes, where we often observe the disappearance of single C_{60} molecules following controlled $I(z)$

or $F(z)$ measurements, but also the relatively consistent appearance of the molecules on each of the four sample substrates we used (two of which were multilayer C_{60} samples). Moreover, in some instances immediately following measurements on C_{60}, we carried out experiments on a clean Cu(111) substrate (in order to recover the tip) where molecular deposition from the tip onto the surface was repeatedly observed.

Quantitative measurements of the force interaction between two molecules [228, 255, 256] can also provide insights into the tip termination. For C_{60} in particular, the pair potential between two molecules can be measured [228] and compared to the analytical Girifalco potential [257]. $F(z)$ measurements taken with the same tip as that shown in Fig. 89 show a maximum attractive force ranging from -0.32 to -0.36nN, an example of which is shown in Fig. 89f. (We stress, however, that there are pitfalls in using 'signature' values of maximum intermolecular force/potential energy to characterize the tip apex as different tip apices can often give rise to similar force curves.) Nonetheless, the average maximum attractive force value of 0.34(6) nN is similar to previous reports where a C_{60}-terminated tip was used, and also falls within the range expected due to the orientation dependence of each C_{60} molecule[2]. It is also worth noting that Gross *et al.* measure a 100pN maximum attractive force for a CO molecule interacting with a C_{60} molecule [258]. Consequently, although we cannot eliminate the possibility of alternative tip terminations, it is likely that the contrast we observe is due to a C_{60} molecule terminating the tip apex. The simulations described below provide strong support for this assertion.

[2]The error in force is estimated from the uncertainty in the oscillation amplitude, which dominates other potential sources of error.

In order to interpret the experimental data, and, in particular, to elucidate the origin of the artifactual intermolecular contrast, Rashid simulated constant height NC-AFM images of a C_{60} island using the simple Lennard-Jones model described above using three different tip terminations. In addition to modelling the flexible CO tip used by other groups [151, 152, 156, 157], both flexible and rigid probe particles using a radius of 5Å in order to approximate a C_{60}-terminated tip were tested. Simulated images of the tip-sample force resulting from these three tip terminations are shown in Fig. 90 at different tip-sample separations.

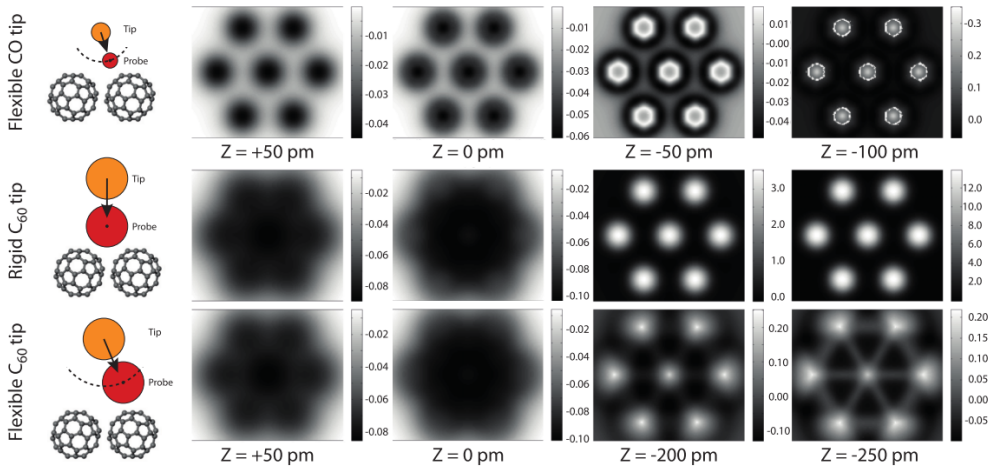

Figure 90: *Simulated NC-AFM images using a flexible Lennard-Jones tip model. (Top) Force images of an island of seven hexagon-up orientated C_{60} molecules modelled using a flexible CO probe particle at decreasing tip-sample separations. At z =-50 pm the hexagonal face of the molecules can clearly be observed. Force images of the same island were also modelled using a large probe radius of 5Å representing a C_{60} terminated tip maintained in either a fixed geometry (middle) or allowed to relax (bottom). While internal features can no longer be resolved due to the large probe radius, clear interconnecting features can be seen for the flexible C_{60} tip model. Smaller tip-sample z heights are shown for the large probe radius tip due to a shallower force profile arising from the choice of Lennard-Jones parameters. The colour scale shown is in nN for all images [253].*

Whereas the flexible CO-tip model clearly resolves the internal atomic structure of each C_{60} molecule within the island, revealing the hexagonal face at $z = -50$pm, interconnecting features between the fullerenes are absent, even at very small tip-sample distances. Similarly, despite using a much larger probe particle radius, simulations using a rigid 'C_{60}' probe also fail to resolve interconnecting features. Only when the large radius probe is allowed to relax do clear interconnecting features, akin to those observed in experiment, appear in the simulations.

Just as was found for the experimental images shown in Fig. 89, the interconnecting intermolecular features only become visible in the simulations at tip-sample distances below ~ -200pm (relative to the force turnaround), past the point at which repulsion is observed within the individual molecules. Surprisingly, even at very small tip-sample separations, interconnecting features are never observed in the fixed C_{60} simulation with the centre point between molecules always appearing as the point of minimum force.

This is surprising, as one of the important effects of the flexible tip model is usually to 'normalize' the intramolecular and intermolecular contributions to the image such that they appear with similar brightness. For instance, at a tip height of $z = -200$pm the fixed C_{60} simulation reveals forces over an order of magnitude greater over the molecule compared to the flexible tip. This confirms that it is only with the combination of both a large radius C_{60} tip and the flexible junction (which we attribute to the weakly bound nature of a single C_{60} at the apex of a molecular tip-cluster) that

interconnecting features can be observed.

It should also be noted that the simulations do not have periodic boundary conditions in place. Thus, it is only the molecule at the centre of the cluster which is associated with a sixfold symmetric potential. The six molecules at the edges of the cluster do not have neighbours, and so the tip-sample interaction potential lacks the same symmetry. The effects of this symmetry-breaking on the images is manifested in two ways. First, the thickness of the intermolecular 'bonds' is different between molecules at the edge of the cluster as compared to the features connecting the centre molecule to its neighbours. Second, the shapes of the molecules themselves differ. Each of the six molecules at the edge of the cluster has a triangular shape, as compared to the much more circularly-symmetric appearance of the centre molecule. As noted above in reference to Fig. 89e, we also see variations in intermolecular contrast along different crystallographic directions in the experimental NC-AFM images within a molecular island. For the experiment, the symmetry is broken not by the surface-adsorbed molecules but by the tip, raising the very intriguing possibility that intermolecular contrast could be exploited to characterise the symmetry of the tip apex.

The success of the flexible tip model, both here and in other papers [151, 152, 156, 157], makes it tempting to ask whether any bond, intermolecular or internal to the molecule, is ever directly imaged in NC-AFM. Even though Lennard-Jones potentials are only a crude approximation of the real electronic density of the molecules, the success of the model sug-

gests that if the overlap of spherical potentials, coupled with the flexibility and finite size of the probe, is sufficient to reproduce the contrast between the atoms, then it is not immediately apparent to what extent the (real) electronic density within a bond contributes to the contrast or whether the experimental images might also be dominated by the electronic density centred over the atoms.

8 Using LEED, XPS and XSW to probe $H_2O@C_{60}$

8.1 Low energy electron diffraction

8.1.1 Preliminary results and analysis

The presence of an adsorbate on the surface, in this case, $H_2O@C_{60}$ on Ag(111), produces a superlattice that often has a lattice constant greater than that of the substrate. A periodic structure composed of two layers of different materials means further LEED spots arise in addition to the original LEED pattern. The width of the LEED spots and the brightness of the background are related to the size of the ordered patches at the surface compared to the coherence length of the electrons. The coherence length tends to be ∼10nm so if the ordered patches are of this diameter or larger the intensity of the spots from each patch add together, resulting in bright, narrow spots. On the other hand, if the ordered patches are smaller than the coherence length, then there's a lot of inelastic scattering giving rise to broader spots and a more intense background, resulting in broad, less intense spots.

A significantly lower electron beam energy is required to observe diffraction spots for molecular overlayers, and due to a high surface sensitivity using LEED, the structure of the $H_2O@C_{60}$ molecules adsorbed on the surface can be observed. Electrons with energy in the range of 20-200eV have a penetration depth of around 10Å which makes LEED a very surface sensitive technique, certainly in comparison to x-rays, which have a larger mean

free path (order of μm).

Figure 91 shows the LEED patterns of two different Ag(111) single crystals which were carefully cleaned using repeated argon ion sputtering and annealing cycles. Both Fig. 91a and Fig. 91b show 6 bright spots representing the Ag(111) hexagonal unit cell. Figure 91a shows each diffraction spot to be elongated, which indicates a poor long-range order and surface structure. Figure 91b shows sharper and more circular spots, suggesting that this single crystal Ag(111) is a *much* higher quality choice for experimentation with a higher degree of surface order.

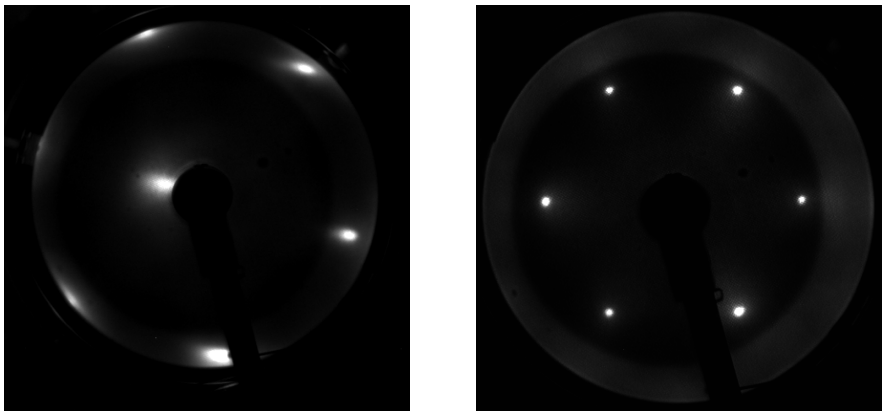

(a) (b)

Figure 91: *LEED patterns for two different single crystal Ag(111) surfaces. Both crystals were carefully cleaned using repeated sputter and anneal cycles. a) LEED energy 51.6eV and b) LEED energy 121.5eV. Crystal a) is a much poorer crystal than b) in quality.*

Figures 92a and 92b shows the LEED pattern for monolayer $H_2O@C_{60}$ on Ag(111) and clean Ag(111) respectively. The hexagonal unit cell of the Ag(111) substrate cannot be apparent due to the spots moving much further out when traversing from 121.5eV to 16.5eV. The extra bright spots are explained by the $(2\sqrt{3}$ x $2\sqrt{3})$R30° structure according to the litera-

ture [104]. The clarity and sharpness of the additional spots suggests a high ordering of $H_2O@C_{60}$. If the adsorbed molecules had a low rotational order, the extra diffraction spots would be elongated and a lower intensity, as previously mentioned. A dimmer Ag(111) diffraction pattern is also indicative of adsorbates on the surface, the diameter of the $H_2O@C_{60}$ is known to be approximately 7Å which is close to the limited mean free path of 10Å for electron diffraction.

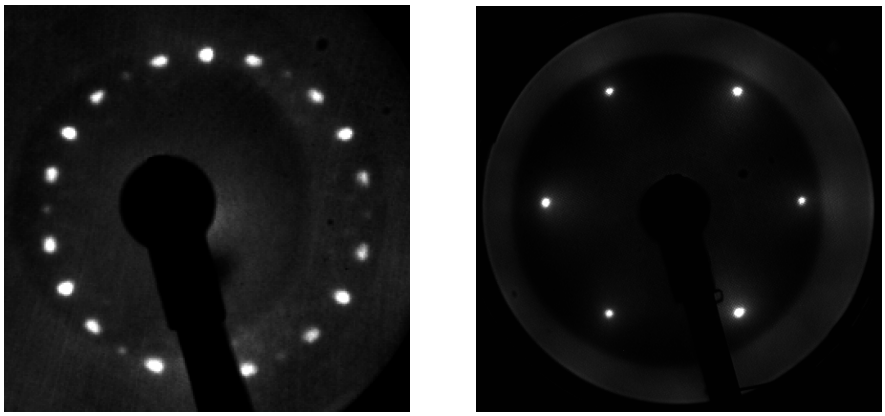

(a) 16.5eV (b) 121.5eV

Figure 92: *a) LEED pattern for monolayer $H_2O@C_{60}$ on Ag(111). b) Clean Ag(111) surface.*

Figures 93a and 93 b show the diffraction patterns for $H_2O@C_{60}$ and C_{60} on Ag(111) respectively. The literature states that annealing C_{60} on Ag(111) converts metastable epitaxially rotated phases to the $(2\sqrt{3}$ x $2\sqrt{3})$R30° structure [103, 260]. The central spots in Fig 93a are comparable to those in Fig. 93b (with a much poorer contrast), which could suggest the LEED pattern observed is a $(2\sqrt{3}$ x $2\sqrt{3})$R30° structure, as shown in Fig. 93c.

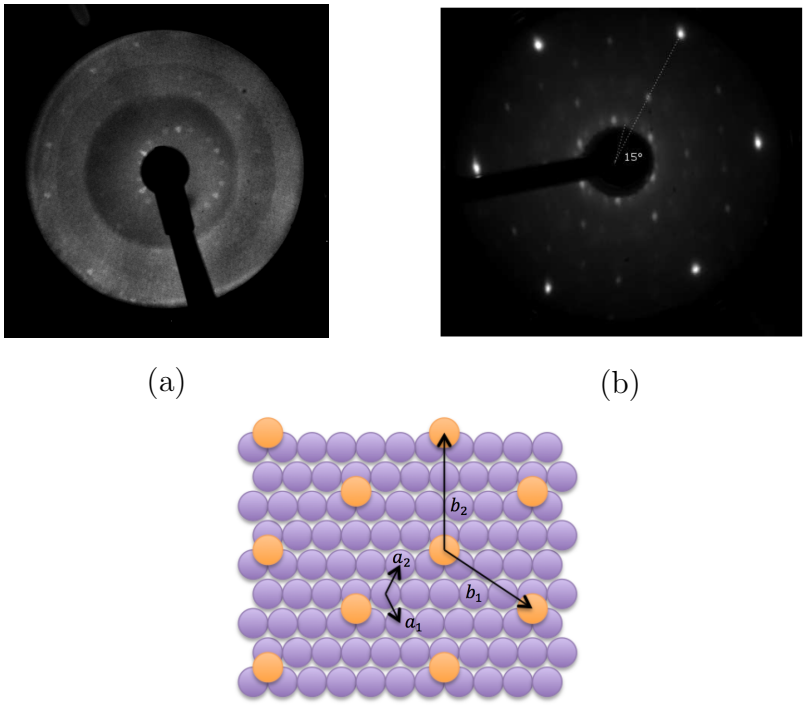

(a) (b)

(c)

Figure 93: *a) (not centered) LEED pattern for monolayer $H_2O@C_{60}$ on Ag(111) taken at 48.6eV. b) LEED pattern of C_{60} on Ag(111) taken at 47eV showing inner spots at 15° to the Ag(111) lattice, from [259]. c) $(2\sqrt{3}$ x $2\sqrt{3})R30°$ illustration.*

Figure 94 shows the LEED pattern of the C_{60} on Ag(111) $(2\sqrt{3}$ x $2\sqrt{3})$R30° structure at energies of 101eV, 365eV and 504eV.

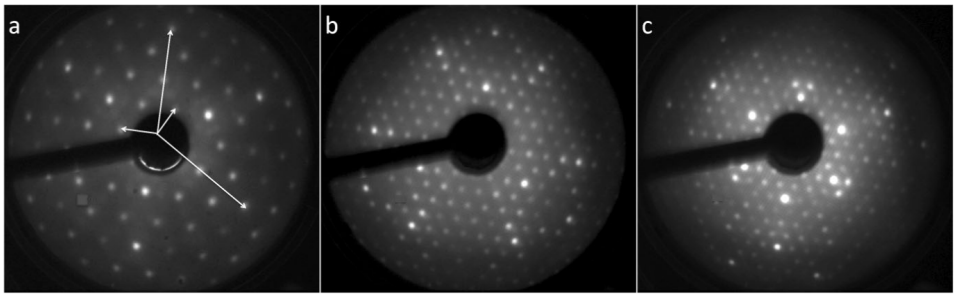

Figure 94: *LEED patterns of C_{60} on Ag(111) $(2\sqrt{3}$ x $2\sqrt{3})R30°$ pattern at a) 101eV, b) 365eV and c) 504 eV. Images from [104].*

Figure 95 was generated using a software package called LEEDPAT and describes the LEED pattern seen in Fig. 94a, with corresponding lattice vectors for Ag(111) denoted by the red arrows and the superlattice vectors of C_{60} by the black arrows.

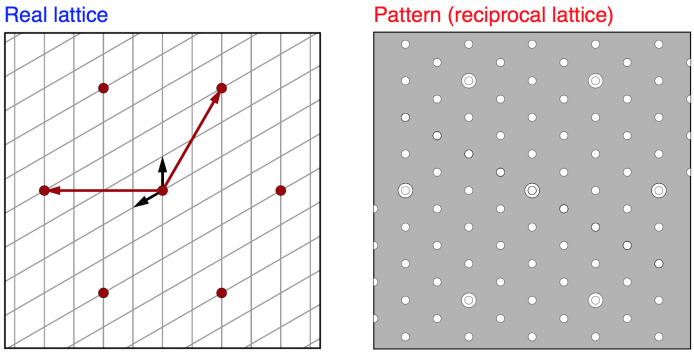

Figure 95: *LEEDPAT* ($2\sqrt{3}$ x $2\sqrt{3}$)*R30° pattern for* $H_2O@C_{60}$ *on Ag(111).*

Figures 96a and 96b show the diffraction patterns for $H_2O@C_{60}$ and C_{60} on Ag(111) respectively.

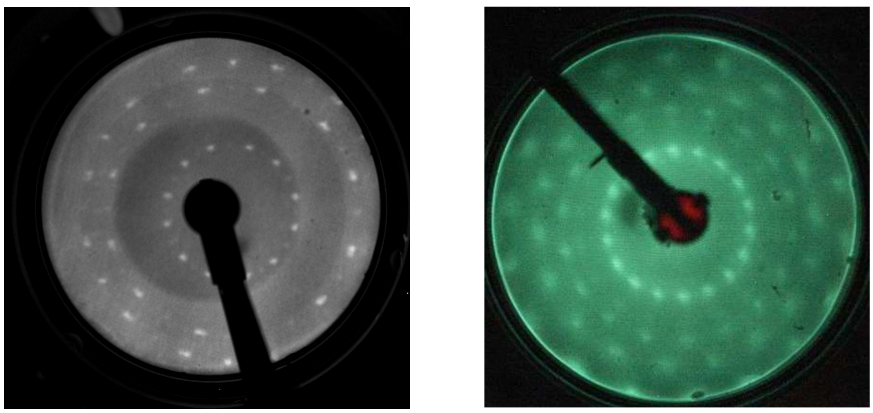

(a) (b)

Figure 96: *a) (not centered) LEED pattern for monolayer* $H_2O@C_{60}$ *on Ag(111) taken at 32.5eV. b) LEED pattern of* C_{60} *on Ag(111) taken at 35eV (from [259]), both showing different structure compared to Figs. 93, 94 and 95.*

Interestingly, all LEED experiments were carried out at 300K, but Fig. 96b shows a LEED experiment (taken from [259]) conducted at 220K which

shows a diffraction pattern close to the ($\sqrt{7}$ x $\sqrt{7}$)R19° structure with equivalent rotational domains. Further study needs to be conducted to fully understand this mechanism.

Figure 97 was also generated by LEEDPAT and is an attempt to replicate the multidomain features seen in Fig. 96a. The generated images show the corresponding lattice vectors for Ag(111) (red arrows) and superlattice vectors of $H_2O@C_{60}$ by the black arrows. The different coloured spots represent the 6 different domains used in the pattern.

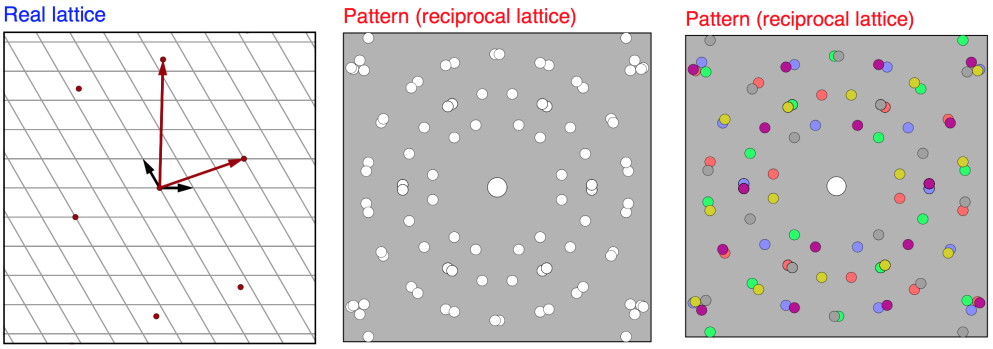

Figure 97: *LEEDPAT multidomain (6 domains) pattern for $H_2O@C_{60}$ on Ag(111). Matrix 2.3000, 4.4000 — 3.0000, 1.0000.*

8.2 X-ray photoelectron spectroscopy

8.2.1 Results and analysis

Figure 98 shows a valence band XPS spectrum between using a photon energy of 110eV. The Fermi edge is apparent at 0eV, as shown by the inset in Figure 98, which has a Fermi-Dirac shape with broadening of approximately 0.2eV. The plateau below 4eV is primarily due to the delocalized Ag 5s states, and between 4eV and 8eV 2 peaks are observed, which are due to the Ag 4d band [261, 262].

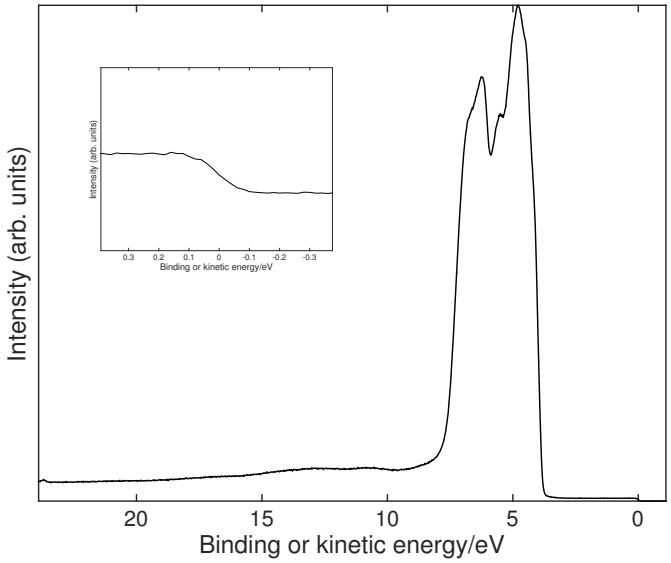

Figure 98: *XPS valence band spectrum of the Ag(111) between binding energies of -1eV and 25eV, at a photon energy of 110eV. Fermi edge is also visible at 0eV shown on inset.*

Figure 99 shows an XPS survey of a thick film of $H_2O@C_{60}$ on Ag(111) between 0eV and 600eV at a photon energy of 700eV, and a pass energy of 50eV. The C1s peak dominates the intensity scale of the XPS spectrum at a binding energy of 284eV, suggesting the substrate is covered in $H_2O@C_{60}$ molecules.

The Ag $3d_{5/2}$ and Ag $3d_{3/2}$ peaks have reduced in intensity by an order of magnitude in comparison to the clean Ag(111) surface, but remain at an intensity ratio of 1.5 due to spin-orbit split degeneracy, so this intensity will remain constant. The pair of Ag Auger peaks at 350eV have both been almost completely attenuated, and the Ag $3p_{3/2}$ peak at 580eV has completely subsided. A new peak at 532eV, which is the O1s state, indicates the presence of incarcerated H_2O in C_{60} on the Ag(111) surface.

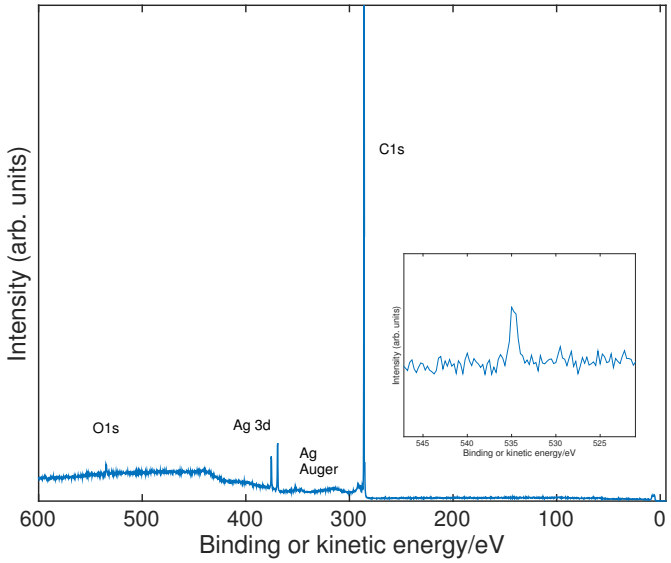

Figure 99: *XPS survey of a thick film of $H_2O@C_{60}$ on Ag(111), introducing new peaks, and surpressing others in the spectrum. O1s peak shown inset.*

Figure 100a shows the valence band of a thick film of $H_2O@C_{60}$ molecules on the Ag(111) surface taken at a photon energy of 110eV. Figure 100b shows an undoped and K-doped C_{60} film on Au(110) and is comparable to Fig 100a (in the undoped C_{60} case). The characteristics of the valence band structure agree very well with a thick film of C_{60} deposited on Ag [261, 264, 265]. Since the Ag surface is covered with a bulk-like film of molecules, the 5s and 4d Ag states have been completely attenuated.

The electronic states of C_{60} are known to interact weakly with the Ag 5s states of the Ag(111) substrate, so the valence band is now almost entirely representative of the molecular orbitals of carbon in the C_{60} cage [265]. Another advantage of Ag over the other noble metals is that the *d* states arise at higher binding energies, providing a larger 'energy window' for observation of C_{60} states close to the Fermi level, without contributions

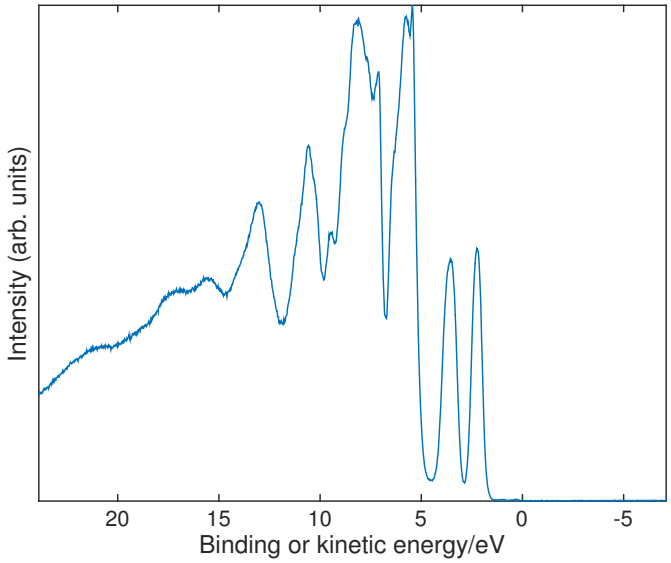

(a)

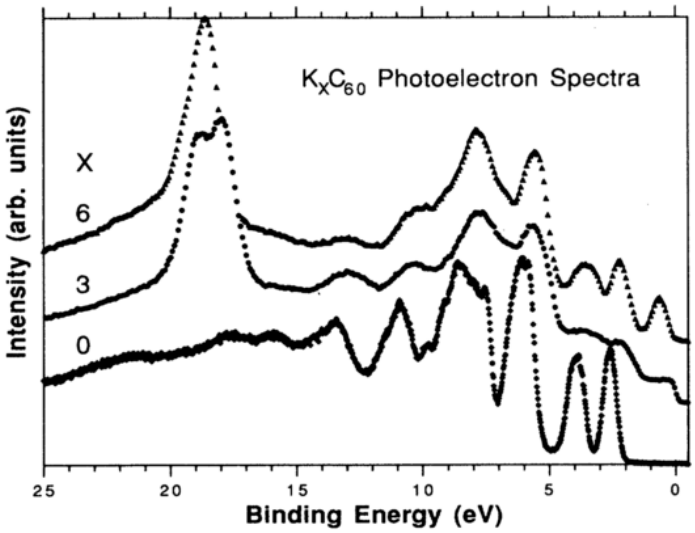

(b)

Figure 100: *a) Valence band survey of a thick film of $H_2O@C_{60}$ on Ag(111). Fermi edge is not visible. b) Valence band survey of a range of K-doped C_{60} film on Au(110) taken at 110eV (from [263]).*

from the Ag d states. The first peak at a BE of 2.25eV is the HOMO. The second peak at 3.60eV is the HOMO+1, both of which arise from π bonding states [261]. Subsequent peaks from 6eV upwards are the result

of a mixture of σ and π bonding orbitals [266].

Figure 101 shows an XPS survey of monolayer $H_2O@C_{60}$ coverage on Ag(111), between binding energies of 0eV and 600eV, at a photon energy of 700eV and pass energy 50eV. The C1s peak has now reduced by a factor of two in intensity compared to the thick film deposition of $H_2O@C_{60}$ on Ag(111) in Fig. 99. The shape and relative intensity (compared to other peaks in Fig. 101) of the Ag Auger peaks at 350eV is comparable to that observed on clean Ag in Fig. 41, but with a reduction in intensity by an order of magnitude. The $3d_{5/2}$ and $3d_{3/2}$ Ag peaks at 367eV and 372eV respectively are approximately a factor of five smaller in magnitude in comparison to the clean Ag surface, and a factor of ten larger than equivalent peaks in the thick film of $H_2O@C_{60}$ deposition. The O1s state at 532eV is still present, and now the $3p_{3/2}$ peak has returned at 580eV.

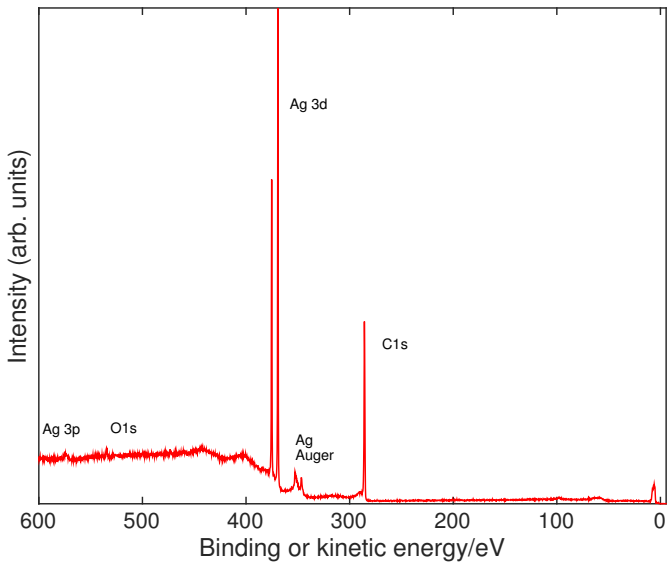

Figure 101: *XPS spectrum of monolayer $H_2O@C_{60}$ on Ag(111).*

Figure 102 shows the valence band spectrum for a monolayer coverage of

$H_2O@C_{60}$ on Ag(111), using a photon energy of 110eV. The thick film coverage of $H_2O@C_{60}$ is also plotted but offset for comparison. The characteristics also agree well with the literature for empty C_{60} [261, 264, 265]. A peak is apparent near the Fermi level, where the signal of the Ag 4d states is almost attenuated [267], but drastically different in shape to the peak near the Fermi edge in the clean Ag valence band spectrum in Fig. 98. This is indicative of the formation of a new band, and is caused by charge transfer from the Ag substrate to the LUMO of the $H_2O@C_{60}$ molecules.

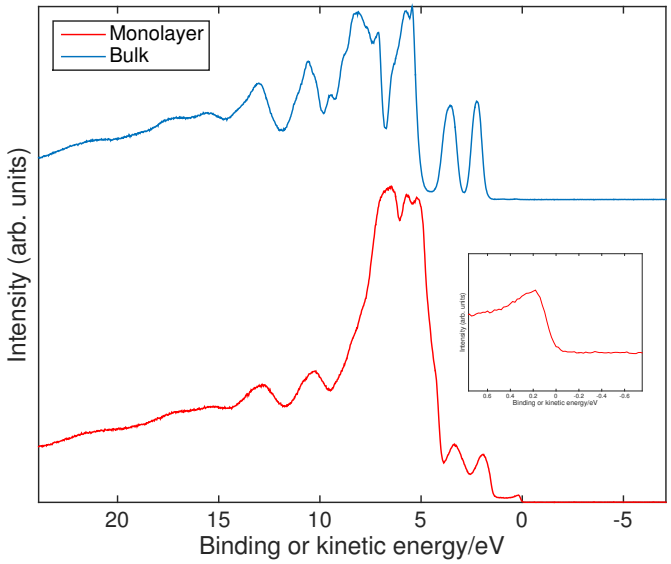

Figure 102: *XPS valence band spectrum of monolayer $H_2O@C_{60}$ on Ag(111), with the bulk $H_2O@C_{60}$ shown offset. Fermi edge now present (inset).*

The Ag 5s background signal is approximately zero up to the Fermi level, indicating a low density of states, and a negligible role in any hybridization occurring. The HOMO and HOMO+1 bands are located at 1.90eV and 3.30eV respectively, but are now broadened, attenuated, and shifted closer to the Fermi level by approximately 0.3eV. The valence band characteristics described for the monolayer of $H_2O@C_{60}$ on Ag(111) in combi-

nation with low binding energy values, are due to the pinning of LUMO of $H_2O@C_{60}$ at the Fermi level [261, 265, 267]. In addition, it is believed that the HOMO and HOMO+1 bands in Fig. 102 contain some degree of hybridization with the valence band of the Ag substrate. This would explain the broadening of the HOMO and HOMO+1 peaks, although similar (yet reduced in amplitude) oscillatory character is retained as observed in Fig. 100. The reduction in intensity of the HOMO and HOMO+1 orbitals in the monolayer $H_2O@C_{60}$ compared to the thick film on Ag(111) could be due to inhomogeneous charge distribution caused by the π bond orbital interaction between the substrate and the HOMO and HOMO+1 levels [261].

Figure 103 shows the experimental data benchmarked against the literature [261, 263]. Fig 103a and 103b show the same characteristics in the valence band for the multi/bulk layer, albeit with $H_2O@C_{60}$ rather than C_{60} on Ag(111) respectively.

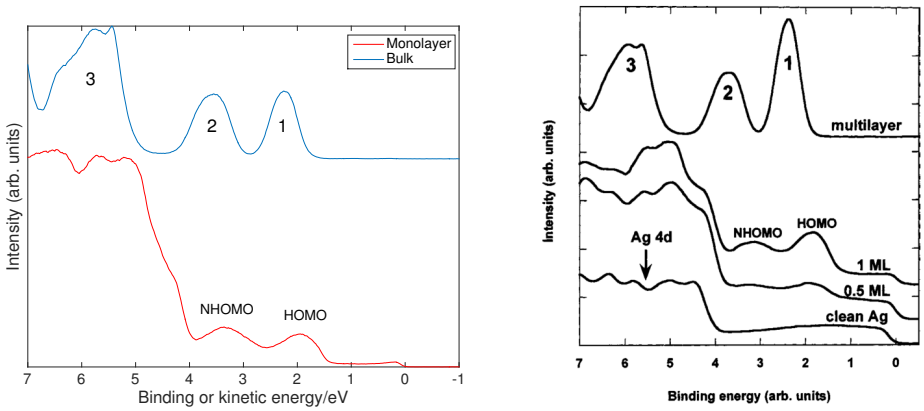

(a) (b)

Figure 103: *a) Valence band surveys for monolayer and thick film $H_2O@C_{60}$ on Ag(111) taken at 110eV. b) Valence band survey of multilayer, monolayer, 0.5 monolayer C_{60} on Ag(111) and clean Ag(111) taken at 45eV (from [261]).*

Peak 1 in Fig. 103a (which represents the HOMO) has a similar shape, but lower intensity than the equivalent peak 1 in Fig. 103b. Peak 2 and peak 3 are very similar in shape and intensity for the multi/bulk layers across all plots, which represent the NHOMO and a mixing of π and σ orbitals respectively [261]. Comparing Fig. 103a and Fig. 103b for the monolayer coverages of $H_2O@C_{60}$ rather than C_{60} on Ag(111) respectively, very similar features are again observed. The HOMO is of a slightly reduced intensity in Fig. 103a than in Fig. 103b, but with regard to the shape (including the Fermi edge) it's difficult to syphon out any subtle differences. Further evaluation into the comparison of Fig. 103b is not possible because monolayer coverages are not presented in the paper, and K-doping experimental procedures were not carried out in this report. It would however, be interesting to conduct a similar experiment in the form of $K_xH_2O@C_{60}$ on Ag(111) or Au(110) and compare it to the work of Brüwiler *et al.* in the future.

The evidence from the valence band XPS surveys emphasises the difficulties in distinguishing $H_2O@C_{60}$ from C_{60} as both molecules display very similar orbital features. This is entirely consistent with our inability to detect which molecules are encapsulated with H_2O, and which are not by SPM.

8.3 The x-ray standing wave technique

8.3.1 Results and analysis

The standing wave data were imported into the Igor Pro software package for curve fitting. This was in order to get an experimental value for both

the coherent position and fractions in particular. In general, a single data import was then fitted using either multiple Gaussian curves on top of a polynomial background, or using Doniach-Šunjić fits. The broadening values calculated for the (111), ($\bar{1}$11) and (200) lattice orientations for the Ag Auger fits were substituted into all corresponding broadening values (with matching lattice orientations) for the O1s and C1s data. A much more detailed description of the XSW fitting method can be found in the appendix.

8.3.2 O1s XSW (Mateck 2)

Figure 104 shows the standing wave measurements for the O1s state of $H_2O@C_{60}$ in the (111) direction, and corresponding fit values in Table 5.

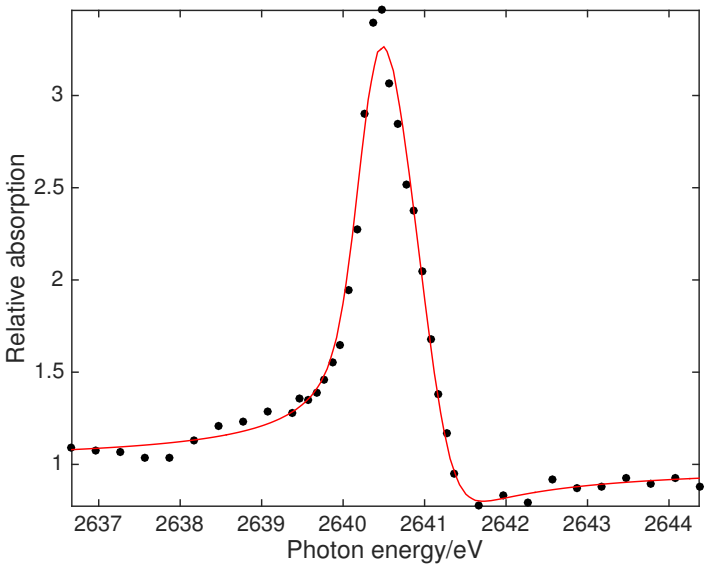

Figure 104: *O1s XSW data for the (111) Ag lattice orientation. Bragg energy of 2640.12eV.*

The Ag(111) Mateck crystal was exposed to several sputter and anneal cycles, followed by a thick film deposition of $H_2O@C_{60}$, which was then later

	(111)
SB	0.19
$\mathbf{P}_c$	0.38
$\mathbf{F}_c$	1.00
$\mathbf{E}_{Bragg}$	2640.12

Table 5: *Values for the O1s XSW data in Fig. 104.*

annealed for 2.5 hours at 350°C to form a monolayer. Hard x-rays for the (111) orientation are taken at normal incidence to the surface, so substrate Ag atoms are most ordered in this direction. A coherent fraction of 1.00 suggests a perfect (and unphysical) coherence with the Ag crystal planes, meaning the O in the H_2O is exceptionally well ordered with respect to the Ag(111) surface, or the best possible fit was using a F_c of 1.00. The electron analyser was positioned perpendicular to the incident x-rays, so the electrons were being measured at grazing incidence (0-30°), making this measurement particularly surface sensitive. The coherent position of 0.38 gives the spatial position in units of the spacing of the diffraction planes. This will be converted to an O-Ag separation in the following section.

Figure 105 shows the standing wave measurements derived from O1s photoemission for $H_2O@C_{60}$ in the $(\bar{1}11)$ direction, and corresponding fit values in Table 6. Measurements are taken at 70.5° relative to the (111) plane for the $(\bar{1}11)$ lattice orientation, i.e. at 19.5° to the surface plane, so it is sensitive to disorder parallel to the surface.

This would explain a coherent fraction of 0.37, suggesting low coherence of the oxygen positions with respect to the Ag diffraction planes. However, another possibility is that there are two well-defined positions which are

producing the reduction in coherent fraction. The broadening is also larger at 0.30eV compared to the (111) broadening of 0.19eV.

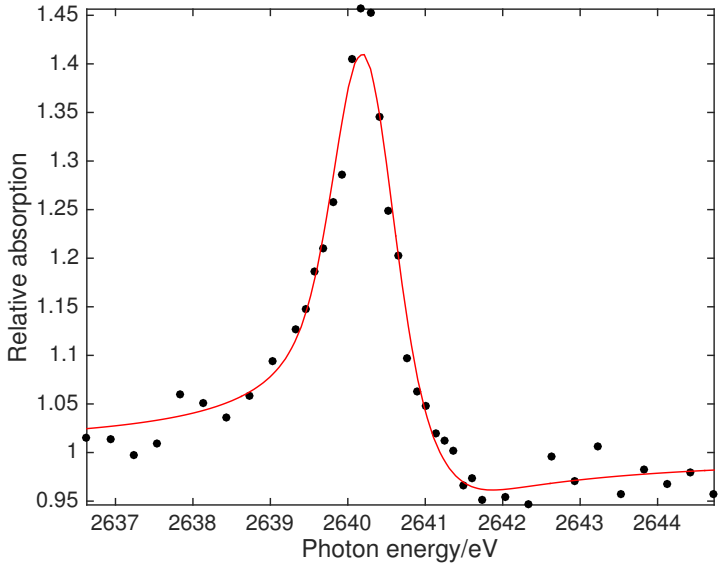

Figure 105: *O1s XSW data for the ($\bar{1}11$) Ag lattice orientation. Bragg energy of 2640.00eV.*

	($\bar{1}11$)
SB	0.30
$\mathbf{P}_c$	0.69
$\mathbf{F}_c$	0.37
$\mathbf{E}_{Bragg}$	2640.00

Table 6: *Values for the O1s XSW data in Fig. 105.*

Figure 106 shows the standing wave measurements for the O1s state of $H_2O@C_{60}$ in the (200) direction, and corresponding fit values in Table 7.

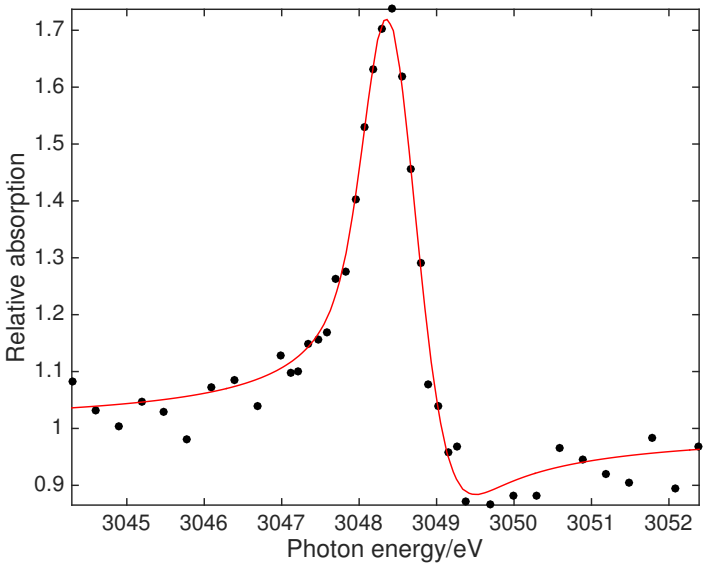

Figure 106: *O1s XSW data for the (200) Ag lattice orientation. Bragg energy 3048.14eV.*

	(200)
SB	0.24
$\mathbf{P}_c$	0.57
$\mathbf{F}_c$	0.37
$\mathbf{E}_{Bragg}$	3048.14

Table 7: *Values for the O1s XSW data in Fig. 106.*

Measurements are taken at 54.7° relative to the (111) plane for the $(\bar{1}11)$ lattice orientation, i.e. at 35.3° to the surface plane, so it is sensitive to disorder parallel to the surface, which is why the coherent fraction of 0.37 could be low, and comparable to the $(\bar{1}11)$ data. As previously mentioned, the low fraction could also be due to a well-defined position in two sites.

8.3.3 Triangulating a molecule within a molecule

The coherent position can be used to triangulate the position of the oxygen relative to the plane spacing of Ag. Each of the (111), $(\bar{1}11)$ and (200)

orientations produced their respective coherent positions for the O1s data[3]. The height of the oxygen atom above a given plane can be determined from the following formula

$$z_{111} = (P_c + n)D_{111} \tag{78}$$

where z_{111} is the distance of the O atom in the H_2O molecule from the surface Ag plane, P_c is the coherent position, n is a sensible estimate for the order of plane wave spacing, and D_{111} is the lattice spacing. Written more simply

$$z_{111} = d_{111} + nD_{111} \tag{79}$$

where $d_{111} = P_c D_{111}$ is the fraction of the plane wave spacing. Depending on the lattice orientation, the Ag plane spacing will vary, D_{111} and $D_{\bar{1}11}$ is 2.361Å whilst D_{200} is 2.045Å . The plane spacing values were calculated using

$$D_{khl} = \frac{a}{\sqrt{h^2 + k^2 + l^2}} \tag{80}$$

where a =0.409nm (lattice constant for Ag), and hkl are the set of Miller indices. The value of n was determined from basic considerations regarding the C_{60}-Ag(111) bond length and the diameter of the C_{60} cage. For example, if $n = 1$ or $n = 3$, the H_2O molecule would be too close (discussed later) to the edge of the cage (assuming $P_c = 1$), so $n = 2$ was used.

[3]C1s data were taken, but the coherent positions were exceptionally low. This is because the C_{60} cage diameter is so large (∼3x) in comparison to the Ag lattice spacing, so in effect, the Ag 'yard stick' was not suitable due to the relative incoherence of the C1s signal.

The distance z_{111} is calculated from the formula $z_{111} = d_{111} + nD_{111}$. The experimental average for the coherent position in the (111) plane is $P_c = 0.372$, multiplying this by $D_{111} = 2.361$Å gives a value of $d_{111} = 0.878$Å . By continuing the calculations for $n = 2, 3...$ then Table 8 can be produced.

n	0	1	2	3	4	5
z_{111}	0.88Å	3.24Å	5.60Å	7.96Å	10.32Å	12.68Å

Table 8: *Possible positions of O above the surface (111) plane of Ag atoms, determined by order of plane wave spacing.*

8.3.4 Adsorption site position of O

The O in an atop position with $n = 2$ (equating to 5.6Å out from the surface layer of Ag) fits for the (200) and ($\bar{1}$11) data. In addition, the O in an hcp 3-fold hollow position with $n = 1$ (3.239Å out from the surface Ag layer) also fits for the (200) and ($\bar{1}$11) data. Both bridge positions A and B can be eliminated as a solution (as shown in Figures 117 and 116 in the appendix), since different values of $n = 1$ for the (200) plane and $n = 0$ for the ($\bar{1}$11) plane are incompatible. Similarly, the O in an fcc 3-fold hollow site can also be eliminated, as this too gives incompatible solutions of $n = 1$ for the (200) plane and $n = 0$ for the ($\bar{1}$11) plane. Other valid solutions are O in atop position with $n = 5$ (equating to 12.683Å out from the surface layer of Ag) and O in an hcp 3-fold hollow position with $n = 4$ (10.322Å out from the surface layer of Ag).

There are two main solutions for O, one in the atop position or one in the hcp 3-fold hollow site. To get a better indication, the Ag-C-O can be aligned in a straight line along the surface normal. We can either assume the C is bonded to the Ag, or just 'touching' by van der Waals interaction. The O will be 'touching' the inside of the C cage by vdW interaction also, so by using the values in Tables 13 and 14 in the appendix, the vdW and chemical bonding extremes can be calculated.

Referring to Figure 107, the atop position with $n = 2$ at 5.600Å is larger than the chemical bond extreme of 5.21Å and smaller than the vdW extreme of 6.245Å which would seem to be the chemically correct answer. The hcp 3-fold hollow site position with $n = 1$ at 3.329Å is too short, even allowing for sinking down when 3 atoms are not in a straight line.

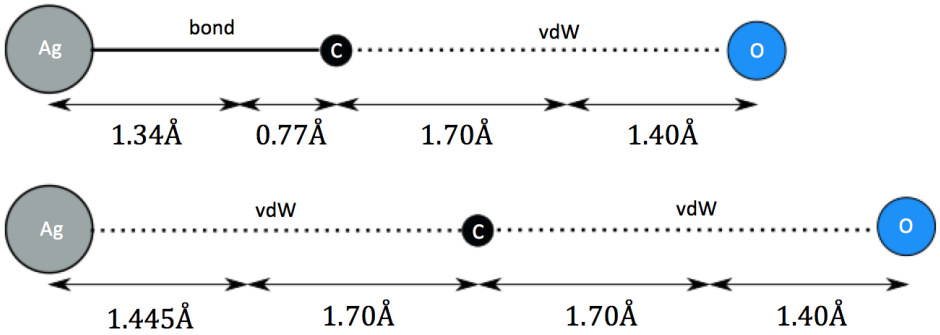

Figure 107: *Illustration showing the chemical bond extreme and vdW extreme of the O position above the Ag substrate. Total lengths are 5.21Å and 6.245Å respectively.*

The coherent fractions for the (111) plane were close to 1, and were therefore well ordered at a distance of 5.600Å relative to the Ag(111) planes. The (200) and ($\bar{1}$11) coherent fractions were quite low at 0.3-0.4, which implies lateral disorder parallel to the surface, which is similar relative to

the (200) and the ($\bar{1}11$) planes (i.e. the level of disorder is close to isotropic within the surface plane, as may be expected for a flat, high symmetry surface like Ag(111)).

9 Conclusion

An analysis of the magnitude of the force between the tip and the sample for the porphyrin data suggests that the tip is most likely to be molecule-terminated, the experiments suggest an 81% overall probability. This is likely due to the high reactivity of both the copper- and gold-terminated tips forming a bond between the tip and molecule. Practising methods for tip termination proved essential for this thesis, especially in later sections where the only way one can observe 'intermolecular' artifacts thus far is to have a molecule terminated tip. A statistical approach is also helpful to in order to make a broad guess at the form of the apex of the tip.

The molecular orbitals of the Br_4TPP molecules were probed electronically using STM, and upon dehalogenation, it was apparent that the orbital structure of the molecule could be modified and visualised through the STM images. It was also consistently shown that after dehalogenation, a Type 1 molecule adopts a Type 2 conformation, where the energy barrier has been surpassed through electron injection in order to switch from Type 1 to Type 2 (there could also be an energetic contribution by the modification of the geometry of the molecule as a direct result of dehalogenation). It would have been beneficial to conduct dI/dV spectra to enhance the validity of the experiment, however it was highly unreliable at the best of times- perhaps due to the molecule-terminated tip causing instabilities.

A direct comparison of low-temperature STM measurements with DFT including the effect of dispersion and classical MD have allowed us to identify the complete adsorption geometry of the two conformers adopted by

Br_4TPP on Cu(111). Through combined STM imaging of each conformer with the surrounding Cu(111) surface we identify the exact experimental adsorption site. Moreover, scanning probe-driven and purely mechanical (0V bias), low-temperature molecular manipulation demonstrates that the Br_4TPP conformers can be mechanically switched and manipulated at 5K temperatures via an intermediate conformational state. On the basis of a comprehensive analysis of molecular geometries calculated by DFT with dispersion and classical MD we determine that vdW forces dominate molecular adsorption based on the alignment of the pyrrole and phenyl groups with the underlying Cu(111) substrate. From a comparison between experimental and calculated adsorption positions and STM images, we can assign the correct adsorption geometry of Br_4TPP on Cu(111) with a high degree of confidence. Surprisingly, we reveal that physisorption is capable of driving significant shifts in the molecular DOS. It is likely that our results have implications for a variety of molecular systems other than porphyrins, as there are many large flexible molecules known to adopt multiple conformations at surfaces. Due to the findings, It would be a good control measure to perform similar experiments on other porphyrin molecules and different substrates to test this hypothesis.

Lateral force measurements show that molecular conformation is capable of driving much larger changes in the mechanical response than expected. This will likely have significant implications for other much larger organic molecules that exhibit variations in conformational structure, both adsorbed on surfaces and in solution. We show that the lateral forces required for manipulation have a strong dependence on conformation type,

even though each conformer shares almost identical adsorption characteristics. NEB calculations using vdW-DFT reveal that despite a similar adsorption energy for each conformer, the energy barriers for diffusion increase by over 50% for one conformational form. It would be beneficial to perform lateral manipulation experiments on other porphyrin molecules and noble metal substrates to act as a control experiment, and it would be especially interesting to see if there are any particular systems which can mediate a Type 2 to Type 1 conformational switch.

As shown in the $F(z)$ spectroscopy and 3D grid spectroscopy data, there were no obvious differences between the molecules to establish which fullerene actually had a H_2O molecule inside. This could be due to a number of factors; the C_{60} could be acting as a Faraday cage, thus creating an electronic shield for the H_2O molecule. There could also be a strong H_2O@C_{60}-Cu(111) coupling also shielding the reaction, or lastly, the H_2O could be completely vacant perhaps due to procedures like de-gassing causing a decomposition of the encapsulates leading up to the deposition of the molecules. A theoretical DFT study into this system would be hugely beneficial, as seen in the porphyrin section and in general, theory combined with experiment evidence is considerably more robust than its individual counterparts.

The observation of features appearing as artificial intermolecular bonds in 2D assemblies of C_{60} molecules has also been presented. Experimental measurements, combined with simulations based on simple analytical potentials support our view that apparent intermolecular features, in this

system, are only visible if the NC-AFM probe is terminated with a flexible $H_2O@C_{60}/C_{60}$ molecule (that is capable of relaxing in the tip-sample junction). Intermolecular artifacts are observed in the nonplanar, vdW-mediated (endhedral) fullerene system, and only in the presence of a C_{60}, rather than a CO-terminated tip apex. This highlights that artifactual intermolecular contrast is a key issue for ultrahigh resolution force microscopy across a range of molecular systems.

Experimentation at the synchrotron provided several different surface science techniques to prove the existence of H_2O encapsulated in C_{60}. Surprisingly, scanning probe experiments were not able to determine which C_{60} cages were encapsulated with H_2O, using both STM or AFM. LEED was used to gauge the quality of both the Ag(111) surface and the ordering of the adsorbates. XPS showed a strong signal at 532eV, which is the O1s state, demonstrating that the C_{60} cages do, in fact, contain water molecules. A control measure was executed to ensure H_2O surface adsorbates were not contributing to the O1s signal for completeness. Valence band XPS measurements were conducted to show a monolayer of $H_2O@C_{60}$ was present on the Ag(111) surface, which are in line with the non-encapsulated literature. This amplifies the difficulties that were faced in using STM in particular, since the valence band structures were almost identical for both endohedral fullerenes and fullerenes. NIXSW experiments were conducted to successfully triangulate an average position of the water molecule inside the carbon cage, relative to the Ag plane spacing. The value is calculated for the O is in the atop position at 5.6Å above the Ag(111) surface, which relative to the C_{60} cage is approximately central.

Evidently, the combination of both XPS and (in particular) NIXSW is a very powerful technique to determine the location of encapsulated H_2O within the C_{60} cage, whereas it is not possible currently to use STM/AFM to depict whether the molecules are encapsulated, or not. It would be interesting to return to encapsulated molecules in STM/AFM after XPS/XSW confirmation of the O1s state, and to perhaps perform more detailed studies such as Kelvin probe force microscopy (KPFM) in a bid to try and differentiate between filled and non-filled fullerenes.

The work presented in this thesis on porphyrin molecules demonstrates their potential toward nanoscale devices in the future. The ability for them to switch conformation could provide the basis for a molecular logic-based system. The encapsulated fullerene is an intriguing molecule, not only for the SPM enthusiast, but for use in potential applications for future molecular transport in biological systems, and in combination with their carbon allotropes- for future nanoscale electronic devices.

References

[1] D. M. Eigler and E. K. Schweizer, "Positioning single atoms with a scanning tunnelling microscope," *Nature*, vol. 344, no. 6266, pp. 524–526, 1990.

[2] M. F. Crommie, C. P. Lutz, and D. M. Eigler, "Confinement of Electrons to Quantum Corrals on a Metal Surface," *Science*, vol. 262, no. 5131, pp. 218–220, 1993.

[3] E. J. Heller, M. F. Crommie, C. P. Lutz, and D. M. Eigler, "Scattering and adsorption of surface electron waves in quantum corrals," *Nature*, vol. 369, pp. 464–466, 1994.

[4] H. Manoharan, C. P. Lutz, and D. M. Eigler, "Quantum mirages formed by coherent projection of electronic structure," *Nature*, vol. 403, pp. 512–515, 2000.

[5] C. R. Moon, L. S. Mattos, B. K. Foster, G. Zeltzer, and H. C. Manoharan, "Quantum holographic encoding in a two-dimensional electron gas," *Nature Nanotech.*, vol. 4, pp. 167–172, 2009.

[6] N. Nilius, T. M. Wallis, and W. Ho, "Development of one-dimensional band structure in artificial gold chains," *Science*, vol. 297, pp. 1853–1856, 2002.

[7] D. Kitchen, A. Richardella, J.-M. Tang, M. E. Flatte, and A. Yazdani, "Atom-by-atom substitution of Mn in GaAs and visualization of their hole-mediated interactions," *Nature*, vol. 442, pp. 436–439, 2006.

[8] I.-W. Lyo and P. Avouris, "Field-induced nanometer- to atomic-scale manipulation of silicon surfaces with the STM," *Science*, vol. 253, pp. 173–176, 1991.

[9] T. A. Jung, R. R. Schlittler, J. K. Gimzewski, H. Tang, and C. Joachim, "Controlled room temperature positioning of individual molecules: Molecular flexure and motion," *Science*, vol. 271, pp. 181–184, 1996.

[10] J. K. Gimzewski, "Rotation of a single molecule within a supramolecular bearing," *Science*, vol. 281, pp. 531–533, 1998.

[11] B. C. Stipe and W. Ho, "Inducing and viewing the rotational motion of a single molecule," *Science*, vol. 279, pp. 1907–1909, 1998.

[12] T. Komeda, Y. Kim, M. Kawai, B. N. J. Persson, and H. Ueba, "Lateral hopping of molecules induced by excitation of internal vibration mode," *Science*, vol. 295, pp. 2055–2058, 2002.

[13] J. I. Pascual, N. Lorente, Z. Song, H. Conrad, and H.-P. Rust, "Selectivity in vibrationally mediated single-molecule chemistry," *Nature*, vol. 423, pp. 525–528, 2003.

[14] F. J. Giessibl, "Surface by Atomic Force Microscopy," *Science*, vol. 267, no. 13, p. 68, 1995.

[15] N. Oyabu, O. Custance, I. Yi, Y. Sugawara, and S. Morita, "Mechanical vertical manipulation of selected single atoms by soft nanoindentation using near contact atomic force microscopy," *Phys. Rev. Lett.*, vol. 90, p. 176102, 2003.

[16] Y. Sugimoto, M. Abe, S. Hirayama, N. Oyabu, O. Custance, and S. Morita, "Atom inlays performed at room temperature using atomic force microscopy," *Nature materials*, vol. 4, no. 2, pp. 156–159, 2005.

[17] L. Gross, F. Mohn, N. Moll, P. Liljeroth, and G. Meyer, "The Chemical Structure of a Molecule Resolved by Atomic Force Microscopy," *Science*, vol. 325, no. 5944, pp. 1110–1114, 2009.

[18] W. Kuster, "Beitrage zur Kenntnis des Bilirubins und Hmins," *Hoppe-Seylers Z. Physiol. Chem.*, vol. 82, pp. 463–483, 1912.

[19] P. Rothemund, "A New Porphyrin Synthesis. The Synthesis of Porphin1," *Journal of the American Chemical Society*, vol. 58, no. 4, pp. 625–627, 1936.

[20] J. T. Groves, "The bioinorganic chemistry of iron in oxygenases and supramolecular assemblies.," *Proceedings of the National Academy of Sciences of the United States of America*, vol. 100, no. 7, pp. 3569–3574, 2003.

[21] I. Fleming, "Absolute Configuration and the Structure of Chlorophyll," *Nature*, vol. 216, pp. 151–152, 1967.

[22] C. E. Castro, "Theory of hemeprotein reactivity," *Journal of theoretical biology*, vol. 33, pp. 475–490, 1971.

[23] D. Filippini, A. Alimelli, C. Di Natale, R. Paolesse, A. D'Amico, and I. Lundström, "Chemical sensing with familiar devices," *Angewandte Chemie - International Edition*, vol. 45, pp. 3800–3803, 2006.

[24] M. A. Baldo, D. F. O'Brien, Y. You, A. Shoustikov, S. Sibley, M. E. Thompson, and S. R. Forrest, "Highly efficient phosphorescent emission from organic electroluminescent devices," *Nature*, vol. 395, no. 6698, pp. 151–154, 1998.

[25] R. W. Y. Sun and C. M. Che, "The anti-cancer properties of gold(III) compounds with dianionic porphyrin and tetradentate ligands," *Coordination Chemistry Reviews*, vol. 253, pp. 1682–1691, 2009.

[26] R. Wai-Yin Sun, D.-L. Ma, E. L.-M. Wong, and C.-M. Che, "Some uses of transition metal complexes as anti-cancer and anti-HIV agents," *Dalton Trans.*, pp. 4884–4892, 2007.

[27] M. R. C. Hunt, S. Modesti, P. Rudolf, and R. E. Palmer, "Charge transfer and structure in C_{60} adsorption on metal surfaces," *Physical Review B*, vol. 51, no. 15, pp. 10039–10047, 1995.

[28] M. R. C. Hunt and R. E. Palmer, "The structural and vibrational properties of C_{60} adsorbed on the graphite(0001) surface," *Surface Review and Letters*, vol. 03, no. 01, pp. 937–942, 1996.

[29] M. R. C. Hunt, P. Rudolf, and S. Modesti, "Localization of substrate-induced modification in the electronic structureof C_{60} fullerene-metal interfaces," *Physical Review B*, vol. 55, pp. 7882–7888, mar 1997.

[30] H. Park, J. Park, A. Lim, E. Anderson, A. Alivisatos, and P. McEuen, "Nanomechanical oscillations in a single-C_{60} transistor," *Nature*, vol. 407, no. 6800, pp. 57–60, 2000.

[31] N. Néel, J. Kröger, L. Limot, T. Frederiksen, M. Brandbyge, and R. Berndt, "Controlled Contact to a C_{60} Molecule," *Physical Review Letters*, vol. 98, no. 6, p. 065502, 2007.

[32] C. Joachim and J. Gimzewski, "An electromechanical amplifier using a single molecule," *Chemical Physics Letters*, vol. 2614, 1997.

[33] R. Yamachika, M. Grobis, a. Wachowiak, and M. F. Crommie, "Controlled atomic doping of a single C_{60} molecule.," *Science (New York, N.Y.)*, vol. 304, no. 5668, pp. 281–4, 2004.

[34] A. Wachowiak, R. Yamachika, K. H. Khoo, Y. Wang, M. Grobis, D.-H. Lee, S. G. Louie, and M. F. Crommie, "Visualization of the molecular Jahn-Teller effect in an insulating K_4C_{60} monolayer," *Science (New York, N.Y.)*, vol. 310, no. 5747, pp. 468–70, 2005.

[35] S. H. Friedman, D. L. DeCamp, R. P. Sijbesma, G. Srdanov, F. Wudl, and G. L. Kenyon, "Inhibition of the HIV-1 protease by fullerene derivatives: model building studies and experimental verification," *Journal of the American Chemical Society*, vol. 115, no. 15, pp. 6506–6509, 1993.

[36] J. R. Heath, S. C. O'Brien, Q. Zhang, Y. Liu, R. F. Curl, F. K. Tittel, and R. E. Smalley, "Lanthanum complexes of spheroidal carbon shells," *Journal of the American Chemical Society*, vol. 107, no. 25, pp. 7779–7780, 1985.

[37] C. Beduz, M. Carravetta, J. Y.-C. Chen, M. Concistre, M. Denning, M. Frunzi, A. J. Horsewill, O. G. Johannessen, R. Lawler, X. Lei, M. H. Levitt, Y. Li, S. Mamone, Y. Murata, U. Nagel, T. Nishida, J. Ollivier, S. Rols, T. Room, R. Sarkar, N. J. Turro, and Y. Yang, "Quantum rotation of ortho and para-water encapsulated in a fullerene cage," *Proceedings of the National Academy of Sciences*, vol. 109, pp. 12894–12898, aug 2012.

[38] B. Meier, S. Mamone, M. Concistrè, J. Alonso-Valdesueiro, A. Krachmalnicoff, R. J. Whitby, and M. H. Levitt, "Electrical detection of orthopara conversion in fullerene-encapsulated water," *Nature Communications*, vol. 6, p. 8112, aug 2015.

[39] G. Rothberg, M. Eisenstadt, and P. Kusch, "Free Evaporation of Alkali Halide Crystals," *The Journal of Chemical Physics*, vol. 30, no. 2, p. 517, 1959.

[40] G. Binnig, H. Rohrer, C. Gerber, and E. Weibel, "Surface Studies by Scanning Tunneling Microscopy," *Physical Review Letters*, vol. 49, pp. 57–61, 1982.

[41] G. Binnig, C. Quate, and C. Gerber, "Atomic Force Microscope," *Physical Review Letters*, vol. 56, pp. 930–933, 1986.

[42] P. Liljeroth, J. Repp, and G. Meyer, "Current-induced hydrogen tautomerization and conductance switching of naphthalocyanine molecules.," *Science (New York, N.Y.)*, vol. 317, pp. 1203–1206, 2007.

[43] F. Moresco, G. Meyer, K. H. Rieder, H. Tang, A. Gourdon, and C. Joachim, "Conformational changes of single molecules induced by scanning tunneling microscopy manipulation: a route to molecular switching," *Physical Review Letters*, vol. 86, pp. 672–675, 2001.

[44] L. Grill, K. H. Rieder, F. Moresco, S. Stojkovic, A. Gourdon, and C. Joachim, "Exploring the interatomic forces between tip and single molecules during STM manipulation," *Nano Letters*, vol. 6, no. 110, pp. 2685–2689, 2006.

[45] V. Iancu, A. Deshpande, and S. W. Hla, "Manipulating Kondo temperature via single molecule switching.," *Nano Letters*, vol. 6, pp. 820–823, 2006.

[46] X. H. Qiu, G. V. Nazin, and W. Ho, "Mechanisms of reversible conformational transitions in a single molecule," *Physical Review Letters*, vol. 93, pp. 1–4, 2004.

[47] T. Yokoyama, T. Kamikado, S. Yokoyama, and S. Mashiko, "Conformation selective assembly of carboxyphenyl substituted porphyrins on Au (111)," *Journal of Chemical Physics*, vol. 121, no. 111, pp. 11993–11997, 2004.

[48] D. Heim, K. Seufert, W. Auwärter, C. Aurisicchio, C. Fabbro, D. Bonifazi, and J. V. Barth, "Surface-assisted assembly of discrete porphyrin-based cyclic supramolecules," *Nano Letters*, vol. 10, pp. 122–128, 2010.

[49] L. Grill, M. Dyer, L. Lafferentz, M. Persson, M. V. Peters, and S. Hecht, "Nano-architectures by covalent assembly of molecular building blocks," *Nature Immunology*, vol. 2, no. 11, pp. 687–691, 2007.

[50] A. Rosa, G. Ricciardi, and E. J. Baerends, "Synergism of porphyrin-core saddling and twisting of meso-Aryl substituants," *Journal of Physical Chemistry A*, vol. 110, pp. 5180–5190, 2006.

[51] S. P. Jarvis, S. Taylor, J. D. Baran, D. Thompson, A. Saywell, B. Mangham, N. R. Champness, J. A. Larsson, and P. Moriarty, "Physisorption Controls the Conformation and Density of States of an Adsorbed Porphyrin," *Journal of Physical Chemistry C*, vol. 119, no. 50, pp. 27982–27994, 2015.

[52] A. Hauschild, K. Karki, B. C. C. Cowie, M. Rohlfing, F. S. Tautz, and M. Sokolowski, "Molecular distortions and chemical bonding of a large π-conjugated molecule on a metal surface," *Physical Review Letters*, vol. 94, pp. 1–4, 2005.

[53] L. Romaner, G. Heimel, J. L. Brédas, A. Gerlach, F. Schreiber, R. L. Johnson, J. Zegenhagen, S. Duhm, N. Koch, and E. Zojer, "Impact of bidirectional charge transfer and molecular distortions on the electronic structure of a metal-organic interface," *Physical Review Letters*, vol. 99, pp. 1–4, 2007.

[54] T. A. Jung, R. R. Schlittler, and J. K. Gimzewski, "Conformational identification of individual adsorbed molecules with the stm," *Nature*, vol. 386, no. 6626, pp. 696–698, 1997.

[55] T. Yokoyama, S. Yokoyama, T. Kamikado, and S. Mashiko, "Nonplanar adsorption and orientational ordering of porphyrin molecules on

Au(111)," *Journal of Chemical Physics*, vol. 115, no. 111, pp. 3814–3818, 2001.

[56] W. Auwarter, A. Weber-Bargioni, A. Riemann, A. Schiffrin, O. Groning, R. Fasel, and J. V. Barth, "Self-assembly and conformation of tetrapyridyl-porphyrin molecules on Ag(111)," *The Journal of chemical physics*, vol. 124, p. 194708, 2006.

[57] L. Lafferentz, V. Eberhardt, C. Dri, C. Africh, G. Comelli, F. Esch, S. Hecht, and L. Grill, "Controlling on-surface polymerization by hierarchical and substrate-directed growth.," *Nature chemistry*, vol. 4, pp. 215–20, 2012.

[58] G. P. Moss, "Basic terminology of stereochemistry (IUPAC Recommendations 1996)," *Pure and Applied Chemistry*, vol. 68, no. 12, 1996.

[59] N. de Souza, "Pulling on single molecules," *Nat. Methods*, vol. 9, pp. 873–877, 2012.

[60] J. A. Shelnutt, "Nonplanar porphyrins and their significance in proteins," *Chem. Soc. Rev.*, vol. 27, pp. 31–41, 1998.

[61] L. Venkataraman, J. E. Klare, C. Nuckolls, M. S. Hybertsen, and M. L. Steigerwald, "Dependence of single-molecule junction conductance on molecular conformation," *Nature*, vol. 442, pp. 904–907, 2006.

[62] M. Forster, M. S. Dyer, M. Persson, and R. Raval, "Probing conformers and adsorption footprints at the single-molecule level in a highly organized amino acid assembly of (S)-proline on Cu(110)," *J. Am. Chem. Soc.*, vol. 131, pp. 10173–10181, 2009.

[63] S. Weigelt, "Chiral switching by spontaneous conformational change in adsorbed organic molecules," *Nat. Mater.*, vol. 5, pp. 112–117, 2006.

[64] P. Moriarty, Y. Ma, M. Upward, and P. Beton, "Translation, rotation and removal of C_{60} on Si(100)-2x1 using anisotropic molecular manipulation," *Surf. Sci.*, vol. 407, pp. 27–35, 1998.

[65] D. L. Keeling, "Bond breaking coupled with translation in rolling of covalently bound molecules," *Phys. Rev. Lett.*, vol. 94, pp. 2–5, 2005.

[66] L. Grill, "Rolling a single molecular wheel at the atomic scale," *Nat. Nanotechnol.*, vol. 2, pp. 95–98, 2007.

[67] F. Moresco, "Recording intramolecular mechanics during the manipulation of a large molecule," *Phys. Rev. Lett.*, vol. 87, p. 88302, 2001.

[68] V. Iancu and S.-W. Hla, "Realization of a four-step molecular switch in scanning tunneling microscope manipulation of single chlorophyll-a molecules," *Proc. Natl Acad. Sci. USA*, vol. 103, pp. 13718–13721, 2006.

[69] N. Wintjes, "A supramolecular multiposition rotary device," *Angew. Chem. Int. Ed. Engl.*, vol. 46, pp. 4089–4092, 2007.

[70] C. Loppacher, "Direct determination of the energy required to operate a single molecule switch," *Phys. Rev. Lett.*, vol. 90, p. 66107, 2003.

[71] W. R. Scheidt, "Explorations in metalloporphyrin stereochemistry, physical properties and beyond," *Journal of Porphyrins and Phthalocyanines*, vol. 12, no. 09, pp. 979–992, 2008.

[72] M. O. Senge, "New trends in photobiology," *Journal of Photochemistry and Photobiology B: Biology*, vol. 16, no. 1, pp. 3–36, 1992.

[73] M. Stepien, N. Sprutta, and L. Latos-Grazynski, "Figure Eights, Möbius Bands, and More: Conformation and Aromaticity of Porphyrinoids," *Angewandte Chemie International Edition*, vol. 50, no. 19, pp. 4288–4340, 2011.

[74] R. Schweitzer-Stenner, "Using spectroscopic tools to probe porphyrin deformation and porphyrin-protein interactions," *Journal of Porphyrins and Phthalocyanines*, vol. 15, pp. 312–337, 2011.

[75] W. Auwärter, D. Écija, F. Klappenberger, and J. V. Barth, "Porphyrins at interfaces," *Nature Publishing Group*, vol. 7, no. 2, pp. 105–120, 2015.

[76] J. Brede, M. Linares, R. Lensen, A. E. Rowan, M. Funk, M. Broring, G. Hoffmann, and R. Wiesendanger, "Adsorption and conformation of porphyrins on metallic surfaces," *Journal of Vacuum Science & Technology B: Microelectronics and Nanometer Structures*, vol. 27, no. 2, p. 799, 2009.

[77] J. Brede, M. Linares, S. Kuck, J. Schwöbel, A. Scarfato, S.-H. Chang, G. Hoffmann, R. Wiesendanger, R. Lensen, P. H. J. Kouwer, J. Hoogboom, A. E. Rowan, M. Bröring, M. Funk, S. Stafström, F. Zerbetto, and R. Lazzaroni, "Dynamics of molecular self-ordering in tetraphenyl porphyrin monolayers on metallic substrates," *Nanotechnology*, vol. 20, no. 27, p. 275602, 2009.

[78] K. Diller, F. Klappenberger, M. Marschall, K. Hermann, A. Nefedov, C. Wöll, and J. V. Barth, "Self-metalation of 2H-tetraphenylporphyrin on Cu(111): an x-ray spectroscopy study.," *The Journal of chemical physics*, vol. 136, no. 1, p. 014705, 2012.

[79] G. Rojas, S. Simpson, X. Chen, D. A. Kunkel, J. Nitz, J. Xiao, P. A. Dowben, E. Zurek, and A. Enders, "Surface state engineering of moleculemolecule interactions," *Physical Chemistry Chemical Physics*, vol. 14, no. 14, p. 4971, 2012.

[80] F. Buchner, J. Xiao, E. Zillner, M. Chen, M. Röckert, S. Ditze, M. Stark, H.-P. Steinrück, J. M. Gottfried, and H. Marbach, "Diffusion, Rotation, and Surface Chemical Bond of Individual 2 H-Tetraphenylporphyrin Molecules on Cu(111)," *The Journal of Physical Chemistry C*, vol. 115, no. 49, pp. 24172–24177, 2011.

[81] F. Buchner, E. Zillner, M. Röckert, S. Gläel, H. P. Steinrück, and H. Marbach, "Substrate-mediated phase separation of two porphyrin derivatives on Cu(111)," *Chemistry - A European Journal*, vol. 17, no. 37, pp. 10226–10229, 2011.

[82] C. M. Doyle, S. a. Krasnikov, N. N. Sergeeva, A. B. Preobrajenski, N. a. Vinogradov, Y. N. Sergeeva, M. O. Senge, and A. a. Cafolla, "Evidence for the formation of an intermediate complex in the direct metalation of tetra(4-bromophenyl)-porphyrin on the Cu(111) surface.," *Chemical communications (Cambridge, England)*, vol. 47, no. 44, pp. 12134–6, 2011.

[83] J. Mielke, F. Hanke, M. V. Peters, S. Hecht, M. Persson, and L. Grill, "Adatoms underneath Single Porphyrin Molecules on Au(111)," *Journal of the American Chemical Society*, vol. 137, no. 5, pp. 1844–1849, 2015.

[84] J. Carrasco, W. Liu, A. Michaelides, and A. Tkatchenko, "Insight into the description of van der Waals forces for benzene adsorption on transition metal (111) surfaces," *The Journal of Chemical Physics*, vol. 140, no. 8, p. 084704, 2014.

[85] W. Liu, S. N. Filimonov, J. Carrasco, and A. Tkatchenko, "Molecular switches from benzene derivatives adsorbed on metal surfaces," *Nature Communications*, vol. 4, 2013.

[86] C. Bürker, N. Ferri, A. Tkatchenko, A. Gerlach, J. Niederhausen, T. Hosokai, S. Duhm, J. Zegenhagen, N. Koch, and F. Schreiber, "Exploring the bonding of large hydrocarbons on noble metals: Diindoperylene on Cu(111), Ag(111), and Au(111)," *Physical Review B*, vol. 87, no. 16, p. 165443, 2013.

[87] O. Custance, R. Perez, and S. Morita, "Atomic force microscopy as a tool for atom manipulation," *Nature Nanotechnology*, vol. 4, no. 12, pp. 803–810, 2009.

[88] S. Torbrugge, O. Custance, S. Morita, and M. Reichling, "Manipulation of individual water molecules on CeO_2(111)," *J. Phys. Condens. Matter*, vol. 24, p. 84010, 2012.

[89] J. Schutte, "Single-molecule switching with non-contact atomic force microscopy," *Nanotechnology*, vol. 22, p. 245701, 2011.

[90] M. Ternes, C. P. Lutz, C. F. Hirjibehedin, F. J. Giessibl, and A. J. Heinrich, "The force needed to move an atom on a surface," *Science*, vol. 319, pp. 1066–1069, 2008.

[91] G. Langewisch, J. Falter, H. Fuchs, and A. Schirmeisen, "Forces during the controlled displacement of organic molecules," *Phys. Rev. Lett.*, vol. 110, p. 36101, 2013.

[92] G. Langewisch, J. Falter, A. Schirmeisen, and H. Fuchs, "Long jumps of an organic molecule induced by atomic force microscopy manipulation," *Adv. Mater. Interface*, vol. 1, p. 1300013, 2013.

[93] H.-Q. Mao, N. Li, X. Chen, and Q.-K. Xue, "Mechanical properties of H2Pc self-assembled monolayers at the single molecule level by non-contact atomic force microscopy," *J. Phys. Condens. Matter*, vol. 24, p. 84004, 2012.

[94] E. Osawa, "(in japenese)," *Kagaku*, vol. 25, pp. 854–863, 1970.

[95] D. Bochvar and E. Gal'pern *Dokl. Akad. Nauk.*, vol. SSSR 209, pp. 610–612, 1973.

[96] H. W. Kroto, J. R. Heath, S. C. O'Brien, R. F. Curl, and R. E. Smalley, "C_{60}: Buckminsterfullerene," *Nature*, vol. 318, no. 6042, pp. 162–163, 1985.

[97] K. Motai, T. Hashizume, H. Shinohara, Y. Saito, H. W. Pickering, Y. Nishina, and T. Sakurai, "C_{60} Grown on the Cu(111)-(1x1) Surface," *Japanese Journal of Applied Physics*, vol. 32, no. 3B, pp. L450–L453, 1993.

[98] T. Hashizume, K. Motai, X. Wang, H. Shinohara, Y. Saito, Y. Maruyama, K. Ohno, Y. Kawazoe, Y. Nishina, H. Pickering, Y. Kuk, and T. Sakurai, "Intramolecular structures of C_{60} molecules adsorbed on the Cu(111)-(1x1) surface," *Physical Review Letters*, vol. 71, no. 18, pp. 2959–2962, 1993.

[99] G. K. Wertheim, J. E. Rowe, D. N. Buchanan, E. E. Chaban, A. F. Hebard, A. R. Kortan, A. V. Makhija, and R. C. Haddon, "Photoemission Spectra and Electronic Properties of K_xC_{60}.," *Science (New York, N.Y.)*, vol. 252, no. 5011, pp. 1419–21, 1991.

[100] E. Altman and R. Colton, "Determination of the orientation of C_{60} adsorbed on Au(111) and Ag(111)," *Physical Review B*, vol. 48, no. 24, pp. 18244–18249, 1993.

[101] E. I. Altman and R. J. Colton, "The interaction of C_{60} with noble metal surfaces," *Surface Science*, vol. 295, no. 1-2, pp. 13–33, 1993.

[102] T. Sakurai, X. Wang, T. Hashizume, V. Yurov, H. Shinohara, and H. Pickering, "Adsorption of fullerenes on Cu(111) and Ag(111) surfaces," *Applied Surface Science*, vol. 87-88, pp. 405–413, 1995.

[103] T. Sakurai, Q. K. Xue, T. Hashizume, and H. Shinohara, "Scanning Microscopy of Fullerenes Study," *Science*, vol. 51, no. 4, pp. 263–408, 1996.

[104] H. I. Li, K. Pussi, K. J. Hanna, L.-L. Wang, D. D. Johnson, H.-P. Cheng, H. Shin, S. Curtarolo, W. Moritz, J. A. Smerdon, R. McGrath, and R. D. Diehl, "Surface Geometry of C_{60} on Ag(111)," *Physical Review Letters*, vol. 103, no. 5, p. 056101, 2009.

[105] D. Schmicker, S. Schmidt, J. Skofronick, J. Toennies, and R. Vollmer, "Epitaxial growth of single-crystal C_{60} on mica by helium-atom scattering," *Physical Review B*, vol. 44, no. 19, pp. 10995–10997, 1991.

[106] P. Benning, F. Stepniak, and J. Weaver, "Electron-diffraction and photoelectron-spectroscopy studies of fullerene and alkali-metal fulleride films," *Physical Review B*, vol. 48, no. 12, pp. 9086–9096, 1993.

[107] G. Gensterblum, K. Hevesi, B.-Y. Han, L.-M. Yu, J.-J. Pireaux, P. Thiry, R. Caudano, A.-A. Lucas, D. Bernaerts, S. Amelinckx, G. Van Tendeloo, G. Bendele, T. Buslaps, R. Johnson, M. Foss, R. Feidenhansl, and G. Le Lay, "Growth mode and electronic structure of the epitaxial C_{60}(111)/GeS(001) interface," *Physical Review B*, vol. 50, no. 16, pp. 11981–11995, 1994.

[108] J. Gimzewski, S. Modesti, and R. Schlittler, "Cooperative self-assembly of Au atoms and C_{60} on Au(110) surfaces," *Physical Review Letters*, vol. 72, no. 7, pp. 1036–1039, 1994.

[109] Z. Dai, H. Naramoto, K. Narumi, and S. Yamamoto, "Preparation and characterization of C_{60} films on ionic substrates," *Journal of Physics: Condensed Matter*, vol. 11, no. 33, pp. 6347–6358, 1999.

[110] R. Schwedhelm, J.-P. Schlomka, S. Woedtke, R. Adelung, L. Kipp, M. Tolan, W. Press, and M. Skibowski, "Epitaxial thin-film growth of C_{60} on VSe_2 studied with scanning tunneling microscopy and x-ray diffraction," *Physical Review B*, vol. 59, no. 20, pp. 13394–13400, 1999.

[111] E. Katz, D. Faiman, S. Shtutina, and A. Isakina, "Deposition and structural characterization of high quality textured C_{60} thin films," *Thin Solid Films*, vol. 368, no. 1, pp. 49–54, 2000.

[112] T. Hashizume and T. Sakurai, "C_{60} adsorption on the Si(100)21 and Cu(111)11 surfaces," *Journal of Vacuum Science & Technology B: Microelectronics and Nanometer Structures*, vol. 12, no. 3, p. 1992, 1994.

[113] J. K. Gimzewski, S. Modesti, T. David, and R. R. Schlittler, "Scanning tunneling microscopy of ordered C_{60} and C_{70} layers on Au(111), Cu(111), Ag(110), and Au(110) surfaces," *Journal of Vacuum Science & Technology B: Microelectronics and Nanometer Structures*, vol. 12, no. 3, p. 1942, 1994.

[114] M. Cuberes, R. Schlittler, and J. Gimzewski, "Manipulation of C_{60} molecules on Cu(111) surfaces using a scanning tunneling microscope," *Applied Physics A: Materials*, vol. 673, no. 1998, pp. 669–673, 1998.

[115] P. A. Heiney, "Structure, dynamics and ordering transition of solid C_{60}," *Journal of Physics and Chemistry of Solids*, vol. 53, no. 11, pp. 1333 – 1352, 1992.

[116] R. Fasel, P. Aebi, R. Agostino, D. Naumovic, J. Osterwalder, a. Santaniello, and L. Schlapbach, "Orientation of adsorbed C_{60} molecules determined via x-ray photoelectron diffraction.," *Physical review letters*, vol. 76, no. 25, pp. 4733–4736, 1996.

[117] M. Abel, A. Dmitriev, R. Fasel, N. Lin, J. Barth, and K. Kern, "Scanning tunneling microscopy and x-ray photoelectron diffraction investigation of C_{60} films on Cu(100)," *Physical Review B*, vol. 67, no. 24, p. 245407, 2003.

[118] W. Pai and C.-L. Hsu, "Ordering of an incommensurate molecular layer with adsorbate-induced reconstruction: C60/Ag(100)," *Physical Review B*, vol. 68, no. 12, p. 121403, 2003.

[119] C.-L. Hsu and W. Pai, "Aperiodic incommensurate phase of a C_{60} monolayer on Ag(100)," *Physical Review B*, vol. 68, no. 24, p. 245414, 2003.

[120] M. Johansson, A. Maxwell, S. Gray, P. Brühwiler, D. Mancini, L. Johansson, and N. Må rtensson, "Scanning tunneling microscopy of C_{60}/Al(111)-66: Inequivalent molecular sites and electronic structures," *Physical Review B*, vol. 54, no. 19, pp. 13472–13475, 1996.

[121] R. Felici, M. Pedio, F. Borgatti, S. Iannotta, M. Capozi, G. Ciullo, and A. Stierle, "X-ray-diffraction characterization of Pt(111) surface nanopatterning induced by C_{60} adsorption.," *Nature materials*, vol. 4, no. 9, pp. 688–92, 2005.

[122] W. Pai, C.-L. Hsu, M. Lin, K. Lin, and T. Tang, "Structural relaxation of adlayers in the presence of adsorbate-induced reconstruction: C_{60}/Cu(111)," *Physical Review B*, vol. 69, no. 12, p. 125405, 2004.

[123] A. Strózecka, J. Mysliveček, and B. Voigtländer, "Scanning tunneling spectroscopy and manipulation of C_{60} on Cu(111)," *Applied Physics A*, vol. 87, no. 3, pp. 475–478, 2007.

[124] M. Saunders, H. a. Jiménez-Vázquez, R. J. Cross, and R. J. Poreda, "Stable compounds of helium and neon: He@C_{60} and Ne@C_{60}," *Science (New York, N.Y.)*, vol. 259, no. 5100, pp. 1428–30, 1993.

[125] M. Saunders, H. A. Jimenez-Vazquez, R. J. Cross, S. Mroczkowski, M. L. Gross, D. E. Giblin, and R. J. Poreda, "Incorporation of helium, neon, argon, krypton, and xenon into fullerenes using high pressure," *Journal of the American Chemical Society*, vol. 116, no. 5, pp. 2193–2194, 1994.

[126] Y. Rubin, T. Jarrosson, G.-W. Wang, M. D. Bartberger, K. N. Houk, G. Schick, M. Saunders, and R. J. Cross, "Insertion of Helium and Molecular Hydrogen Through the Orifice of an Open Fullerene," *Angewandte Chemie*, vol. 113, no. 8, pp. 1591–1594, 2001.

[127] S.-i. Iwamatsu and S. Murata, "H_2O@open-cage fullerene C_{60}: control of the encapsulation property and the first mass spectroscopic identification," *Tetrahedron Letters*, vol. 45, no. 34, pp. 6391–6394, 2004.

[128] Z. Xiao, J. Yao, D. Yang, F. Wang, S. Huang, L. Gan, Z. Jia, Z. Jiang, X. Yang, B. Zheng, G. Yuan, S. Zhang, and Z. Wang, "Synthesis of [59]fullerenones through peroxide-mediated stepwise cleavage of fullerene skeleton bonds and X-ray structures of their water-encapsulated open-cage complexes," *Journal of the American Chemical Society*, vol. 129, no. 51, pp. 16149–62, 2007.

[129] K. Komatsu, M. Murata, and Y. Murata, "Encapsulation of molecular hydrogen in fullerene C_{60} by organic synthesis.," *Science (New York, N.Y.)*, vol. 307, no. 5707, pp. 238–40, 2005.

[130] K. Kurotobi and Y. Murata, "A single molecule of water encapsulated in fullerene C_{60}," *Science (New York, N.Y.)*, vol. 333, no. 6042, pp. 613–6, 2011.

[131] J.-M. Lehn, "Toward complex matter: Supramolecular chemistry and self-organization," *Proceedings of the National Academy of Sciences*, vol. 99, no. 8, pp. 4763–4768, 2002.

[132] J.-M. Lehn, "From supramolecular chemistry towards constitutional dynamic chemistry and adaptive chemistry," *Chem. Soc. Rev.*, vol. 36, no. 2, pp. 151–160, 2007.

[133] J. A. Theobald, N. S. Oxtoby, M. A. Phillips, N. R. Champness, and P. H. Beton, "Controlling molecular deposition and layer structure with supramolecular surface assemblies," *Nature*, vol. 424, no. 6952, pp. 1029–1031, 2003.

[134] J. V. Barth, G. Costantini, and K. Kern, "Engineering atomic and molecular nanostructures at surfaces," *Nature*, vol. 437, no. 7059, pp. 671–679, 2005.

[135] L. Gross, F. Mohn, N. Moll, B. Schuler, A. Criado, E. Guitian, D. Pena, A. Gourdon, and G. Meyer, "Bond-Order Discrimination by Atomic Force Microscopy," *Science*, vol. 337, no. 6100, pp. 1326–1329, 2012.

[136] N. Pavliček, B. Fleury, M. Neu, J. Niedenführ, C. Herranz-Lancho, M. Ruben, and J. Repp, "Atomic force microscopy reveals bistable configurations of Dibenzo[a,h]thianthrene and their interconversion pathway," *Phys. Rev. Lett.*, vol. 108, no. 8, 2012.

[137] D. G. de Oteyza, P. Gorman, Y.-C. Chen, S. Wickenburg, A. Riss, D. J. Mowbray, G. Etkin, Z. Pedramrazi, H.-Z. Tsai, A. Rubio, M. F. Crommie, and F. R. Fischer, "Direct Imaging of Covalent Bond Structure in Single-Molecule Chemical Reactions," *Science*, vol. 340, no. 6139, pp. 1434–1437, 2013.

[138] S. P. Jarvis, S. Taylor, J. D. Baran, N. R. Champness, J. A. Larsson, and P. Moriarty, "Measuring the mechanical properties of molecular conformers," *Nature Commun.*, vol. 6, p. 8338, 2015.

[139] A. Sweetman, S. P. Jarvis, P. Rahe, N. R. Champness, L. Kantorovich, and P. Moriarty, "Intramolecular bonds resolved on a semiconductor surface," *Physical Review B*, vol. 90, no. 16, 2014.

[140] L. Gross, "Recent advances in submolecular resolution with scanning probe microscopy," *Nature Chemistry*, vol. 3, no. 4, pp. 273–278, 2011.

[141] S. Jarvis, "Resolving Intra- and Inter-Molecular Structure with Non-Contact Atomic Force Microscopy," *International Journal of Molecular Sciences*, vol. 16, no. 8, pp. 19936–19959, 2015.

[142] F. Mohn, B. Schuler, L. Gross, and G. Meyer, "Different tips for high-resolution atomic force microscopy and scanning tunneling microscopy of single molecules," *Applied Physics Letters*, vol. 102, no. 7, 2013.

[143] G. Kichin, C. Weiss, C. Wagner, F. S. Tautz, and R. Temirov, "Single Molecule and Single Atom Sensors for Atomic Resolution Imaging of Chemically Complex Surfaces," *Journal of the American Chemical Society*, vol. 133, no. 42, pp. 16847–16851, 2011.

[144] O. Guillermet, S. Gauthier, C. Joachim, P. de Mendoza, T. Lauterbach, and A. Echavarren, "STM and AFM high resolution intramolecular imaging of a single decastarphene molecule," *Chemical Physics Letters*, vol. 511, no. 4-6, pp. 482–485, 2011.

[145] S. Kawai, A. Sadeghi, X. Feng, P. Lifen, R. Pawlak, T. Glatzel, A. Willand, A. Orita, J. Otera, S. Goedecker, and E. Meyer, "Obtaining Detailed Structural Information about Supramolecular Systems on Surfaces by Combining High-Resolution Force Microscopy with ab Initio Calculations," *ACS Nano*, vol. 7, no. 10, pp. 9098–9105, 2013.

[146] A. M. Sweetman, S. P. Jarvis, H. Sang, I. Lekkas, P. Rahe, Y. Wang, J. Wang, N. R. Champness, L. Kantorovich, and P. Moriarty, "Mapping the force field of a hydrogen-bonded assembly.," *Nature communications*, vol. 5, no. 2014, p. 3931, 2014.

[147] H. Sang, S. P. Jarvis, Z. Zhou, P. Sharp, P. Moriarty, J. Wang, Y. Wang, and L. Kantorovich, "Identifying tips for intramolecular NC-AFM imaging via in situ fingerprinting," *Scientific Reports*, vol. 4, p. 6678, 2014.

[148] N. Pavliček, B. Fleury, M. Neu, J. Niedenführ, C. Herranz-Lancho, M. Ruben, and J. Repp, "Atomic Force Microscopy Reveals Bistable Configurations of Dibenzo[a,h]thianthrene and their Interconversion Pathway," *Physical Review Letters*, vol. 108, no. 8, 2012.

[149] J. Zhang, P. Chen, B. Yuan, W. Ji, Z. Cheng, and X. Qiu, "Real-Space Identification of Intermolecular Bonding with Atomic Force Microscopy," *Science*, vol. 342, no. 6158, pp. 611–614, 2013.

[150] R. Temirov, S. Soubatch, O. Neucheva, A. C. Lassise, and F. S. Tautz, "A novel method achieving ultra-high geometrical resolution in scanning tunnelling microscopy," *New Journal of Physics*, vol. 10, no. 5, p. 053012, 2008.

[151] P. Hapala, G. Kichin, C. Wagner, F. S. Tautz, R. Temirov, and P. Jelínek, "Mechanism of high-resolution STM/AFM imaging with functionalized tips," *Physical Review B*, vol. 90, no. 8, p. 085421, 2014.

[152] S. K. Hämäläinen, N. van der Heijden, J. van der Lit, S. den Hartog, P. Liljeroth, and I. Swart, "Intermolecular Contrast in Atomic Force Microscopy Images without Intermolecular Bonds," *Physical Review Letters*, vol. 113, no. 18, p. 186102, 2014.

[153] S. Kawai, A. Sadeghi, F. Xu, L. Peng, A. Orita, J. Otera, S. Goedecker, and E. Meyer, "Extended Halogen Bonding between Fully Fluorinated Aromatic Molecules," *ACS Nano*, vol. 9, no. 3, pp. 2574–2583, 2015.

[154] N. Moll, B. Schuler, S. Kawai, F. Xu, L. Peng, A. Orita, J. Otera, A. Curioni, M. Neu, J. Repp, G. Meyer, and L. Gross, "Image Distortions of a Partially Fluorinated Hydrocarbon Molecule in Atomic Force Microscopy with Carbon Monoxide Terminated Tips," *Nano Letters*, vol. 14, no. 11, pp. 6127–6131, 2014.

[155] M. Neu, N. Moll, L. Gross, G. Meyer, F. J. Giessibl, and J. Repp, "Image correction for atomic force microscopy images with functionalized tips," *Physical Review B*, vol. 89, no. 20, p. 205407, 2014.

[156] M. P. Boneschanscher, S. K. Hämäläinen, P. Liljeroth, and I. Swart, "Sample Corrugation Affects the Apparent Bond Lengths in Atomic Force Microscopy," *ACS Nano*, vol. 8, no. 3, pp. 3006–3014, 2014.

[157] P. Hapala, R. Temirov, F. S. Tautz, and P. Jelínek, "Origin of High-Resolution IETS-STM Images of Organic Molecules with Functionalized Tips," *Physical Review Letters*, vol. 113, no. 22, p. 226101, 2014.

[158] C.-S. Guo, X. Xin, M. A. Van Hove, X. Ren, and Y. Zhao, "Origin of the Contrast Interpreted as Intermolecular and Intramolecular Bonds in Atomic Force Microscopy Images," *The Journal of Physical Chemistry C*, vol. 119, no. 25, p. 1419514200, 2015.

[159] C. Davisson and L. Germer, "Reflection and Refraction of Electrons by a Crystal of Nickel," *Proceedings of the National Academy of Sciences of the United States of America*, vol. 14, no. 8, pp. 619–627, 1928.

[160] H. Hertz, "Ueber einen einfluss des ultravioletten lichtes auf die electrische entladung," *Annalen der Physik*, vol. 267, no. 8, pp. 983–1000, 1887.

[161] A. B. Arons and M. B. Peppard, "Einstein's proposal of the photon concept translation of the annalen der physik paper of 1905," *American Journal of Physics*, vol. 33, no. 5, pp. 367–374, 1965.

[162] R. A. Millikan, "A direct photoelectric determination of planck's h," *Physical Review*, vol. 7, no. 3, pp. 355–388, 1916.

[163] "The nobel prize in physics 1921," *Nobelprize.org*, 1921.

[164] "The nobel prize in physics 1923," *Nobelprize.org*, 1923.

[165] "The nobel prize in physics 1981," *Nobelprize.org*, 1981.

[166] M. von Laue, *Rontgenstrahl-Interferenzen*. Akademische Verlagsgesellschaft, Becker and ErlerKolm.-Ges, 1941.

[167] W. Kossel and H. Voges, "Rontgenstrahl-interferenzen an der einkristallantikathode," *Annalen der Physik*, vol. 415, no. 8, pp. 677–704, 1935.

[168] J. Zegenhagen and A. Kazimirov, "X-ray standing waves in a nutshell," in *Series on Synchrotron Radiation Techniques and Applications*, vol. Volume 7, pp. 3–35, World Scientific, 2011.

[169] G. Borrmann, "ber extinktionsdiagramme der rntgenstrahlen von quarz," *Physik Z.*, vol. 42, pp. 157–162, 1941.

[170] B. W. Batterman and H. Cole, "Dynamical diffraction of x-rays by perfect crystals," *Reviews of Modern Physics*, vol. 36, no. 3, pp. 681–717, 1964.

[171] J. A. Golovchenko, B. W. Batterman, and W. L. Brown, "Observation of internal x-ray wave fields during Bragg diffraction with an application to impurity lattice location," *Physical Review B*, vol. 10, no. 10, pp. 4239–4243, 1974.

[172] P. L. Cowan, J. A. Golovchenko, and M. F. Robbins, "X-Ray Standing Waves at Crystal Surfaces," *Physical Review Letters*, vol. 44, no. 25, pp. 1680–1683, 1980.

[173] M. Bedzyk, D. Bilderback, G. Bommarito, M. Caffrey, and J. Schildkraut, "X-ray standing waves: a molecular yardstick for biological membranes," *Science*, vol. 241, no. 4874, pp. 1788–1791, 1988.

[174] D. Bahr, J. Falta, G. Materlik, B. Müller, and M. Horn-von Hoegen, "X-ray interface characterization of Ge δ layers on Si (001)," *Physica B: Condensed Matter*, vol. 221, no. 1-4, pp. 96–100, 1996.

[175] M. Takahasi, S. Nakatani, T. Takahashi, X. Zhang, M. Ando, S. Fukatsu, and Y. Shiraki, "Si/1ML-Ge/Si(001) Interface Structure Characterized by Surface X-Ray Diffraction and X-Ray Standing-Wave Method," *Japanese Journal of Applied Physics*, vol. 34, no. 5A, pp. 2278–2283, 1995.

[176] S. Nakatani, K. Sumitani, A. Nojima, T. Takahashi, K. Hirano, S. Koh, T. Irisawa, and Y. Shiraki, "Characterization of amorphous-Si/1ML-Ge/Si(001) Interface Structure by X-ray Standing Waves," *Japanese Journal of Applied Physics*, vol. 42, no. 11, pp. 7050–7052, 2003.

[177] T. Yamanaka and S. Ino, "Atomic depth distribution and effects of surfactants in growth of Ag and Au on Si(111)-$\sqrt{3}$ x $\sqrt{3}$-Ga(1ML), 4 x 1-In and -2$\sqrt{3}$ x 2$\sqrt{3}$-Sn surfaces at room temperature," *Physical Review B*, vol. 66, no. 8, p. 085316, 2002.

[178] A. E. M. J. Fischer, E. Vlieg, J. F. van der Veen, M. Clausnitzer, and G. Materlik, "Structure determination of the CoSi:Si(111) interface by x-ray standing-wave analysis," *Physical Review B*, vol. 36, no. 9, pp. 4769–4773, 1987.

[179] J. Zegenhagen, K. G. Huang, B. D. Hunt, and L. J. Schowalter, "Interface structure and lattice mismatch of epitaxial $CoSi_2$ on Si(111)," *Applied Physics Letters*, vol. 51, no. 15, pp. 1176–1178, 1987.

[180] J. Zegenhagen, J. R. Patel, P. E. Freeland, and R. T. Tung, "Co on Si(111): Silicide formation," *Physical Review B*, vol. 44, no. 24, pp. 13626–13630, 1991.

[181] E. Vlieg, A. Fischer, J. van Der Veen, B. Dev, and G. Materlik, "Geometric structure of the $NiSi_2$ Si(111) interface: An X-ray standing-wave analysis," *Surface Science*, vol. 178, no. 1-3, pp. 36–46, 1986.

[182] J. Zegenhagen, K.-G. Huang, W. M. Gibson, B. D. Hunt, and L. J. Schowalter, "Structural properties of epitaxial NiSi on Si(111) investigated with x-ray standing waves," *Physical Review B*, vol. 39, no. 14, pp. 10254–10260, 1989.

[183] K. G. Huang, W. M. Gibson, and J. Zegenhagen, "X-ray standing-wave analysis with high reflection order and near-normal incidence," *Physical Review B*, vol. 40, no. 6, pp. 4216–4219, 1989.

[184] J. Zegenhagen and J. R. Patel, "CaF_2/Si heteroepitaxy: Importance of stoichiometry, interface bonding, and lattice mismatch," *Physical Review B*, vol. 41, no. 8, pp. 5315–5318, 1990.

[185] K. Huang, J. Zegenhagen, J. M. Phillips, and J. Patel, "Interface and overlayer structure of epitaxial CaF_2 thin films on Si(111): An X-ray scattering study," *Physica B: Condensed Matter*, vol. 221, no. 1-4, pp. 192–200, 1996.

[186] J. D. Denlinger, M. A. Olmstead, E. Rotenberg, J. R. Patel, and E. Fontes, "Atomic-size effects on the growth of SrF and (Ca,Sr)," *Physical Review B*, vol. 43, no. 9, pp. 7335–7338, 1991.

[187] V. Eteläniemi, E. Michel, and G. Materlik, "RbBr/Si(111) interface studied by the X-ray standing wave method," *Surface Science*, vol. 287-288, pp. 288–293, 1993.

[188] J. Zegenhagen, "Surface structure determination with X-ray standing waves," *Surface Science Reports*, vol. 18, no. 7-8, pp. 202–271, 1993.

[189] D. Woodruff, "Normal incidence X-ray standing wave determination of adsorbate structures," 1998.

[190] D. P. Woodruff, D. L. Seymour, C. F. McConville, C. E. Riley, M. D. Crapper, N. P. Prince, and R. G. Jones, "Simple x-ray standing-wave technique and its application to the investigation of the Cu(111) ($\sqrt{3}$ x $\sqrt{3}$) R30°-Cl structure," *Physical Review Letters*, vol. 58, no. 14, pp. 1460–1462, 1987.

[191] D. Woodruff, D. Seymour, C. McConville, C. Riley, M. Crapper, N. Prince, and R. G. Jones, "A simple X-ray standing wave technique for surface structure determination - theory and an application," *Surface Science*, vol. 195, no. 1-2, pp. 237–254, 1988.

[192] M. Kerkar, A. B. Hayden, D. P. Woodruff, M. Kadodwala, and R. G. Jones, "An unusual adsorption site for methoxy on Al(111) surfaces," *Journal of Physics: Condensed Matter*, vol. 4, no. 22, pp. 5043–5052, 1992.

[193] K. Schulte, R. A. J. Woolley, L. Wang, P. J. Moriarty, P. R. Birkett, H. W. Kroto, and B. C. C. Cowie, "XSW feasibility study of

C_{60}Ph5-OH on Ag(111): Combining hard X-rays, low Z and, low coverage," *Nuclear Instruments and Methods in Physics Research, Section A: Accelerators, Spectrometers, Detectors and Associated Equipment*, vol. 547, no. 1, pp. 208–215, 2005.

[194] R. A. J. Woolley, K. H. G. Schulte, L. Wang, P. J. Moriarty, B. C. C. Cowie, H. Shinohara, M. Kanai, and T. J. S. Dennis, "Does an Encapsulated Atom feel' the Effects of Adsorption?: X-ray Standing Wave Spectroscopy of Ce@C_{82} on Ag(111)," *Nano Letters*, vol. 4, no. 2, pp. 361–364, 2004.

[195] C. Ton-That, A. G. Shard, S. Egger, V. R. Dhanak, A. Taninaka, H. Shinohara, and M. E. Welland, "Orientation and constraints of endohedral lanthanum in La@C_{82} molecules adsorbed on Cu(111)," *Physical Review B*, vol. 68, no. 4, p. 045424, 2003.

[196] R. Woolley, C. Martin, G. Miller, V. Dhanak, and P. Moriarty, "Adsorbed molecular shuttlecocks: An NIXSW study of Sn phthalocyanine on Ag(111) using Auger electron detection," *Surface Science*, vol. 601, no. 5, pp. 1231–1238, 2007.

[197] J. Stroscio and W. Kaiser, "Scanning Tunnelling Microscopy," *Academic Press*, 1993.

[198] J. Tersoff and D. Hamann, "Theory and application for the scanning tunneling microscope," *Physical review letters*, vol. 50, no. 25, p. 1998, 1983.

[199] J. Bardeen, "Tunnelling from a Many-Particle Point of View," *Physical Review Letters*, vol. 6, no. 2, pp. 57–59, 1961.

[200] C. J. Chen, "Theory of scanning tunneling spectroscopy," *Journal of Vacuum Science & Technology A: Vacuum, Surfaces, and Films*, vol. 6, no. 2, p. 319, 1988.

[201] L. Gross, N. Moll, F. Mohn, A. Curioni, G. Meyer, F. Hanke, and M. Persson, "High-Resolution Molecular Orbital Imaging Using a p-Wave STM Tip," *Physical Review Letters*, vol. 107, no. 8, p. 086101, 2011.

[202] J. N. Israelachvili, *Intermolecular and Surface Forces*. Academic Press, 2010.

[203] Y. Sugimoto, P. Pou, M. Abe, P. Jelinek, R. Pérez, S. Morita, and O. Custance, "Chemical identification of individual surface atoms by atomic force microscopy," *Nature*, vol. 446, no. 7131, pp. 64–7, 2007.

[204] H. C. Hamaker, "The london-van der waals attraction between spherical particles," *Physica*, vol. 4, no. 10, pp. 1058 – 1072, 1937.

[205] F. London, "The general theory of molecular forces," *Transactions of the Faraday Society*, vol. 33, pp. 8–26, 1937.

[206] F. Giessibl, "Forces and frequency shifts in atomic-resolution dynamic-force microscopy," *Physical Review B*, vol. 56, pp. 16010–16015, 1997.

[207] S. Sadewasser and M. Lux-Steiner, "Correct Height Measurement in Noncontact Atomic Force Microscopy," *Physical Review Letters*, vol. 91, no. 26, p. 266101, 2003.

[208] J. E. Lennard-Jones, "Cohesion," *Proceedings of the Physical Society*, vol. 43, no. 5, pp. 461–482, 1931.

[209] G. Meyer and N. Amer, "Novel optical approach to atomic force microscopy," *Applied Physics Letters*, vol. 53, pp. 1045–1047, 1988.

[210] U. Durig, "Conservative and dissipative interactions in dynamic force microscopy," *Surface and Interface Analysis*, vol. 27, no. 5-6, pp. 467–473, 1999.

[211] U. Durig, "Relations between interaction force and frequency shift in large-amplitude dynamic force microscopy," *Applied Physics Letters*, vol. 75, no. 3, p. 433, 1999.

[212] A. I. Livshits, A. L. Shluger, and A. L. Rohl, "Contrast mechanism in non-contact SFM imaging of ionic surfaces," *Applied Surface Science*, vol. 140, no. 3-4, pp. 327–332, 1999.

[213] A. Sweetman and A. Stannard, "Uncertainties in forces extracted from non-contact atomic force microscopy measurements by fitting of long-range background forces," *Beilstein Journal of Nanotechnology*, vol. 5, pp. 386–393, 2014.

[214] J. Sader and S. Jarvis, "Accurate formulas for interaction force and energy in frequency modulation force spectroscopy," *Applied Physics Letters*, vol. 84, p. 1801, 2004.

[215] J. Welker, E. Illek, and F. Giessibl, "Analysis of force-deconvolution methods in frequency-modulation atomic force microscopy," *Beilstein Journal of Nanotechnology*, vol. 3, pp. 238–248, 2012.

[216] C. Darwin, "XXXIV. The theory of X-ray reflexion," *Philosophical Magazine Series 6*, vol. 27, no. 158, pp. 315–333, 1914.

[217] F. Giessibl, "Atomic resolution of the silicon (111)-(7x7) surface by atomic force microscopy.," *Science (New York, N.Y.)*, vol. 267, no. 5194, pp. 68–71, 1995.

[218] K. Besocke, "An easily operable scanning tunneling microscope," *Surface Science*, vol. 181, pp. 145–153, 1987.

[219] G. Kelsey, "The anodic oxidation of tungsten in aqueous base," *Journal of the Electrochemical Society*, pp. 814–819, 1977.

[220] G. J. Jackson, B. C. C. Cowie, D. P. Woodruff, R. G. Jones, M. S. Kariapper, C. Fisher, A. S. Y. Chan, and M. Butterfield, "Atomic quadrupolar photoemission asymmetry parameters from a solid state measurement," *Physical Review*, vol. 84, no. 11, p. 2346, 2000.

[221] J. J. Lee, C. J. Fisher, D. P. Woodruff, M. G. Roper, R. G. Jones, and B. C. C. Cowie, "Non-dipole effects in photoelectron-monitored X-ray standing wave experiments: Characterisation and calibration," *Surface Science*, vol. 494, no. 3, pp. 166–182, 2001.

[222] "Image from diamond light source," *diamond.ac.uk*, 2015.

[223] "Image from slri," *slri.or.th*, 2015.

[224] K. Prabhakaran and T. Ogino, "Oxidation of Ge(100) and Ge(111) surfaces: an UPS and XPS study," *Surface Science*, vol. 325, no. 3, pp. 263–271, 1995.

[225] T. Kreuch, S. Meierott, N. Néel, W. J. D. Beenken, and J. Kröger, "Atom-by-Atom Dehalogenation of a Porphyrin Molecule Adsorbed on Ag(111)," *The Journal of Physical Chemistry C*, vol. 118, no. 51, pp. 30162–30169, 2014.

[226] A. Deshpande, K. Felix Braun, and S.-W. Hla, "Determination of chemical specific atomic interaction with scanning tunneling microscope," *Applied Physics Letters*, vol. 99, no. 22, p. 221902, 2011.

[227] A. Weber-Bargioni, W. Auwärter, F. Klappenberger, J. Reichert, S. Lefrançois, T. Strunskus, C. Wöll, A. Schiffrin, Y. Pennec, and J. V. Barth, "Visualizing the Frontier Orbitals of a Conformationally Adapted Metalloporphyrin," *ChemPhysChem*, vol. 9, no. 1, pp. 89–94, 2008.

[228] C. Chiutu, A. M. Sweetman, A. J. Lakin, A. Stannard, S. Jarvis, L. Kantorovich, J. L. Dunn, and P. Moriarty, "Precise Orientation of a Single C_{60} Molecule on the Tip of a Scanning Probe Microscope," *Physical Review Letters*, vol. 108, no. 26, p. 268302, 2012.

[229] B. Schuler, W. Liu, A. Tkatchenko, N. Moll, G. Meyer, A. Mistry, D. Fox, and L. Gross, "Adsorption Geometry Determination of Single Molecules by Atomic Force Microscopy," *Physical Review Letters*, vol. 111, no. 10, p. 106103, 2013.

[230] A. Sweetman, A. Stannard, Y. Sugimoto, M. Abe, S. Morita, and P. Moriarty, "Simultaneous noncontact AFM and STM of Ag:Si(111)-($\sqrt{3}$ x $\sqrt{3}$) R30°," *Physical Review B*, vol. 87, no. 7, p. 075310, 2013.

[231] A. Bondi, "van der Waals Volumes and Radii," *The Journal of Physical Chemistry*, vol. 68, no. 3, pp. 441–451, 1964.

[232] A. Schwarz, D. Z. Gao, K. Lämmle, J. Grenz, M. B. Watkins, A. L. Shluger, and R. Wiesendanger, "Determining Adsorption Geometry, Bonding, and Translational Pathways of a MetalOrganic Complex on an Oxide Surface: Co-Salen on NiO(001)," *The Journal of Physical Chemistry C*, vol. 117, no. 2, pp. 1105–1112, 2013.

[233] N. Kovačević and A. Kokalj, "DFT Study of Interaction of Azoles with Cu(111) and Al(111) Surfaces: Role of Azole Nitrogen Atoms and DipoleDipole Interactions," *The Journal of Physical Chemistry C*, vol. 115, no. 49, pp. 24189–24197, 2011.

[234] B. W. Caplins, D. E. Suich, A. J. Shearer, and C. B. Harris, "Metal/Phthalocyanine Hybrid Interface States on Ag(111)," *The Journal of Physical Chemistry Letters*, vol. 5, no. 10, pp. 1679–1684, 2014.

[235] R. Temirov, S. Soubatch, A. Luican, and F. S. Tautz, "Free-electron-like dispersion in an organic monolayer film on a metal substrate," *Nature*, vol. 444, no. 7117, pp. 350–353, 2006.

[236] W. Liu, J. Carrasco, B. Santra, A. Michaelides, M. Scheffler, and A. Tkatchenko, "Benzene adsorbed on metals: Concerted effect of covalency and van der Waals bonding," *Physical Review B*, vol. 86, no. 24, p. 245405, 2012.

[237] J. D. Baran, H. Grönbeck, and A. Hellman, "Analysis of Porphyrines as Catalysts for Electrochemical Reduction of O_2 and Oxidation of H_2O," *Journal of the American Chemical Society*, vol. 136, no. 4, pp. 1320–1326, 2014.

[238] W. Auwarter, K. Seufert, F. Klappenberger, J. Reichert, A. Weber-Bargioni, A. Verdini, D. Cvetko, M. DellAngela, L. Floreano, A. Cossaro, G. Bavdek, A. Morgante, A. P. Seitsonen, and J. V. Barth,

"Site-specific electronic and geometric interface structure of Co-tetraphenyl-porphyrin layers on Ag(111)," *Physical Review B*, vol. 81, no. 24, p. 245403, 2010.

[239] H. Vazquez, Y. Dappe, J. Ortega, and F. Flores, "A unified model for metal/organic interfaces: IDIS, pillow effect and molecular permanent dipoles," *Applied Surface Science*, vol. 254, no. 1, pp. 378–382, 2007.

[240] B. Chilukuri, U. Mazur, and K. W. Hipps, "Effect of dispersion on surface interactions of cobalt(II) octaethylporphyrin monolayer on Au(111) and HOPG(0001) substrates: a comparative first principles study," *Phys. Chem. Chem. Phys.*, vol. 16, no. 27, pp. 14096–14107, 2014.

[241] C. Gong, G. Lee, B. Shan, E. M. Vogel, R. M. Wallace, and K. Cho, "First-principles study of metalgraphene interfaces," *Journal of Applied Physics*, vol. 108, no. 12, p. 123711, 2010.

[242] F. Mohn, "Probing electronic and structural properties of single molecules on the atomic scale," *PhD Thesis*, 2012.

[243] L. Bartels, G. Meyer, and K.-H. Rieder, "Basic steps of lateral manipulation of single atoms and diatomic clusters with a scanning tunneling microscope tip," *Phys. Rev. Lett.*, vol. 79, pp. 697–700, 1997.

[244] Y. Sugimoto, "Complex patterning by vertical interchange atom manipulation using atomic force microscopy," *Science*, vol. 322, pp. 413–417, 2008.

[245] A. Sweetman, "Toggling bistable atoms via mechanical switching of bond angle," *Phys. Rev. Lett.*, vol. 106, p. 136101, 2011.

[246] N. Atodiresei, V. Caciuc, P. Lazic, and S. Blugel, "Chemical versus van der Waals interaction: the role of the Heteroatom," *Phys. Rev. Lett.*, vol. 102, p. 136809, 2008.

[247] C. Burker, C. Bürker, N. Ferri, A. Tkatchenko, A. Gerlach, J. Niederhausen, T. Hosokai, S. Duhm, J. Zegenhagen, N. Koch, and F. Schreiber, "Exploring the bonding of large hydrocarbons on noble metals: Diindoperylene on Cu(111), Ag(111), and Au(111)," *Physical Review B*, vol. 87, no. 16, p. 165443, 2013.

[248] G. Li, I. Tamblyn, V. R. Cooper, H.-J. Gao, and J. B. Neaton, "Molecular adsorption on metal surfaces with van der Waals density functionals," *Phys. Rev. B*, vol. 85, p. 121409, 2012.

[249] C. Wagner, "Non-additivity of molecule-surface van der Waals potentials from force measurements," *Nat. Commun.*, vol. 5, p. 5568, 2014.

[250] B. A. J. Lechner, "Quantum influences in the diffusive motion of pyrrole on Cu(111)," *Angew. Chem. Int. Ed. Engl.*, vol. 52, pp. 5085–5088, 2013.

[251] R. Pawlak, S. Kawai, S. Fremy, T. Glatzel, and E. Meyer, "Atomic-Scale Mechanical Properties of Orientated C_{60} Molecules Revealed by Noncontact Atomic Force Microscopy," *ACS Nano*, vol. 5, no. 8, pp. 6349–6354, 2011.

[252] R. Pawlak, S. Kawai, S. Fremy, T. Glatzel, and E. Meyer, "High-resolution imaging of C_{60} molecules using tuning-fork-based non-contact atomic force microscopy," *Journal of Physics: Condensed Matter*, vol. 24, no. 8, p. 084005, 2012.

[253] S. P. Jarvis, M. A. Rashid, A. Sweetman, J. Leaf, S. Taylor, P. Moriarty, and J. Dunn, "Intermolecular artifacts in probe microscope images of C_{60} assemblies," *Physical Review B*, vol. 92, no. 24, p. 241405, 2015.

[254] F. Rossel, M. Pivetta, F. Patthey, E. Ćavar, A. P. Seitsonen, and W.-D. Schneider, "Growth and characterization of fullerene nanocrystals on NaCl/Au(111)," *Physical Review B*, vol. 84, no. 7, p. 075426, 2011.

[255] Z. Sun, M. P. Boneschanscher, I. Swart, D. Vanmaekelbergh, and P. Liljeroth, "Quantitative Atomic Force Microscopy with Carbon Monoxide Terminated Tips," *Physical Review Letters*, vol. 106, no. 4, p. 046104, 2011.

[256] N. Hauptmann, F. Mohn, L. Gross, G. Meyer, T. Frederiksen, and R. Berndt, "Force and conductance during contact formation to a C_{60} molecule," *New Journal of Physics*, vol. 14, no. 7, p. 073032, 2012.

[257] L. A. Girifalco, "Interaction potential for carbon (C_{60}) molecules," *The Journal of Physical Chemistry*, vol. 95, no. 14, pp. 5370–5371, 1991.

[258] L. Gross *Private communication*, 2015.

[259] H.-I. Li, "Structural analysis and interactions of C_{60} on Ag(111) and Pb(111)," *Dissertation*, vol. 1, pp. 1689–1699, 2010.

[260] K. Pussi, H. I. Li, H. Shin, L. N. Serkovic Loli, A. K. Shukla, J. Ledieu, V. Fournée, L. L. Wang, S. Y. Su, K. E. Marino, M. V. Snyder, and R. D. Diehl, "Elucidating the dynamical equilibrium of C_{60} molecules on Ag(111)," *Physical Review B*, vol. 86, no. 20, p. 205406, 2012.

[261] C. Ton-That, A. G. Shard, S. Egger, V. R. Dhanak, and M. E. Welland, "Modulations of valence-band photoemission spectrum from C_{60} monolayers on Ag(111)," *Physical Review B*, vol. 67, no. 15, p. 155415, 2003.

[262] A. Barrie and N. E. Christensen, "High-resolution x-ray photoemission spectra of silver," *Physical Review B*, vol. 14, no. 6, pp. 2442–2447, 1976.

[263] P. A. Bruhwiler, A. J. Maxwell, A. Nilsson, N. Mårtensson, and O. Gunnarsson, "Auger and photoelectron study of the Hubbard U in C_{60} , K_3C_{60} , and K_6C_{60}," *Physical Review B*, vol. 48, no. 24, pp. 18296–18299, 1993.

[264] L. H. Tjeng, R. Hesper, a. C. L. Heessels, a. Heeres, H. T. Jonkman, and G. a. Sawatzky, "Development of the electronic structure in a K-doped C_{60} monolayer on a Ag(111) surface," *Solid State Communications*, vol. 103, no. 1, pp. 31–35, 1997.

[265] G. Wertheim and D. Buchanan, "Interfacial reaction of C_{60} with silver," *Physical Review B*, vol. 50, no. 15, pp. 11070–11073, 1994.

[266] R. Haddon, L. Brus, and K. Raghavachari, "Electronic structure and bonding in icosahedral c_{60}," *Chemical Physics Letters*, vol. 125, no. 5, pp. 459 – 464, 1986.

[267] S. J. Chase, W. S. Bacsa, M. G. Mitch, L. J. Pilione, and J. S. Lannin, "Surface-enhanced Raman scattering and photoemission of C_{60} on noble-metal surfaces," *Physical Review B*, vol. 46, no. 12, pp. 7873–7877, 1992.

10 Appendix

10.1 STM

10.1.1 The finite potential barrier

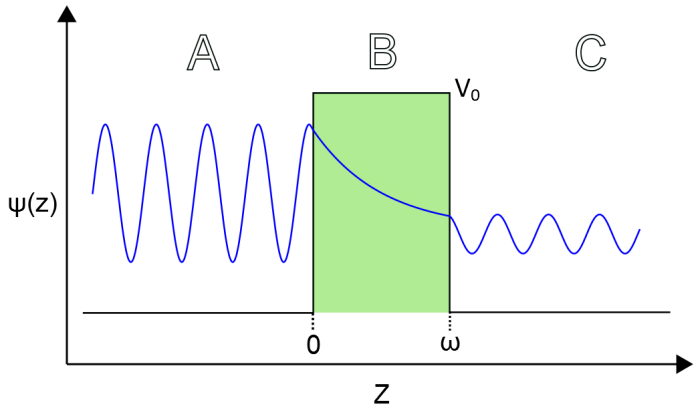

Figure 108: *Schematic showing an electron wavefunction with energy E incident on a 1D barrier of energy V_0. Region A shows the propagating electron, region B shows the exponentially decaying wavefunction through the potential barrier of width ω and region C shows the emergence of the wavefunction with a diminished amplitude.*

To derive α and k we consider a particle moving in the positive z direction with kinetic energy E. We then take the wavefunction of the particle in each region (A for $z < 0$, B for $0 < z < \omega$ and C for $z > \omega$) and insert them into the time-independent 1D Schrödinger equation

$$\frac{-\hbar^2}{2m}\frac{\partial^2\Psi}{\partial z^2} + V(z)\Psi = E\Psi \tag{81}$$

by inserting the wavefunction in region A

$$\Psi_A = Ae^{ikz} + Be^{-ikz} \tag{82}$$

into the Schrödinger equation, where the positive exponent describes the incident wavefunction on the barrier, and the negative exponent represents the reflected wavefunction from the potential barrier, and assuming $V(z) = 0$ for $0 > z > \omega$, then

$$k = \frac{\sqrt{2mE}}{\hbar} \tag{83}$$

to calculate α, or the decay constant, we use the wavefunction in region B

$$\Psi_B = Ce^{\alpha z} + Be^{-\alpha z} \tag{84}$$

after inserting Ψ_B into the Schrödinger equation, with potential barrier energy $V(z) = V_0$, then

$$\alpha = \frac{\sqrt{2m(V_0 - E)}}{\hbar} \tag{85}$$

finally, the wavefunction for region C

$$\Psi_C = Fe^{ikz} \tag{86}$$

can also be inserted into the Schrödinger equation (single exponent represents the wavefunction travelling in the positive z direction), so that

$$k = \frac{\sqrt{2mE}}{\hbar} \tag{87}$$

which is similar to region A, as expected, where $V(z) = 0$ for $0 > z > \omega$.

10.1.2 Deriving the transmission coefficient

In quantum mechanics, the current density flux in 1D is represented by

$$j = \frac{\hbar}{2im}\left[\Psi^* \frac{\partial \Psi}{\partial z} - \frac{\partial \Psi^*}{\partial z}\Psi\right] \tag{88}$$

We shall consider $\frac{j_C}{j_A} = T$, where T is the transmission coefficient. The reflected part of the wavefunction in region A Be^{-ikz} will be ignored as it will not contribute to the transmission amplitude.

By inserting the positive exponent of the wavefunction in region A, $\Psi_A = Ae^{ikz}$, into the current density flux equation then

$$j_A = \frac{\hbar}{2im}\left[2ik\Psi_A^*\Psi_A\right] \tag{89}$$

where $\Psi_A^*\Psi_A = AA^*$, so

$$j_A = \frac{\hbar k}{m}\left[AA^*\right] \tag{90}$$

then by considering the wavefunction in region C Fe^{ikz}, and insterting into the current density flux equation

$$j_C = \frac{\hbar}{2im}\left[2ik\Psi_C^*\Psi_C\right] \tag{91}$$

yielding

$$j_C = \frac{\hbar k}{m}\left[FF^*\right] \tag{92}$$

where $\Psi_C^*\Psi_C = FF^*$.

The transmission coefficient is then

$$T = \frac{j_C}{j_A} = \frac{FF^*}{AA^*} = \left|\frac{F}{A}\right|^2 \tag{93}$$

where $||^2$ is a complex number multiplied by its conjugate.

A similar mathematical process can be used to calculate the reflection coefficient, by calculating the ratio of probability amplitudes for the negative and positive parts of the Ψ_A wavefunction, and inserting them into the current density flux equation: $\frac{j_{A-}}{j_{A+}}$. It turns out that

$$R = \frac{j_{A-}}{j_{A+}} = \frac{BB^*}{AA^*} = \left|\frac{B}{A}\right|^2 \tag{94}$$

to acquire an analytical solution for the transmission coefficient, the boundary constraints at $z = 0$ and $z = \omega$ must be both continuous and continuously differentiable to satisfy Schrödinger's equation.

$$\Psi_A = \Psi_B \rightarrow Ae^{ikz} + Be^{-ikz} = Ce^{\alpha z} + De^{-\alpha z} \tag{95}$$

$$\frac{\partial \Psi_A}{\partial z} = \frac{\partial \Psi_B}{\partial z} \rightarrow ikAe^{ikz} + ikBe^{-ikz} = \alpha Ce^{\alpha z} + \alpha De^{-\alpha z} \tag{96}$$

$$\Psi_B = \Psi_C \rightarrow Ce^{\alpha z} + De^{-\alpha z} = Fe^{ikz} \tag{97}$$

$$\frac{\partial \Psi_B}{\partial z} = \frac{\partial \Psi_C}{\partial z} \rightarrow \alpha Ce^{\alpha z} + \alpha De^{-\alpha z} = ikFe^{ikz} \tag{98}$$

By inserting boundary constraints in equations 95 and 98

$z = 0$

$$A + B = C + D \tag{99}$$

$$ik(A - B) = \alpha(C - D) \tag{100}$$

$z = \omega$

$$Fe^{ik\omega} = Ce^{\alpha\omega} + De^{-\alpha\omega} \tag{101}$$

$$ikFe^{ik\omega} = \alpha Ce^{\alpha\omega} + \alpha De^{-\alpha\omega} \tag{102}$$

T has previously been derived as $\left|\frac{F}{A}\right|^2$ so equations 99 - 102 can be solved by eliminating B, C and D. Multiplying equation 101 by α, and adding to equation 102

$$C = \frac{(\alpha + ik)}{2\alpha} Fe^{\omega(ik-\alpha)} \tag{103}$$

and multiplying equation 101 by α and subtracting from equation 102

$$D = \frac{(\alpha - ik)}{2\alpha} Fe^{\omega(ik+\alpha)} \tag{104}$$

then multiplying equation 99 by ik and adding equation 100 to eliminate B and express A in terms of C and D

$$A = \frac{(ik + \alpha)C}{2ik} + \frac{(ik - \alpha)D}{2ik} \tag{105}$$

now by inserting expressions for C and D, we obtain A in terms of F

$$A = \frac{(ik + \alpha)^2}{4ik\alpha} Fe^{\omega(ik-\alpha)} - \frac{(ik - \alpha)^2}{4ik\alpha} Fe^{\omega(ik+\alpha)} \tag{106}$$

and after a little rearranging

$$A = \frac{Fe^{ik\omega}}{4ik\alpha}\left[k^2(e^{\alpha\omega} - e^{-\alpha\omega}) + 2ik\alpha(e^{\alpha\omega} + e^{-\alpha\omega}) - \alpha^2(e^{\alpha\omega} - e^{-\alpha\omega})\right] \quad (107)$$

using the hyperbolic identities $sinh(z) = \frac{e^z - e^{-z}}{2}$ and $cosh(z) = \frac{e^z + e^{-z}}{2}$, then

$$A = \frac{Fe^{ik\omega}}{4ik\alpha}\left[(k^2 - \alpha^2).2sinh(\alpha\omega) + 4ik\alpha cosh(\alpha\omega)\right] \quad (108)$$

and its conjugate

$$A^* = \frac{Fe^{-ik\omega}}{-4ik\alpha}\left[(k^2 - \alpha^2).2sinh(\alpha\omega) - 4ik\alpha cosh(\alpha\omega)\right] \quad (109)$$

now $AA^* = |A|^2$ and $FF^* = |F|^2$ so

$$|A|^2 = \frac{|F|^2}{16k^2\alpha^2}\left[(k^2 - \alpha^2).4sinh^2(\alpha\omega) + 16k^2\alpha^2\alpha cosh^2(\alpha\omega)\right] \quad (110)$$

and using the identity $cosh^2(z) - sinh^2(z) = 1$ with more rearranging

$$|A|^2 = |F|^2\left[\frac{(k^2 + \alpha^2)^2 sinh^2(\alpha\omega)}{4k^2\alpha^2} + 1\right] \quad (111)$$

and finally

$$T = \left|\frac{F}{A}\right|^2 = \left[\frac{(k^2 + \alpha^2)^2 sinh^2(\alpha\omega)}{4k^2\alpha^2} + 1\right]^{-1} \quad (112)$$

If we assume a wide potential barrier, ($\alpha\omega >> 1$, and so $e^{\alpha\omega} >> e^{-\alpha\omega}$), then the $sinh^2(\alpha\omega)$ term dominates, resulting in

$$T \approx sinh^{-2}(\alpha\omega) \approx e^{-2\alpha\omega} \quad (113)$$

10.2 AFM

10.2.1 Relationship between Δf and F_{TS}

The tip-sample interaction force is detected as the resonant frequency shift of the cantilever (in FM-AFM mode). The relationship was first derived by Giessibl using a Hamiltonian-Jacobi approach, which is essentially first order perturbation theory. Similar results have also been achieved using a least-action principle [210]. The oscillatory motion of the cantilever can be written as a Fourier series, and the action integral can be written as

$$\bar{S} = \int_0^{T_0} \left[\frac{1}{2}\dot{s}^2 - \frac{1}{2}\omega_0^2 s^2 - \frac{\omega_0^2}{k} U_{ts}(s + s_0) \right] \tag{114}$$

By minimising the action, $\bar{S}$, the variation must vanish (i.e. $\frac{\delta \bar{S}}{\delta s} = 0$), therefore

$$\delta \bar{S} = \left[\frac{d}{dt}\left(\frac{\partial L}{\partial \dot{s}} \right) - \frac{\partial L}{\partial s} \right] \delta s = \int_0^T \left[\ddot{s} + \omega_0^2 s - \frac{\omega_0^2}{k} F_{ts}(s + s_0) \right] \delta s dt = 0 \tag{115}$$

where $-\frac{\partial U_{ts}}{\partial z} = F_{ts}$. We can then make the periodic ansatz

$$s(t) = \sum_{n=1}^{\infty} \frac{\partial s}{\partial a_n} cos(n\omega t) \delta a_n \tag{116}$$

then

$$\frac{\delta s}{\delta a_n} = \sum_{n=1}^{\infty} \frac{\partial s}{\partial a_n} = \sum_{n=1}^{\infty} cos(n\omega t) \tag{117}$$

so

$$\delta s = \sum_{n=1}^{\infty} cos(n\omega t)\delta a_n \tag{118}$$

we can also deduce derivations from the anstaz for $\dot{s}$ and $\ddot{s}$

$$\dot{s} = -\sum_{n=1}^{\infty} a_n sin(n\omega t).n\omega \tag{119}$$

$$\ddot{s} = -\sum_{n=1}^{\infty} a_n cos(n\omega t).n^2\omega^2 \tag{120}$$

and by substituting equations 118-120 into equation 115

$$\delta\bar{S} = \int_0^T \left[-\sum_{n=1}^{\infty} a_n cos(n\omega t)n^2\omega^2 + \sum_{n=1}^{\infty} \omega_0^2 a_n cos(n\omega t) \ldots \right. \tag{121}$$
$$\left. \ldots \frac{\omega_0^2}{k} F_{ts}(s + s_0) \right] \sum_{n=1}^{\infty} cos(n\omega t)\delta a_n dt$$

By using the Prosthaphaeresis formula $cos(\theta)cos(\psi) = \frac{cos(\theta-\psi)+cos(\theta+\psi)}{2}$

$$\int_0^T -\sum_{n=1}^{\infty} a_n cos(n\omega t)n^2\omega^2 \sum_{n=1}^{\infty} cos(n\omega t)\delta a_n dt \tag{122}$$

can be written as

$$-a_n n^2\omega^2\delta a_n \sum_{n=1}^{\infty} \int_0^T \underbrace{cos(n\omega t)cos(n\omega t)}_{\frac{cos(n-n)+cos(2n\omega t)}{2}} dt \tag{123}$$

where

$$\int_0^T \frac{1}{2} + \frac{1}{2}cos(2n\omega t) = \frac{\pi}{\omega} \tag{124}$$

as any integral over time for $cos(2n\omega t) = 0$ and the period $T = \frac{2\pi}{\omega}$.

Equation 121 then becomes

$$\delta\bar{S} = \frac{\pi}{\omega}\sum_{n=1}^{\infty}\left(-n^2\omega^2+\omega_0^2\right)a_n\delta a_n - \ldots \tag{125}$$
$$\ldots\int_0^T\left[\frac{\omega_0^2}{k}F_{ts}(s+s_0)\sum_{n=1}^{\infty}cos(n\omega t)\delta a_n\right]dt$$

for $n = 1$, $a_n = a_1$ (assuming $a_n = 0$ for $n \leq 2$) we need to vary and minimise by $\frac{\delta\bar{s}}{\delta a_1} = 0$

$$\frac{\delta\bar{s}}{\delta a_1} = \frac{\pi}{\omega}(-\omega^2+\omega_0^2)a_1 - \int_0^T\left[\frac{\omega_0^2}{k}F_{ts}(s+s_0)cos(\omega t)\right]dt = 0 \tag{126}$$

with some rearranging

$$\omega = \omega_0\sqrt{1-\frac{\omega}{\pi k a_1}\int_0^T F_{ts}(s+s_0)cos(\omega t)dt} \tag{127}$$

then by using the substitution $u = cos(\omega t)$

$$\omega = \omega_0\sqrt{1+\frac{1}{\pi k a_1}\int_0^T F_{ts}(s+s_0)\frac{u}{\sqrt{1-u^2}}du} \tag{128}$$

the integral limits can be modified from $\int_0^T$ to $2\int_{-1}^1$ by considering the oscillation of the cantilever over one complete cycle and $T = \frac{2\pi}{\omega}$ so

$$\omega = \omega_0\left[1-\frac{2}{\pi k a_1}\int_{-1}^1 F_{ts}(s+s_0)\frac{u}{\sqrt{1-u^2}}du\right]^{\frac{1}{2}} \tag{129}$$

we can then approximate by $(1-x)^{\frac{1}{2}} \approx 1-\frac{1}{2}x$ so

$$\omega = \omega_0\left[1-\frac{1}{\pi k a_1}\int_{-1}^1 F_{ts}(s+s_0)\frac{u}{\sqrt{1-u^2}}du\right] \tag{130}$$

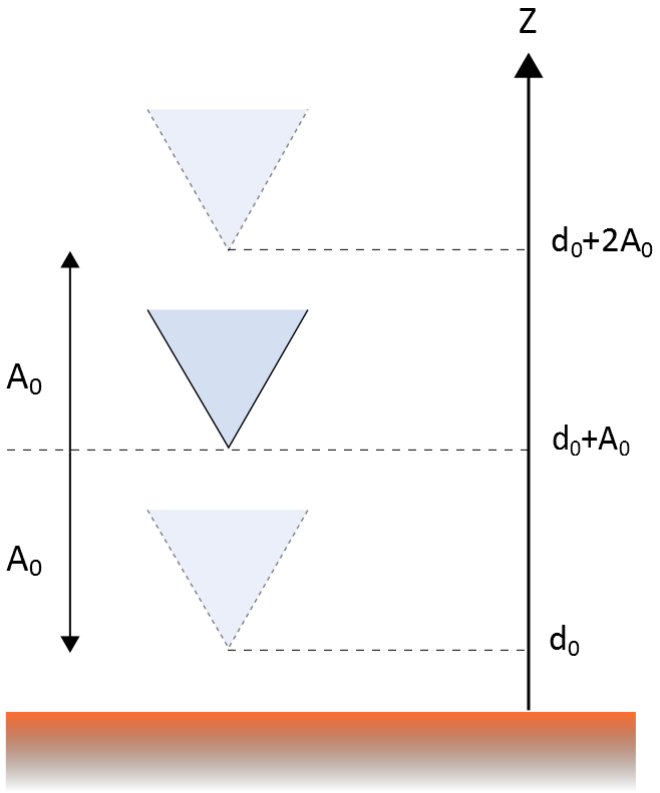

Figure 109: *Schematic showing the oscillating cantilever close to a surface. A_0 is the oscillation amplitude and d_0 is the distance of closest approach.*

now $a_1 = A_0$, $s = cos(\omega t)$ for $n = 1$, $s_0 = d_0 + A_0$ and $\Delta\omega = \omega - \omega_0$

$$\Delta\omega = -\frac{\omega_0}{\pi k A_0} \int_{-1}^{1} F_{ts} \left[A_0 cos(\omega t) + d_0 + A_0\right] \frac{u}{\sqrt{1-u^2}} du \tag{131}$$

and finally, $u = cos(\omega t)$, $\Delta\omega = 2\pi\Delta f$ and $\omega_0 = 2\pi f_0$ so

$$\Delta f = -\frac{f_0}{\pi k A_0} \int_{-1}^{1} F_{ts} \left[d_0 + A_0(1+u)\right] \frac{u}{\sqrt{1-u^2}} du \tag{132}$$

10.3 XSW

10.3.1 Reflectivity curves

Figure 110 shows the reflectivity curves for the ($\bar{1}11$) and (200) lattice orientations for ML $H_2O@C_{60}$ on Ag(111). Experimental values of E_{Bragg} are very close to their theoretical values of 2625eV and 3031eV respectively for ($\bar{1}11$) and (200) Ag planes. Broadening values for the respective planes are all approximately 1eV, suggesting a high quality crystal lattice structure beneath the surface. The asymmetry of the reflectivity curve (a physical effect of a reduction in scattering events as the standing wave propagates deeper into the single crystal, as defined by Darwin's extinction theory) for the (200) orientation is somewhat less pronounced than in the ($\bar{1}11$) plane.

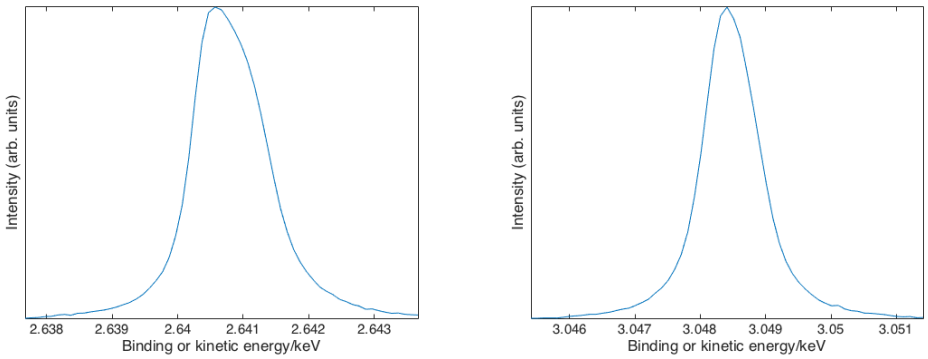

(b) ($\bar{1}11$) (c) (200)

Figure 110: *Reflectivity curves for the ($\bar{1}11$) and (200) Ag lattice orientations. Bragg energies 2640.8eV and 3048.5eV respectively.*

10.3.2 Ag Auger curves

Figure 111 shows the x-ray standing wave data for the Ag Auger measurements. For the ($\bar{1}11$) lattice, both coherent position and coherent fraction are also high at 0.963 and 1.00 respectively, with a broadening of 0.3eV.

This should be the same broadening as the (111) planes, but an increase could be due to a mosaic spread of angles in the crystal lattice. A broadening of 0.3eV will be used for subsequent ($\bar{1}11$) data. The (200) orientation has also a high coherent position of 1.00, but a lower coherent fraction of 0.827 is indicative of the x-ray picking up disorder parallel to the surface in this lattice direction. A broadening of 0.24eV will be used for (200) data.

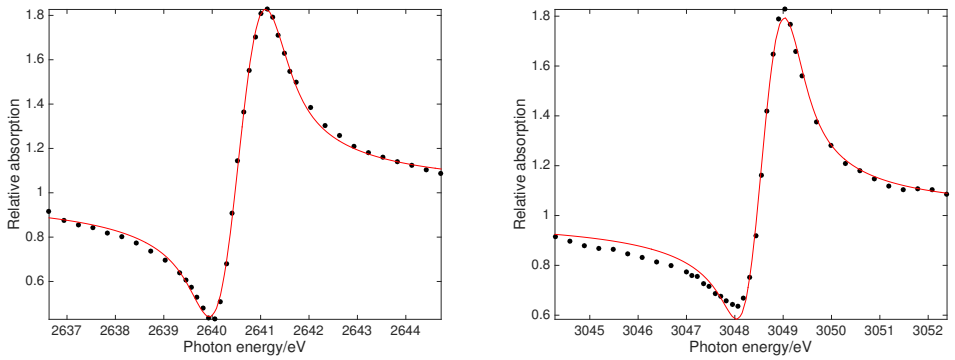

(b) ($\bar{1}11$) (c) (200)

Figure 111: *Ag Auger XSW data for the ($\bar{1}11$) and (200) Ag lattice orientations. Bragg energies 2639.98eV and 3048.16eV respectively.*

	($\bar{1}11$)	(200)
SB	0.306	0.235
$\mathbf{P}_c$	0.963	1.00
$\mathbf{F}_c$	1.00	0.827
$\mathbf{E}_{Bragg}$	2639.98	3048.14

Table 9: *Broadening (SB in eV), coherent position (P_c), coherent fraction (F_c), Q and Bragg energy (E_{Bragg} in eV) values for the Ag Auger data in Fig. 111.*

10.3.3 O1s XSW Mateck 2

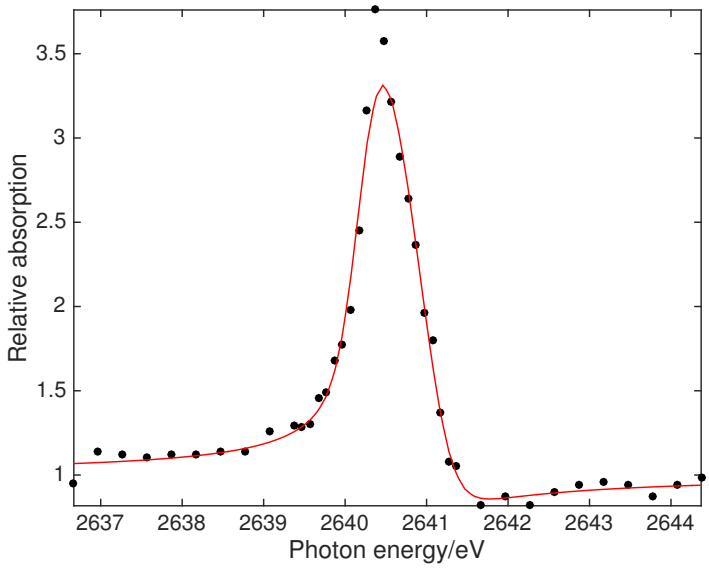

(b)

Figure 112: *Extra O1s XSW data for the (111) Ag lattice orientation. Bragg energy of 2640.07eV.*

	(b)
SB	0.19
$\mathbf{P}_c$	0.36
$\mathbf{F}_c$	1.00
$\mathbf{E}_{Bragg}$	2640.07

Table 10: *Values for the O1s XSW data in Fig. 112.*

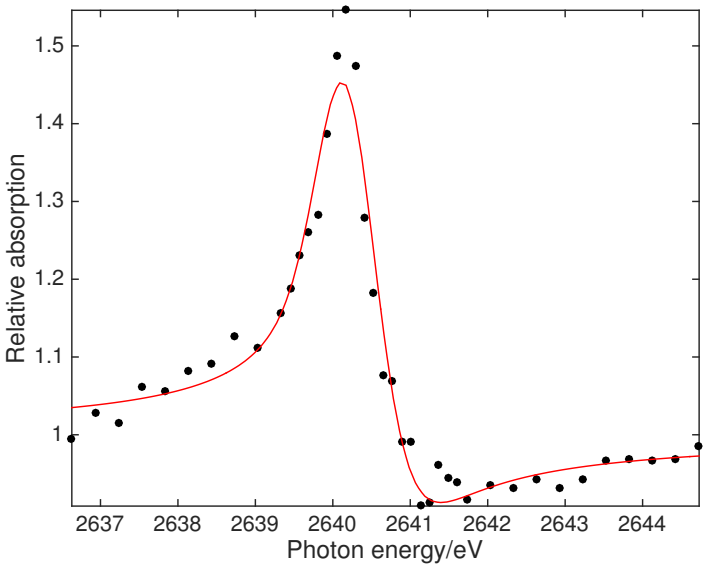

(b)

Figure 113: *Extra O1s XSW data for the ($\bar{1}11$) Ag lattice orientation. Bragg energy of 2639.98eV.*

	(b)
SB	0.30
$\mathbf{P}_c$	0.67
$\mathbf{F}_c$	0.43
$\mathbf{E}_{Bragg}$	2639.98

Table 11: *Values for the O1s XSW data in Fig. 113.*

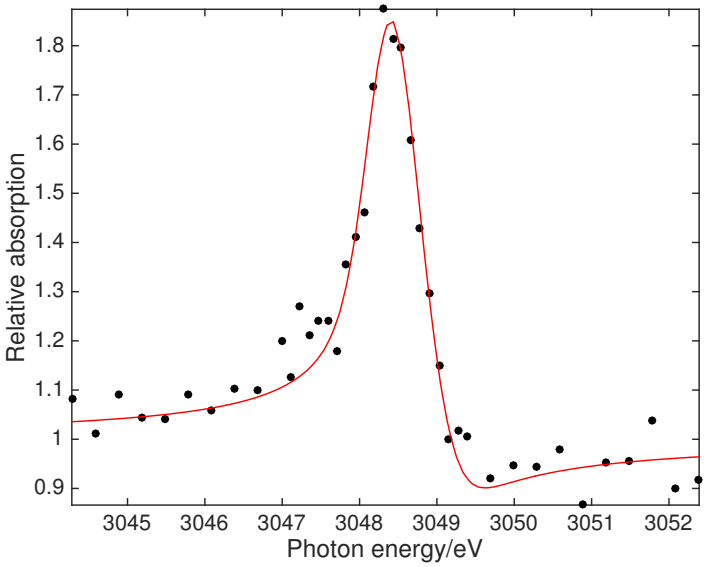

Figure 114: *O1s XSW data for the (200) Ag lattice orientation. Bragg energy 3048.14eV.*

	(b)
SB	0.24
$\mathbf{P}_c$	0.51
$\mathbf{F}_c$	0.36
$\mathbf{E}_{Bragg}$	3048.14

Table 12: *Values for the O1s XSW data in Fig. 114.*

10.3.4 Fitting technique

In synchrotron runs, a mass of data is accumulated in a HDF5 file. The data is of the form of a series of energy distribution curves (EDCs) of counts per second versus binding energy (BE) or kinetic energy (KE). The aim is to extract this data and plot an intensity versus photon energy plot to represent the standing wave data.

In short, it's a three step process. The EDCs and BE/KE values are extracted from the original HDF5 file containing the EDC counts (wave9++), the data is then read into the 'edcfitprog' which is then fitted using a series of Gaussian or Doniach-Šunjić fits and exported into intensity versus photon energy files (exfitpeak1), and finally, the data is imported into an NIXSW program to fit the structural parameters.

The most complicated and time consuming aspect is fitting the data in the 'edcfitprog' and requires special care. Typically, once the data is imported, most values need to be fixed (1) and estimated. A background is the first value to estimate (bkgrnd ht), whilst holding all other values fixed. Once the background looks reasonable, the positions of the peaks (peak 1 pos, peak 2 pos etc, in eV) that need fitting can be input. After the energy values have been fitted, values for the peak heights (peak 1 mult/ht) can be input followed by an estimate for the broadening of the peak (pk1sig, pk2sig etc). At this point the fit should be taking shape, and variables such as the 2nd poly const and bkgrnd ht can be changed to 0 to allow the program to fit more accurately. From personal experience, it's then best to release the fixing of other values one-by-one and not changing them all to vary simultaneously, otherwise the fitting may need to be started over from scratch.

Figure 115 shows an example of the edcfitprog in action, and shows a good fit to the data. Once the parameters are all free to vary with the fitting program, the noise of the fits can be reduced by fixing certain parameters again, such as the peak positions (in eV). The data once fitted and noise

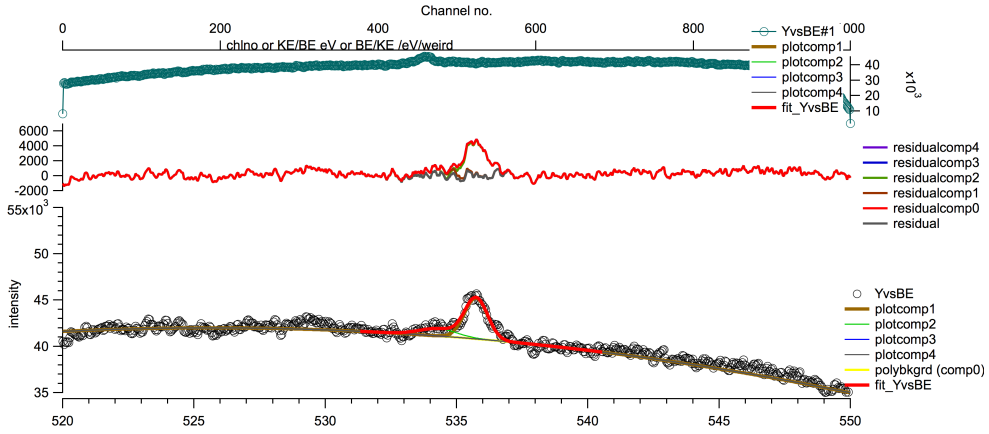

Figure 115: *An example of using the edcfitprog to fit imported data.*

reduction is achieved is then exported to determine the structural parameters for the XSW data.

Determining the structural parameters is much more simple than fitting in edcfitprog. The Q value is always zero, and the broadening is also fixed. Sometimes, strange values for the coherent position and fraction could occur (non-physical, either negative or above 1) so they would be fixed at sensible values then be allowed to vary once manually ensuring the fit is similar to the XSW data.

10.3.5 (200) plane techniques

By considering triangles ABC, ADE and AFG in Fig. 116, values for d_{200} can be calculated through simple trigonometry.

Consider line 1 to 2, at $n = 0$ then $m = 0$, the distance from an Ag atom to the O in atop or bridge A is

$$d_{200} = d_{111} sin(35.26°) \tag{133}$$

and for $n = 1$ and $m = 1$

$$d_{200} = (d_{111} + D_{111})sin(35.26^{\circ}) \tag{134}$$

and for $n = 2$ and $m = 2$

$$d_{200} = (d_{111} + 2D_{111})sin(35.26^{\circ}) \tag{135}$$

and in general

$$d_{200} = (d_{111} + mD_{111})sin(35.26^{\circ}) \tag{136}$$

By considering line 3 to 4, at $n = 0$ then $m = 2$, the distance from an Ag atom to the O in the fcc 3-fold hollow site is

$$d_{200} = (d_{111} + 2D_{111})sin(35.26^{\circ}) \tag{137}$$

and for $n = 1$ and $m = 0$

$$d_{200} = d_{111}sin(35.26^{\circ}) \tag{138}$$

and for $n = 2$ and $m = 1$

$$d_{200} = (d_{111} + D_{111})sin(35.26^{\circ}) \tag{139}$$

By considering line 5 to 6, at $n = 0$ then $m = 1$, the distance from an Ag atom to the O in the hcp 3-fold hollow site is

$$d_{200} = (d_{111} + D_{111})sin(35.26^{\circ}) \tag{140}$$

and for $n = 1$ and $m = 2$

$$d_{200} = (d_{111} + 2D_{111})sin(35.26^{\circ}) \tag{141}$$

and for $n = 2$ and $m = 0$

$$d_{200} = d_{111}sin(35.26^{\circ}) \tag{142}$$

Finally, by considering line 7 to 8 and triangle HIJ, at $n = 0$ then $m = 3/4$, the distance from an Ag atom to the O in the bridge B site is

$$d_{200} = (d_{111} + \frac{3D_{111}}{4})sin(35.26^{\circ}) \tag{143}$$

and for $n = 1$ and $m = 7/4$

$$d_{200} = (d_{111} + \frac{7D_{111}}{4})sin(35.26^{\circ}) \tag{144}$$

and for $n = 2$ and $m = 11/4$

$$d_{200} = (d_{111} + \frac{11D_{111}}{4})sin(35.26^{\circ}) \tag{145}$$

10.3.6 The (200) plane

Figure 116 shows a detailed illustration of the triangulation procedure for the Ag (200) plane. The value of d_{200} for the O in different sites (atop, hcp 3-fold hollow, bridge 2-fold and hcp 3-fold hollow) and different distances (n=0, 1, 2, etc) out from the surface can be predicted. The distance z_{200} is calculated from the (200) planes, and subtracted from multiples of nD_{200} to get a value for d_{200} between 0 and D_{200}.

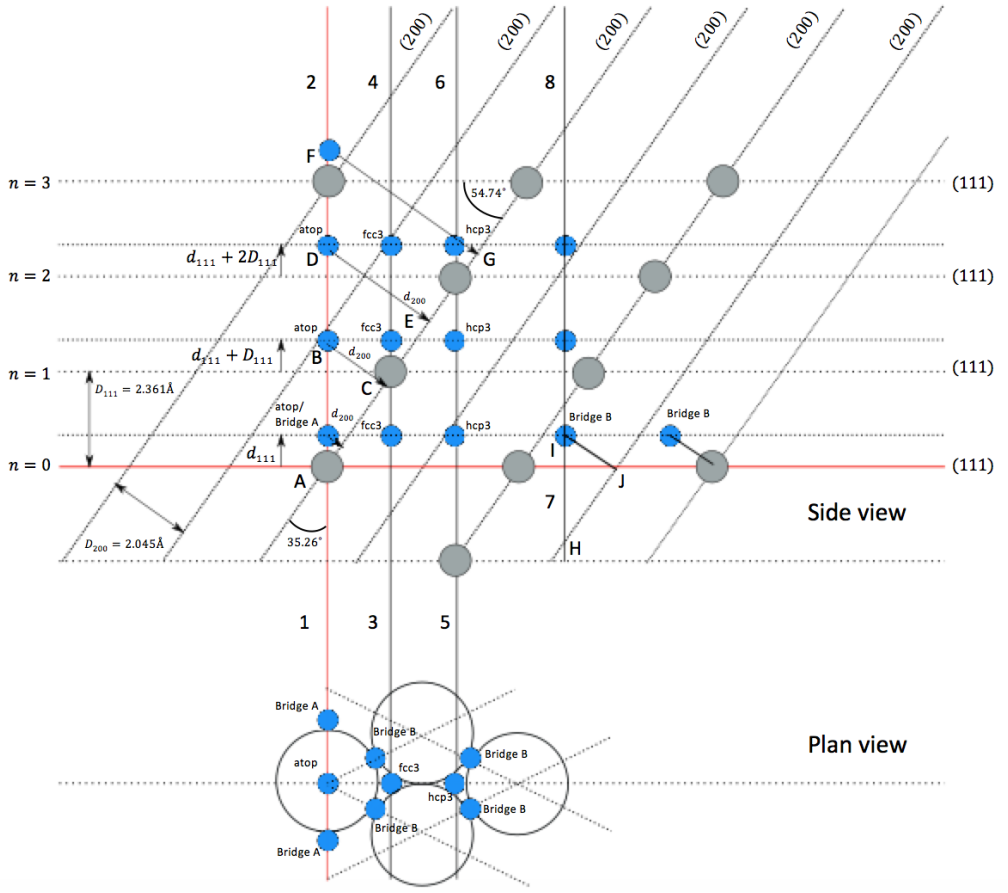

Figure 116: *Illustration showing a side-on view of the (200) plane ((111) plane indicated), and a plan view with possible O (blue circles) positions above the Ag (grey circles) surface layer (n=0).*

The experimental average for the coherent position in the (111) plane is $P_c = 0.513$, multiplying this by $D_{200} = 2.045$Å gives a value of $d_{111} = 1.049$Å in real units. Furthermore

$$z_{200} = (d_{111} + mD_{111})sin(\theta) \tag{146}$$

and inserting values for P_c, n and d_{111}, and θ (refer to Fig. 116)

$$z_{200} = (0.878 + m(2.361))sin(35.26°) \tag{147}$$

d_{200} values can then be calculated for different heights, n, above different adsorption sites. For bridge sites A and B, p denotes the relative population (i.e. for 1 unit cell, there is 4 bridge B sites and 2 bridge A sites, so $p = 2/3$ and $p = 1/3$ respectively). Total bridge sites is given by site B with a max coherent fraction of 1/3.

Adsorption site	$n = 0$	$n = 1$	$n = 2$
atop	$m = 0$ 0.509Å	$m = 1$ 1.870Å	$m = 2$ **1.188**Å
hcp 3-fold hollow	$m = 1$ 1.870Å	$m = 2$ **1.188**Å	$m = 0$ 0.507Å
2-fold bridge A	$m = 0$ $p = 1/3$ 0.507Å	$m = 1$ $p = 1/3$ 1.870Å	$m = 0$ $p = 1/3$ 1.188Å
2-fold bridge B	$m = 3/4$ $p = 2/3$ 1.529Å	$m = 7/4$ $p = 2/3$ 0.847Å	$m = 11/4$ $p = 2/3$ 0.165Å
Total bridge	1.529Å	**0.847**Å	0.165Å
fcc 3-fold hollow	$m = 2$ **1.188**Å	$m = 0$ 0.507Å	$m = 1$ 1.870Å

Table 13: *Possible adsorption sites for O on Ag in the (200) plane.*

From Table 13, the experimental value of $d_{200} = 1.109$Å agrees with the atop adsorption site with order $n = 2$ and 1.188Å for z_{111}.

10.3.7 The ($\bar{1}11$) plane

A similar procedure to the (200) plane calculations was done for the ($\bar{1}11$) plane. The distance $z_{\bar{1}11}$ is calculated from the ($\bar{1}11$) planes, and subtracted from multiples of $D_{\bar{1}11}$ to get a value for $d_{\bar{1}11}$ between 0 and $D_{\bar{1}11}$.

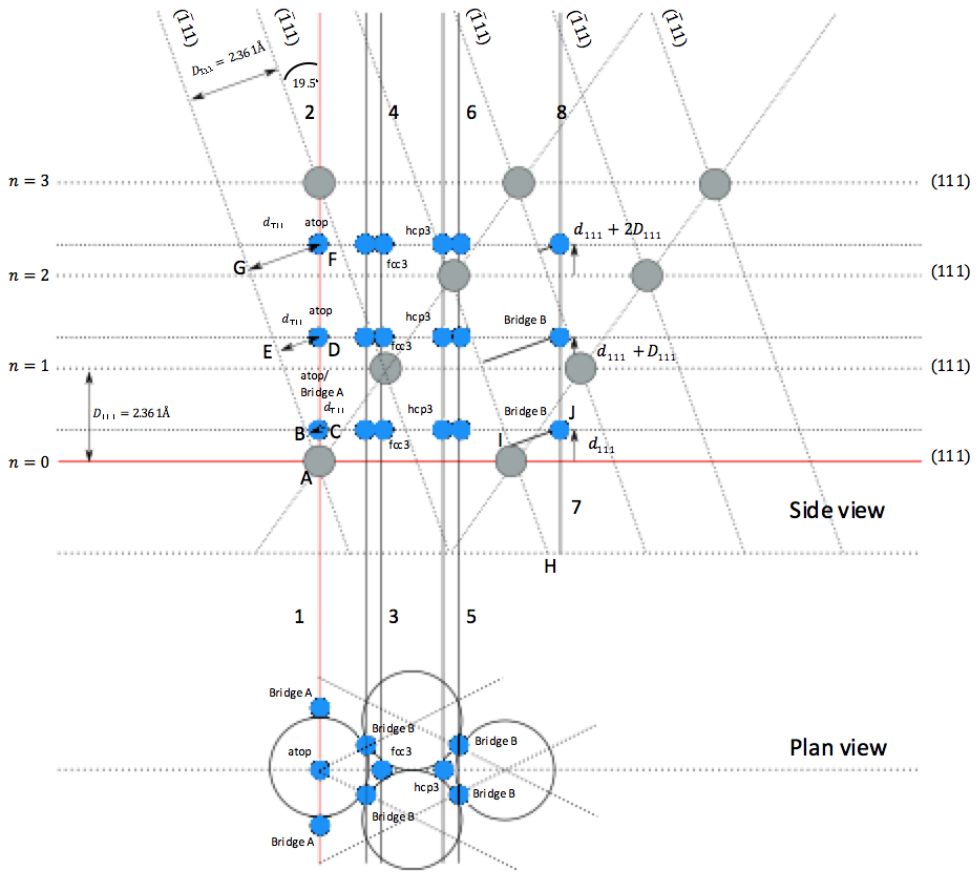

Figure 117: *Illustration showing a side on view of the ($\bar{1}$11) plane ((111) plane indicated), and a plan view with possible O (blue circles) positions above the Ag (grey circles) surface layer (n=0).*

Figure 117 shows a detailed illustration of the triangulation procedure for the Ag ($\bar{1}$11) plane. As for the (200) plane, a table of possible values can be predicted for the adsorption site of the O atom above the Ag atoms, as shown in Table 14.

In general

$$z_{\bar{1}11} = (d_{111} + mD_{111})sin(\theta) \tag{148}$$

and plugging in experimental values

$$z_{\bar{1}11} = (1.613 + m(2.361)sin(19.5^\circ) \tag{149}$$

where $d_{\bar{1}11} = 2.361$Å multiplied by the coherent position $P_c = 0.683$ to get 1.613Å for the experimental $(\bar{1}11)$ data.

Adsorption site	$n = 0$	$n = 1$	$n = 2$
atop	$m = 0$ 0.293Å	$m = 1$ 1.081Å	$m = 2$ **1.869**Å
hcp 3-fold hollow	$m = 1$ 1.081Å	$m = 2$ **1.869**Å	$m = 0$ 0.293Å
2-fold bridge A	$m = 0$ $p = 1/3$ 0.293Å	$m = 1$ $p = 1/3$ 1.081Å	$m = 0$ $p = 1/3$ 1.869AA
2-fold bridge B	$m = 3/2$ $p = 2/3$ 1.475Å	$m = 5/2$ $p = 2/3$ 2.263Å	$m = 1/2$ $p = 2/3$ 0.687Å
Total bridge	**1.475**Å	2.263Å	0.687Å
fcc 3-fold hollow	$m = 2$ **1.869**Å	$m = 0$ 0.293Å	$m = 1$ 1.081Å

Table 14: *Possible adsorption sites for O on Ag in the* $(\bar{1}11)$ *plane.*

With reference to Table 14, the experimental value of $d_{\bar{1}11} = 1.869$Å agrees with the atop adsorption site with order $n = 2$ and 1.869Å for $z_{\bar{1}11}$.